

# **Hydrogen-rich syngas production from waste biomass using pyrolysis with non-thermal plasma-catalysis tar reduction**

Ella Blanquet

Submitted in accordance with the requirements for the degree of  
Doctor of Philosophy

The University of Leeds  
CDT of Bioenergy  
School of Chemical and Process Engineering

October 2019

The candidate confirms that the work submitted is his/her own, except where work which has formed part of jointly-authored publications has been included. The contribution of the candidate and the other authors to this work has been explicitly indicated below. The candidate confirms that appropriate credit has been given within the thesis where reference has been made to the work of others.

This copy has been supplied on the understanding that it is copyright material and that no quotation from the thesis may be published without proper acknowledgement.

### **Journal Papers**

Chapter 5 was based on the following published paper:

1. Blanquet, E., Nahil, M.A., and Williams, P.T. (2019) Enhanced hydrogen-rich gas production from waste biomass using pyrolysis with non-thermal plasma-catalysis. *Catalysis Today*, 337, 216-224.

### **Conference Contributions**

1. Blanquet, E., Nahil, M.A., and Williams, P.T. Non-thermal plasma-catalytic processing for tar reduction to deliver high quality syngas from real biomass gasification, In the 25<sup>th</sup> edition of the European Biomass Conference and Exhibition, Stockholm, Sweden, 2017.
2. Blanquet, E., Nahil, M.A., and Williams, P.T. Reduction of tars from real biomass gasification by a non-thermal plasma-catalytic system, In the 23<sup>rd</sup> International Symposium on Plasma Chemistry, Montreal, Canada, 2017.
3. Blanquet, E., Nahil, M.A., and Williams, P.T. Reduction of tar compounds and production of high quality syngas from biomass gasification by non-thermal plasma-catalysis, In the 22<sup>nd</sup> International Symposium on Analytical and Applied Pyrolysis, Kyoto, Japan, 2018.
4. Blanquet, E., Nahil, M.A., and Williams, P.T. Non-Thermal Plasma-Catalytic System Downstream of a Real Biomass Gasification Reactor to Reduce Tar Compounds and Produce High Quality Syngas, In the 11<sup>th</sup> International Symposium on Non-Thermal/Thermal Plasma Pollution Control Technology & Sustainable Energy, Montegrotto Terme, Italy, 2018.

The candidate Ella Blanquet performed the experimental and analytical work, wrote the initial drafts of the papers along with supporting material, and carried out the calculation and summarization of the results and developed the discussion part.

The co-author, Prof. P. T. Williams supervised and supported the entire research work, proofread the drafts and made suggestions and corrections to the draft papers. Co-author Nahil helped with the development of the analytical work.

The right of Ella Blanquet to be identified as Author of this work has been asserted by her in accordance with the Copyright, Designs and Patents Act 1988.

© 2019 The University of Leeds and Ella Blanquet

## Acknowledgements

I would like to thank all the people who have helped and supported me during my doctoral study. First and foremost, I would like to express my deepest and sincere gratitude to my supervisor Prof. Paul T. Williams, for his continuous support, guidance and help throughout my PhD. Thank you for always being available, for sharing your knowledge and for your endless trust and support during this project. I am very fortunate to have had such a valuable assistance and admirable supervisor.

I am grateful to the UK Engineering and Physical Sciences Research Council, who financed my research through EPSRC Grants EP/M013162/1 and EP/L014912/1. I would like to acknowledge the support from the Royal Society of Chemistry and Energy Leeds for the funding to present my research in an international conference in Canada and Italy respectively. Also, I would like to thank the European Union Horizon 2020 research and innovation programme (Flexi-pyrocat, No.:643322), for providing funding for my two-month research stays at the Department of Engineering Physics, Tsinghua University, Beijing, China and at the Laboratory for Catalysis Engineering, School of Chemical and Biomolecular Engineering, at the University of Sydney, Australia.

I want to especially thank Dr. Mohamad Anas Nahil for his support and guidance during the past four years. Special thanks are extended to Ed Woodhouse and Kevin Dyer, for their help with technical support in the design and modification of the plasma reactors. I also would like to thank the members of Paul's lab for their help and support: Dr. Yeshui, Kenneth, Andrew, Japhet, Peace, Julius, Aaron, Mussab, Rayed and Idris. I am grateful for the opportunity to meet and work with many friendly researchers, past and present members of CDT of Bioenergy and CP3. In particular, I would like to thank Jeni, Natalie, Alex, Ben, Iram, Nicola, Charlotte, Daisy, Sam, David and Rick. It has been a great experience to work with you all. I also want to thank the management team of the CDT, especially Emily Bryan-Kinns and James McKay for their continuous help and support throughout these four years.

Finally, I would like to thank my friends and family, for being always accessible from across the Channel or at the other side of the planet. I would not have made it this far without your unconditional support and distractions. Above all, I am most grateful to my husband, Jonathon, for his unconditional help, support and sense of direction, helping me maintaining a clear focus in everything I do.

## Abstract

Biomass and organic biomass waste can be used as feed into thermal processes such as pyrolysis and/or gasification to produce syngas enriched in hydrogen. However, the process yield is significantly reduced by limitations arising from the formation of tars. In this work, a two-stage fixed bed reactor system was used for hydrogen-rich syngas production and tar reduction, with a first stage of pyrolysis of biomass, then using a plasma-catalytic steam reforming system as a second stage reactor. First, Biomass was pyrolyzed at 600°C and the produced vapours passed through to the second plasma-catalytic stage, where plasma and catalytic reactions occurred in the presence of steam, to produce syngas and reduce tar compounds. Different analytical techniques were used to characterise biomasses, produced gases, produced liquid (tars/oils) and fresh/reacted catalysts. First, the pyrolysis of various biomasses was studied to investigate the composition of the vapour produced by biomass pyrolysis before entering the plasma-catalytic system. Waste wood was used as the feedstock.

Second, the use of a dielectric barrier discharge (DBD) plasma-catalytic reactor was investigated. The study of the effect of plasma revealed that pyrolysis-plasma-catalysis resulted in the highest hydrogen and syngas production, the highest gas yield, the lowest tar content and lowest coke deposition, when compared to pyrolysis-catalysis, with a tar reduction of 64% and a coke reduction of 25%, and pyrolysis-plasma systems, with a tar reduction of 21%. Toluene was used to confirm the reproducibility of literature results using tar model compounds with the experimental setup. The components of biomass were studied to identify that a high content of lignin in biomass might favour methane and tar production, whereas a high cellulose content might promote higher syngas production. The influence of power input showed that with increase power, more hydrogen-rich syngas produced, more tar compounds reduced, and less coke deposited. The study of steam flow rate demonstrated the presence of an optimum steam flow rate for a given power input to stimulate steam reforming and avoid water saturation on the catalyst active sites, such as an optimal steam flow rate of 2 g/h for a power input of 40 W. The influence of catalyst particle size showed that larger particle size resulted into stronger interaction between the plasma and the catalyst through the increase of void space and filamentous discharges. The study of catalyst/feedstock ratio demonstrated that more

catalyst in the plasma-catalytic system, i.e. a catalyst/feedstock ratio of 2 compared to a ratio of 0.5 and 1, led to more hydrogen and syngas produced and to more efficient reduction of tar compounds.

Third, a more in-depth study of the catalyst was conducted. The effect of metal promoters, 5 wt.% Mg, Co, Ce, Cu, Fe and Ni added to 5 wt.% Ni supported on alumina catalysts was studied. Metal promoters did not seem to have a strong influence on the results obtained with a 10 wt.% nickel supported on alumina catalyst as syngas production and tar compound reduction were similar for all studied promoters, with a slight increase in syngas production using Ce (+3% compared to 10 wt.% Ni catalysts) and a slight decrease using Cu (-6% compared to 10 wt.% Ni catalysts). To further investigate the influence of catalyst metal, the effect of Ni loading on an alumina catalyst, with loadings of 0, 5 and 10 wt.%, was investigated. These result variations did not seem significant to determine a clear advantage into choosing a specific catalyst. Finally, the study of different catalyst supports on the pyrolysis-plasma-catalysis of biomass process was studied, using Alumina, titanium oxide and Y-zeolite catalysts for the wide spectra of applications they covered – from steam reforming enhancement and photo-catalysis to oil cracking and refining – and their different properties. The results varied depending on the support used, with their main differences were the pore size, the dielectric constant, and the surface area. To obtain a higher syngas quality, the use of alumina can be recommended with more than 7.1 mmol of syngas per gram of feedstock; whereas to obtain a lower tar content, the use of y-zeolite should be encouraged with a detected tar content below 20 mg.m<sup>-3</sup>. Thus, the use of pyrolysis-plasma-catalysis to obtain high quality syngas and higher tar reduction seemed mainly influenced first by the pore size when choosing a catalyst support, followed by the surface area and the dielectric constant of the support.

Finally, the plasma-catalysis process has been investigated to produce hydrogen-rich syngas using biomass and its components for a packed bed DBD plasma-catalytic system. The influence of plasma was investigated for the different feedstocks. The results showed that plasma-catalysis processes with a packed bed DBD configuration, led to higher production of syngas (+38%), higher production of hydrogen (+49%) and lower weight loss (-3%), compared to the pyrolysis-catalysis system. Within the biomass, high content of cellulose might result into higher syngas production and

higher productions of carbon monoxide, carbon dioxide and hydrogen; whereas high content lignin might favour higher production of methane. The influence of power input demonstrated that with increasing power input, syngas production increased, as well as hydrogen production, at a given packing bed length. At a given power input, the influence of packing bed length showed that increasing the packing bed length decreased the syngas production and hydrogen production. Finally, the amount of coke deposition was negligible in all reacted packing material.

Overall, this research demonstrates that the use of plasma-catalytic systems is a promising low-energy and low-cost process to generate hydrogen-rich syngas and reduce tar compounds from biomass pyrolysis.

## Table of Contents

<b>Acknowledgements</b> .....	<b>iii</b>
<b>Abstract</b> .....	<b>v</b>
<b>Table of Tables</b> .....	<b>xii</b>
<b>Table of Figures</b> .....	<b>xiv</b>
<b>Chapter 1: Introduction</b> .....	<b>21</b>
1.1. Energy challenge and climate change .....	21
1.2. Bioenergy and energy recovery from waste .....	23
1.2.1. Bioenergy .....	23
1.2.2. Energy recovery from waste.....	24
1.2.3. Thermochemical conversion processes.....	24
1.3 Waste as a feed source .....	26
1.3.1. Municipal Solid Waste (MSW) and organic biomass waste .....	27
1.3.2. Biomass.....	27
1.4. Description and objective of this research .....	28
<b>Chapter 2: Literature review</b> .....	<b>32</b>
2.1. Pyrolysis systems .....	32
2.1.1 Basic principle .....	32
2.1.2 Available technologies .....	36
2.1.3 Pyrolysis of biomass components .....	39
2.1.4 Biomass pyrolysis.....	41
2.2. Gasification systems .....	45
2.2.1. Basic principle.....	45
2.2.2. Available technologies: types of gasification, state of art and current plants .....	45
2.2.3. Technical issue of syngas .....	49
2.2.4. Gas cleaning processes .....	52
2.3. Plasma systems .....	61
2.3.1. Principle and classification of plasma technologies.....	61
2.3.2. Thermal and non-thermal plasmas. ....	66
2.3.3. Non-thermal plasma and different generation methods.....	70
2.4. Plasma-catalysis systems.....	81
2.4.1. Type of plasma-catalytic reactors .....	81
2.4.2. Synergetic effect of plasma-catalytic systems .....	83

2.4.3. Effect of the addition of catalyst on a plasma discharge .....	84
2.4.4. Effect of plasma on catalysis .....	86
2.4.5. Catalyst selection for plasma-catalytic systems .....	95
2.5 Hydrogen rich syngas generation and reduction of tar compounds with plasma-catalysis systems .....	97
2.5.1 Generation of syngas using plasma-catalytic system .....	97
2.5.2 Tar reduction using plasma-catalytic systems.....	100
<b>Chapter 3: Materials and Methods .....</b>	<b>106</b>
3.1 Materials .....	106
3.1.1 Biomass samples .....	106
3.1.2 Researched catalysts .....	109
3.2 Experimental methods .....	121
3.2.1 Pyrolysis system.....	121
3.2.2 Dielectric Barrier Discharge (DBD) plasma-catalytic system....	126
3.2.3 Packed-bed Dielectric Barrier Discharge (DBD)plasma- catalytic system .....	132
3.3 Characterisation of materials and products .....	144
3.3.1 Sample characterisation.....	144
3.3.2 Catalyst characterisation.....	148
3.3.3 Gas product analysis .....	155
3.3.4 Oil sample characterisation .....	161
<b>Chapter 4: Pyrolysis of different feedstocks. ....</b>	<b>169</b>
4.1 Gas composition.....	169
4.2 Solid Phase Adsorption (SPA)tar sampling method results.....	172
4.3 Summary.....	176
<b>Chapter 5: Dielectric barrier discharge (DBD) plasma-catalysis to produce high-quality syngas and reduce tar compounds .....</b>	<b>177</b>
5.1 Plasma effect .....	178
5.1.1 Plasma effect on gas production .....	178
5.1.2 Plasma effect on tar reduction .....	182
5.1.3 Plasma effect on reacted catalyst .....	194
5.2 Tar model compounds and biomass components used as feedstock in the DBD plasma-catalytic reactor .....	196
5.2.1 Toluene .....	196
5.2.2 Biomass components: cellulose and lignin.....	200

5.3. Study of different process parameters .....	211
5.3.1 Input power effect.....	211
5.3.2 Steam effect .....	218
5.3.3 Catalyst particle size effect .....	223
5.3.4 Ratio Catalyst/Feedstock effect .....	228
5.4 Summary.....	232
<b>Chapter 6: Study of the catalytic effect on DBD plasma-catalysis .....</b>	<b>234</b>
6.1 Effect of metal promoters on 5 wt.% Ni supported on alumina .....	235
6.1.1 Metal promoter effect on gas production .....	235
6.1.2 Metal promoter effect on tar reduction .....	238
6.1.3 Metal promoter effect on reacted catalyst .....	243
6.2 Effect of Nickel loading on plasma-catalysis .....	246
6.2.1 Nickel loading effect on gas production .....	246
6.2.2 Nickel loading effect on tar reduction .....	249
6.2.3 Nickel loading effect on reacted catalyst .....	252
6.3 Effect of catalyst support.....	253
6.3.1 Catalyst support effect on gas production .....	253
6.3.2 Catalyst support effect on tar reduction .....	257
6.3.3 Catalyst support effect on reacted catalyst .....	260
6.4 Summary.....	265
<b>Chapter 7: Packed-bed DBD plasma-catalysis to produce higher quality syngas.....</b>	<b>267</b>
7.1 Tar model compounds and biomass components used as feedstock in the packed-bed DBD plasma-catalytic reactor.....	267
7.1.1 Effect on gas production.....	268
7.1.2 Effect on reacted catalyst.....	277
7.2 Packing length and input power effect .....	279
7.2.1 Effect on gas production.....	279
7.2.2 Effect on reacted catalyst.....	286
7.3 Summary.....	289
<b>Chapter 8: Conclusions and Future Work .....</b>	<b>290</b>
8.1 General conclusions.....	290
8.1.1 Analysis of gas and vapour products from pyrolysis of selected biomasses: wood pellets, corn stalk, peanut shell and coconut shell .....	290

8.1.2 Study of the dielectric barrier discharge (DBD) plasma-catalysis system via the effect of plasma, the use of biomass components – cellulose and lignin – and the influence of different operating parameters .....	291
8.1.3 Study of influence of the catalyst promoters, metal loading and catalyst support on the DBD plasma-catalysis .....	292
8.1.4 Study of the packed bed DBD plasma-catalytic reactor through the effect of plasma, the effect of biomass components – cellulose, hemi-cellulose and lignin – and the study of the influence of different operating parameters .....	294
8.1.5 General remarks .....	295
8.2 Future work .....	295
8.2.1 Analysis and study of the electrical parameters .....	296
8.2.2 Optimisation of packed-bed DBD reactor .....	296
8.2.3 Further study of influence of the catalyst on the DBD plasma-catalysis from biomass pyrolysis .....	296
8.2.4 Use of different feedstocks within the plasma-catalytic system .....	296
8.2.5 Mechanism or pathways to draw from the decomposition of biomass pyrolysis products in plasma-catalysis system .....	297
<b>References .....</b>	<b>298</b>

## Table of Tables

<b>Table 2.1-1: Evolution of pyrolysis reactions depending on temperature (Bilitewski et al., 1997; Astrup and Bilitewski, 2010) .....</b>	<b>33</b>
<b>Table 2.1-2: Characteristics of general pyrolysis products (Tchobanoglous et al., 1993; Astrup and Bilitewski, 2010) .....</b>	<b>33</b>
<b>Table 2.1-3: Yield of products for different types of pyrolysis of woody biomass (Bridgwater, 2006) .....</b>	<b>34</b>
<b>Table 2.1-4: Properties of bio-oil, petroleum light and heavy fuel oils (Mohan et al., 2006) .....</b>	<b>35</b>
<b>Table 2.1-5: Types and characteristics of pyrolysis reactors (Wang et al., 2014).....</b>	<b>37</b>
<b>Table 2.3-6: Main characteristics of thermal and non-thermal plasmas (Tendero et al., 2006; Go, 2012; Mei, 2016) .....</b>	<b>68</b>
<b>Table 3.1-1: Feedstock analysis of different biomasses .....</b>	<b>107</b>
<b>Table 3.1-2: Ultimate analysis (as received) of different biomasses .....</b>	<b>108</b>
<b>Table 3.1-3: Feedstock analysis of the components of biomass (wood pellet) .....</b>	<b>109</b>
<b>Table 3.1-4: Ultimate analysis (as received) of the components of biomass (wood pellet) .....</b>	<b>110</b>
<b>Table 3.1-5: Alumina catalyst characteristics for different diameter sizes ....</b>	<b>111</b>
<b>Table 3.1-5: Characteristics of different catalyst supports.....</b>	<b>114</b>
<b>Table 3.1-6: Characteristics of different packings for DBD plasma-catalytic reactor .....</b>	<b>119</b>
<b>Table 3.2-2: General and gas analysis summary for validation of the pyrolysis reactor .....</b>	<b>124</b>
<b>Table 3.2-1: SPA analysis summary for validation of the pyrolysis reactor with A.C. Average Concentration, Std. Dev. Standard Deviation and Re.Std.Dev. Relative Standard Deviation.....</b>	<b>125</b>
<b>Table 3.2-2: General and gas analysis summary for validation of the DBD plasma-catalysis reactor .....</b>	<b>132</b>
<b>Table 3.2-3: Oil analysis summary for validation of the DBD plasma-catalysis reactor .....</b>	<b>132</b>
<b>Table 3.2-4: Results of non-heated reactor trials .....</b>	<b>135</b>
<b>Table 3.2-5: Results of heated reactor trials .....</b>	<b>138</b>
<b>Table 3.2-6: General and gas analysis summary for validation of the packed-bed DBD plasma-catalysis reactor .....</b>	<b>144</b>
<b>Table 3.3-1: Reproducibility of GC analysis.....</b>	<b>160</b>

<b>Table 3.3-2: List of selected compounds used as standards for GC-MS calibration .....</b>	<b>165</b>
<b>Table 4.1-1: General product composition after pyrolysis.....</b>	<b>170</b>
<b>Table 4.2-1: Tar analysis via SPA method.....</b>	<b>175</b>
<b>Table 5.1-1: Experimental summary for identifying the effect of plasma .....</b>	<b>179</b>
<b>Table 5.2-1: Experimental summary for experiments using toluene as a tar model compound .....</b>	<b>197</b>
<b>Table 5.2-2: Experimental summary for pyrolysis-catalysis, pyrolysis-plasma and plasma-catalysis experiments using biomass components..</b>	<b>202</b>
<b>Table 5.3-1: Experimental summary for different power input.....</b>	<b>212</b>
<b>Table 5.3-2: Experimental summary for different steam flows at a power input of 40 W .....</b>	<b>218</b>
<b>Table 5.3-3: Experimental summary for different catalyst particle sizes .....</b>	<b>224</b>
<b>Table 5.3-4: Experimental summary for different catalyst/feedstock ratios..</b>	<b>228</b>
<b>Table 6.1-1: Experimental summary for identifying the effect of metal promoters .....</b>	<b>236</b>
<b>Table 6.1-2: Particle size for different metal promoters at <math>2\theta=51.8^\circ</math> .....</b>	<b>243</b>
<b>Table 6.2-1: Experimental summary for identifying the effect of Nickel loading.....</b>	<b>247</b>
<b>Table 6.3-1: Experimental summary for identifying the effect of catalyst support .....</b>	<b>255</b>
<b>Table 6.3-2: Crystallite size for different catalyst supports at <math>2\theta=44.5^\circ</math> .....</b>	<b>260</b>
<b>Table 7.1: Experimental summary for pyrolysis-catalysis and plasma-catalysis experiments using biomass components .....</b>	<b>275</b>
<b>Table 7.2-1: Experimental summary for different power input and different packing length .....</b>	<b>284</b>
<b>Table 8.1-1: Comparison of Thermal catalysis and Plasma-catalysis for syngas production .....</b>	<b>295</b>

## Table of Figures

<b>Figure 1.1-1: (a) Observed globally average combined land and ocean surface temperature anomalies between 1850 and 2012 (b) Observed changes in atmospheric greenhouse gas generation concentrations. (IPCC, 2014) .....</b>	<b>21</b>
<b>Figure 1.1-2: Global anthropogenic greenhouse gas emissions (IPCC, 2014).....</b>	<b>22</b>
<b>Figure 1.3-1: Global waste composition (Kaza et al., 2018) .....</b>	<b>27</b>
<b>Figure 2.1-4: Pyrolysis steps for various process temperature .....</b>	<b>32</b>
<b>Figure 2.5-2: Pathways to upgrade bio-oil to biofuel(Bridgwater, 2012).....</b>	<b>38</b>
<b>Figure 2.6-3: Example of partial molecular structures of common woody cellulose, hemi-cellulose and lignin (Pettersen, 1984).....</b>	<b>39</b>
<b>Figure 2.2-7: Relation between scale, efficiency and technology for electricity production in the case of biomass gasifiers (Bridgwater, 2006).....</b>	<b>48</b>
<b>Figure 2.3-1: Sunspot, taken by NASA’s TRACE (Transition Region and Coronal Explorer) in September 2000, and showing in bright red the gas emissions (about 1 million degrees) and in dark the absorbing structures (about 10,000 degrees). (NASA, 2015).....</b>	<b>61</b>
<b>Figure 2.3-2: Principles of plasma generation. (Conrads and Schmidt, 2000).....</b>	<b>62</b>
<b>Figure 2.3-3: Voltage-current characteristic in a DC atmospheric pressure electrical discharge tube (Roth, 2001) .....</b>	<b>63</b>
<b>Figure 2.3-4: Diverse plasma configurations with different appearance and chemical characteristics (a) Microwave (MW), (b) DC torch, (c) dielectric barrier discharge (DBD), (d) Pulse corona discharge (PCD), (e) Rotating arc (RA), (f) Spark. (Lee et al., 2013).....</b>	<b>64</b>
<b>Figure 2.3-5: Plasma temperatures and densities (Fridman, 2008).....</b>	<b>65</b>
<b>Figure 2.3-6: Types of corona discharges (Chang et al., 1991).....</b>	<b>74</b>
<b>Figure 2.3-7: Evolution of a gliding arc discharge: (A) reagent gas break-down; (B) equilibrium heating phase; (C) non-equilibrium reaction phase. (Fridman et al., 1999) .....</b>	<b>75</b>
<b>Figure 2.3-8: Ions and electrons frequencies in non-thermal plasmas.(Tendero et al., 2006) .....</b>	<b>76</b>
<b>Figure 2.3-9: Different types of RF discharges.(Eliasson and Kogelschatz, 1991).....</b>	<b>77</b>
<b>Figure 2.3-10: Common configurations of dielectric-barrier discharges with planar configuration (a, b, c) and cylindrical configuration (d). (Fridman, 2008) .....</b>	<b>79</b>

Figure 2.3-11: Schematic of a packed-bed corona discharge.(Fridman, 2008).....	80
Figure 2.4-1: Types of plasma-catalyst reactors according to catalyst bed position and number (Kim et al., 2016) .....	82
Figure 2.4-2: Synergetic effect of plasma-catalysis for destruction of toluene at 25°C. (Whitehead, 2010) .....	84
Figure 2.4-3:Major components of plasma with electrons (e), photons (hv), neutral molecule (N), excited molecule (E*), positive ion (Po) and negative ion (Ne). (Kim et al., 2016) .....	87
Figure 2.4-4: Characteristic timescales in plasma and catalytic reaction (Kim et al., 2016).....	90
Figure 2.4-5: Illustration of the mechanisms to enhance the performance of a single stage plasma-catalysis (Chen et al., 2009).....	95
Figure 3.1-1: Ni/Alumina catalyst BET isotherm for different particle diameter size .....	112
Figure 3.1-2: BET isotherm for different supports – titanium oxide, Y-zeolite and alumina .....	115
Figure 3.1-3: SEM images of Nickel supported on a. Alumina, b. TiO <sub>2</sub> and c. Y-zeolite .....	117
Figure 3.1-4: XRD graph of a. different fresh catalyst supports – alumina, titanium oxide and y-zeolite – and b. Nickel supported catalyst on different supports for reduced and non-reduced catalysts .....	118
Figure 3.1-5: Barium titanate support – BET isotherm .....	119
Figure 3.1-6: (a) XRD graph and (b) SEM picture of Barium titanate .....	120
Figure 3.2-1: Schematic diagram of the experimental setup for pyrolysis.....	122
Figure 3.2-2: Photograph of the pyrolysis system .....	123
Figure 3.2-3: Reactor description (a) drawing of the two-stage reactor (b) drawing of cross section cut of the plasma-catalytic reactor; (c) picture of the plasma-catalytic stage without the outer electrode and picture of the plasma zone .....	127
Figure 3.2-4: Plasma-catalysis experimental setup – Dielectric Barrier Discharge.....	129
Figure 3.2-5: Photograph of the pyrolysis-plasma-catalysis experimental setup – Dielectric Barrier Discharge (a) and annotated picture (b) .....	130
Figure 3.2-6: Reactor description before experiment trials (a) drawing of the packed bed plasma-catalytic reactor (b) drawing of the packed bed plasma-catalytic reactor assembly .....	134
Figure 3.2-7: Illustrations of usage of Ru/Ni- Al <sub>2</sub> O <sub>3</sub> (a) at 40 W, (b) at 60 W, (c) at 30 W and (d) flame pictures in the bed. ....	136

<b>Figure 3.2-8: Illustrations of usage of Ni- Al<sub>2</sub>O<sub>3</sub> (a) at 50 W, (b) at 40 W and (c) at 25 W.....</b>	<b>137</b>
<b>Figure 3.2-9: Pictures of plasma for Alumina packing (length: 2.5 cm) (a) for 20 W after a minute, (b) for 20 W when steam reached the bottom reactor, (c) for 40 W after a minute, (d) for 40 W when steam reached the bottom reactor.....</b>	<b>138</b>
<b>Figure 3.2-10: Final Reactor description (a) drawing of the reactor (b) drawing of the upper electrode assembly .....</b>	<b>140</b>
<b>Figure 3.2-11: Plasma-catalysis experimental setup - Packed-bed Dielectric Barrier Discharge.....</b>	<b>142</b>
<b>Figure 3.2-12: Photograph of the packed-bed DBD plasma-catalytic reactor .....</b>	<b>143</b>
<b>Figure 3.3-1: TGA equipment.....</b>	<b>145</b>
<b>Figure 3.3-2: Example of thermogram using TGA for woody biomass.....</b>	<b>146</b>
<b>Figure 3.3-3: Example thermogram for the proximate analysis of woody biomass.....</b>	<b>147</b>
<b>Figure 3.3-4: Example of BET isotherm for alumina catalytic support of 1 mm diameter beads.....</b>	<b>149</b>
<b>Figure 3.3-5: Example of a TPO thermogram a catalysis experiment using the DBD plasma-catalytic setup.....</b>	<b>151</b>
<b>Figure 3.3-6: Example of XRD graph for fresh reduced Ni-alumina .....</b>	<b>152</b>
<b>Figure 3.3-7: An example of a SEM-EDX spectrum for barium titanate a. picture with a magnification of 1.25K, b. picture with a magnification of 5.14K, c. EDX spectrum obtained from the map in d. and e. elemental content (wt.%) of the highlighted zone .....</b>	<b>154</b>
<b>Figure 3.3-8: Schematic GC system .....</b>	<b>155</b>
<b>Figure 3.3-9: Example of obtained chromatograms using gas chromatography for a. permanent gases, b. hydrocarbon gases and c. carbon dioxide.....</b>	<b>159</b>
<b>Figure 3.3-10: Water content and dehydration of the liquid produced. (a) Measurement of the water content. (b) Dehydration of the liquid produced.....</b>	<b>161</b>
<b>Figure 3.3-11: Schematic diagram of Gas Chromatography/Mass Spectroscopy (GC-MS) equipment .....</b>	<b>162</b>
<b>Figure 3.3-12: Example of a. a full chromatogram and b. a zoom-in view of said chromatogram .....</b>	<b>163</b>
<b>Figure 3.3-13: Calibration curves for example compounds a. Toluene b. o-Xylene c. Naphthalene.....</b>	<b>166</b>
<b>Figure 3.3-14: Size Exclusion Chromatography (SEC) equipment .....</b>	<b>168</b>

<b>Figure 3.3-15: Example of a Molecular weight (Mw) range obtained using the SEC for a pyrolysis experiment .....</b>	<b>168</b>
<b>Figure 4.1-1: Gas product composition after pyrolysis experiment for different feedstocks .....</b>	<b>170</b>
<b>Figure 5.1-1: Effect of plasma on the quantity of syngas produced (a) and its effect on the detailed produced gas composition (b) for DBD rig.....</b>	<b>181</b>
<b>Figure 5.1-2: Effect of plasma on the tar production (a) and on selected tar compounds (b) of produced liquid for DBD rig.....</b>	<b>184</b>
<b>Figure 5.1-3: Effect of plasma on the weight average (Mw) (a) and on the Mw range (b) of produced liquid for DBD rig.....</b>	<b>185</b>
<b>Figure 5.1-4: Possible reaction pathways of steam reforming of toluene (S. Liu et al., 2017) .....</b>	<b>191</b>
<b>Figure 5.1-5: Possible reaction pathways of steam reforming of naphthalene (Y. Wang et al., 2019) .....</b>	<b>192</b>
<b>Figure 5.1-6: Possible reactions mechanisms for toluene and naphthalene removal in plasma-catalysis system (Mei, Liu, et al., 2019) .....</b>	<b>192</b>
<b>Figure 5.1-7: Possible reaction pathways of plasma reforming of toluene and naphthalene (Mei, Wang, et al., 2019) .....</b>	<b>193</b>
<b>Figure 5.1-8: Effect of plasma on coke deposition on the catalyst for pyrolysis-catalysis (black) and plasma-catalysis (red) systems .....</b>	<b>195</b>
<b>Figure 5.1-9: XRD on catalyst before reduction (black), after reduction (red) and after plasma experiment at 40 W (blue) .....</b>	<b>195</b>
<b>Figure 5.2-1: Effect of plasma-catalysis and power increase on the quantity of syngas produced (a) and its effect on the detailed produced gas composition (b) for DBD rig when using Toluene as a feedstock.....</b>	<b>198</b>
<b>Figure 5.2-2: Effect of plasma-catalysis and power increase on tar production for DBD rig when using Toluene as a feedstock.....</b>	<b>199</b>
<b>Figure 5.2-3: Effect of plasma-catalysis and power increase on coke deposition for DBD rig when using Toluene as a feedstock .....</b>	<b>199</b>
<b>Figure 5.2-4: Quantity of syngas produced for different biomass components in plasma-catalysis (a), pyrolysis-plasma (b) and pyrolysis-catalysis (c) systems.....</b>	<b>204</b>
<b>Figure 5.2-5: Detailed composition of produced gas for different biomass components in plasma-catalysis (a), pyrolysis-plasma (b) and pyrolysis-catalysis (c) systems.....</b>	<b>205</b>
<b>Figure 5.2-7: Effect of plasma on the tar content for different biomass components in plasma-catalysis (a), pyrolysis-plasma (b) and pyrolysis-catalysis (c) systems.....</b>	<b>209</b>

<b>Figure 5.2-8: Coke deposition on reacted catalyst for different biomass component in plasma-catalysis (a) and pyrolysis-catalysis (b) systems .....</b>	<b>210</b>
<b>Figure 5.3-1: Effect of plasma power input on the quantity of syngas produced (a), its effect on the detailed produced gas composition for plasma system (b) and its effect on the detailed produced gas composition for plasma-catalytic system (c) .....</b>	<b>214</b>
<b>Figure 5.3-2: Effect of plasma power input on tar content (a), its effect on the selected tar compounds for plasma system (b) and its effect on the detailed produced gas composition for plasma-catalytic system (c) .....</b>	<b>216</b>
<b>Figure 5.3-3: Effect of plasma on XRD for reacted catalyst in plasma-catalysis system at different power input – 40 W (black), 60 W (red) and 80W (blue). .....</b>	<b>217</b>
<b>Figure 5.3-4: Effect of plasma power input on coke deposition on the catalyst at 40 W (black), 60 W (red), 80W (blue) and 0 W/catalysis (pink).....</b>	<b>217</b>
<b>Figure 5.3-5: Effect of steam flow rate on the quantity of syngas produced (a) and its effect on the detailed produced gas composition (b) .....</b>	<b>219</b>
<b>Figure 5.3-6: Effect of steam flow rate on the tar production (a) and on selected tar compounds (b) .....</b>	<b>221</b>
<b>Figure 5.3-7: Effect of steam flow rate on coke deposition on the catalyst ....</b>	<b>222</b>
<b>Figure 5.3-8: Effect of steam flow rate on the quantity of syngas produced at a power input of 20 W (black), 40 W (red) and 60 W (green).....</b>	<b>223</b>
<b>Figure 5.3-9: Effect of catalyst particle size on the quantity of syngas produced (a) and its effect on the detailed produced gas composition (b).....</b>	<b>225</b>
<b>Figure 5.3-10: Effect of catalyst particle size on the tar production (a) and on selected tar compounds (b) .....</b>	<b>226</b>
<b>Figure 5.3-11: Effect of catalyst particle size on coke deposition on the catalyst .....</b>	<b>227</b>
<b>Figure 5.3-12: Effect of catalyst/feedstock ratio on the quantity of syngas produced (a) and its effect on the detailed produced gas composition (b).....</b>	<b>229</b>
<b>Figure 5.3-13: Effect of catalyst/feedstock ratio on the tar production (a) and on selected tar compounds (b).....</b>	<b>230</b>
<b>Figure 5.3-14: Effect of catalyst/feedstock ratio on coke deposition on the catalyst .....</b>	<b>231</b>
<b>Figure 6.1-2: Effect of metal promoters on the quantity of syngas produced (a) and its effect on the detailed produced gas composition (b)in relation to the pyrolysis, plasma-catalysis of biomass with the DBD reactor .....</b>	<b>239</b>

<b>Figure 6.1-2: Effect of metal promoters on the tar production (a) and on selected tar compounds (b) of produced liquid in relation to the pyrolysis, plasma-catalysis of biomass with the DBD reactor.....</b>	<b>241</b>
<b>Figure 6.1-3: Effect of metal promoters on the weight average (Mw) (a) and on the Mw range (b) of produced liquid in relation to the pyrolysis, plasma-catalysis of biomass with the DBD reactor.....</b>	<b>242</b>
<b>Figure 6.1-4: XRD on the reduced metal promoted catalysts for different metal promoters.....</b>	<b>245</b>
<b>Figure 6.1-5: Effect of metal promoters on coke deposition on the catalyst for plasma-catalysis system .....</b>	<b>245</b>
<b>Figure 6.2-1: Effect of Nickel loading on the quantity of syngas produced (a) and its effect on the detailed produced gas composition (b) in relation to the pyrolysis, plasma-catalysis of biomass with the DBD reactor .....</b>	<b>248</b>
<b>Figure 6.2-2: Effect of Nickel loading on the tar production (a) and on selected tar compounds (b) of produced liquid in relation to the pyrolysis, plasma-catalysis of biomass with the DBD reactor.....</b>	<b>251</b>
<b>Figure 6.2-3: Effect of Nickel loading on the weight average (Mw) of produced liquid in relation to the pyrolysis, plasma-catalysis of biomass with the DBD reactor. ....</b>	<b>251</b>
<b>Figure 6.2-4: Effect of nickel loading on coke deposition on the catalyst in relation to the pyrolysis, plasma-catalysis of biomass for plasma-catalysis system.....</b>	<b>252</b>
<b>Figure 6.3-1: Effect of catalyst support on the quantity of syngas produced (a) and its effect on the detailed produced gas composition (b) in relation to the pyrolysis, plasma-catalysis of biomass with the DBD reactor .....</b>	<b>256</b>
<b>Figure 6.3-2: Effect of catalyst support on the tar production (a) and on selected tar compounds (b) of produced liquid in relation to the pyrolysis, plasma-catalysis of biomass with the DBD reactor.....</b>	<b>258</b>
<b>Figure 6.3-3: Average molecular weight by SEC for Nickel supported catalyst and catalysts for Alumina, Y-zeolite and TiO<sub>2</sub> for the product liquid in relation to the pyrolysis, plasma-catalysis of biomass with the DBD reactor. ....</b>	<b>259</b>
<b>Figure 6.3-4: XRD plots for Nickel supported catalyst and catalysts before and after reduction and experiment for Alumina (a) Y-zeolite (b) and TiO<sub>2</sub> (c) .....</b>	<b>263</b>
<b>Figure 6.3-5: Effect of catalyst support on coke deposition on the catalyst for plasma-catalysis systems with Nickel loading (a) or without Nickel (b) .....</b>	<b>264</b>
<b>Figure 7.1-1: Quantity of syngas produced for different biomass components in plasma-catalysis (a)and pyrolysis-catalysis (b) systems .....</b>	<b>274</b>

<b>Figure 7.1-2: Detailed composition of produced gas for different biomass component in plasma-catalysis (a) and pyrolysis-catalysis (b) systems .....</b>	<b>276</b>
<b>Figure 7.1-3: Coke deposition on reacted catalyst for different biomass component in plasma-catalysis (a) and pyrolysis-catalysis (b) systems .....</b>	<b>278</b>
<b>Figure 7.2-1: Effect of packing length on the quantity of syngas produced at a power input of 20 W (black), 30 W (red) and 40 W (blue).....</b>	<b>284</b>
<b>Figure 7.2-2: Detailed composition of produced gas for different packed bed length at 20 W (a) and different power inputs for a packed bed length of 4.5 cm (b) .....</b>	<b>285</b>
<b>Figure 7.2-3: XRD on fresh packing material (black), reacted packing material at 20 W (red) and reacted packing material at 40 W (blue)....</b>	<b>286</b>
<b>Figure 7.2-4: Effect of packing length and power inputs on the quantity of coke deposited on the packing material.....</b>	<b>288</b>

## Chapter 1: Introduction

### 1.1. Energy challenge and climate change

The climate has observed atmosphere changes since the 1950s by getting warmer linked to ocean changes, also by getting warmer, as presented in Figure 1.1-1(a). Human responsibility on these changes has clearly been demonstrated and the emissions of greenhouse gases such as nitride oxide, methane or carbon dioxide are the highest for at least the past 800,000 years. Figure 1.1-1(b) shows the increase for greenhouse gas concentrations in the past 250 years. (IPCC, 2014)

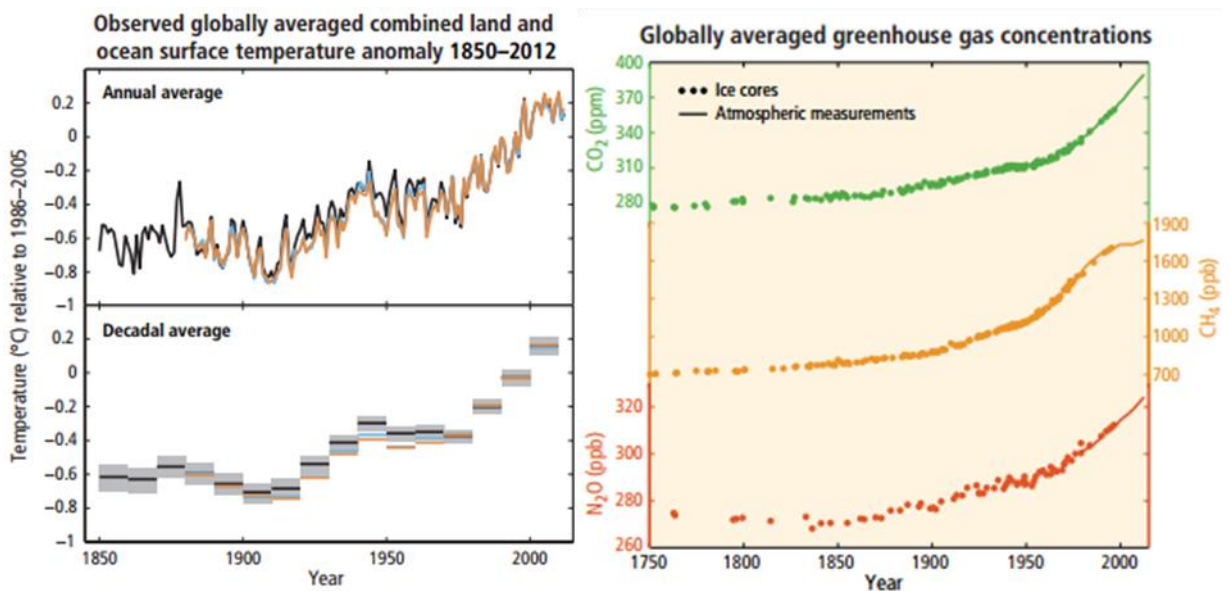


**Figure 1.1-1: (a) Observed globally average combined land and ocean surface temperature anomalies between 1850 and 2012 (b) Observed changes in atmospheric greenhouse gas generation concentrations. (IPCC, 2014)**

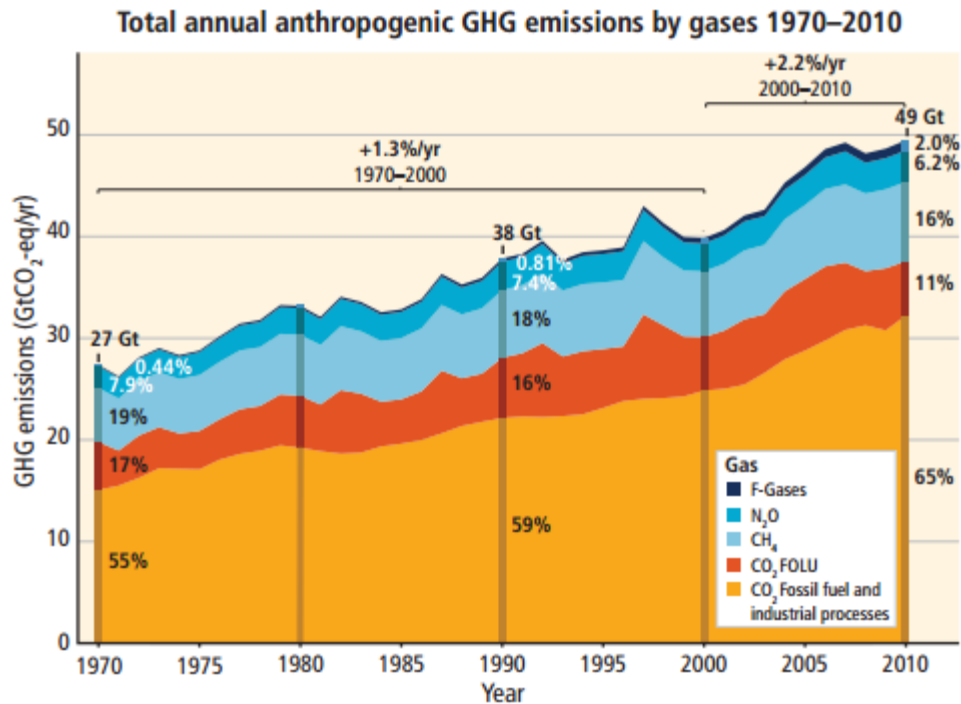


**Figure 1.1-2: Global anthropogenic greenhouse gas emissions (IPCC, 2014)**

Anthropogenic greenhouse gas emissions are presented in Figure 1.1-2. The carbon dioxide produced can be separated into two categories: from fossil fuel and industrial processes and from forestry and other land use (FOLU), supposedly carbon neutral. The other gases mentioned in Figure 1.1-2, methane, nitrous oxide and the fluorinated gases (F-gases) are covered under the Kyoto Protocol. (IPCC, 2014)

With climate change, people, societies, ecosystems and economic systems are at risk as extreme weather and climate events have been reported for the past fifty years. Heavy precipitations, storms, sea level increase and degradation of the cryosphere are affecting vulnerable communities as well as natural systems.

The European Commission, 2030 Energy Strategy has been put in place with three new targets for 2030: 40% in greenhouse gas emissions, at least 27% of renewable energy in the EU energy production and improving the energy efficiency by 27%. (European Commission, 2017) With those strategies, the European Commission is promoting the use of renewable energy such as wind energy, solar energy, hydraulic energy, geothermal energy or biomass energy.

## **1.2. Bioenergy and energy recovery from waste**

Renewable energy is a general term gathering all energy requiring a different source of energy than fossil fuels. This includes energies such as wind energy, solar energy, hydraulic energy, geothermal energy or biomass energy, also called bioenergy. The difference between bioenergy and other renewals is the type of feedstock used to produce energy: biomass or biomass waste.

### **1.2.1. Bioenergy**

Bioenergy is used for electricity and heat generation, as well as the production of biofuels for road transport. The main technologies available for bioenergy processes are thermochemical, mechanical/physical and biochemical conversion processes (Bridgwater, 2006). Biochemical conversion processes are slow processes where the components of biomass are decomposed via biological processes such as fermentation (after hydrolysis via enzyme and acid hydrolysis) and digestion (microbial conversion of organic materials), producing ethanol and biogas respectively. Mechanical conversion processes result in the production of rape oil by cold press. Thermochemical conversion processes are processes where organic matter is thermally decomposed, in order to produce syngas, fuel oil or heat energy, through gasification, pyrolysis or incineration respectively. Thermochemical processes result in multiple complex products whereas biochemical processes result in specific products. (Bridgwater, 2006)

Bioenergy is a field continuously evolving, improving its related technologies to make them competitive to be used on a commercial scale. Whereas the first generation of biofuel is an established technology and is produced from edible crops, thus competing with food production; the following generations of biofuels moved away from such competition. Second generation of biofuels are based on inedible crops, agricultural and municipal waste, third generation of biofuels are based on alga biomass and fourth generation on bioengineered crops and bio organisms. Although all these generations of biofuels have their own disadvantages and research advancement, they all aim at being more sustainable to minimise their environmental impact. (Alalwan et al., 2019) In this research project, the focus will be put on bioenergy and energy recovery from waste biomass.

### **1.2.2. Energy recovery from waste**

By 2050, the generation of waste is expected to more than double. The global generation of municipal solid waste in 2016 was of 2.01 billion tonnes annually, with landfills remaining the most widely used disposal option. From this global waste, about 37% of waste is disposed of in landfill, 33% is dumped in open air, 19% is recovered through recycling and composting, and 11% of waste is disposed of via incineration, the most common thermochemical conversion process. (Kaza et al., 2018) This repartition depends on countries' income, the low-income countries dumping most of their waste (93%); upper-middle-income countries disposing of waste mainly in landfill (54%); and high-income countries disposing of their waste in diverse ways, being landfilled (39%), diverted to recycling and composting (35%), or incinerated (22%) (Kaza et al., 2018).

An important role could be played by waste, by meeting the increasing energy need and mitigating the role of waste management in environmental pollution. Thus, the use of waste-to-energy technologies would benefit the environment by limiting the overall amount of waste sent to landfill and reducing the use of fossil-fuel to produce energy, thereby decreasing the emissions of carbon dioxide (Begum et al., 2012). In the following section, thermochemical conversion processes used for waste-to-energy are described.

### **1.2.3. Thermochemical conversion processes**

Bioenergy using thermal processes to produce electricity, heat or upgraded chemicals are pyrolysis, direct liquefaction, gasification and combustion/incineration. Direct liquefaction of biomass results in the decomposition of the macro-molecule compounds to produce light molecules in presence of a catalyst at high temperature (500-600 K) and high pressure (5-20 MPa). (Demirbaş, 2000) Combustion of biomass is mainly used as co-processing of biomass with coal for its relatively low costs due to the possibility to use most of the facilities used for coal combustion. (Bridgwater, 2006) However, combustion processes primely use specific biomass, such as clean wood pellets. When biomass waste is used in combustion processes, it is usually referred to as waste incineration. Incineration can be applied to a wide range of wastes, reduction the volume and hazard of the given waste. (European Commission, 2006) However, waste incineration results into the production of gas emissions, such as CO,

HF, HCl, NO<sub>x</sub> or SO<sub>2</sub>, which are limited by the European Commission in the Industrial Emissions Directive 2010, Waste Incineration Directive 2000. (European Commission, 2010).

Pyrolysis can be described as a thermal degradation of biomass waste in an oxygen-free environment, to produce gas, liquid such as tars and oils, and char. (Belgiorno et al., 2003) Product yields from biomass pyrolysis are dependent on the operating conditions, such as residence time, heating rate and pyrolysis temperature. Different modes of pyrolysis can be identified depending on the operating conditions. For a low temperature, around 400 °C and a long residence time, the pyrolysis is slow, also called carbonisation. For a moderate temperature, around 500 °C, and a moderate residence time of vapour products (~10-20 seconds), the pyrolysis is called intermediate. A fast pyrolysis is a pyrolysis at moderate temperature, around 500 °C, and a short residence time of vapour products (~1 second). In the case of wood pyrolysis, fast pyrolysis produces the most liquid, about 75%, whereas a slow pyrolysis resulted into a similar production of liquid, char and gas, about 30%, 35% and 35% respectively. (Bridgwater, 2006) Char produced from biomass pyrolysis can be recovered and used as an adsorbent or upgraded to activated carbon. Gas produced from biomass pyrolysis depends on the biomass pyrolysed with high content of carbon oxides for pyrolysis of biomass and biomass waste, and with high content of hydrogen and hydrocarbon gases from pyrolysis of tyres. (Wu et al., 2013) This gas can be used for electricity generation in power turbines and engines. The bio-oil produced from pyrolysis liquid product can be sent to refinery for upgrading to be used in engines or boilers with a reduced environmental impact. It can also be used as part of the second generation of biofuel, which does not compete with food as biomass pyrolysis is used to produce bio-oil, as a substitute of crude oil. (Wang et al., 2014)

With the recent increase of fossil fuel prices and the climate change awareness mentioned previously, gasification of waste appears as an interesting alternative for producing energy. (Fabry et al., 2013) Gasification is a process converting carbonaceous compounds into combustible gas, called synthesis gas or syngas, at high temperature (higher than 600 °C) and in the presence of an oxidising agent, such as steam, oxygen or air (Lombardi et al., 2015). The most commonly used gasifying agent is steam (Belgiorno et al., 2003). The heating value of the produced gas varies

depending on the oxidising agent: the use of steam or oxygen leads to a moderate heating value (10-18 MJ.m<sup>-3</sup>), whereas the use of air results into a low heating value gas (4-7 MJ.m<sup>-3</sup>). (Wu et al., 2013) The composition of the produced gas from biomass gasification depends on the gasifying agent, with the use of steam resulting in a higher hydrogen content (Gil et al., 1999). The main product of biomass gasification is syngas, consisting of hydrogen and carbon monoxide, alongside smaller quantities of methane and carbon dioxide (Rogoff et al., 2011). Syngas can be used for electricity and heat production, or it can be processed further for hydrogen production via water-gas shift reaction, for fuel synthesis by Fisher Tropsch process, for ethanol production by fermentation and for methanol generation which can be further processed to generate other fuels and chemicals, such as olefins, formaldehyde, gasoline and dimethyl ether (Huber et al., 2006).

### **1.3 Waste as a feed source**

Developing products with added value and derived from waste is an interesting route to resolve the environmental issues linked to the increasing production of waste (Olivares-Marin et al., 2012). Energy and management of waste have become a global issue. Thus, a sustainable management of waste along with a development of waste to energy processes mentioned previously, would help to solve both energy and waste management issues.

### 1.3.1. Municipal Solid Waste (MSW) and organic biomass waste

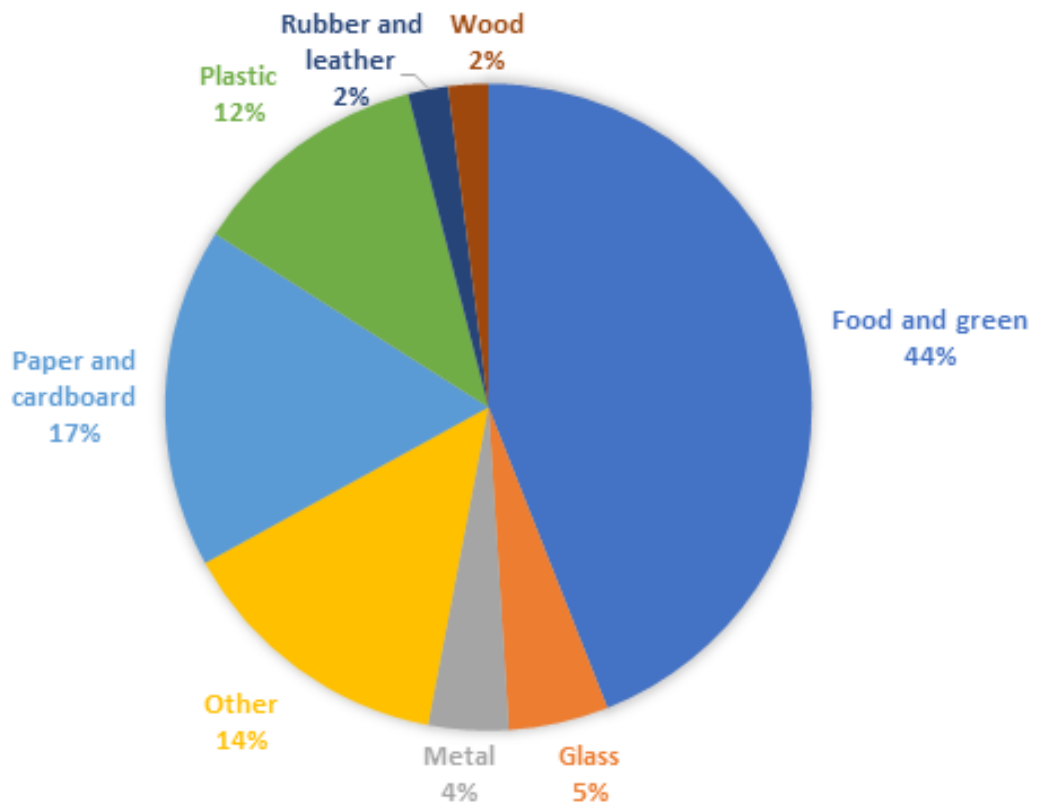


**Figure 1.3-1: Global waste composition** (Kaza et al., 2018)

The World Bank described the global waste composition as shown in Figure 1.3-1. The largest type of waste is food or green waste, also called organic biomass waste, representing 44% of global waste. Dry recyclables (paper and cardboard, plastic, glass and metal) makes up for 38% of waste. As expected, waste composition varies with countries' income levels: the higher the income, the lower the percentage of organic waste. (Kaza et al., 2018)

### 1.3.2. Biomass

Biomass is an interesting energy source as biomass energy systems can be used for heating, electricity generation and transport fuel. Biomass is considered as energy neutral and sustainable as greenhouse gas emitted by the transformation into energy is balanced by the carbon dioxide absorbed by the plant to grow. (Greenpeace International et al., 2015). Nowadays, the largest energy resource of biomass is still wood. However, other sources have been introduced such as residues from forestry or agriculture, plants or the organic content of industrial and municipal solid wastes. The term biomass is referring to any plant-based material convertible to energy, including

sugarcane, wood, forestry residues, crops etc. By its diversification and wide range of products, biomass is considered as a highly flexible fuel supply as it can originate from centralised or dispersed manner and be produced at large or small scales. It can be converted thermally or to liquid fuels, burnt or anaerobically digested for biogas production. (Hrbek, 2016)

Biomass available for bioenergy in the UK is also wide and varied, from agricultural residues, forestry, energy crops and organic waste. This includes energy crops, agricultural and forestry residues, steam wood, arboricultural arisings, sawmill co-products, sewage sludge, livestock manure, organic wastes, landfill gas and waste wood. Wood waste and agricultural waste are the main biomasses used in the UK and are predicted to keep their position until 2030 (Howes et al., 2011).

#### **1.4. Description and objective of this research**

Climate change and its harmful effects on the environment has become one of the most important social and political issues in recent years. To tackle climate change, renewable energies are promoted in order to reduce our society's dependence of fossil-fuels. In using renewable, low-carbon energies, thermal processes such as pyrolysis and gasification are an attractive way to produce energy and high-valued chemical products from biomass and waste. The main product of the gasification of biomass is syngas (a mixture of hydrogen and carbon monoxide). Syngas can be combusted for power and heat generation or can be used in the production of fuels and chemicals as a cleaner, alternative raw material to fossil-fuels. The main drawback however for large-scale industrial implementation of this technology is the presence of tars in the syngas produced from biomass gasification. Tars (a mixture of hydrocarbons, resins and alcohols) can accumulate within the engines resulting in damaged machinery, as well as reduced efficiency of the desirable processes from syngas.

The main objective of this research project is to produce a high quality, hydrogen-rich syngas, using a plasma-catalytic system to reduce tar compounds from biomass pyrolysis. The research involves the development of new plasma reactor systems downstream of a fixed bed pyrolysis steam reforming reactor. Limited attention has been devoted to the production of a hydrogen-rich syngas and to the reduction of tar compounds, using non-thermal plasma-catalysis, from a real biomass gasification-

pyrolysis system. Most publication focuses on the study of tar model compounds or methane reforming to study plasma-catalytic system to produce hydrogen enriched syngas and to reduce tar compounds. To the author's best knowledge, no such study has been conducted previously and no related report can be found in the literature.

This research uses pyrolysis of biomass and not gasification in order to produce a suite of hydrocarbon gases which have a similar composition and wide range of hydrocarbons as the composition of tar compounds. A novel development for the production of hydrogen-rich syngas from biomass involves a first stage pyrolysis of the biomass that produces a wide range of hydrocarbon gases, which are then passed to a catalytic steam reforming reactor for hydrogen production. Thereby the process mimics the natural gas catalytic steam reforming of natural hydrocarbons but involves a much more complex range of hydrocarbons.

The main aim of this research is to build a low-energy pyrolysis-plasma-catalytic system with steam reforming, as an alternative low-energy and low-cost route to produce high quality, hydrogen rich syngas. This was done by:

- Building and studying different plasma-catalytic systems. The design of different plasma configurations downstream of a fixed bed pyrolysis reactor will enable a better understanding of the low-temperature plasma and the interactions between the plasma discharge and the catalyst. It will also permit a better understanding of the design and operating condition limitations to optimise the design and operating conditions for a wider range of utilisation and a more sustainable plasma discharge.
- Optimising the systems for higher syngas and hydrogen content. For each experimental setup designed, optimal operating conditions can be found within the limitations of the system determined during the design phase. The investigation of the influence of different parameters will be conducted to determine the optimal operating conditions. These parameters can be related to the plasma operating conditions, such as power input or plasma configuration; to the pyrolysis operating conditions, such as the type of biomass or the flowrate of steam; or to the catalysis operating conditions, such

as the type of catalyst used (metal deposited and/or support used), the quantity of catalyst or its particle size.

- Studying the reduction of tar compounds through the reduction of high molecular weight hydrocarbons using plasma-catalysis steam reforming. By understanding the reduction of tar compounds through the reduction of high molecular weight hydrocarbons using plasma-catalysis steam reforming, the systems can be optimised to produce higher quality hydrogen-rich syngas.
- Investigating different biomasses and effect of biomass components. The study of different type of biomasses will show the feasibility of the plasma-catalysis systems for different molecular structures of biomass. It will also determine which type of biomass to promote for using the plasma catalytic-systems to produce hydrogen-rich syngas, depending on the content of biomass components – cellulose, hemi-cellulose and lignin – within the composition of biomass.

To achieve the aforementioned aims, various phases of research were determined, each phase having its own objectives. These were:

Phase 1: Preliminary experimental work. This phase includes:

- Study of the gas and vapour products from the pyrolysis of different biomasses – waste wood, corn stalk, peanut shell and coconut shell.

Phase 2: Study of the dielectric barrier discharge (DBD) plasma-catalytic system. This phase includes:

- Comparison of the use of pyrolysis-catalysis, pyrolysis-plasma and pyrolysis-plasma-catalysis systems on the gas and liquid products and reacted catalysts.
- Study of the plasma-catalytic system with toluene, a tar model compound, as well as with the components of biomass – cellulose and lignin.
- Determination of the relationship between contents of biomass components and products from the DBD plasma-catalytic reactor.
- Analysis of various operating parameters – power input, steam flowrate, catalyst particle size and ratio catalyst/feedstock.

Phase 3: Study of the influence of the catalyst in the DBD plasma-catalytic system.

This phase includes:

- Use of promoters on a nickel supported on alumina catalysts and their effect on the produced liquid and gas, and reacted catalysts.
- Study of the influence of metal loading on nickel supported on alumina catalysts.
- Comparison of the use of different catalyst supports and determination of influential properties of the catalyst on the products of the two stage fixed bed reactor.

Phase 4: Study of the packed-bed DBD plasma-catalytic reactor. This phase includes:

- Comparison of the use of pyrolysis-catalysis and pyrolysis-plasma-catalysis systems on produced gas and reacted catalysts.
- Study of the plasma-catalytic system with biomass and the components of biomass – cellulose, hemi-cellulose and lignin. Determination of the relationship between contents of biomass components and products from the packed bed DBD plasma-catalytic reactor.
- Analysis of the influence of power input and packing bed length on gas products and reacted catalysts.

## Chapter 2: Literature review

### 2.1. Pyrolysis systems

#### 2.1.1 Basic principle

Pyrolysis is endothermic thermal conversion of biomass in the absence of oxygen at an elevated temperature. When followed by partial or total oxidation of the primary products, it is the first step in gasification and combustion. De Souza-Santos et al proposed a general pathway between pyrolysis temperature and formed products as shown in Figure 2.1-1 (de Souza-Santos, 2010). The evolution of chemical reactions during pyrolysis is described in Figure 2.1-1.

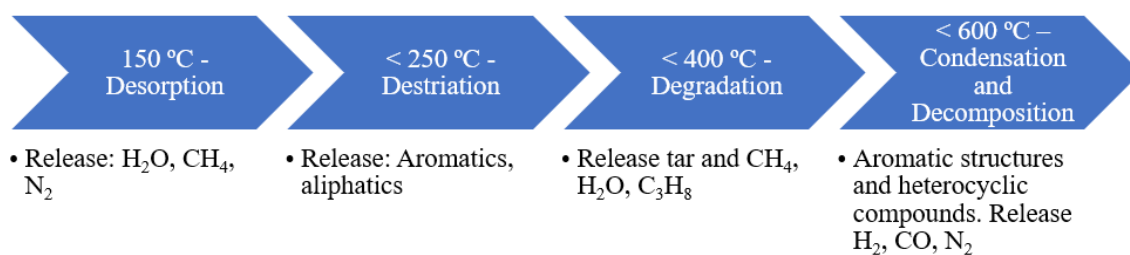


**Figure 2.1-1: Pyrolysis steps for various process temperature**

The composition and characteristics of pyrolysis products is dependent on multiple variables such as operational conditions (temperature, pressure or heating rate) and raw material composition (Williams, 2005). The characteristics of the different fractions from general pyrolysis are reported in Table 2.1-2.

**Table 2.1-1: Evolution of pyrolysis reactions depending on temperature**  
(Bilitewski et al., 1997; Astrup et al., 2010)

Temperature (°C)	Chemical reaction
100-120	Thermal drying, dehydration
250	Deoxidation, desulphurisation, molecular separation of H <sub>2</sub> O and CO <sub>2</sub> leading to cleaving hydrogen sulphide
340	Breakage of aliphatic bonds, splitting of methane and other aliphatic compounds
380	Carbonisation phase
400	Breakage of carbon-nitrogen and carbon-oxygen bonds
400-600	Bituminous compounds decomposed into low-temperature carbonisation oils and tars
600	Bituminous compounds cracking into heat resistant compounds, aromatic formation (light hydrocarbons and derivatives)
>600	Olefin dimerization, dehydrogenation to form butadiene, ethylene reacts to cyclohexane, thermal aromatisation to benzene and other highly volatile aromatic compounds

**Table 2.1-2: Characteristics of general pyrolysis products** (Tchobanoglous et al., 1993; Astrup et al., 2010)

Product	Characteristics
<b>Gaseous</b>	H <sub>2</sub> , CH <sub>4</sub> , CO, CO <sub>2</sub> , other volatile compounds and hydrocarbons. For a heating value between 3-12 MJ.Nm <sup>-3</sup> , pyrolysis gas yield is 20-50 wt.% of input.
<b>Liquid</b>	Contain mainly oil, tar and water in different quantities. Mostly oxygenated compounds and polyaromatic hydrocarbons. For a heating value between 5-15 MJ.Nm <sup>-3</sup> , pyrolysis liquid yield is 30-50 wt.% of input.
<b>Solid</b>	Char-like compound consisting of carbon and some inert material impurities found in the raw material, such as metals or glass. Heating value of the char is between 10-35 MJ.Nm <sup>-3</sup> .

Different pyrolysis modes are described as fast, intermediate and slow pyrolysis. The typical product yields for such pyrolysis are described in Table 2.1-3. These yields are dependent to process temperatures: low temperature and longer residence times promoted charcoal production; high temperature and longer vapour residence times improved biomass conversion into gas; whereas moderate temperatures and short residence times are optimum to produce liquids. (Bridgwater, 2006)

**Table 2.1-3: Yield of products for different types of pyrolysis of woody biomass**  
(Bridgwater, 2006)

Mode	Temperature	Residence time	Liquid	Solid	Gas
Fast	~ 500 °C	1 s	75%	12% char	13%
Intermediate	~ 500 °C	10-30 s	50% in two phases	25% char	25%
Carbonisation (slow)	~ 400 °C	days	30%	35% char	35%

Bio-oil is the main product obtained from pyrolysis of biomass. The dark brown liquid has an elemental composition close to biomass and is composed of a complex mixture of oxygenated hydrocarbons and water, from the reaction products and original moisture content. Solid char can be present as well. Bio-oil can be a substitute for diesel or fuel oil in applications such as boilers, furnaces, engines and turbines for electricity production. (Bridgwater, 2006) Petroleum compounds are usually hydrocarbons between C<sub>5</sub> and C<sub>17</sub>, being mainly one ring aromatic compounds and the less carbon chain compounds. Comparison of petroleum crude oil derived light fuel oil and heavy fuel oil and crude bio-oil is presented in Table 2.1-4.

Viscosity is an important property of the fuel oil as the equipment to inject fuel can be damaged if not used properly. Bio-oil and fuel oil have similar viscosity and blending diesel with bio-oil can be used to adjust to the appropriate viscosity (Mohan et al., 2006). Oxygen content in the pyrolysis oil results in a low heating value of the bio-oil and a low pH, when the oxygen content is in acidic form. Appropriate material for downstream equipment, such as stainless steel, should be used to overcome this

pH issue (Mohan et al., 2006). In order to use bio-oil as direct fuel, downstream treatments should be conducted to lead bio-oil properties, such as acidity and stability, closer to fuel oil (Mohan et al., 2006).

**Table 2.1-4: Properties of bio-oil, petroleum light and heavy fuel oils (Mohan et al., 2006)**

<b>Property</b>	<b>Bio-oil from wood pyrolysis</b>	<b>Light fuel oil</b>	<b>Heavy fuel oil</b>
<b>Heat of combustion (MJ/L)</b>	16-19	37	~40
<b>pH</b>	2.5	-	-
<b>Viscosity at 50 °C (centistokes)</b>	7	4	50
<b>Carbon content (wt.%)</b>	54-58	-	85
<b>Hydrogen content (wt.%)</b>	5.5-7	-	11
<b>Oxygen content (wt.%)</b>	35-40	-	1.0
<b>Nitrogen content (wt.%)</b>	0-0.2	0	0.3
<b>Ash content (wt.%)</b>	<0.2	<0.01	0.03
<b>Sulphur content (wt.%)</b>	trace	0.15-0.5	0.5-3
<b>Moisture content (wt.%)</b>	15-30	-	0.1
<b>Distillation residue (wt.%)</b>	Up to 50	-	1
<b>Pour point (°C)</b>	-33	-15	-18
<b>Turbine emissions (g/MJ) NO<sub>x</sub></b>	<0.7	1.4	N.A.
<b>Turbine emissions (g/MJ) SO<sub>x</sub></b>	0	0.28	N.A.

## **2.1.2 Available technologies**

### **2.1.2.1 Pyrolysis reactors**

Different technologies are available to pyrolyse feedstocks. Various types of pyrolysis reactors are presented in Table 2.1-5. The most attractive reactors for fast pyrolysis are the auger reactor, fluidised bed and circulated fluid bed, due to the strong technology knowledge of these reactors and their market attractiveness to be used in continuous processes (Butler et al., 2011), which are the key to commercialisation and development of pyrolysis.

### **2.1.2.2 Bio-oil upgrading**

As described in section 2.1.1, bio-oil obtained from pyrolysis of biomass being very viscous, chemically instable and with high solid content. For pyrolysis bio-oil to be used commercially, the liquid product from biomass pyrolysis needs to be upgraded which will bring the liquid to a higher quality, closer to conventional fuels. For example, to be used as a realistic candidate for liquid transport fuel substitution, the water and oxygen content of bio-oil should be reduced to better resemble the composition of traditional transport fuels. This section presents a summary of the different methods used to upgrade bio-oils.

First, bio-oil upgrading can be conducted by physical methods such as filtration, emulsification or solvent addition. Hot-vapour filtration can be used to filter biochar and other particles present in the produced liquid (Bridgwater, 2012). Emulsification consists of the injection of additives in bio-oil to stabilise the liquid, reducing the corrosive and viscous properties of bio-oil in order to facilitate the use of emulsified bio-oil in engines (Chiaromonti et al., 2003; Wang et al., 2014). Solvent addition can be used to reduce and homogenise biomass viscosity by adding polar solvents, which will affect oil stability (Diebold et al., 1997).

**Table 2.1-5: Types and characteristics of pyrolysis reactors** (Wang et al., 2014)

<b>Reactor type</b>	<b>Heating technology</b>	<b>Advantages, Disadvantages and Features</b>
<b>Ablative</b>	Wall heating	Heat supply limitations No requirement of heat transfer gas High char abrasion from biomass Particulate transport gas not mandatory Large size feedstock Compact design
<b>Circulated fluidised bed</b>	In bed circulation of char to heat sand	High heat transfer rates Requirement for char heat carrier separation and solid recycle High char abrasion from biomass and char erosion High char production Possible catalytic activity and liquid cracking from hot char Particle size <6 mm Greater reactor wear possible
<b>Fluidised bed</b>	Heated recycled gas	High heat transfer rates Limited char abrasion High direct supply to fluidising bed or gas Very good solid mixing Particle size <2 mm Simple reactor configuration
<b>Entrained flow</b>	Char combustion products	Low heat transfer rates Limited gas/solid mixing Particle size <2 mm
<b>Screw auger</b>	Hot sand	For heterogeneous and difficult to handle feedstocks

To upgrade bio-oil to biofuels, different pathways can be used and are reported in Figure 2.1-2. The main upgrading techniques are esterification, steam reforming, catalytic cracking and hydrotreating. Esterification can be catalytic, to enable a higher conversion of undesired products leading to higher quality of bio-oil, or non-catalytic by removing reactants or water from bio-oil or by implementing an in-situ process (Moens et al., 2009). Steam forming can be used to produce hydrogen from bio-oil via gasification process using Ni-based catalysts (Butler et al., 2011). Catalytic cracking using zeolite catalysts, such as ZSM-5 or HZSM-5 catalysts, is intensively used to crack bio-oil as they promote generation of high yield of produced liquid and propylene. They do however tend to produce undesired by-products (such as H<sub>2</sub>O or CO<sub>2</sub>) and to coke easily. (Bridgwater, 2012) Finally, hydrotreating is a high temperature (250-400 °C) and high pressure (70-200 bars) where hydrogen is used as a reducing agent for bio-oil oxygen content through catalytic reaction to increase bio-oil heating value. Naphtha and water are by-products of the process and can be easily removed from the mixture at high deoxygenation of crude bio-oil. (Bridgwater, 1996)

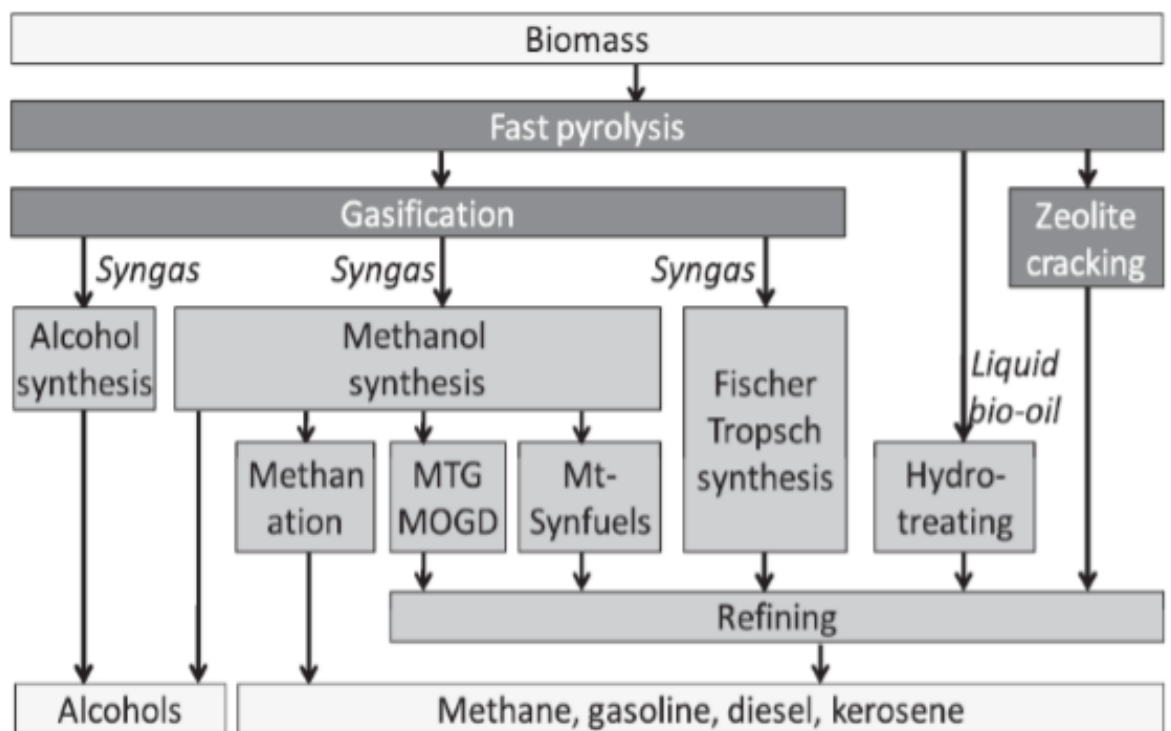


**Figure 2.1-2: Pathways to upgrade bio-oil to biofuel** (Bridgwater, 2012)

### 2.1.3 Pyrolysis of biomass components

The components of biomass, cellulose, hemi-cellulose and lignin, have different composition which might result in different pyrolysis products. These compositions are presented in Figure 2.1-3. Cellulose is a glucan polymer comprising of linear chains of anhydroglucose units. Hemicellulose is a mixture of polysaccharides, from monomers such as glucose, mannose, xylose or galactose. Lignin is a phenolic substance comprising irregular array of variously bonded hydroxy- and methoxy-substituted phenylpropane units. (Pettersen, 1984)

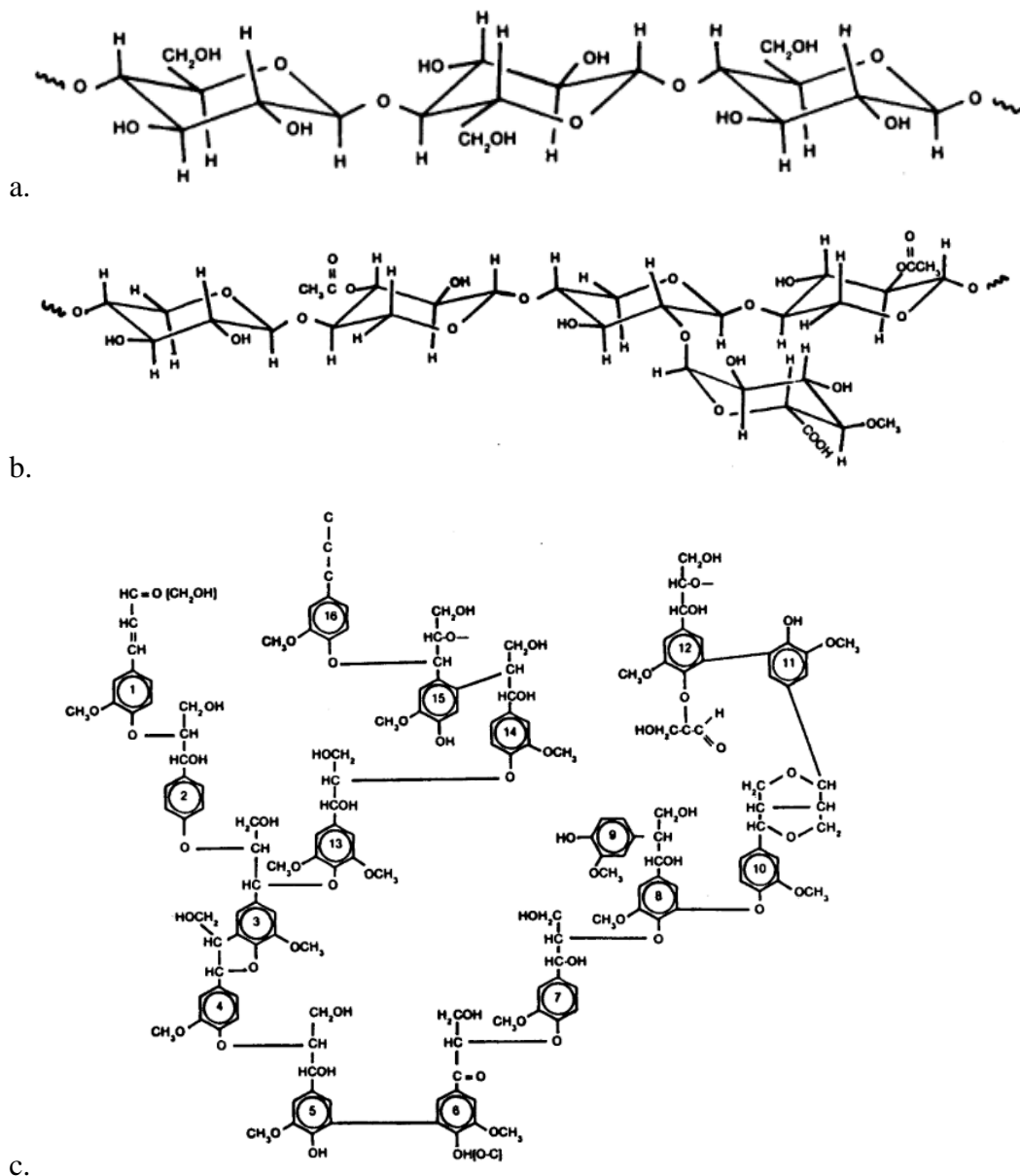


Figure 2.1-3: Example of partial molecular structures of common woody cellulose, hemicellulose and lignin (Pettersen, 1984)

Yang et al. (Yang et al. 2007) studied the characteristics of hemicellulose, cellulose and lignin pyrolysis. First, the pyrolysis happened quickly for cellulose and hemicellulose, with a pyrolysis temperature range of 220-315°C and 315-400°C respectively; whereas the pyrolysis of lignin was more difficult, through a wide temperature range (160-900°C) and with a high solid residue yield (~40%). The release of main gases produced from biomass pyrolysis was analysed and demonstrated dependent of each biomass components. Yang et al. observed that cellulose resulted in higher carbon monoxide yield, hemicellulose had higher carbon dioxide yield, and lignin higher hydrogen and methane yield. The molecular structure of biomass components resulted in various trends for the release of product gas during the pyrolysis of each biomass component. During this process, the abundance of C-O chemical groups in cellulose might promote the production of carbon monoxide. The numerous C=O chemical groups in hemicellulose mostly likely favours the production of carbon dioxide. The high lignin content in methoxyl (O-CH<sub>3</sub>) might promote the production of methane. (Yang et al., 2007)

Yu et al. (Yu et al., 2014) compared the tar formation characteristics of the gasification process of cellulose, hemicellulose and lignin. They observed that more tar compounds were obtained from experiments using lignin than cellulose, with cellulose resulting in the lowest tar content out of the three biomass components. At higher temperature, tar content consisted of higher molecular weight compounds, such as polycyclic aromatic hydrocarbons (PAHs). PAHs from lignin gasification process originated from phenol and its derivatives. From cellulose and hemicellulose gasification processes, PAHs derived mainly from benzene, toluene, ethylbenzene and xylene isomers and miscellaneous hydrocarbons. (Yu et al., 2014) This can be explained by the molecular structures of biomass components. Liu et al described lignin as a phenolic macromolecule, containing electron-rich methoxy groups, which can easily form oxygenated compounds such as phenol and its alkyl derivatives. (Liu, 2008) Nada and Hassan described cellulose and hemicellulose as polymers rich in glycosidic bonds, reactive bonds which are more likely to break and dehydrate to generate small carbonyl derivatives among others. These intermediary compounds can then separate to produce benzene and its derivatives, furan and toluene. (Nada et al., 2000) To generate PAH from these derivatives, two main paths were considered by Yu et al: benzene use as a precursor, with benzene generated by diene synthesis

reaction of propylene and butadiene in decomposition products of cellulose and hemi-cellulose; or the use of phenol as a precursor, by breaking of the ether bond in lignin structure, to produce phenol under acidic conditions, and by losing a CO radical by phenolic compounds to form cyclopentadiene. (Yu et al., 2014)

Wu et al studied the pyrolysis/gasification of cellulose, hemi-cellulose and lignin with the use of nickel-based catalysts. They observed that the catalyst addition onto the process promoted steam reforming of hydrocarbon oils, such as aromatics, and reforming of oxygen compounds, such as alcohols. Therefore, Wu et al. suggested the dominance of derived hydrocarbons from lignin pyrolysis, compared to cellulose and hemi-cellulose pyrolysis, at the first reaction stage. The amount of coke deposited on the surface of the catalyst was quite negligible. Finally, Wu et al observed that the presence of nickel-based alumina catalyst promoted reforming of oxygenated compounds, enhancing the hydrogen generation for lignin pyrolysis/gasification. High hydrogen yield was also observed for the use of cellulose in catalytic steam pyrolysis/gasification. (Wu et al., 2013)

#### **2.1.4 Biomass pyrolysis**

Biomass pyrolysis is a complex process, which products vary depending on the experimental conditions and biomass in use. For example, Elliott (1986) demonstrated a relation between pyrolysis temperature and chemical compounds within bio-oil from various biomass pyrolysis. As the temperature increased, alkyl chemical groups cleaved from aromatics, which condensed into polycyclic aromatics hydrocarbons (PAHs) at higher temperatures. At 400 °C, product liquid fraction consisted mainly of oxygenated compounds; at 500 °C, it was mainly composed of phenolic ethers; and at 600 °C, it comprised mostly alkyl phenolic compounds. (Elliott, 1986) Optimum pyrolysis temperatures have been reported for different biomasses. Between 500 °C and 600 °C enhanced the production of bio-oil (Uzun et al., 2009; Guo et al., 2015), whereas 575 °C was proved ideal for coconut shell pyrolysis (Rout et al., 2016).

Considering the wide range of studies in biomass pyrolysis, this section of the literature review is focusing on the pyrolysis of woody biomass and the pyrolysis of agricultural waste.

#### **2.1.4.1 Woody biomass pyrolysis**

The pyrolysis of woody biomass can be carried out on different types of wood. This section reviews the pyrolysis of selected beech wood, paulownia wood, wood pellets and pine wood to review pyrolysis of woody biomass.

Boot-Handford et al. investigated the pyrolysis of beech wood, two rice husks and a solid wastewater treatment in a 2-stage fixe-bed reactor a 500°C. With increasing ash content in biomass, char yields increased whereas volatile yields decreased. Beech wood was producing around 22 wt.% of char, 35.5 wt. % of tars, 4 wt.% of CO<sub>2</sub>, 2.4 wt.% of CO and 0.3 wt.% of methane. The tar produced by beech wood contained about 55 wt.% of carbon, 38 wt.% of oxygen and 6 wt.% of hydrogen. When volatile products were exposed to high temperature (700-900°C) and calcined limestone or dolomite, tar yield decreased. This tar cracking enhanced the production of carbon monoxide, with yield of around 23 wt.% at 900°C. (Boot-Handford et al., 2018)

Pyrolysis of paulownia wood was studied by Yorgun et al. in a fixed bed reactor studying the effect of pyrolysis temperature, heating rate, particle size and sweep gas flow rate. The maximum pyrolysis conversion was obtained for a pyrolysis temperature of 500°C, at 77.4% conversion. The highest yield of produced liquid, 54wt.%, was obtained for at pyrolysis temperature of 500°C, heating rate of 50 °C.min<sup>-1</sup>, nitrogen flow rate of 100 mL.min<sup>-1</sup> and particle size in the range of 0.425 and 1 mm. the bio-oil obtained in these experimental conditions was analysed by <sup>1</sup>H NMR to determine the type of hydrogen and thus, type of chemical groups within the bio-oil. Aliphatic hydrogens represented more than 66 mol% of total hydrogen, aromatic hydrogens 19 mol% and phenolic or olefinic proton represented 14.5 mol.% of total hydrogen. (Yorgun et al., 2015)

In Kim et al.'s (2019) study, pyrolysis behaviours of wood pellets were investigated to identify kinetic parameters for a heating rate of 10°C.min<sup>-1</sup>. Such parameters could be identified when separating the pyrolysis into 3 stages and following a first order reaction model: 150-310°C, 310-360°C and 360-875°C. (Kim et al., 2019) Other parameters have been studied to improve the predictability of wood biomass pyrolysis. Rezaei et al. studied the effect of particle size (0.25-5 mm) and density of pyrolysis of pine chips and ground pellets (five times heavier than chips). Pellets took longer to dry than chips, between 25 and 88 % more time, depending on the heating

rate (in the range of 10-50°C.min<sup>-1</sup>). Pyrolysis weight loss was about 80 wt.% for both chips and pellets. Cracks appeared on chipped particles during drying. Pyrolysis led to enlarged pores and cracked cell walls in chips. Drying of pellet particles did not modify the particle topography and no such damage was observed during pellet pyrolysis. (Rezaei et al., 2016)

Hu et al. (2019) investigated the impact of C/H ratio in woody biomass on pyrolysis products, showing its strong effect on the products distribution. With a higher C/H content, poplar pyrolysis resulted in yield char and lower tar yield. On the other hand, pine wood pyrolysis, with its lower C/H ratio, resulted in lower char yield but higher tar and gas yields. C/H ratio also affected the tar composition and stability, as well as aromatic formation in tars. Lower C/H ratio led to lower tar stability. Higher C/H content resulted in more aromatic compounds with smaller ring size within tar, whereas lower C/H content led to more aromatic with bigger ring size. Tar produced by biomass pyrolysis had similar functionalities, their intensity varying depending on the C/H ratio of the original raw biomass. These tar compounds could also continue to decompose to generate CO via decarbonylation, CO<sub>2</sub> through decarboxylation and H<sub>2</sub> via dehydrogenation. (Hu et al., 2019)

#### **2.1.4.2 Pyrolysis of agricultural waste biomass**

The agricultural waste biomasses studied in this section are corn stalk, peanut shell and coconut shell. The pyrolysis of corn stalk and rice husk was studied by Yu et al. (2016) in an auger pyrolysis reactor at different temperatures, between 350 and 600 °C. They found that, for increasing temperatures, molar fractions of combustible gases, CO and CH<sub>4</sub>, increased, whereas molar fraction of CO<sub>2</sub> decreased. Cracking and reforming of heavy hydrocarbons present in pyrolysis vapours resulted in the release of lighter hydrocarbons. Hydrogen became detectable for pyrolysis temperature higher than 500°C, and its molar fraction increased with increasing temperature, resulting in a higher heating value of produced gas (Yu et al., 2016). Bio-oil content from corn stalk pyrolysis was studied by Guo et al. for different pyrolysis temperature. Higher temperature led to more intense bio-oil cracking, resulting in lower bio-oil yield and higher syngas yield. Oxygen content of the original feedstock was higher than the one of the bio-oil. As pyrolysis temperature increased, heavy

product oil content (asphaltene) increased, most likely as a result of higher energy for pyrolysing macromolecules from biomass. (Guo et al., 2015)

Pyrolysis of peanut shell for bio-oil production in a fluidised bed was studied by Zhang et al. They observed that the maximum yield of bio-oil (60%) was obtained at a pyrolysis temperature of 500°C and a nitrogen flow rate of 3.2 Nm<sup>3</sup>.h<sup>-1</sup>. Phenols, ketones and acids were the main components of bio-oil produced, with percentages higher than 48%, 19% and 12% respectively, depending where the oil sample was taken out. Other chemical species present within the bio-oil were aldehydes, esters and other chemicals. The product gas had a small hydrogen content with a CO:H<sub>2</sub> ratio of 12:1 and a high production of carbon oxides, about 40 vol.%, with a CO:CO<sub>2</sub> ratio of 1:1. (Zhang et al., 2011) Messina et al. (2017) studied in-situ catalytic pyrolysis of peanut shells using modified natural zeolite in a fixed bed reactor at 500°C, and comparing its products with conventional pyrolysis. Solid yields were similar with or without catalyst, whereas the yield of bio-oil reduced when catalyst was introduced to increase the yield of produced gas. The bio-oil pyrolysis of peanut shell presented about 50 wt.% of carbon, 40 wt.% of oxygen and 8 wt.% of hydrogen. This bio-oil also consisted of 51 wt.% of water, 16.5 wt.% of phenols, 6.2 wt.% of sugars and had a pH of 3.1. The addition of catalyst increased the water content, phenol content but reduced the sugar content, while keeping a stable pH. (Messina et al., 2017)

Pyrolysis of coconut shell at different temperature was investigated by Wang et al. They observed CO and CO<sub>2</sub> generation trends as a function of temperature were similar, with a higher production of CO<sub>2</sub> than CO. This was attributed to biomass content in higher carbonyl and carboxyl groups, for CO and CO<sub>2</sub> generation respectively. Maximum methane production was reached at 550°C and was attributed to higher biomass content of aromatic ring and O-CH<sub>3</sub> functional groups. (Wang et al., 2018). Pyrolysis bio-oil from coconut shell pyrolysis has been studied by Fardhyanti et al., for a low pyrolysis temperature, between 300 and 350 °C. This low temperature range resulted in high phenolic content within pyrolysis bio-oil (Fardhyanti et al., 2017). This was also demonstrated at higher pyrolysis temperature by Rout et al. Aliphatic and phenolic content within bio-oil were about 6% and 69% respectively, for a pyrolysis temperature of 575 °C. (Rout et al., 2016).

## **2.2. Gasification systems**

### **2.2.1. Basic principle**

Gasification is a thermal process that can be described as an incomplete oxidation of organic matter to produce syngas by the mean of gasifying agents like oxygen, air, steam water or carbon dioxide. (Fabry et al., 2013) Syngas, the main product of gasification, is mainly a mixture of carbon monoxide and hydrogen, with some impurities such as water, carbon dioxide, hydrocarbons or tars. The whole reaction can be simplified in a four-step process: drying, pyrolysis, oxidation, followed by reduction. (Kumar et al., 2014)

Gasification includes a group of chemical reactions happening at once. Those reactions are described in the literature as in Table 2.2-1. (Fabry et al., 2013) As indicated by the endothermic reaction enthalpy of dry and steam reforming reactions (number 2 and 3), higher temperature favoured hydrogen and carbon monoxide formation while reducing the by-products production, carbon dioxide, methane and hydrocarbon. It also favoured the syngas generation by carbon consumption as predicted by the Boudouard and Water-gas reaction enthalpy (reactions 6 and 7).

### **2.2.2. Available technologies: types of gasification, state of art and current plants**

A whole gasification system is composed of five main components: a system to handle the feedstock (about 12% of the total cost of construction); a gasifier, syngas cooling and air separation unit (about 30% of the cost); pipping and gas clean up (about 7% of the cost); a combined cycle power block (about 33% of the cost) and remaining components and controls (about 18% of the cost). The gasifier and associated units as well as the combined cycle power block represent around two third of the total cost of a gasification units. (Mondal et al., 2011) This can be increased by using a higher syngas upgrade technology or different type of gasifier. In fact, many gasifiers have been under demonstration and/or commercialisation such as fixed bed, entrained bed or fluidised bed. The main gasifier used in industry and their characteristics, under oxygen blow, are shown in Table 2.2-1. This table does not differentiate the updraft

and downdraft technologies, which are when the feedstock and gasifying agent are counter and co-current respectively.

**Table 2.2-1: Main chemical reactions during gasification (a-T=298K, P=P<sub>atm</sub>, carbon as solid and water as vapor) (Fabry et al., 2013)**

N.o	Reaction name	Chemical reaction	Reaction enthalpy $\Delta H^a$
1	$C_nH_mO_k$ partial oxidation	$C_nH_m + n/2 O_2 \leftrightarrow m/2 H_2 + n CO$	Exothermic
2	Steam reforming	$C_nH_m + nH_2O \leftrightarrow (n + m/2)H_2 + n CO$	Endothermic
3	Dry reforming	$C_nH_m + nCO_2 \leftrightarrow m/2 H_2 + 2n CO$	Endothermic
4	Carbon oxidation	$C + O_2 \rightarrow CO_2$	-393.65 kJ.mol <sup>-1</sup>
5	Carbon partial oxidation	$C + 1/2 O_2 \rightarrow CO$	-110.56 kJ.mol <sup>-1</sup>
6	Water-gas reaction	$C + H_2O \leftrightarrow CO + H_2$	+131.2 kJ.mol <sup>-1</sup>
7	Boudouard reaction	$C + CO_2 \leftrightarrow 2 CO$	+172.52 kJ.mol <sup>-1</sup>
8	Hydrogasification	$C + 2H_2 \leftrightarrow CH_4$	-74.87 kJ.mol <sup>-1</sup>
9	Carbon monoxide oxidation	$CO + 1/2 O_2 \rightarrow CO_2$	-283.01 kJ.mol <sup>-1</sup>
10	Hydrogen oxidation	$H_2 + 1/2 O_2 \rightarrow H_2O$	-241.09 kJ.mol <sup>-1</sup>
11	Water-gas shift reaction	$CO + H_2O \leftrightarrow CO_2 + H_2$	-41.18 kJ.mol <sup>-1</sup>
12	Methanation	$CO + 3H_2 \leftrightarrow CH_4 + H_2O$	-206.23 kJ.mol <sup>-1</sup>

The output of those gasification technologies for biomass can be linked to the efficiency and the type of technologies. This relation is summarised in Figure 2.2-1. (Bridgwater, 2006) Downdraft gasifiers have the lowest efficiency and output whereas entrained bed and CFB have the highest output and efficiency. The fact that those technologies have many companies utilising them can thus be explained by the high output and efficiency of the CFB and entrained bed.

**Table 2.2-2: Type of gasifier and their characteristics with T Temperature, R.T. Residence Time, P Pressure. (Mondal et al., 2011)**

Gasifier	Technology	Typical process conditions	Comments
Fixed bed	Lurgy Dry ash, BGL	Combustion T: 1300 and 1500-1800 °C P: 0.15-2.45 MPa R.T.: 15-30 min Gas outlet T: 400-500 °C O <sub>2</sub> /Feed: 0.64 Nm <sup>3</sup> /kg Feed particle size: 2-50 mm Gas heat value (MJ/Nm <sup>3</sup> ): 10.04 Cold gas efficiency: high	Good for coal containing up to 35% of ash No use of liquid fuels High steam required Loss of fine particles during feed preparation High tar content (and phenolic compounds)
Entrained bed	Hitachi, MHI, BBP, PRENFLO, E-Gas, SCGP, Texaco	Combustion T: 1500 °C P: 2.94-3.43 MPa R.T.: 1-10 s Gas outlet T: 900-1400 °C O <sub>2</sub> /Feed: 1.17 Nm <sup>3</sup> /kg Feed particle size: <200 mesh Gas heat value (MJ/Nm <sup>3</sup> ): 9.58 Cold gas efficiency: medium	Good for co-gasification for pet coke and coal containing about 22% of ash Preference for low reactivity fuels (up to 22% ash) No tars or phenolic compound Moderate steam required No fine loss and in-situ sulphur removal
Fluidized bed (CFB)	IDGCC, KRW, HTW, Mitsui Babcock	Combustion T: 900-1200 °C P: 0.1-2.94 MPa R.T.: 1-100 s Gas outlet T: 700-900 °C O <sub>2</sub> /Feed: 0.37 Nm <sup>3</sup> /kg Feed particle size: 0.5-5.0 mm Gas heat value (MJ/Nm <sup>3</sup> ): 10.71 Cold gas efficiency: medium	Recommended for high reactive feedstocks such as waste fuels or biomass For high conversion, char to be recycled Moderate steam required No tars Reduced loss of fines Sulphur capture needed if sulphur content over 2 wt. %
Transport reactor	KBR	Combustion T: 900 -1050 °C P: 0.29-1.47 MPa R.T.: 1-10 s Gas outlet T: 590-980 °C O <sub>2</sub> /Feed: 1.06 Nm <sup>3</sup> /kg Feed particle size: <50 µm Cold gas efficiency: medium	Only char production and improved process efficiency High conversion and throughput To prevent combustion of volatile products, no feedstock exposure to oxidant Not well studied

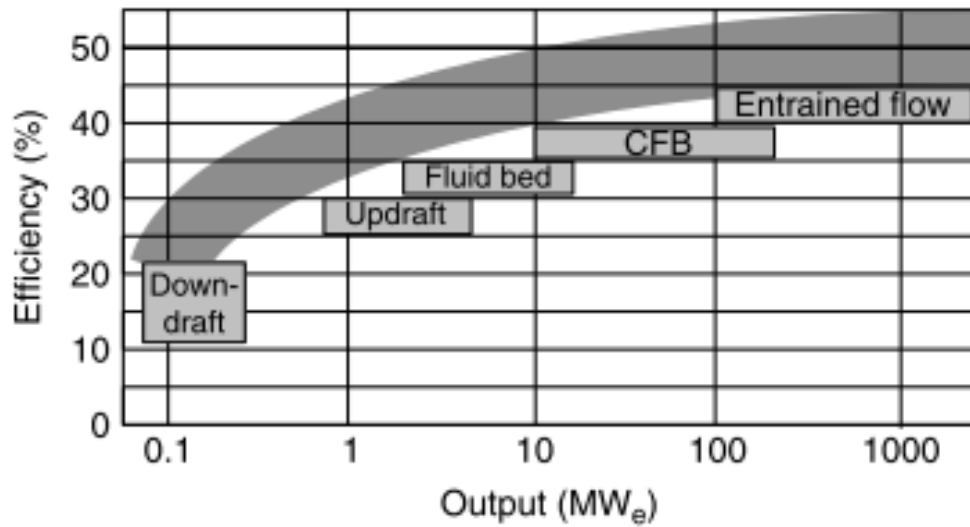


**Figure 2.2-1: Relation between scale, efficiency and technology for electricity production in the case of biomass gasifiers** (Bridgwater, 2006)

Some commercial biomass gasification plants have been reported from different companies. For example, 100 km north from Helsinki (Finland), the world's fourth biggest biomass power plant from Lahti Energy has been used commercially from 2012. Unclean plastic, cardboard, paper or wood can be used as feedstock for this plant with a 160 MW capacity. The feedstock is then sent to a circulated fluidised bed gasifier of 5-meter wide and 25-meter height, connected to a steam boiler, itself connected to a gas turbine and a generator to produce electricity and heat. (Power-technology.com, 2014) Another example is the Hitachi Metals plant, started in 2003 in Hokkaido Island (Japan), which is using a plasma technology to process shredded municipal solid waste and auto shredder residue (up to 220 tonnes a day). The technology in used is a DC plasma from Westinghouse. The syngas produced goes into an afterburner followed by a steam boiler connected to a steam turbine generator. After recovering the heat from the exit gas, it is cleaned and sent into the atmosphere. (Willis et al., 2010) In the U.K., the first plasma gasification plant for commercial use, BioSNG, has started construction in November 2016 and should be completed by the end of 2017. This commercial plant was made possible by the success of a demonstration plant using a fluidised bed gasifier and an arc plasma converter. This collaboration between Advanced Plasma Power, National Grid and Progressive

Energy will convert ten thousand tonnes per annum of household waste to produce 22 GWh of gas. (Advanced Plasma Power et al., 2017)

Although this gasification technology is of high interest nowadays, some issues limit the development to large scale gasification plant. First, to enable different fuel compositions for a same gasifier, process control and automation are the key challenges to overcome. Managing the highest thermal conductivity while keeping the gas temperature downstream of the gasifier within a given range is one of the most difficult step to overcome to be attractive for the technology to be interesting for large scale industries. (Crocker, 2010) Second, the impurities found in the exit gas need to be treated before a cleaner syngas is sent to end-use applications. Those impurities and their appropriate cleaning method will be presented in the next section.

### **2.2.3. Technical issue of syngas**

Various impurities can be found from the produced gas: tars, ammonia, hydrogen sulphide, sulphur oxides, nitrogen oxides, particulates or alkalis, potentially harmful for the downstream application of this produced gas. (Kumar et al., 2014) A summary of the contaminants, their issues and their clean-up techniques is presented in Table 2.2-3.

For industrial gasification processes, the presence of tar in syngas is the highest concern. Appropriate design and operation of gasifier is usually implied to control the reaction conditions as tar content can indicate the overall level of reactor performance and design. (Brage et al., 1997) Tars have been defined during the introduction of the protocol measurement of tar at the IEA Gasification Task meeting in 1998 at Brussels (Neeft et al., 1999) as a complex mixture of condensable organic compounds or hydrocarbons with a molecular weight higher than the one of benzene ( $C_6H_6$ ). Tar classification based on molecular weight of tar compounds has been reported in Table 2.2- 4. Five groups have a different reaction to temperature increase: class 1 and 2 are more decomposed whereas class 3 and 5 concentration in tars increased. (Han et al., 2008) Thus, tars have a wide molecular weight range with the composition depending on the type of biomass feedstock, gasification process and operational conditions (Abu El-Rub et al., 2004).

**Table 2.2-3: Overview of issues caused due to producer gas contaminants and popular clean-up technologies (Kumar et al., 2014)**

<b>Gas contaminant</b>	H <sub>2</sub> S	NH <sub>3</sub>	Alkalis	Particulates	Tars
Issues	Poison catalysts	Precursor for NO <sub>x</sub> and photo-chemical smog Poison catalysts Corrosion enhanced	Vapor deposition Deactivation of catalysts Slagging, fouling and corrosivity	Alteration of valve functioning Fouling of equipment surfaces Clog fuel lines	Plugging and fouling Disposal and handling difficulties Forming char and coke by dehydration
Cleanup technics	Adsorption on metal oxides Wet scrubbers	Mixed metal oxide catalysts Dolomite or Ni/Fe-based catalyst	Condensation of products Electrostatic separation	Cyclonic or barrier filters Electrostatic separation	Wet electrostatic separation Ni/dolomite/biochar catalyst Thermal treatment

The tar content represents the quantity of tars mixed with syngas downstream of the gasifier. It varies, depending on the feedstock in use (lignin content etc.), but also on the gasifier used. It has been summarised for the most common gasifiers and presented in Table 2.2-5. (Morf, 2001) Morf's results showed that to reduce the tar content in the outlet gas to a minimum, a concurrent fixed bed should be used. The same conclusion was drawn by Milne et al. (Milne et al., 1998): the main impurities in syngas (tar, particulates, fly ash) depend on the gasifier type as the more air circulation there is, the more particles are generated.

**Table 2.2-4: Classification of tar components** (Han et al., 2008; Woolcock et al., 2013)

Group	Name	Composition	Properties
Class 1	GC-undetectable	Determination by subtraction of the GC detectable tar fraction from the total gravimetric tar	Very heavy tars
Class 2	Heterocyclic aromatics	Phenol, pyridine, cresol, quinoline	Soluble in water Containing at least one hetero atom
Class 3	Aromatics (1 ring)	Toluene, styrene, xylene	No solubility or condensation issue Usually light aromatic with a single ring
Class 4	Light PAH compounds (2-3 rings)	Biphenyl, naphthalene, acenaphthylene, fluorine, anthracene, phenanthrene	Condensation at low temperatures from low concentration 2-3 ring compounds
Class 5	Heavy PAH compounds (4-7 rings)	Pyrene, fluoranthene, chrysene, benzo-pyrene, benzo-fluoranthene, perylene	Condensation at high temperatures from low concentration Compounds containing more than 3 rings

**Table 2.2-5: Tar content in most common gasifiers (Morf, 2001)**

	Fixed bed		Fluidised bed	
	Countercurrent	concurrent	bubbling	circulating
Mean tar content (g/Nm <sup>3</sup> )	50	0.5	12	8
Range of tar (g/Nm <sup>3</sup> )	10 – 150	0.01 – 6	1 – 23	1 – 30

However, no matter which gasifier is used in a process, the tar content in the syngas is too high for the most common downstream applications. For engines, Stirling engines do not require any treatment for the outlet gas, although they will have a low energetic efficiency, internal combustion engine are more restricted: they can be used for a tar concentration between 10 and 100 mg.Nm<sup>-3</sup> and a maximum of 30 mg.Nm<sup>-3</sup> for solid particles. Usual turbines can be directly downstream of the gasifier but not gas turbine as they require a tar concentration lower than 0.5 mg.Nm<sup>-3</sup> and can tolerate a solid particle concentration within an interval 0.1 and 120 mg.Nm<sup>-3</sup> containing less than 0.1 mg.Nm<sup>-3</sup> alkali. To prevent tar condensation in the pipes connecting the gasifier to a furnace, for close-coupled combustion for example, the tar concentration is limited from 60 to 600 mg.Nm<sup>-3</sup>. Furnaces themselves do not have a requirement for tar concentration although their emissions are regulated. Compressors to store syngas require a tar concentration between 50 and 500 mg.Nm<sup>-3</sup>. However, only the cleanest gas will be used for further application such as the Fischer-Tropsch process in which the solid particle concentration is lower than 0.02 mg.Nm<sup>-3</sup> and the tar concentration is inferior to 0.1 mg.Nm<sup>-3</sup>. (Milne et al., 1998) Thus, the need of clean processes to remove the tar, solid particle, or other contaminants is essential in the development and globalisation of biomass gasification.

#### **2.2.4. Gas cleaning processes**

To remove impurities such as particulate dust and tar removal, two types of technologies can be drawn: primary methods which take place during gasification and secondary methods which are gas cleaning technics downstream of the gasifier. (Wang et al., 2008) Table 2.2-3 summarised the most used methods for different kind of contaminants. To clean the product gas downstream of the gasifier, two methods can be used: hot and cold gas cleaning. Cold gas cleaning, mainly physical separation such as cyclones or filters, can remove chlorine, tars, particulates and alkali all together, even though they are most common for HCl removal. Hot gas cleaning can be used with specific sorbent such as carbon, alumina or common alkali sorbents, to remove chlorine. To remove particulates, hot gas cleaning can be used through inertial separation, electrostatic separation (also called ESP) or barrier filtration among others. To remove sulphur compounds (sulphur dioxide or hydrogen sulphur), adsorption on metal oxides using sorbents such as lime or zinc sorbents are mainly used as a hot gas

cleaning method. Ammonia can be removed by thermal catalytic decomposition and the removal of alkali contaminants can be done via condensation or hot adsorption on sorbent such as water or acid washing. Tars are reduced via thermal cracking, catalytic cracking, non-thermal plasma or physical separation. (Han et al., 2008) The methods for tar reduction are reviewed in detail in the present section.

#### **2.2.4.1. Primary methods**

The primary methods to reduce tars consist of controlling the parameters inside the gasifier to optimise and limit the production of tar. Their production is dependent on temperature, gasifying agent, equivalent ratio, residence time, size of biomass particles and the catalysts used. The most effective reduction of tar can be obtained by combining gasifier configuration with the right catalyst mix. (Ruiz et al., 2013) The modification of each parameter is reviewed in this section.

It has been intensively reported in the literature that a higher temperature lead to lower tar content in the produced gas. (Kinoshita et al., 1994; Narvaez et al., 1996; Lucas et al., 2004) Narvaez et al. reported for bubbling fluidised bed gasification of biomass a tar content decrease from  $19 \text{ gN.m}^{-3}$  at  $700^\circ\text{C}$  down to  $5 \text{ gN.m}^{-3}$  at  $800^\circ\text{C}$ . (Narvaez et al., 1996) Kinoshita et al. showed that tar yield decreased when the temperature increased. Lower temperature favoured aromatic tar species formation with diversified groups of substituents whereas higher temperature favoured the formation of polyaromatic groups, fewer aromatic tar species without substituent groups. (Kinoshita et al., 1994) Nevertheless, too high temperature inside the gasifier may lead to ash agglomeration and sintering as well as a decrease of energy efficiency. (Wang et al., 2008)

Pressurised biomass gasification has hardly been investigated but can be advantageous as no additional downstream compression of syngas will be required for upgrading syntheses of fuels and chemicals. The research conducted by Knight showed that an increase of pressure from 8 to 21.4 bar reduced the tar content from 4.4 wt.% to 3.4 wt.% with a significant influence on the species found in tars: polyaromatic hydrocarbons content increased while aqueous and phenols content decreased. Operating at high pressure enabled a drastic decrease of the oxygenated compounds that could be found in tars. (Knight, 2000)

Being the most economical, air is the most common gasifying agent used for gasification. However, the high concentration of nitrogen lead to a low calorific value of the produced syngas. Steam can also be used as gasifying agent with a moderate cost and calorific value of syngas. (Wang et al., 2008) Oxygen is the most expensive gasifying agent, required for advanced applications and mainly used in coal gasification. (Kirkels et al., 2011) CO<sub>2</sub> or a mixture of gasifying agents can also be used. (Wang et al., 2008) Wang et al. summarised the effect of each gasifying agent on tar content. The use of carbon dioxide or steam required catalytic tar reforming to reduce the tar content in the outlet gas. Using steam as a gasifying agent lead to particularly high tar content in the syngas. Air seemed the most appropriate gasifying agent when looking at the tar content as a moderate tar content can be found in the outlet gas. (Wang et al., 2008)

The equivalent ratio is the ratio between the air-fuel ratio for the current process and the one for complete combustion. An air-fuel ratio is defined by moles of air divided by moles of fuel used during the process. The equivalent ratio is inferior to the value 1, corresponding to complete combustion, and has a great influence on the calorific value of produced syngas. (Ruiz et al., 2013) Increasing the equivalence ratio decreased the calorific value of the produced syngas but enabled low char and tar content. (Kinoshita et al., 1994; Wang et al., 2008)

The residence time considered critical here is the duration of biomass within the gasifier. (Schaschke, 2014) For each type of reactor, the residence time should be long enough to enable the complete gasification of the feedstocks for syngas generation. The higher the degree of fluidisation of the beds, the shorter the residence time is as there is more stirring inside the bed. (Ruiz et al., 2013) Kinoshita et al. showed that tar yield was little affected by the residence time variation but the tar composition was as oxygen-containing compounds decreased with residence time. (Kinoshita et al., 1994)

The biomass preparation and its particle size are factors that should be considered to optimise a gasifier. Moisture is an important parameter for the fuel as the higher the moisture content of the biomass, the higher the tar content in the produced gas and the lower the temperature inside the gasifier is. However, the moisture limit is dependent of the type of gasifier: for example, updraft and fluidised bed gasifiers required less

drying than other gasifiers. (Crocker, 2010) Another key parameter is the fuel particle size. Too large fuel particles are more likely to produce a low-quality gas. Besides, to avoid an irregular gasifier temperature profile due to an irregular gas circulation leading to a pressure drop inside the gasifier, homogeneous feedstock should be used inside the gasifier. (Crocker, 2010) Thus, a pre-treatment of the biomass would lead to a more homogeneous fuel, reducing the gasifier instability. This could be conducted through torrefaction or pelletisation. (Ruiz et al., 2013) Studies have been conducted on specific gasifier and for specific biomasses to optimise them. For example, for a downdraft reactor fed on pine bark, increasing the particle size led to lower flame front velocities due to maximum process temperatures, lower consumption rates of biomass and fuel/air equivalent ratios. For such a process, the optimum particle size was found to be between 2 and 6 mm. (Pérez et al., 2012)

The different types of catalyst can be used for tar reforming: naturally occurring catalysts (Dolomite, Olivine, Clay or Zeolite) which are cheap with moderate reforming efficiency. Alkali and salts (KOH,  $\text{KHCO}_3$  or  $\text{K}_2\text{CO}_3$ ) act as catalysts with high reforming efficiency and leading to higher hydrogen content in produced syngas. However, other metal catalysts may be deactivated at high temperature and plugging may increase. Stable metal with oxide support ( $\text{NiO}/\text{Al}_2\text{O}_3$ ,  $\text{Ni}/\text{CeO}_2/\text{Al}_2\text{O}_3$ ,  $\text{RhCeO}_2\text{SiO}_2$  or  $\text{LaNi}_{0.3}\text{Fe}_{0.7}\text{O}_3$ ) are also catalysts with high reforming efficiency and leading to higher hydrogen content in produced syngas. Those metals are expensive and require support materials that are hot water resistant. They can be easily contaminated by  $\text{H}_2\text{S}$ , sintered by ash melting or deactivated by coke. (Wang et al., 2008) In the following section, the most studied catalysts are presented in more details and reviewed.

#### **2.2.4.2. Catalysts**

The simplified mechanism for tar reforming using an appropriate catalyst is described by Dayton as follow: First, metal-catalysed dehydrogenation occurs on metal site where hydrocarbons are adsorbed. Water is hydroxylating the surface by being adsorbed onto the ceramic support. The OH radicals migrate to the metal sites at appropriate temperature, inducing oxidation of the intermediate hydrocarbon fragments and surface carbon to syngas (carbon monoxide and hydrogen). (Dayton, 2002)

To find appropriate catalyst for tar reforming, Sutton summarised the main criteria for catalysts used in gasification processes: (Sutton et al., 2001)

- Efficient tar removal.
- Methane reforming if the desired product is syngas.
- Provides a syngas ratio suitable for the end-use process.
- Resists deactivation due to carbon fouling and sintering.
- Easy regeneration.
- Strong and inexpensive catalysts.

Sutton also reviewed tar cracking and separated the catalysts into three groups as mentioned in the previous section and studied below.

#### 2.2.4.2.1. Dolomite catalysts

Dolomite catalysts are composed of magnesium ore with the general chemical formula  $MgCO_3 \cdot CaCO_3$ . Their chemical composition varies but contains about 30 wt.% CaO, 21 wt.% MgO and 45 wt.%  $CO_2$  in general. Cheap and disposable, dolomite can also reduce the tar content in the syngas, dry-mixed with the biomass or as a guard bed, downstream to the main reactor. (Yang et al., 2015) To improve this type of catalyst, Simell and co-workers studied different types of low-cost materials and concluded that an increase of activity for dolomite catalysts could be achieved by increasing the ratio of Ca/Mg, a reduction of the grain size and an increase of active metal content such as iron. (Simell et al., 1992) The catalytic activity of calcined dolomite has been extensively studied and has been proven to have a higher activity than un-calcined dolomite for tar reduction due to its high surface oxide content and large inner surface area. (Shen et al., 2013) Comparing a calcined and un-calcined dolomite, as well as a calcined and raw olivine, used downstream of the steam gasification of apricot stone, Hu et al. observed that calcined dolomite was the most effective catalyst to increase hydrogen production. (Hu et al., 2006) Gusta et al. studied dolomite effect on tar reduction to gaseous products. Using an isothermal catalyst bed of 750°C, the use of dolomite catalyst (1.6 cm<sup>3</sup>/g of biomass) improved the conversion of tar to gaseous products of 21% compared to a non-catalytic experiment. The maximum carbon conversion was obtained when using a Canadian dolomite with 0.9 wt.% of iron. (Gusta et al., 2009)

#### 2.2.4.2.2. Alkali metal and alkaline-earth metal catalysts

Alkali metal and alkaline-earth metal catalysts have been demonstrated to catalyse the gasification of carbonaceous materials by steam, oxygen and carbon dioxide. (McKee, 1983) Added to biomass by direct dry-mixing or wet-impregnation, they catalyse the reduction of tar and upgrade the produced syngas. However such incorporation makes the recovery difficult and this technic hardly cost effective as the ash content is increased and should be disposed of. (Yang et al., 2015) In Demirba's experiments, (Demirba, 2002) the effect of alkali metal catalysts on hydrogen yield was studied through the gaseous products obtained from the pyrolysis and gasification of three different feedstocks: cotton cocoon shell, tea factory waste and olive husk.  $ZnCl_2$  catalyst demonstrated an increase of the hydrogen yield production in the pyrolysis of biomass, even if the total gas yield was reduced to increase the charcoal and liquid product yield. The catalytic effect of  $Na_2CO_3$  was found to be greater than the one of  $K_2CO_3$  for cotton cocoon shell and tea factory waste. The opposite catalytic effect was observed for olive husk. Besides, their effect on the pyrolysis products is irregular. A study of the pyrolysis of xylan polysaccharides and related compounds showed that alkalis weakened the intermolecular interaction of the polymeric chains and promoted intra-link dehydration, thermal cleavage process and product condensation. (Shafizadeh et al., 1972) In fact, alkali metal catalysts prevent the formation of stable chemical structures: C-C bounds are weaken and their activation energy decreased by an oxygen transfer mechanism. (Tran et al., 1978)

#### 2.2.4.2.3. Nickel-based catalysts

Ni-based catalysts are widely used in industry to catalyse steam and dry reforming. Steam reforming of hydrocarbons and methane for an increase of hydrogen and carbon monoxide content can be achieved by using Ni-catalysts at high temperature, above 740°C. Such catalysts can be used after use of dolomite or alkali catalyst for a higher efficiency with a first cracking of tar with a cheaper catalyst such as dolomite followed by methane reforming with a Ni catalyst. (Yang et al., 2015) Simell et al. studied the reforming of toluene at 900 °C, pressures between 0.5 and 20 MPa, and use of Ni alumina catalyst. At 5 bars and a residence time of one second, a complete tar reduction and 80% conversion of ammonia were observed downstream a pilot scale bed gasifier. (Simell et al., 1996) These high temperatures for the catalyst bed

are common in gasification. However, Zhang et al. described the activation of Nickel catalyst supported on silica, used for tar conversion, at a low temperature, 823 K. Their disadvantages are a short active time for the catalysts as high amount of coke deposited on the catalyst surface. (Zhang et al., 1998) The cracking of different model tar compounds – benzene, toluene, naphthalene, anthracene and pyrene – was studied by Coll for two Nickel catalysts in the commerce. (Coll et al., 2001) The order of reactivity of these different tar model compounds on Nickel catalysts was benzene > toluene >> anthracene >> pyrene > naphthalene. This made naphthalene a very appropriate compound to use for studying tar from biomass gasification. Looking more into the catalytic tar reduction and the hydrogen yield, Zhang identified the efficiency of three commercial Nickel catalysts: more than 99% of tars were cracked and the hydrogen yield improved slightly (6-11%). (Zhang et al., 2004) Recently, additive modification methods have been studied by researchers to improve the efficiency of Nickel catalysts and reach an optimum for tar conversion and hydrogen production. (Shen et al., 2013)

#### 2.2.4.2.4. Zeolite catalysts

Zeolite catalysts have been used first in oil refining and are now widely used in chemical industry for various applications such as ion-exchangers, size selective catalysts or encapsulators, Their chemical and physical stability, surface properties, like their acidity, and tunability of pore size make the zeolite use economically very relevant. (Möller et al., 2013) In thermal processes applied to biomass, Zeolites catalysts have been mostly used for catalytic cracking of the bio-oil in pyrolysis processes. ZSM-5 or HZSM-5 catalysts have mainly been studied as it has been reported that they lead to a higher liquid production yield, even though they coked easily and lead to unwanted products such as carbon dioxide or water. (Bridgwater, 2012) Zeolites catalysts also studied to upgrade bio-oil are H-Y zeolite and H- $\beta$  zeolite. Kotrel et al. (Kotrel et al., 1999) studied them three in the case of hexane cracking and proved that the activity between H-ZSM-5 and H- $\beta$  have similar effect on the adsorption rate.

However, due to their traditionally very small pore size, around 1 nm or smaller, bulky molecules are not in contact with the internal surface of the zeolite. To maximise the external surface of the zeolite to increase the conversion efficiency can be achieved

by two methods: to reduce the individual size of a crystal and thus promote intercrystalline mesopores, or to implement a secondary network of mesopores into single crystals of zeolite. (Möller et al., 2013) Such surface treatment is necessary to enable the reduction of tars by zeolite catalysts. To catalyse a condensation reaction, mesoporous materials are important as showed by Choi et al. when the use of mesoporous catalyst enabled to critically improve the catalytic activity to form jasminaldehyde from 3.9% with microporous zeolites to 98% with mesoporous zeolites. (Choi et al., 2006) Escola et al. compared four catalysts (two mesoporous catalysts, also called hierarchical catalysts, and two mesostructured materials) for hydroreforming of the polyethylene thermal cracking oil: Ni/h-ZSM-5, Ni/h- $\beta$ , Ni/Al-MCM-41 and Ni/Al-SBA-15. The mesostructured materials and the hierarchical  $\beta$  zeolite lead to complete hydrogenation of olefins. The zeolite catalyst use lead to an intensive promotion of hydrocracking reactions with a 54% of gasoline production. Hydroisomerisation and aromatisation reactions were promoted the same way using all four catalysts. (Escola et al., 2011) Thus, the use of mesoporous zeolite can be applied to tar reduction for a more efficient catalytic cracking of the tars.

#### **2.2.4.3. Secondary methods**

Primary methods for tar cleaning are the most common but downstream cleaning unit might be necessary to reach the tar level acceptance for end-use application. Cold gas cleaning, or physical separation, can be used for tar removal with methods such as cyclones, filters, rotating particles separators, water scrubbers or electrostatic precipitators (ESP). Hasler et al. reported the tar and particle reduction efficiency by various secondary methods. Results are presented in Table 2.2-6 showing a better reduction of particles than tar by using the methods mentioned. Sand bed filter was the most efficient method for both tar and particles with respectively more than 50 and 70 percent reduction. The less efficient method was fabric filter. (Hasler et al., 1999) However, one of the drawback of such method is the temperature used for the sand bed filter to be efficient: the syngas need to be significantly cooled down to be efficient.

**Table 2.2-6: Reduction of particles and tars in various producer gas cleaning systems (Hasler et al., 1999)**

<b>Reduction method</b>	<b>Temperature (°C)</b>	<b>Particle reduction (%)</b>	<b>Tar reduction (%)</b>
<b>Sand bed filter</b>	10 – 20	70 – 99	50 – 97
<b>Wash tower</b>	50 – 60	60 – 98	10 – 25
<b>Fabric filter</b>	130	70 – 95	0 – 50
<b>Rotational particle separator</b>	130	85 – 90	30 – 70
<b>Fixed bed tar adsorber</b>	80	-	50

The most common secondary methods for hot-gas tar reduction are: catalytic cracking, thermal cracking, mechanical methods, self-modifications of operating parameters and plasma treatment. (Fabry et al., 2013) The modification of the operating parameters has been described in the section 2.4.1 and the catalysts used for catalytic cracking are reviewed in the section 2.4.2, both having the effect than in the previous sections. However, tar cracking is mostly happening at very high temperature, higher than the gasifier temperature (~930-1030 °C), making thermal cracking without catalyst hardly efficient on usual gasifiers. For a higher reactor temperature, an efficient gas purification, a higher production of hydrogen and an easy retrofitting to current design, plasma gasification can be considered. (Fabry et al., 2013) This type of plasma gasification, used with thermal plasmas, is not the only type of plasma that can be used for tar reduction. Non-thermal plasmas such as pulsed corona or corona discharge, have also proven to be effective. However, the cost, device lifetime, operational complexities and the energy demand limit the wide application to such technology. (Woolcock et al., 2013)

To better understand the treatment by non-thermal plasma and the possibility to combine plasma with a catalyst to improve the technology and guide it to the large-scale gasification technology, the following section will describe what plasma is, the different type of plasma, to then focus on non-thermal plasmas and finally review the plasma-catalysis technology.

## 2.3. Plasma systems

### 2.3.1. Principle and classification of plasma technologies

Plasma is, according to *A Dictionary of Chemical Engineering* « A state of matter resulting from the ionization of gases in which the number of positive and negative ions is approximately the same [...]. It was first identified in 1879 and the nature of the matter was then identified by British scientist Sir Joseph John Thomson (1856–1940) in 1897. Irving Langmuir first used the term plasma in 1928. » (Schaschke, 2014) Plasma conducts electricity thanks to its free electric charges. Those make plasma internally interactive and highly sensitive to electromagnetic fields. Plasmas are electrically neutral and contain enough charged particles to give to the plasma a ionized gas behaviour and electrical properties. Plasmas happen naturally as they represent 99% of the visible universe. Closer to us, lightning and auroras are natural plasmas. They also happen in laboratories or industries for applications such as electronics, thermonuclear synthesis, etc. (Fridman, 2008) Generating a plasma can be used through different kinds of energy: thermal energy, electric fields or magnetic fields. For example, adiabatic compression of a gas or the use of charged particle beams can lead to plasma generation. Those are represented in Figure 2.3-1. (Conrads et al., 2000)

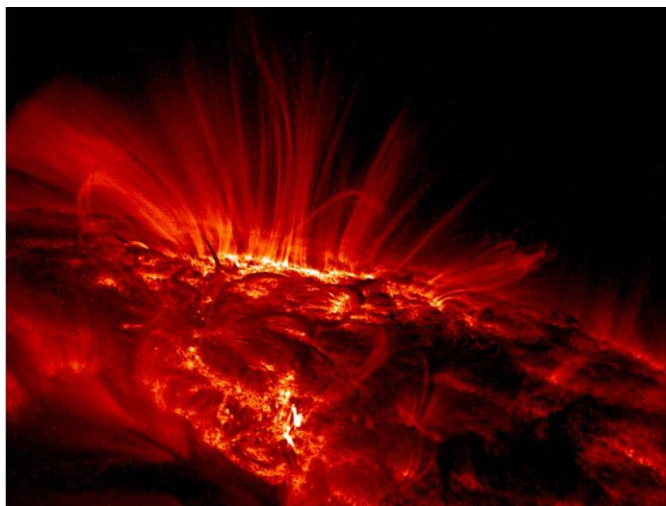


**Figure 2.3-1: Sunspot, taken by NASA's TRACE (Transition Region and Coronal Explorer) in September 2000, and showing in bright red the gas emissions (about 1 million degrees) and in dark the absorbing structures (about 10,000 degrees). (NASA, 2015)**

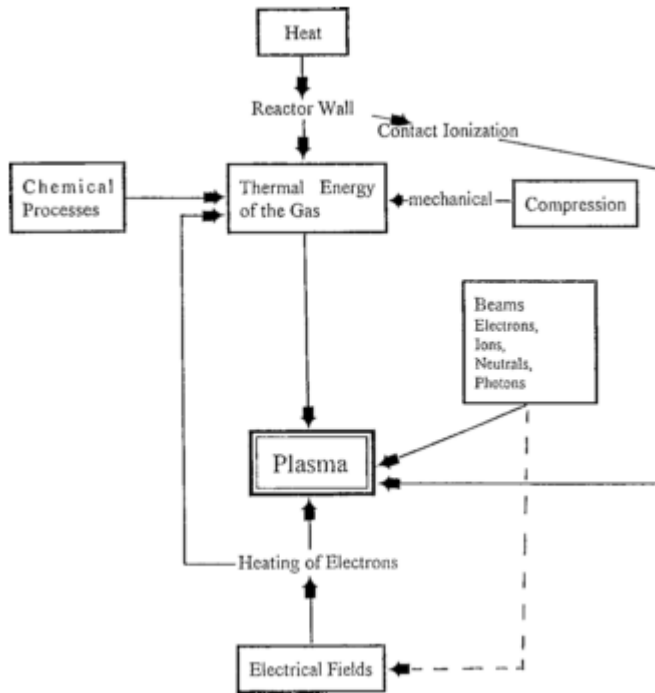


**Figure 2.3-2: Principles of plasma generation. (Conrads et al., 2000)**

The plasma is commonly generated and sustained by applying an external electric field resulting in new species formation highly reactive. Those reactive species are electrons, ions, excited molecules, radicals or photons at different wavelength. Those free charged particles are accelerated by the electric field until they collide with atoms, molecules and/or the surface of the electrodes, creating new charged particles. This phenomenon is often referred to as an avalanche of charged particles and the plasma reaches its steady state when the charge carrier losses balanced the creation of new charged species. Those plasmas are so-called plasma discharges and can be classified depending on the current and voltage applied. The shape of the curve is independent to the gas used in the plasma system and represented in Figure 2.3-2. At low discharge current, a self-sustained discharge is produced, also called Townsend discharge. The normal glow discharge is characterised by a low voltage for a moderate current. At very high currents, the discharge undergoes from a glow to an arc state. This transition is irreversible. (Conrads et al., 2000; Roth, 2001) Plasmas are quasi-neutral with a well-balanced concentration of negatively and positively charged particles. In plasma considered for chemical systems, not all particles have to be ionised: the ionisation degree, or ratio of density of main charged species to that of neutral gas, is considered

between  $10^{-7} - 10^{-4}$ . Completely ionised plasmas (density of main charged species very close to that of neutral gas) are mainly thermonuclear plasma systems. (Fridman, 2008)

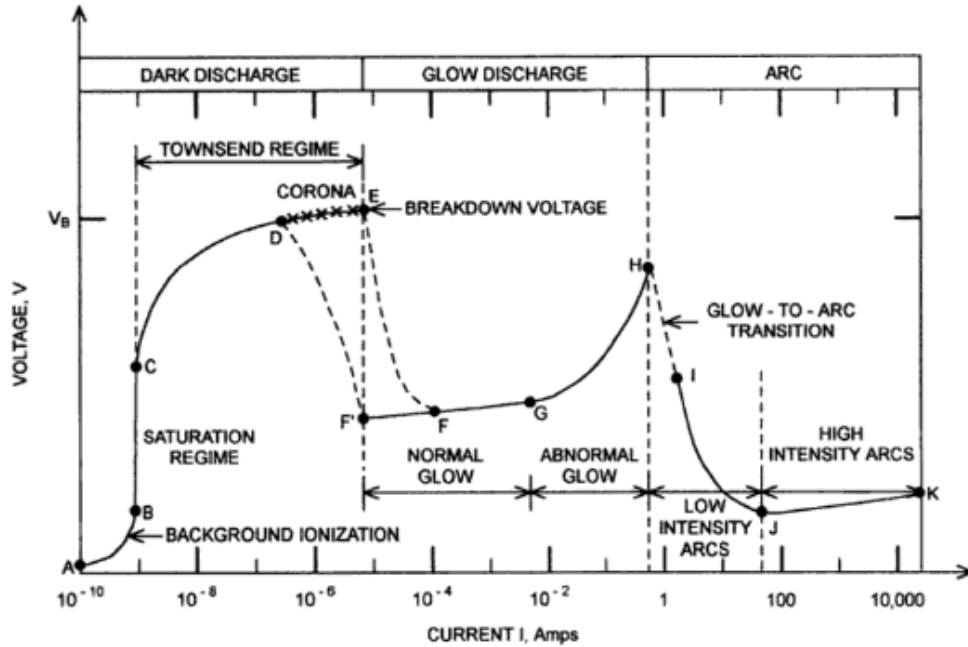


**Figure 2.3-3: Voltage-current characteristic in a DC atmospheric pressure electrical discharge tube (Roth, 2001)**

Plasmas have various characteristics and configurations, dependent of the plasma generation. For example, various plasma configurations can be used in laboratory: Microwave plasma (MW), direct current (DC) torch, dielectric barrier discharge (DBD), pulsed corona discharge (PCD), rotating gliding arc (RGA) or spark discharge. They are represented in Figure 2.3-4. (Lee et al., 2013)

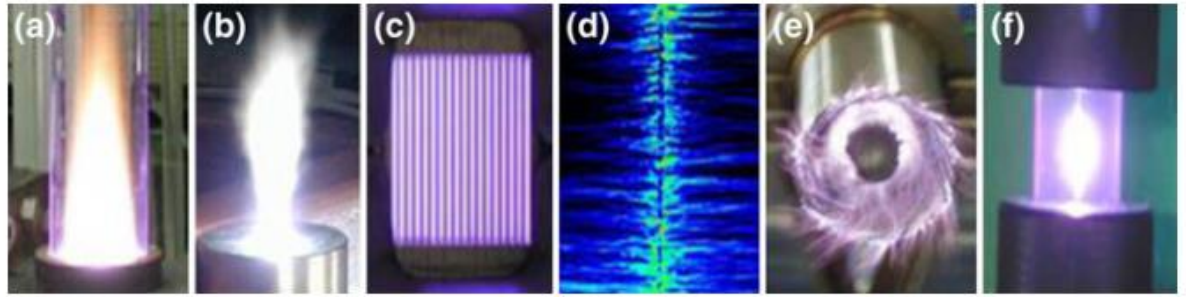


**Figure 2.3-4: Diverse plasma configurations with different appearance and chemical characteristics (a) Microwave (MW), (b) DC torch, (c) dielectric barrier discharge (DBD), (d) Pulse corona discharge (PCD), (e) Rotating arc (RA), (f) Spark. (Lee et al., 2013)**

Their different characteristics such as gas temperature, charged gas species and degree of ionisation mainly results in the appearance differences between the plasma in Figure 2.3-4. Those characteristics may be related to parameters such as ion temperature, electron temperature and density, which can be modified by pressure, discharges types, power supply and/or operating temperatures. Different electrical fields can be used to obtain direct current (DC) or alternative current (AC) discharges. The first discharges can be sustained by a pulsed-periodic current or maintained by a constant current. To limit the heat increase by electrons and thus the electron density, the current is restricted through the circuit by application of an external ballast. AC discharges can be generated at high and low frequencies, whereas radiofrequency (RF) discharges operates between 1 and 100 MHz and microwave (MW) discharges around 25 GHz, as high as high frequency AC discharges. (Mei, 2016)

A wide range of electron densities, electron temperatures and pressures are available for plasma generation. A wide range of examples are represented in Figure 2.3-5 where plasmas can be categorised by their electron temperature and electron densities only. (Fridman, 2008) The ionosphere plasma can be characterised by a low electron density and a small electron temperature. On the opposite side of the spectrum, thermonuclear fusion is a plasma with high electron density and temperature. Other plasmas can be described with a high electron temperature and low electron density like solar corona, with a high electron density and a low electron temperature such as

MHD (magnetohydrodynamic) plasma or with a median electron density and temperature as the glow discharges.

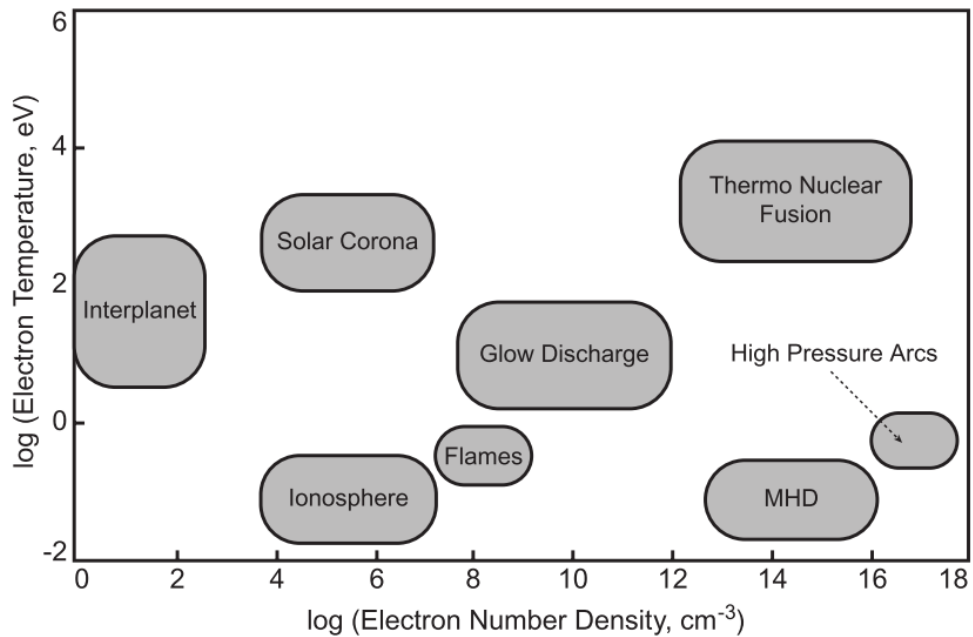


**Figure 2.3-5: Plasma temperatures and densities (Fridman, 2008)**

The gas pressure is an important parameter, defining the gas particle density and thus the probability of collisions between particles known as the collision frequency. At low pressure (between 0.1 and 10 Pa), inelastic collisions between heavy particles and electrons are ionising or exciting and do not raise the heavy particle temperature, which is lower than the electronic particle temperature. As the pressure increases, the collision frequency increases, and the energy transfer becomes more efficient. Therefore, heavy particle temperature is increasing and an equilibrium is reached in the plasma. (Tendero et al., 2006) Temperature is another very important parameter, enabling the categorisation of plasma into non-thermal and thermal plasmas via the relationship between particle temperatures. The temperatures inside plasma and their categorisation will be presented in the next section.

## **2.3.2. Thermal and non-thermal plasmas.**

### **2.3.2.1. Plasma temperatures and plasma categorisation**

Plasma temperatures are determined by the characteristics of plasma particles, neutral and charged: their average energy and their degree of freedom such as vibrational, rotational or translational or those linked to electronic excitation. Therefore, plasma temperatures can vary greatly representing the fact that plasmas are multi-component systems. For electric discharges to be generated in plasma laboratories, energy is first accumulated from the electric field by the electrons during their mean free path and is then transferred to heavy particles by collision between an electron and a heavy particle. The energy transferred between them via collision is a very small part of the energy accumulated by the electron as electrons are much lighter than heavy particles. This explains the difference of temperature between the electrons and heavy particles, the electron temperature being initially higher than the heavy particle temperature. (Fridman, 2008) There are two types of collisions: the elastic collisions changing the internal energy of neutrals but rise their kinetic energy (temperature) and the inelastic collisions modifying the electronic structure of neutrals, with a high enough electric energy, via excitation or ionisation or higher energies. (Tendero et al., 2006) Through those collisions, the temperature of electrons and heavy particles can equilibrate, a phenomenon called Joule heating. This equilibrium can be prevented by insufficient time or energy, such as in pulsed discharges or coronas, or by an intensive cooling mechanism on the entire gas, such as in wall-cooled low-pressure discharges. (Fridman, 2008)

Due to Joule heating, the difference of temperatures between heavy neutral particles and electrons in a collisional, weakly ionised plasmas is defined as proportional to the square of the electric field  $E$  to the pressure  $p$  ratio. Only if the ratio of  $E/p$  is small both temperatures can equilibrate. This small ratio is one of the basic requirement for local thermodynamic equilibrium (LTE) in plasma. Other conditions for a local thermodynamic equilibrium are chemical equilibrium and restrictions on the gradients. Thus, an LTE plasma is subject to the main laws of thermodynamic equilibrium and can be described by a single temperature wherever in space. Temperature, and indirectly the electric field via Joule heating, is the key parameter

to determine chemical processes and ionization in this type of plasma. Those plasmas, almost in equilibrium, are commonly called thermal plasmas and can be found in nature as solar plasmas. (Fridman, 2008)

Numerous other plasmas, which cannot be described by thermodynamic equilibrium, are defined by their range of different temperatures linked to different plasma particles and degrees of freedom. Because of the collision mechanism described previously, the electron temperature is often drastically bigger than the heavy particle temperature ( $T_e \gg T_0$ ). In this kind of non-equilibrium plasma, electron temperature determines directly ionisation and chemical processes. Thus, ionisation and chemical processes are hardly sensitive to the gas temperature and thermal processes. Those non-equilibrium plasma are commonly called non-thermal plasma and can be found in nature as aurora borealis. (Fridman, 2008)

In non-thermal plasmas, the different temperatures are usually presented as follow in the collisional weakly ionised plasma:  $T_e > T_v > T_r \sim T_i \sim T_0$ . The highest temperature in the system is the electron temperature  $T_e$ , followed by  $T_v$  the temperature of vibrational excitation of molecules. The temperature of ions ( $T_i$ ), the temperature of rotational degrees of freedom of molecules ( $T_r$ ) and the temperature of heavy particles ( $T_0$ , through transitional degrees of freedom or gas temperature) are the lowest temperatures, usually with very close values. For example, in numerous non-thermal plasma systems, the gas temperature is around room temperature whereas the electron temperature is close to 1 eV or 10,000K. Non-thermal plasmas can be generated at low power levels or low pressures or in different kinds of pulsed discharge systems. (Fridman, 2008)

### **2.3.2.2. Thermal and non-thermal plasma: comparison**

Characteristics of both thermal and non-thermal plasmas are presented in Table 2.3-1. The gas and electron temperatures presented in the table have been detailed previously: with single temperature for the whole system, the gas, or heavy particles, temperature and the electron temperature are similar ( $T_e \sim T_0$ ) for thermal plasmas; the electron temperature is much greater than the one of heavy particles ( $T_e \gg T_0$ ) in the case of non-thermal plasmas. In a thermal plasma, the collisions between electrons and heavy particles increase the temperature of the heavy particles through elastic

collisions and create reactive species via inelastic collisions. On the other hand, in a non-thermal plasma, the electron energy stays very high as plasma chemistry is induced by inelastic collisions between heavy particles and electrons and heavy particles are slightly heated. (Tendero et al., 2006)

The ionisation mechanism can be step-wise or direct in plasmas. Direct ionisation is the electron impact ionisation, when a neutral particle is collided by an electron to create a positive ion and a second free electron. A step wise ionisation is typically an ionisation following those steps: first the electron impact ionisation; then the ion impact ionisation, where the collision between an ion and a neutral lead to a free electron and a second ion; finally the step (Penning) ionisation where an excited particle ( $A^*$ ) collides with a neutral particle ( $B$ ) to generate an ion and electron from the neutral particle resumed as  $A^* + B \rightarrow A + B^+ + e^-$ . (Lieberman et al., 2005; Go, 2012)

**Table 2.3-1: Main characteristics of thermal and non-thermal plasmas** (Tendero et al., 2006; Go, 2012; Mei, 2016)

Properties	Thermal plasma	Non-thermal plasma
Gas temperature	10,000 – 50,000 K	300-1000 K
Electron temperature	1 – 5 eV ( $T_e \sim T_0$ )	1 – 10 eV ( $T_e \gg T_0$ )
Ionisation mechanism	Step-wise	Direct
Ionisation degree ( $n_e/n$ )	$> 10^{-3}$	$< 10^{-6}$
Inelastic collision effect	Creation of reactive species	Induction of plasma chemistry
Elastic collision effect	Great increase in temperature of heavy molecules	Slight increase in temperature of heavy particles
Electron density	$10^{21} - 10^{26} \text{ m}^{-3}$	$< 10^{19} \text{ m}^{-3}$
Cathode current density	$10^4 - 10^7 \text{ A/cm}^2$	$10 - 10^2 \text{ A/cm}^2$

As expected with such differences in their collision and ionisation mechanisms leading to less free electron generation, the ionisation degree, the electron density as well as the cathode current density are higher for thermal plasmas than for non-thermal plasmas. (Mei, 2016)

### **2.3.2.3. Thermal and non-thermal plasma: applications**

Plasmas are widely used in industry with numerous applications. Plasmas used for chemical processes are attractive for three reasons: their high selectivity, high specific productivity (per reactor unit volume) and high-energy efficiency (energy cost compared to the minimum given by thermodynamic laws). For plasma technology to be this attractive, the key point is to find the appropriate regime for a specific plasma chemical process and to optimise the plasma parameters as well as common parameters optimised to reach thermodynamic equilibrium. Ideally, high selectivity of energy input and high operating power for the plasma reactor as well as sustaining the non-equilibrium plasma conditions. (Fridman, 2008)

Due to their different properties presented in Table 2.3-1, thermal and non-thermal plasmas have also different application areas and engineering aspects: thermal and non-thermal plasmas are respectively more powerful, with higher electron and cathode current densities, and more selective by their direct ionisation mechanism. Various industrial applications use thermal plasma generator in a range between 1 kW to 50 MW. Although presenting sufficient power levels, high efficiency and reactant selectivity are difficult to reach and thus hardly convenient for plasma chemistry processes. For plasma chemical applications, the main drawback of thermal plasmas is the overheating of the reaction media occurring through the uniform energy consumption of all reagents in all degrees of freedom. A special and highly energetic quenching is required for the reagents in thermal plasma technologies, making the selectivity and energy efficiency of those processes rather small. (Fridman, 2008)

Microwave discharges have recently been used to provide powerful and energy-efficient plasma-chemical systems. A high level of electron density and a high electric field simultaneously in “cold” gas (around room temperature) are enabled by the skin effect. Microwave plasma technology provides dense, non-equilibrium plasma at low pressure and for a power in the order of MW. Arc discharges can also achieve these

plasma parameters. Such powerful, energy-effective and non-equilibrium plasma systems are optimal by their high productivity and minimum electricity energy cost for hydrogen production and fuel conversion applications. (Fridman, 2008) For example, Bromberg studied and compared the use of a non-thermal plasmatron with a thermal plasmatron for hydrogen manufacturing showing that both plasma reactors could achieve similar hydrogen yields. (Bromberg et al., 2001) However, non-thermal plasmas required much less energy than thermal plasma. With such advantages, non-thermal plasmas seem the most appropriate for hydrogen manufacturing.

### **2.3.3. Non-thermal plasma and different generation methods.**

#### **2.3.3.1. Non-thermal plasma: generation method**

As mentioned in the previous section, non-thermal plasma is an attractive technology for its high energy efficiency and selectivity while using quite low temperatures in comparison with thermal plasma. Those low temperatures are due to the fact that the input power is mainly used to generate energetic electrons instead of heating heavy particles. An external electric field is most commonly used to generate plasma. When it is higher than a particular value, specific to the formation of a conductive channel, electrical breakdown occurs. Breakdown mechanisms in non-thermal plasmas are usually starting with an avalanche of electrons, a high increase of primary electron quantity in cascade ionisation. With a relatively low ionisation degree and electron density (see Table 2.3-2), the electron energy from the electric field is increasing between collisions and the probability of electron-neutral collision is decreasing, reducing their heating effect. In non-thermal plasma, the gas temperatures are close to room temperature. They can however be excited or store energy by energetic electron-neutral collisions, which generate electronic, rotational and vibrational excitation of neutral particles, particle fragmentation, ionisation, and lead to the production of active species acting as powerful reducing or oxidising agents. (Mei, 2016) With a non-equilibrium property, a lower energy required and electrode corrosion, much less cooling system required for the electrodes, as well as a compact and low weight, non-thermal plasmas seem applicable to various processes, including environmental applications. (Tatarova et al., 2014)

As well as highly energetic electrons, reactive species are generated in non-thermal plasma, such as radicals or excited atoms. Thus, plasma chemistry is quite complex. The main reactions in plasma are summarised in the following table, Table 2.3-2. (Eliasson et al., 1991) Each component has a specific role in the kinetics of plasma chemistry. Electrons are most of the time first to interact with an electric field and to receive its energy, before distributing the energy between the other components of plasma and the specific degree of freedom of the plasma system. Thus, controlling and optimising a plasma process can be done by modifying key parameters of the electron gas such as its density, temperature or the distribution function of the electron energy. The high energy of ions (such as in reactive ion etching or sputtering case) as well as their ability to drastically modify the energy of activation of chemical reactions, give ions a significant contribution to the kinetics of a plasma system. By going up to suppressing the activation barriers, ions are essentials in plasma-catalysis and its many applications such as fuel conversion and hydrogen production. Vibrational excitation is essential to plasma kinetics as it is the main transfer of energy for electron with an energy around 1 eV to gases in the system and it enables higher energy efficiency. Electronic excitation of particles can be significant, particularly when those particle lifetimes are quite long as for metastable excited molecules. The role of radicals is greatly significant and the contribution of photons can be essential in specific applications such as plasma light source. Due to the non-equilibrium nature of plasma, the active specie concentrations may be bigger by order of magnitudes than the quasi-equilibrium system concentrations. Therefore, to control and optimise a plasma system, deep understanding of the fundamentals of plasma as well as the plasma kinetics are essential for a selective, directed and optimised process. (Fridman, 2008)

#### **2.3.3.2. Non-thermal plasma: type of discharges**

Different types of discharges have been used for environmental applications such as carbon dioxide utilisation, including microwave discharge, corona discharge, dielectric barrier discharge (DBD), gliding arc and packed bed reactor. (Mei, 2016) A brief description of the different discharges will be presented in the following section. Non-thermal plasmas can be generated at low pressure and at atmospheric pressure.

**Table 2.3-2: Main chemical reactions in plasma with e for electron, atoms A and B, molecules B<sub>2</sub> and A<sub>2</sub>, M for temporary collision partner and (\*) for the excited state. (Eliasson and Kogelschatz, 1991)**

Electron/Molecule Reactions	
<i>Excitation</i>	$e + A_2 \rightarrow A_2^* + e$
<i>Dissociation</i>	$e + A_2 \rightarrow 2A + e$
<i>Attachment</i>	$e + A_2 \rightarrow A_2^-$
<i>Dissociative attachment</i>	$e + A_2 \rightarrow A^- + A$
<i>Ionisation</i>	$e + A_2 \rightarrow A_2^+ + 2e$
<i>Dissociative ionisation</i>	$e + A_2 \rightarrow A^+ + A + e$
<i>Recombination</i>	$e + A_2 \rightarrow A_2$
<i>Detachment</i>	$e + A_2 \rightarrow A_2 + 2e$
Atom/Molecule Reactions	
<i>Penning dissociation</i>	$M^* + A_2 \rightarrow 2A + M$
<i>Penning ionisation</i>	$M^* + A_2 \rightarrow A_2^+ + M + e$
<i>Charge transfer</i>	$A^\pm + B \rightarrow B^\pm + A$
<i>Ion recombination</i>	$A^- + B^+ \rightarrow AB$
<i>Neutral recombination</i>	$A + B + M \rightarrow AB + M$
Decomposition	
<i>Electronic</i>	$e + AB \rightarrow A + B + e$
<i>Atomic</i>	$A^* + B_2 \rightarrow AB + B$
Synthesis	
<i>Electronic</i>	$e + A \rightarrow A^* + e$
	$A^* + B \rightarrow AB$
<i>Atomic</i>	$A + B \rightarrow A$

#### 2.3.3.2.1. Corona discharges

Corona discharges are usually taking place at a pressure close to atmospheric pressure using a relatively low power electrical discharge. The name “corona” comes from the observation of discharges by mariners from the masts of their ships during electrical storm. (Chang et al., 1991) A non-thermal corona discharge can be generated in regions of sharply non-uniform electric fields: the field in the gas should be weaker than the one around one or both electrodes. This happens near edges, sharp points or small-diameter wires, which are mainly low-power plasma sources, limited by the onset of the gas electrical breakdown. In corona discharges, the gas stays at room temperature whereas the electron temperature is higher than 1 eV. (Fridman, 2008) This type of plasma is the most common example of atmospheric pressure non-thermal discharge and can be observed at high voltage transmission lines or lightning rods. (Chang et al., 1991) Corona discharges are also used in industry to treat polymer materials, such as to improve adhesion of synthetic fabrics before dyeing. (Fridman, 2008)

Laboratory corona discharges are generated by pulsed or continuous DC voltage between two electrodes. The different types of corona discharges are represented in Figure 2.3-6. The electrode configuration as represented in Figure 2.6-6 is the most common with a grounded cylindrical outer electrode with a rod inner electrode or a concentric high voltage wire, or as point-to-plate or point-to-point electrode. Gas, either static or with a continuous flow, is occupying the volume between the electrodes. The electric field, non-uniform, is formed at the sharp end of the electrodes, where the curvature radius is small. This region where the gas ionisation occurs is called the ionisation zone. Between this zone and the cylindrical collecting electrode, the ions created in the ionisation zone drift to the collecting electrode. In this “drift zone”, the production of negative ions is enhanced through electron attachment reaction. (Mei, 2016) Thus, the electric current is transmitted from one electrode to the other by the drift of charged molecules in a low electric field. Close to the electrode source of plasma, ionisation as well as luminosity and strong electric field can be found. (Fridman et al., 2005) Due to the low electric field near the collecting electrode leading to lower current and power discharge, a continuous corona discharge can be achieved. A spark connecting both electrodes can be obtained

by increasing the applied voltage. (Chang et al., 1991) Effective and fast transfer of power between electrodes can be obtained by using pulsed-periodic voltage, without spark forming which are instable and inappropriate for industrial applications. (Mei, 2016)

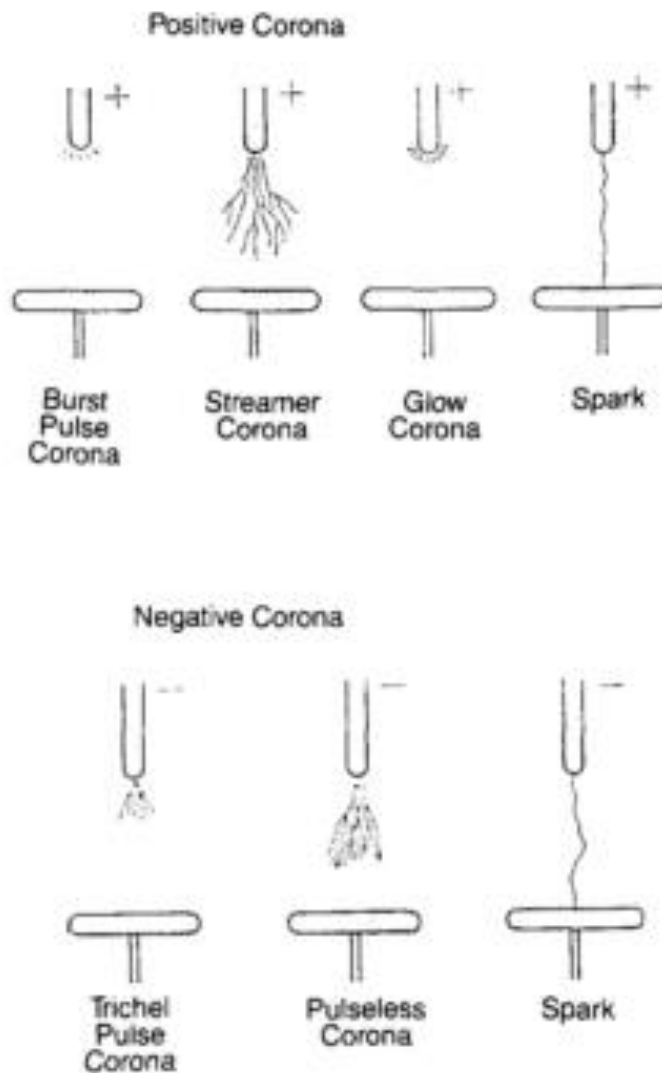


**Figure 2.3-6: Types of corona discharges (Chang et al., 1991)**

#### 2.3.3.2.2. Gliding arc discharges

With two diverging electrodes under a turbulent or fast laminar gas flow, an oscillating phenomenon called gliding arc discharge can be generated. First, a plasma arc column is created by an initiation of a breakdown at the shortest distance between both electrodes (2-5 mm), under an appropriate electric field. The arc is then pushed

downstream via the convective gas flow along the electrode axis, elongated its length until the supplied power cannot sustain itself. (Mei, 2016) This can be separated into two phases: the equilibrium heating phase, where the gas is under thermal plasma conditions (with a temperature between 7,000 and 10,000K), and the non-equilibrium reaction-phase, where the heat losses by the plasma exceed the energy supplied and the gas is under non-thermal plasma conditions. A representation of the plasma cycle is represented in Figure 2.3-7. (Fridman et al., 1999) Therefore, a gliding arc discharge is a type of plasma presenting a high level of non-equilibrium, characteristic of non-thermal plasmas, as well as high electron density and high electron temperature, characteristics of thermal plasmas. Advantages of both plasma type can be combined in this transient arc by the use of a periodic discharge, evolving from an arc to a highly non-equilibrium discharge and keeping a high electron density. Thus, this kind of plasma is non-homogeneous in space and time, as well as transiting from thermal to non-thermal ionisation mechanisms. (Fridman et al., 2005)

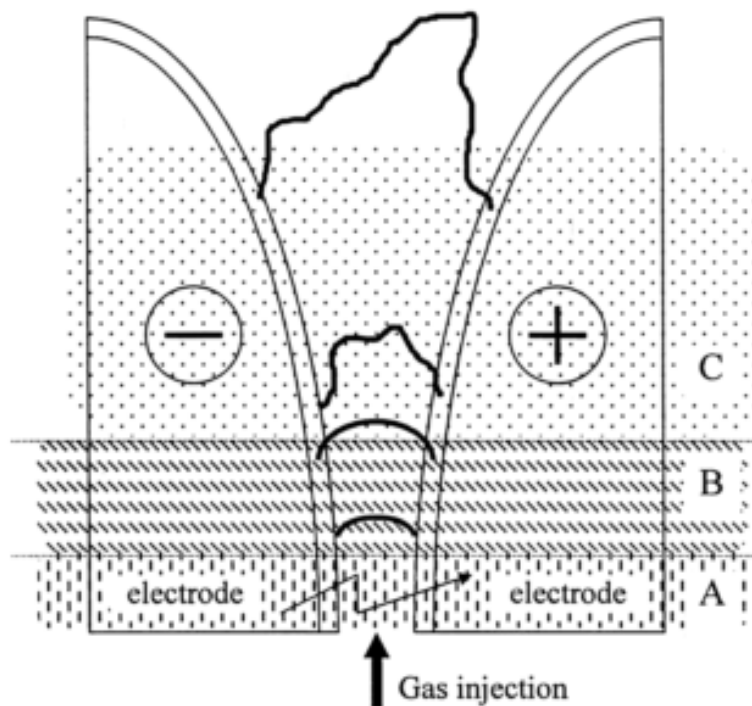


**Figure 2.3-7: Evolution of a gliding arc discharge: (A) reagent gas break-down; (B) equilibrium heating phase; (C) non-equilibrium reaction phase. (Fridman et al., 1999)**

The traditional gliding arc discharge has been designed by Czernichowski, called the plate gliding arc discharge, has been used in fields of energy or environment such as air depollution from volatile organic compounds, for its characteristics and simple configuration. (Czernichowski, 1994) Generating powerful non-equilibrium atmospheric pressure plasma is gradually more popular through the increase use of gliding arc discharges in chemical processes. The plasma stabilisation in reverse vortex "tornado" rose interest by its combination of a high power, characteristic of arc discharges, and a high level of non-equilibrium, characteristic of non-thermal atmospheric pressure discharges. (Fridman, 2008)

### 2.3.3.2.3. High frequency discharges: RF and MW discharges

The frequency used to excite the gas to be plasmarised is essential as it influences the electron and ion behaviour. Figure 2.3-8 represents the frequency effect on which component of the plasma. (Tendero et al., 2006) The first group at low frequencies are the gliding arc, corona or dielectric barrier discharges. The second and third group are respectively the radio frequency (RF) discharges and microwave (MW) discharges.

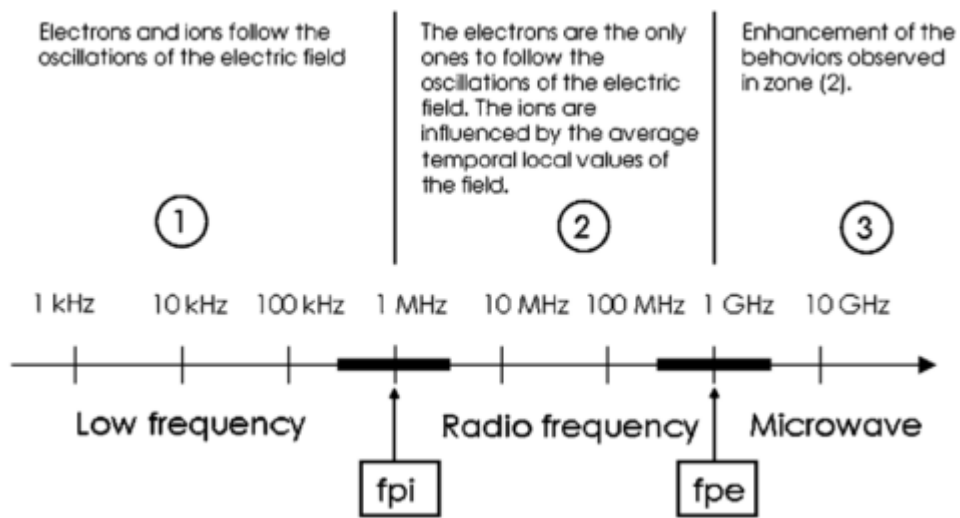


**Figure 2.3-8: Ions and electrons frequencies in non-thermal plasmas.(Tendero et al., 2006)**

Non-equilibrium, low-pressure RF discharges are commonly used in plasma chemistry: for example in micro-electronic processes such as etching and deposition

or in the treatment of polymer materials. (Fridman, 2008) For such a discharge, the electrodes are mainly kept outside the discharge volume, avoiding the usual deterioration of the electrodes through erosion or plasma contamination with metal vapours. The plasma can be considered homogeneous as the electric field wavelength is very large compared to the dimensions of the vessels. However, non-equilibrium plasma are usually generated at low pressure whereas at atmospheric pressure, thermal plasmas are generated. Three typical RF discharges configuration are shown in figure 2.3-9 with a and b using capacitive coupling and used at low pressure, and c used at higher pressure (up to atmospheric) and using an inductive coupling where the discharge take place in the magnetic field of an induction coil. (Eliasson et al., 1991)

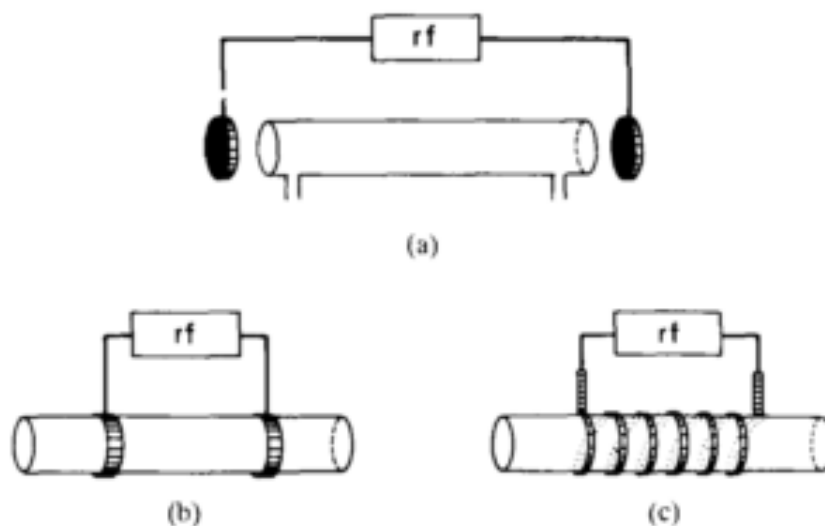


**Figure 2.3-9: Different types of RF discharges.(Eliasson and Kogelschatz, 1991)**

Microwave (MW) discharges are usually using frequencies below 3 GHz to generate plasma as the electromagnetic field wavelength is similar to the discharge vessel dimensions. Microwave induced plasmas are usually far from the local thermodynamic equilibrium as the high frequencies allow only light electrons to follow the electric field oscillations. They can also be generated at low and high pressures (up to atmospheric). (Eliasson et al., 1991) Microwave induced plasmas can be separated in three categories since 1993: discharges produced in open structures, closed structures and in resonance structure in presence of a magnetic field. (Marec et al., 1993; Conrads et al., 2000) Closed structures can be microplasmas (compact microwave induced plasma source) whereas plasma in open air can be free expanding

torches using different torches such as metallic torches, or semi-metallic torch. Resonant cavity plasmas amplify the wave sent to the system through the resonance phenomena: waves bounce back and forth inside the cavity, combine together, reinforcing and increasing their energy. This phenomena at the appropriate frequency (the generator and the cavity resonance frequency should be the same) will trigger the discharge. (Tendero et al., 2006)

#### 2.3.3.2.4. Dielectric barrier discharges

Dielectric barrier discharges, also known as DBD, were first introduced in 1857 by Siemens to generate ozone, determining the direction for DBD investigations and applications for many years. (Fridman et al., 2011) After their main use in ozone generation, DBD plasmas can be used in carbon dioxide lasers, to produce methanol, to deposit thin-film or for plasma display. (Conrads et al., 2000)

A dielectric barrier discharge is composed of two electrodes, usually metal plates, with at least one of the plates covered by a dielectric layer. The gap between both electrodes, a space of few millimetres, is where the plasma takes place, ignited through a pulsed or a sinusoidal power generator. (Tendero et al., 2006) Different types of DBD configurations are presented in Figure 2.3-10 with planar and cylindrical configurations. These discharges are usually sustained at frequencies between 50 Hz and 1 MHz, along with voltages between 1 to 100 kV. (Conrads et al., 2000) The so-called silent discharge formed can be a glow or a filamentary discharge, depending on the voltage and frequency in use, as well as the gas composition. Filament discharges are formed on the surface of the dielectric layer by forming streamers or micro-discharges. (Tendero et al., 2006) Glow discharges appear to be favour by the use of helium due to He metastable species (Yokoyama et al., 1990) and Penning effect (Massines et al., 1998; Goossens et al., 2001)

The dielectric layer has an important role as it limits the discharge current as well as avoids the transition to arc discharge, enabling the current to be continuous or pulsed. Besides, it ensures a homogeneous treatment as the streamers will randomly appear on the electrode surface, due to the accumulation of electrons on the dielectric layer. (Tendero et al., 2006) Thus, the whole DBD zone is composed of microdischarges spread quite uniformly with a short lifetime (1-20 ns for a 1mm air gap), leading to

very little overheating of the DBD. (Fridman et al., 2011) The main advantage of DBD plasmas compared to other discharges is the possibility to use atmospheric non-thermal and their relatively easiness to scale-up. (Conrads et al., 2000)

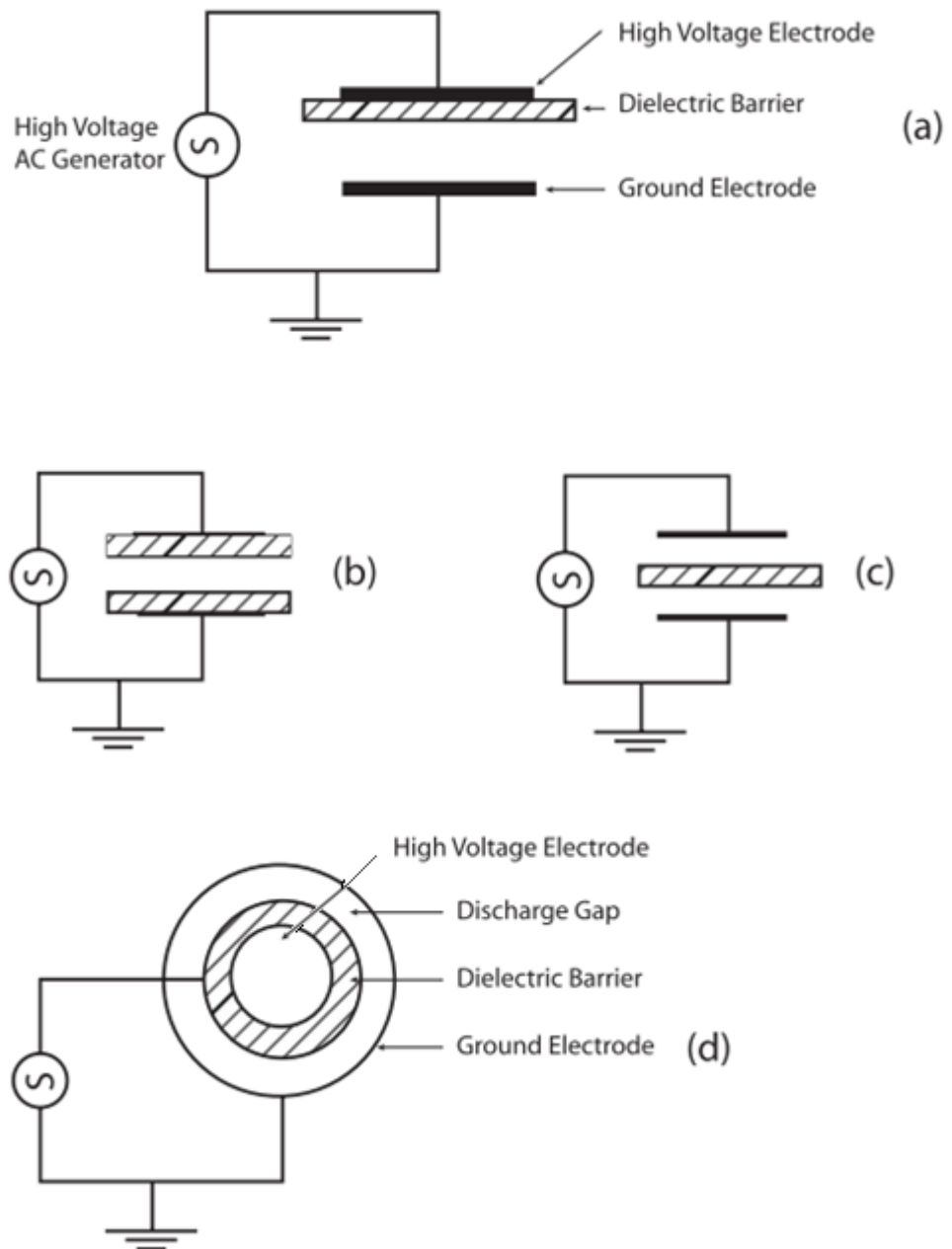


**Figure 2.3-10: Common configurations of dielectric-barrier discharges with planar configuration (a, b, c) and cylindrical configuration (d). (Fridman, 2008)**

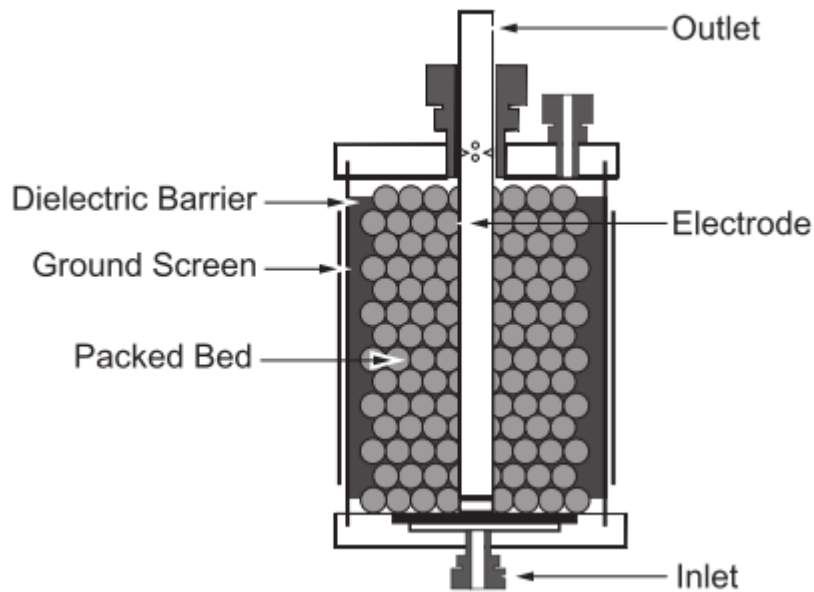


**Figure 2.3-11: Schematic of a packed-bed DBD discharge. (Fridman, 2008)**

Other types of DBD such as surface discharges, packed-bed corona discharges or non-thermal, high-voltage, atmospheric-pressure, floating-electrode dielectric barrier discharge (FE-DBD) can be of interest. For example, FE-DBD are interesting as they use the human body as a second electrode to generate plasma, without damaging the living tissue. They could be very interesting for medical and biological applications. On the other hand the surface discharges are mainly of interest to reduce the breakdown voltage for unification of the electric field and local overvoltage. (Fridman, 2008) Packed bed corona discharges are a combination of DBD and sliding surface discharge and represented in Figure 2.3-11. A high voltage is applied to the packed bed and a non-equilibrium plasma will be created in the void space between the dielectric pellets of catalyst. By refracting of the electric field on the pellets, the electric field becomes non-uniform and stronger with an intensity dependent of the porosity, shape and dielectric constant of the pellets. (Fridman et al., 2011)

## **2.4. Plasma-catalysis systems**

Plasma systems are of interest for some chemical applications as they involve greater temperatures and higher energy density as well as very high concentration of active species. The fact that plasmas are not ruled by the thermodynamic equilibria whichever are the concentrations of reactive species and the reactor temperature, make their use in chemical processes even more attractive. (Fridman, 2008) To combine the high selectivity of the catalysis reaction and the advantages of the plasma technique, the combination of plasma and catalyst, also called plasma-catalysis, have been of interest for the scientific community. The interest in plasma-catalysis increased due to its possible application to environment such as destruction of pollutant in the waste gas stream or minimisation of unwanted products like nitride oxides or carbon dioxide. (Whitehead, 2010) Even though the mechanisms of these kind of processes are hardly understood, plasma-catalysis presents many advantages compared to thermal catalysis such as a lower temperature. (Neyts et al., 2014) In this section, the different types of plasma-catalytic configurations and the synergetic effect of plasma-catalysis will be presented, as well as the reported effect of plasma on the catalyst and the reported effect of the catalyst on plasma. Finally, a way to choose a catalyst for plasma-catalysis will be discussed.

### **2.4.1. Type of plasma-catalytic reactors**

The classification of plasma-catalytic reactor can be found in Figure 2.4-1, dependent of the position and the number of catalyst beds. A single-stage plasma system is a plasma reactor containing the catalyst. In a two-stage reactor, the plasma reactor comes first, followed by a catalyst reactor. This kind of configuration is used for ozone production for example whereas the single-stage reactor has been reported for acetaldehyde removal. (Kim et al., 2016) Single-stage plasma catalysis processes are mostly suitable for non-thermal plasmas whereas the two-stage plasma-catalysis system are suitable for both thermal and non-thermal plasmas. (Neyts et al., 2014) To prevent the formation of arc, plasma-catalysis reactors are mainly operated in the presence of one barrier minimum, dielectric barrier discharge being the most common type of plasma. However, discharge characteristics can be altered when barrier discharge plasma, with or without catalyst, are operating at a temperature higher than

100 °C or at high frequencies. As the temperature increases, the discharge can become unstable, affecting the current and voltage of it. (Kim et al., 2016)

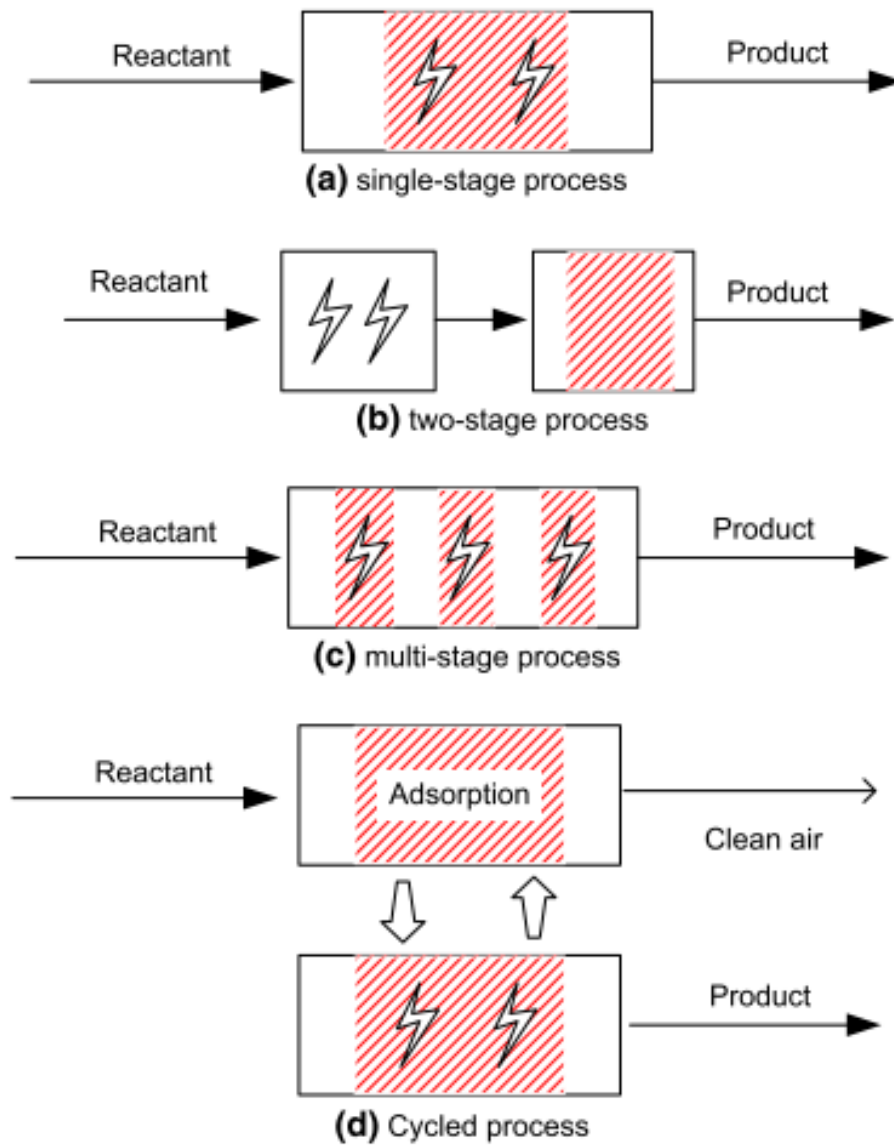


**Figure 2.4-1: Types of plasma-catalyst reactors according to catalyst bed position and number (Kim et al., 2016)**

As the optimisation of the catalyst and the plasma can be done separately in a two-stage system, simplifying the process optimisation, most commercial application use this type of configuration. On the other hand, in single-stage processes, the interactions between the non-thermal plasmas and the catalyst are more complex and their understanding is behind the understanding of the two-stage processes. Plasma-

catalysis performance are highly influenced by the position of the catalyst. In most catalyst cases, a single-stage process is better than a two-stage process, with some exceptions such as  $\text{MnO}_2$  and  $\text{Ba-CuO-Cr}_2\text{O}_3$  on alumina support. The use of multi-stage processes for the industry can be interesting in future plasma-catalysis work. This will enable different combination of catalysts, each with a different function depending on its position and expected reaction. Another process of interest is the cycled system consisting of two steps absorption and plasma decomposition of the adsorbed pollutants. They are attractive as less energy is required than for continuous processes and they presented higher performance than usual desorption technics. (Kim et al., 2016)

#### **2.4.2. Synergetic effect of plasma-catalytic systems**

The characteristics for plasma-catalysis such as product selectivity or energy efficiency, result in an improvement by using plasma-catalysis compared to the sum of the processes taken individually. This is defined as the synergetic effect of the plasma-catalytic system. (Neyts et al., 2014) Mainly reported for volatile organic compounds (VOCs), it has for example been reported for decomposition of toluene at room temperature using  $\text{TiO}_2$  as catalyst by Whitehead and his co-workers. (Whitehead, 2010) Figure 2.4-2 showed the synergetic effect for destruction of toluene as using plasma only or thermal catalysis only lead to a 10% destruction approximately. Their combination however led to, not the sum of the two destruction percentages - 20%, but a 65% destruction of toluene. The synergetic effect has thus been demonstrated at 25°C for toluene destruction using  $\text{TiO}_2$  catalyst but was not observed at high temperature. (Whitehead, 2010)

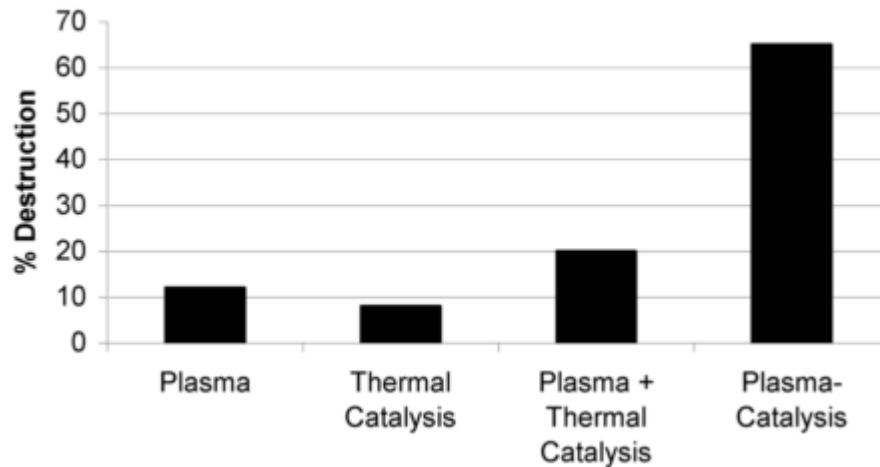


**Figure 2.4-2: Synergetic effect of plasma-catalysis for destruction of toluene at 25°C. (Whitehead, 2010)**

Synergetic effects in both hydrocarbon reforming and VOC abatement have been reported in many papers and listed by Neyts et al. in a review. (Neyts et al., 2014) This synergetic effect has been studied for phenol or toluene destruction, ammonia reforming, methane reforming or carbon dioxide splitting. It is actually dependent on specific conditions in which the plasma-catalysis takes place. Besides, interactions between catalyst surface conditions and plasma generation are interconnected: as the plasma characteristics are affected by the catalyst ones, plasma may alter the conditions on the catalyst surface. (Kim et al., 2016)

### **2.4.3. Effect of the addition of catalyst on a plasma discharge**

After discussing the synergetic effect of plasma-catalysis, the effect of catalyst on the plasma will be presented in this section. Four main effects have been reported: an electric field enhancement, microdischarges formation in pores (often put together with the electric field), changes in discharge type and adsorption of pollutant on the catalyst surface.

First, roughness and reactor distortion can result in an enhancement of the electric field. Pellets, granulates or fibres in the discharge volume as well as porosity, together or not with roughness may be at the origin of the enhancement. (Takuma, 1991) The “packed bed effect” is not always related to the catalytic component of the packing material. This effect is usually considered as a physical effect as the pellets can be

dielectric material, such as glass beads, coated or not with catalyst material, or can be combined with zeolite or catalytic pellets. (Neyts et al., 2014) Polarisation effects as well as charge accumulation on the dielectric layer surface lead to an enhancement of the electric field. The contact angle, dielectric constant of the pellets and the curvature are key to this enhancement: on a porous catalyst surface, a large surface curvature enables a field enhancement. (Chang, 2000; Woo Seok et al., 2003) The modified electric field is affecting the electron energy distribution and thus the electron dissociation and ionisation rates, which are determining the plasma chemical composition. (Neyts et al., 2014) Zeolites (Liu et al., 2002) and ferroelectric materials (Holzer et al., 2005) used in a plasma system have been shown to lead to an enhanced electric field, with values ten or more times bigger, modifying the energy distribution of the electrons close to the surface. The oxidative power of the plasma have also been demonstrated along with the enhanced electric field for compounds such as toluene et methyl tert-butyl ether (Holzer et al., 2005). However, an increase of oxidation in plasma environment was not found for all compounds: compounds like diethyl ether and p-cumene did not see their oxidation increased. (Chae et al., 1999)

Linked to the electric field enhancement, micro-discharges can appear inside the catalyst pores. (Holzer et al., 2005; Hensel et al., 2005; Hensel, 2009) Due to a very strong electric field inside the pores, the characteristics of the discharge inside the pores are different to the bulk ones. This leads to different rates of production and loss of plasma species and consequently in a change of chemistry. (Neyts et al., 2014) Studying the formation of discharge as a function of the pore size in view of waste gas treatment, Hensel et al studied the behaviour of the discharge under nitrogen, oxygen or air flow. (Hensel et al., 2005; Hensel, 2009) For a small pore size (smaller than one micrometre diameter), surface discharge could be observed on the porous material but no discharge could be seen inside the pores. For bigger pore size (over 15 micrometres) however, stable microdischarges could also be observed inside the pores along with the surface discharge, resulting in a large stable volume of atmospheric pressure plasma.

The presence of catalyst, considered as an insulating surface, results in an expansion of the discharge region as streamers propagate on the surface, leading to a more intensive discharge around points of contact than for volume streamers. (Malik et al.,

2005; Van Durme et al., 2007) This surface discharge increased the removal efficiency for VOC destruction, consequence of higher concentration of reactive species due to higher electron dissociation and ionisation rates. Tu et al (2011) reported the effect of the addition of Nickel-alumina pellet catalyst into the reactor: the introduction of the catalyst lead to a discharge shift from a filamentary discharge to a predominant surface discharge on the catalyst as wells as a combination of limited microdischarges. (Tu et al., 2011) Zeolites have shown similar behaviour: those zeolite supported metal nanoparticles promoted the plasma expansion over a wide surface area. (Kim et al., 2009) In the case of a honeycomb monolith, a surface discharge can develop at the inner wall of each honeycomb hole, called a honeycomb discharge. This discharge is able to fill the whole reactor with a surface discharge. (Mizuno, 2013)

Finally, the presence of catalyst may modify the degradation processes in the plasma or pollutant concentration. As pollutants can be adsorbed on the catalyst surface, they increase their retention time inside the reactor leading to a higher destruction rate for plasma-catalytic processes compared to plasma only processes. (Van Durme et al., 2007) Considering the relative concentration of the pollutants in the inlet flow, their concentrations are unlikely to affect greatly the discharge. The adsorption of reactive species and pollutants is increasing with the porosity of the material. (Rousseau et al., 2004) Consequently, microporous zeolite, having a vast surface area, tend to adsorb a large quantity of pollutants over time, reducing the abatement efficiency. (Neyts et al., 2014) Therefore, the decomposition of VOCs is more influenced by the absorption process than by the discharge characteristics. (Van Durme et al., 2007)

#### **2.4.4. Effect of plasma on catalysis**

##### **2.4.4.1. Effect of plasma components to a catalytic stage**

As mentioned previously, plasma can be described as a mixture of six key elements: photons, electrons, neutrals, negative and positive ions and excited molecules. For any type of application, plasma chemistry involves multiple interactions between all these components. The role played by plasma components can explain the effect of plasma on catalysts. The major components are represented on Figure 2.4-3. (Kim et al., 2016) A chemically active plasma system is highly reactive due to its high charged particles concentration (ions and electrons), excited particles with a heavy

contribution of vibrational and electric excitations, UV photons, active atoms and radicals. Electrons first collect energy from the electric field and distribute this energy via collision by generating new species. Excited particles by vibrational excitation are able to transfer energy through gas heating, accelerating the reaction in the plasma. Ions and radicals can react in the plasma at much lower temperatures than required by thermal processes and thus, are essential to plasma-catalysis processes.

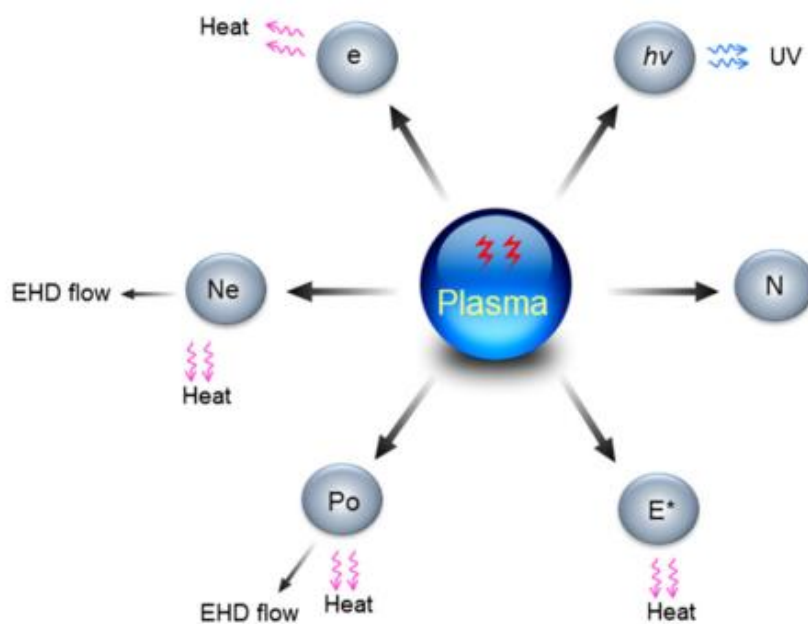


**Figure 2.4-3: Major components of plasma with electrons (e), photons (hv), neutral molecule (N), excited molecule (E\*), positive ion (Po) and negative ion (Ne). (Kim et al., 2016)**

Ultraviolet (UV) radiations have different effects on the system. The radiations from photons in an atmospheric pressure non-thermal plasma have been proven to be smaller than the one of the outside light which is about several  $\text{mW}\cdot\text{cm}^{-2}$ . As the velocity of the photocatalytic reactions is much smaller (2 to 3 orders of magnitude) than the reactions in plasma-catalysis, catalytic reactions induced by UV radiations are negligible. (Kim et al., 2016) However, the Joshi effect may affect plasma generation through UV radiations on the surface of the reactor: microdischarge number or plasma intensity are enhanced by external UV-radiation of the plasma reactor. (Falkenstein, 1997) The kind and bilateral interaction should be studied in more details to be better understood.

Another secondary effect in the plasma from its key components is the generation of electrohydrodynamic (EHD) flow, also mentioned as ionic wind or corona. Ions carried along the discharge channel collide with gas molecules, transferring their energy to the molecules and generating a gas flow. (Nygaard, 1965) The velocity of the electrohydrodynamic flow is a function of the square root of the discharge current and is proportional to a constant  $K$  depending on the configuration of the electrodes, with a typical value of  $10 \text{ ms}^{-1}$ . The electrohydrodynamic flow may enhanced mass transfer from the gas-phase to the catalyst surface and lead to turbulent conditions around the catalyst bed. Thus, it can affect the mass transfer of reactants and long lifetime active species in the plasma system. (Kim et al., 2016)

The migration flow of charged species such as ions and electrons, will lead to a temperature increase in the system via dielectric loss, joule heating and gas heating in the plasma channel. A higher dielectric constant generates a higher dielectric loss: the use of ferroelectric material may increase the temperature inside the reactor more easily. This can, for example, be observed on ozone generation on a  $\text{BaTiO}_3$  packed-bed. (Jogan et al., 1993) However, the reactor temperature increase is primarily dependent on the reactor energy input and more care should be provided when the reactor is operating at high power input. This is also due to the high importance of the temperature role in the chemical reactor designs. In fact, chemical reactions are classified depending on their enthalpy changes into endothermic and exothermic reactions. An endothermic reaction is a reaction during which the system is absorbing heat, resulting in a positive enthalpy change, whereas an exothermic reaction is releasing heat and its enthalpy change is negative. As a temperature change leads to an equilibrium change, Le Chatelier's principle declares that endothermic and exothermic reactions favour respectively high and low temperatures. Thus, the enthalpy changes of the chemical reaction of interest are important to determine and control properly the temperature of the plasma-catalytic system. For example, gliding-arc and arc discharge have performed better than non-thermal plasma such as pulsed discharge or DBD when used for endothermic reactions like dry or steam reforming. (Kim et al., 2016)

#### **2.4.4.2. Effect of the addition of plasma to a catalytic stage**

Catalytic reactions can be represented as a three-step process: adsorption, followed by surface reaction and desorption. The main role of the catalyst is to reduce the activation energy of the intended reaction by providing to the chemical reaction new pathways. Catalysts can also provide a higher reaction selectivity through the new reaction pathway. Instead of thermal catalysis, plasma can be used for heat substitution with different consequences. The fact that adsorption is inversely proportional to temperature makes the use of low-temperature plasma-catalysis highly beneficial for the process. Two additional functions are provided by the plasma for adsorption processes: the generation of highly reactive molecules and the production of intermediates more easily adsorbed by the catalyst than the original molecules. (Kim et al., 2016)

First, by generating excited molecules and reactive radicals through electron collisions in plasmas, electrophilic atoms are created by the presence of unpaired electrons in them. Thus, adsorption of radicals is promoted on the electron-rich catalyst surfaces. The dissociation of excited molecules on the catalyst surface can also be more easily obtained than the dissociation of non-excited molecules as underlined by a threshold shift to lower energy and an increased cross section. (Kim et al., 2016) Second, the conversion of some reactants in the gas-phase by radicals into intermediates often leads to more easily adsorbed molecules. Adsorbed reactant concentration on the catalyst surface can also modify the plasma-catalysis reaction. This can be observed for toluene decomposition on zeolites in a plasma-catalytic reactor, as described by Oh et al. (2006)

Radicals induced by plasma may react directly with adsorbed molecules, as it can be seen for CO oxidation over Au/TiO<sub>2</sub> catalyst, fully deactivated, in presence of plasma. (Kim et al., 2007) Those reactions seem to follow the Eley-Rideal (E-R) mechanism where a molecule in the gas phase reacts with another molecule, adsorbed on the catalyst, without being adsorbed itself. However, this radical-induced process in gas phase is referred to as reverse E-R reaction in opposition to the traditional E-R reaction where the active molecules are fixed on the catalyst surface. Actually, desorption processes are promoted by plasma through electron and ion bombardment, as shown by Yoshida et al. for desorption of carbon dioxide induced by plasma for

example. (Yoshida et al., 2007) As plasma-catalysis temperature is mostly much smaller than the one of a catalytic chamber, desorption can become a limiting step of plasma-catalysis. Thus, plasma interaction with the surface is happening at every elementary step with different influences on the whole reaction. (Kim et al., 2016)

The characteristic timescales in catalytic and plasma reactions are compared in Figure 2.4-4. The plasma reaction can be separated in two types: the fast reaction where radicals are created and reacting and, once those have disappeared, the slow reaction where highly reactive molecules such as ozone are being involved. Ion molecules are reacting even faster than radicals but their contribution to the overall plasma-catalysis reaction is considered negligible. (Nozaki et al., 2004) For the catalytic reaction, the initial step, chemisorption happens within  $10^{-9}$  s. Due to surface rearrangement via surface diffusion and spillover as well as diffusion into micropores, a longer time is needed for the whole adsorption process, about 1 s. The global catalytic reaction time is usually between  $10^{-2}$  and  $10^2$  s, about two to three orders of magnitude bigger than the fast reaction for radicals in plasma systems. (Somorjai, 1992) Thus, the rate-limiting step for plasma-catalytic systems in gas phase is surface reaction and not plasma: the chemical reaction is more likely to go from the plasma to the catalyst.

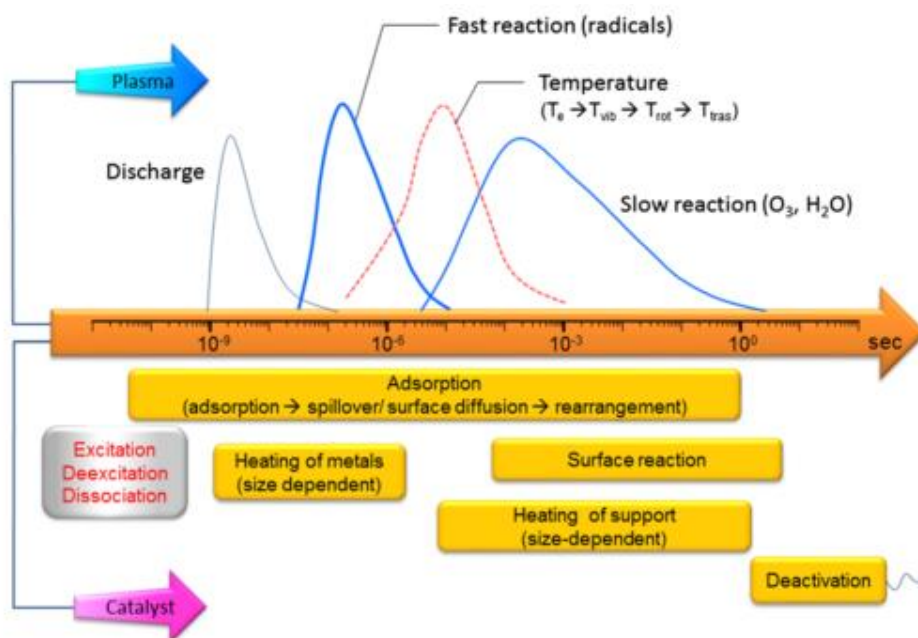


**Figure 2.4-4: Characteristic timescales in plasma and catalytic reaction (Kim et al., 2016)**

The contribution of plasma heating to plasma-catalysis is still unclear. The increase of temperature in a plasma-catalytic system is dependent of the energy input. Besides, transitions of a vibrational-translational temperature and a vibrational-vibrational temperature take place within about  $10^{-4}$  s after the discharge period. In presence of humidity, the vibrational-translational rates of transition are accelerated for oxygen and nitrogen. It is unknown if those changes in transition temperature can affect the catalytic reaction and the catalyst heating. Thus, those interactions in plasma-catalytic systems require further investigation. Such fundamental studies on the non-thermal plasmas and catalysts and their interactions are often restricted by the lack of appropriate instruments available, particularly for in-situ measurements. Techniques used for conventional thermal catalysis analyses such as electron spin resonance (ESR), Fourier transform infra-red (FTIR), X-ray photon spectroscopy (XPS), operando scanning tunnelling microscopy (STM) or X-ray diffraction (XRD), are difficult to apply to plasma –catalytic processes due to the presence of electrical insulation, electrical discharge and electromagnetic noise. Nevertheless, those analysis techniques have been implemented in different plasma systems, as has been laser-induced fluorescence technique. With the development of plasma-catalysis, in-situ monitoring techniques will be more and more implemented and perfected. (Kim et al., 2016)

#### **2.4.4.3. Effect of plasma on the catalyst**

As well as modifying the mechanisms of catalysis reactions, plasma may induce changes in catalyst properties as the discharge expand over the catalyst surface. Different effects have been observed. First, a higher adsorption probability on the catalyst surface is observed in case of plasma-catalysis. As presented in the previous section, the adsorption-desorption mechanisms and their equilibrium are affected by the discharge. Neyts et al. (2014) suggested that the electric surface properties of the catalysts are modified by the discharge, affecting the Keesom, Debye and London dispersion (respectively dipole-dipole, dipole-induced dipole and induced dipole-induced dipole) and thus the adsorption-desorption. Such modifications will modify the surface reactions mechanisms such as Langmuir-Hinshelwood (reactants adsorbed on the surface), Eley-Rideal (one reactant adsorbed and one in gas phase) or Mars-van-Krevelen mechanism (one reactant adsorbed, the other being the catalyst surface).

The plasma influence on Eley-Rideal mechanisms has been presented in the previous section. Second, a higher surface area of catalyst can be observed as plasma may lead to form smaller nanoparticles, higher dispersion and thus, a larger surface area. (Hong et al., 2010) The increase of particle dispersion can also lead to a stronger catalytic activity, as it has been demonstrated for the conversion of methane and carbon dioxide into value-added chemicals using a nickel supported on alumina catalyst. (Shang et al., 2009) As those particles are less ordered surface, with vacancies, defects, undercoordinated sites, corners and edges, this unpolished surface induced by plasma will enhance the catalytic activity. (Neyts et al., 2014) The whole morphology of the catalyst can be changed by plasma as it has been shown on SEM images of manganese oxide catalysts before and after being treated by plasma. (Guo et al., 2006)

Even more, in this example, the oxidation state changed after plasma treatment, going from a third oxidation of manganese to an oxidation state +2 and +3. This is another effect of plasma on catalyst: change in oxidation stage of catalyst. It has been found that oxygen plasma could reduce metals and thus increasing their activity. For example, this phenomena has also been observed for Ag, Cu and Au supported on  $ZrO_2$  after oxygen plasma treatment. (Pylinina et al., 2013) Whereas Guo presented a decrease in manganese oxidation state, (Guo et al., 2006) Demidyuk and Whitehead observed an increase in oxidation state from Manganese +4 to +5 in a Manganese oxide supported by alumina. (Demidyuk et al., 2007) From those papers, the oxidation state of the catalyst may change due under the influence of discharge or via interactions with reactive oxygen species promoting electron transfer from those reactive species to Mn active sites. As presented before, plasma can induce the reduction of metal oxide catalyst to metallic form for metals such as Ni or Fe. The reduction of nickel oxide to nickel was reported under an atmospheric pressure for a DBD plasma (Tu et al., 2011) or a glow discharge (Shang et al., 2009) used for dry reforming. Besides, a reduced coke formation on catalyst can be observed in presence of plasma, preventing the catalyst deactivation. This has been illustrated by Shang et al for dry reforming (Shang et al., 2009) and can be attributed to a higher dispersion of the catalyst in the plasma. (Neyts et al., 2014) Finally, a change in work function can be observed, the work function being described as the required energy to remove an electron from the catalyst (or ionisation energy for metal catalyst case). The work

function of a catalyst is influenced by its surface conditions and can be changed through contamination or surface reactions. (Neyts et al., 2014) Under plasma environment, the voltage and current applied to the catalyst surface may modify the work function of the catalyst, resulting in a potential electron extraction from the catalyst via plasma-induced polarisation. (Wu et al., 1997) A higher work function improves active metal reduction and promotes oxidative reactions, resulting in a modified catalytic activity of the surface. (Poppe et al., 1999)

As suggested by van Durme et al., (2007) the enhancement of catalytic activity in plasma-catalysis might be related to the formation of hot spots on the surface of the catalyst. Hot spots can be described as regions that are locally higher than the mean temperature, due to the formation of strong microdischarges in areas with high curvature like pellets or the catalyst pores. (Van Durme et al., 2007) Those hot spots are linked to the enhancement of the electric field described previously. They can modify the local plasma chemistry (Holzer et al., 2005) or thermally activate the catalyst locally as demonstrated by Kim et al for benzene degradation on Pt/Al<sub>2</sub>O<sub>3</sub> catalyst. (Kim et al., 2006) On the other hand, it is argued that hot spots can also have a negative influence with catalyst deactivation and low selectivity for targeted products, due to the catalyst damage induced by plasma. (Löfberg et al., 2011)

Other components of plasma can activate the catalyst surface, like photons by photon irradiation. The use of a catalyst activated by photon is known as photocatalysis, TiO<sub>2</sub> being the most common catalyst used in this type of catalysis (anatase form). This oxide, with a bandgap of 3.2 eV, can be activated for redox reactions by any photon with a wavelength below 387 nm. This mechanism is most likely to be important in so-called 'photon-rich' plasmas. It is however, subject to debate in the scientific community. In some studies, the photons have been shown not to enhance catalytic activity. (Kim et al., 2008) On the other hand, studies have demonstrated to enhance the catalytic activity, even if this enhancement was negligible without using UV lamps. (Guaitella et al., 2008)

In presence of plasma, a high proportion of the species are in vibrationally excited states, which are more reactive than their non-excited counterparts. This state may lead to lower the activation barrier for surface reactions as the initial energy of the

reactants is higher. This mostly happens in case where the lifetime of those excited species is long enough for them to reach the surface before returning to their ground state. When dealing with excited molecules, the activation energy may be even more reduced with a smaller energy of the metastable state, resulting in a non-adiabatic barrier crossing. Thus, processes for which the product states are close to the transitional states (a.k.a. late transition barrier process) are the only ones affected by the vibrational excitation, whereas early transition barrier processes (transition state close to reactants) are hardly affected. This non-adiabatic barrier crossing is probably the main mechanism in the discharge as the higher state of excited molecules is limited for the vibrationally excited reactants. (Neyts et al., 2014) Moreover, the treatment of plasma on the catalyst, modifying its surface may lead to an even lower activation barrier. This could be seen for example for toluene decomposition in Demidyuk and Whitehead's paper. (Demidyuk et al., 2007) Arrhenius plot have been obtained for different catalysts ( $\gamma$ -Al<sub>2</sub>O<sub>3</sub>, MnO<sub>2</sub>-Al<sub>2</sub>O<sub>3</sub> and Ag<sub>2</sub>O-Al<sub>2</sub>O<sub>3</sub>) before and after plasma treatment to identify the mechanism of plasma activation. No energy activation difference was found before and after being introduced inside the discharge. Changes could though be observed related to the oxidation state of the catalyst, leading to an increase of active sites for MnO<sub>2</sub>-Al<sub>2</sub>O<sub>3</sub> or a smaller activation energy for Ag<sub>2</sub>O-Al<sub>2</sub>O<sub>3</sub>.

As described in section 2.4.4.1, the numerous components of the plasma discharge lead to a very different gas mixture than the one before the plasma, which results in a different choice of reactants available for the catalysis reaction. Thus, in presence of plasma, the reaction pathways are going to be different from the traditional catalysis reaction. All components of the plasma may participate to the reaction pathways: not only electrons and photons, but also ions and electronically excited species. Even if most their lifetime in the plasma is very short, lowering their probability to bombard the catalyst surface, electrons and photons may be in contact with adsorbed molecules on the catalysts, creating ions and electronically excited species participating to the reaction pathways. Notorious excited species with longer lifetime, such as <sup>1</sup>Δ<sub>g</sub> singlet oxygen, are known to be very reactive and appear of importance in pathways such as for VOCs oxidation. (Neyts et al., 2014)

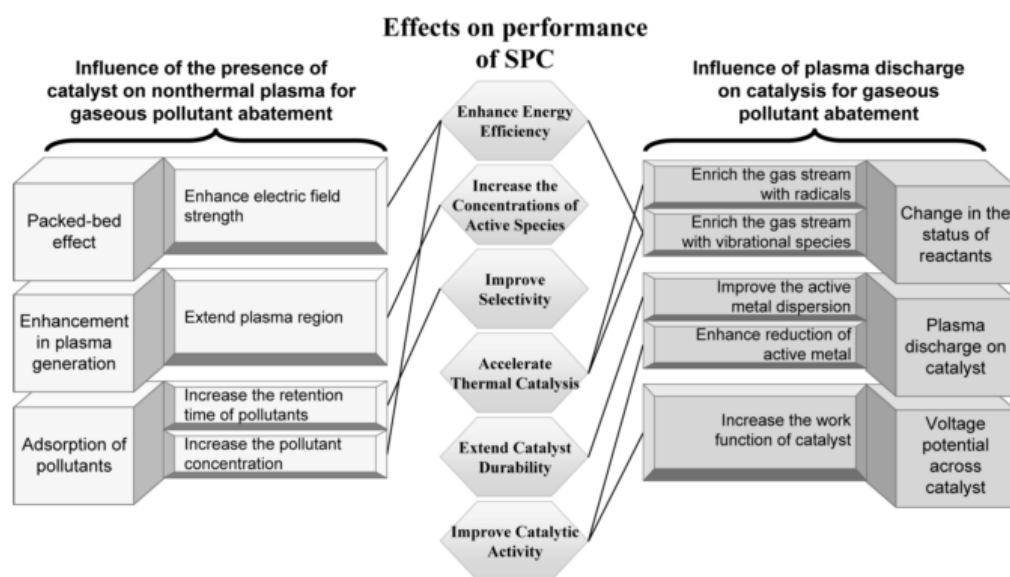


**Figure 2.4-5: Illustration of the mechanisms to enhance the performance of a single stage plasma-catalysis (Chen et al., 2009)**

To conclude, the main mechanisms to improve the performance of a single stage plasma catalysis can be summarised as in Figure 2.4-5 from Chen’s review on VOC removal by single or two-stage plasma-catalysis system. (Chen et al., 2009) The effects are presented on the left with the effect of catalyst on plasma and on the right with the effect of plasma on the catalyst, presented in the previous section.

### **2.4.5. Catalyst selection for plasma-catalytic systems**

No rule has been yet determined to choose an appropriate catalyst for a specific plasma-catalytic reaction. This can be explained by the extensive choice of available catalysts and of their preparation. As the catalytic performance can be affected by the type of precursors used, different catalysts are being studied, for different reactions and under different conditions. Thus, the best approach to choose the right catalyst for a specific plasma-catalytic reaction might be to use the information on the thermal-catalytic reaction associated. (Kim et al., 2016) Such an approach leads to a wide range of possible combinations for plasma-catalysis for which the best combination might need to be demonstrated experimentally. Furthermore, plasma-catalysis enables the use of different form of catalysts such as honeycomb monolith, foam, coating on the electrodes or reactor walls or packed bed in form of granulates, pellets, powder or coated fibre. (Neyts et al., 2014)

Observation of the relation between the catalytic performance and the surface streamer propagation has been conducted via intensified charge-coupled device (ICCD) camera imaging of plasma on catalysts. (Kim et al., 2009; Kim et al., 2015) Two different modes of discharge have been observed. It is usually around catalyst contact points that partial discharge is observed. By increasing the voltage, plasma can be observed on the catalyst surface as well as on the contact points, even if it does not propagate to the surface. Necessary for strong interaction and to obtain efficient catalyst in plasma, the contact area should be the largest possible. Thus, the distance between the plasma and the catalyst should be as small as possible for an efficient utilisation of the short-lived radicals on the surface. (Kim et al., 2016)

A parameter  $K$ , dimensionless, (Kim et al., 2014) has been created to describe the interaction between plasma and catalysts, for any process requiring the transport from plasma to target material of short-lived species. It is dependent of the migration length of ionic species and the diffusion length of reactive species ( $L_{ef}$  and  $L_D$  respectively). (Kim et al., 2016) As catalysts can be described by their electrical capacitance, resistivity and dielectric constant, the overall equivalent circuit of a packed bed is modified by those values and the plasma generation itself is affected. This has been experimented and three main changes could be drawn: first, it decreased the plasma ignition voltage; second, the number of microdischarges increased; third, the loading of metal nanoparticles on the catalyst surface extended the plasma area. The electrical resistivity of the catalyst can be optimised and used in a specific range, yet to be determined as studies are yet to be conducted. (Kim et al., 2016)

Using the tip of scanning tunnelling spectroscopy (Lee et al., 2011) or a bias-voltage (Deshlahra et al., 2011), the dissociation of absorbed species via external electron injection has been reported as well as its enhancement. This may also be applicable to plasma-catalysis where surface streamers are propagating on the catalyst surface and the relaxation and accumulation of charged molecules happens in the range of  $10^{-8}$  s. (Kim et al., 2016) For plasma-catalysis to be practical and used in large-scale applications, durability is essential. Although long-term testing (> thousand-hour experiment) and pilot-scale of plasma-catalysis processes have hardly been studied, deactivation mechanisms are known: poisoning via S, Hg, P, Cl or Pb, carbon (coke) deposition, nanoparticle accumulation and mechanical or thermal stress. To prevent

the accumulation of nanoparticles, also called sintering, the low-temperature used in plasma-catalysis may have a positive effect. To reduce the size of active metals, plasma treatment has proven to be effective. (Kim et al., 2016)

## **2.5 Hydrogen rich syngas generation and reduction of tar compounds with plasma-catalysis systems**

### **2.5.1 Generation of syngas using plasma-catalytic system**

Production of syngas by dry methane reforming and carbon dioxide conversion have been the subject of many studies for their potential to alleviate global warming by utilising methane and carbon dioxide to produce syngas for further use. These two processes are described in this section.

#### **2.5.1.1 Dry methane reforming and biogas reforming**

Dry methane reforming or biogas reforming have been the subject of studies recently for its utilisation of greenhouse gases for produce added-value products. Aziznia et al. compared the catalytic dry reforming of methane over Ni/Al<sub>2</sub>O<sub>3</sub> catalyst (923-1023 K) to the low temperature plasma-catalytic corona reforming. The effect of power discharge, feed flow rate and catalysts were investigated. The use of catalyst in the plasma reactor increased the conversions of methane and carbon dioxide, resulting into higher selectivity to CO, less by-product formation, such as oxygenates and hydrocarbons. Higher loadings of nickel on alumina catalyst and higher power discharges led to higher CO<sub>2</sub> and CH<sub>4</sub> conversions. These conversions decreased for increasing feed flowrates. (Aziznia et al., 2012)

Tu et al. investigated dry reforming of methane in a coaxial dielectric barrier discharge reactor (Tu et al., 2011) and worked toward understanding the synergetic effect at low temperature (Tu et al., 2012). These works were conducted over Ni/Al<sub>2</sub>O<sub>3</sub>. In the work from 2011, the catalyst is packed within the plasma discharge zone and the electrical characteristics of the discharge are studied. A change of the discharge behaviour was observed when pellets were introduced, from a filamentary micro-discharge to a

combination of surface discharge on the catalyst surface and limited spatial micro-discharges. Moreover, when the catalyst is fully packed in the discharge zone, the breakdown voltage of the mixture  $\text{CH}_4/\text{CO}_2$  was shown to decrease. The enhancement of charge transfer and expansion of discharge was attributed to the presence of Ni active site, conductive, and dispersed on the catalyst surface. When the catalyst was added to the system, the molar product ratio  $\text{H}_2/\text{CO}$  raised from 0.84 to 2.53 and the  $\text{H}_2$  selectivity was increased. (Tu et al., 2011) The work from 2012 demonstrated the presence of reactive species such as  $\text{C}_2$ ,  $\text{CO}$ ,  $\text{CH}$ ,  $\text{CO}_2^+$  and  $\text{N}_2^+$ . The catalyst presence was shown to have little effect on the discharge temperature. The synergetic effect obtained from the plasma-catalysis system was observed for 10wt.%  $\text{Ni}/\text{Al}_2\text{O}_3$ , partially packed in the discharge zone, showing a high  $\text{CH}_4$  conversion (56.4%) and  $\text{H}_2$  generation (17.5%). The synergy effect resulted in a significant improvement of energy efficiency. This effect could be the result of strong interactions between the plasma and the catalyst and a high activity of the  $\text{Ni}/\text{Al}_2\text{O}_3$  catalyst. (Tu et al., 2012)

Zeng et al. (2018) studied the low temperature biogas reforming in a plasma-catalytic system. The use of K, Mg and Ce promoted Ni catalyst supported on alumina led to an enhancement of the conversion of  $\text{CH}_4$ , yield of hydrogen and energy efficiency of the plasma process. This behaviour differs than the one from thermal catalysis for methane conversion and carbon deposition. Potassium showed the best performance with best conversion of methane and carbon dioxide, hydrogen yield, carbon monoxides and smaller carbons yields as well as the energy efficiency of the plasma process. The promoters enhanced the reforming in the following order,  $\text{Mg} < \text{Ce} < \text{K}$ . Whereas all promoters promoted  $\text{CH}_4$  conversion, K and Ce also improved  $\text{CO}_2$  conversion. When the catalyst was placed in the plasma reforming system, the conversion reached its highest with 22.8% for carbon dioxide and 31.6% for methane. Magnesium increased the molar ratio between hydrogen and carbon monoxide in the produced gas (up to 2.2) by a smaller carbon dioxide conversion. (Zeng et al., 2018)

### 2.5.1.2 Carbon dioxide conversion

CO<sub>2</sub> conversion in plasma systems has been reported to produce excited CO\* and O<sub>2</sub>\* species. (Brock et al., 1999; Zheng et al., 2003) Brock et al. described the production of these reactive species in the case of CO<sub>2</sub> decomposition in an AC arc glow discharge reactor, for mixture of 2.5, 10 and 20 % of CO<sub>2</sub> in He. Conversion of CO<sub>2</sub> into CO and O<sub>2</sub> was observed to decrease for increase CO<sub>2</sub> concentration. (Brock et al., 1999) Zheng et al. studied the mutual conversion of CO<sub>2</sub> and CO in dielectric barrier discharge (DBD). The results demonstrated that CO conversion ratio increased with higher voltage, whereas CO<sub>2</sub> conversion did not. Moreover, high voltage and high concentration of reactant led to lower energy efficiency. (Zheng et al., 2003)

Paulussen et al. (2010) investigated the conversion of carbon dioxide to added value chemicals in atmospheric pressure DBD reactor. Varying power input, discharge frequency, feed flow rates and gas temperature were investigated. The most important parameter was demonstrated to be feed flow rate, where a low flow resulted in a higher CO<sub>2</sub> conversion and higher CO yield. Optimum frequency used was observed dependent of power input. Increase in gas temperature and power input resulted in increased conversion levels with a limited effect on CO generation yield. When the power input increase, it increased electric field, electron temperature and discharge temperature; which in turns created more energetic electrons and reactive species, leading to an easier breakdown of molecules. (Paulussen et al., 2010)

Mei et al. (2015) studied plasma-assisted conversion of carbon dioxide in a DBD reactor and the effect of its packing materials through BaTiO<sub>3</sub> and glass beads. The introduction of packing into the DBD plasma changed the physical characteristics of the plasma discharge, switching from a filamentary discharge to a combination of surface discharge and filamentary discharge. Higher energy efficiency and CO<sub>2</sub> conversion were reached when used BaTiO<sub>3</sub> as packing material. It also improved average electric field and mean electron energy of CO<sub>2</sub> discharge, affecting plasma-chemical reactions and leading to an improved CO<sub>2</sub> conversion, CO yield and plasma energy efficiency; even though residence time is reduced through smaller discharge volume with the same feed flow rates. Highly energetic electrons could activate photocatalysis properties of BaTiO<sub>3</sub>, creating electron-hole pairs on the packing surface which took part in enhancing CO<sub>2</sub> conversion. (Mei et al., 2015)

## **2.5.2 Tar reduction using plasma-catalytic systems**

Plasma catalysis has been used to reduce model tar compounds. First, studies have been conducted on single tar compounds only, to be able to draw a mechanism in different conditions. The most common tar model compound studied is toluene. Toluene is a cheap and stable tar compound. Thus, it is considered as a good representative for tars in general and their ability to break down in plasma-catalytic systems. Other compounds could be used such as naphthalene or benzene.

### **2.5.2.1 Toluene tar reduction**

Confirming literature results of plasma-catalysis on model compounds such as toluene (Liu et al., 2017; Wang et al., 2017; Whitehead, 2009), plasma-catalysis technology enabled to reduce more toluene, than plasma or catalysis systems. Oh et al studied toluene decomposition through surface-discharge reactor combined with zeolite catalysts. Zeolite catalyst was put at the entrance of the plasma region, at the plasma tail and downstream of the plasma reactor, in a separate reactor. When the zeolite at the plasma reactor entrance was not properly reducing toluene, toluene decomposition happened at the tail, as well as downstream of the plasma reactor thanks to the presence of ozone and radical oxygen species. With increasing temperature, the decomposition of toluene and CO selectivity increased, the latter due to an improved decomposition of HCOOH, resulting from a better adsorption of formaldehyde on the zeolite catalyst (Oh et al., 2006).

Wang et al. investigated the destruction of toluene in a DBD reactor coupled with CeO<sub>2</sub>-MnO<sub>x</sub> catalysts. The influence of molar ratio Ce/Mn, gas flow rate, toluene initial concentration and power input on the removal efficiency and CO selectivity were studied. As power increased, removal efficiency of toluene and carbon dioxide were improved in the plasma-catalytic system using CeO<sub>2</sub>-MnO<sub>x</sub> catalyst, compared to plasma systems. The pathway of toluene removal was discussed. Wang et al identified some degradation products, a range of aliphatic and aromatic hydrocarbons including methyl- and dimethyl-benzenes, benzaldehyde and methyl-butanol. (Wang et al., 2017)

Toluene decomposition in a wire-plate DBD reactor with manganese oxide/alumina/nickel foam catalyst have been studied by Guo et al. The influence of

gas flow rate and oxygen content were investigated. Combining the DBD with the foam catalyst resulted in improving the removal efficiency of toluene, CO<sub>2</sub> selectivity and limit by-product formation. Characterisation of the reacted catalyst showed that DBD improved dispersion of active species, increased activity and stability of catalyst, as well as reinforced oxidation capability of the foam catalyst. (Guo et al., 2006)

### **2.5.2.2 Steam reforming of toluene**

As presented in previous sections, plasma and plasma-catalysis systems produce reactive species most likely responsible for the reduction in tar yield, such as high energy electrons or free radicals - OH<sup>•</sup>, O<sup>•</sup> and N<sup>•</sup> and excited N<sub>2</sub><sup>\*</sup> species – reacting with biomass vapours. (Liu et al., 2017) This has been shown by Liu et.al (Liu et al., 2017), who studied the conversion of toluene in an arc discharge plasma with nitrogen as a gas carrier. The introduction of steam within the plasma system resulted to a higher toluene conversion and energy efficiency: steam inside the discharge produced OH radicals leading to new pathways to convert toluene through a stepwise oxidation of toluene and intermediates.

Other studies demonstrated the importance of hydroxyl radical in steam reforming of toluene using plasma-catalytic systems. While using plasma systems only, Nunnally et al. demonstrated the important role of hydroxyl radicals in steam reforming. OH radicals were produced either with water interaction with electrically excited O<sub>2</sub><sup>\*</sup> and N<sub>2</sub><sup>\*</sup> or electron interaction with water. Generated radicals readily react with tar compounds resulting in their reduction. At higher steam input, tar content increased, showing a lower tar reduction efficiency. (Nunnally et al., 2014) This was also demonstrated in plasma-catalysis systems as showed by Van Durme et al. on toluene removal by a plasma-catalytic system in humid air. An excess of water led to the formation of mono or multi-layers on catalyst surface, preventing access to active sites of the catalyst. (Van Durme et al., 2007)

Liu et al used a DBD reactor to study the steam reforming of toluene in plasma-catalytic systems, using Ni-based and Fe-based catalysts on alumina with different molar ratio between metals and alumina. The Ni-based catalyst with a molar ratio M:Al of 1:3 showed the highest potential to convert biomass tars into hydrogen-rich syngas, with a toluene conversion of 96% and a hydrogen yield of 2.18 mol per mol

of toluene. (Liu et al., 2017) Liu et al expanded their study with a similar experiment on a DBD reactor with Ni-based and Fe-based catalysts, but with different supports. The main products from toluene decomposition were benzene and ethylbenzene, alongside lower concentrations of xylene, styrene, cumene, propylbenzene, 1,2-diphenylethane and 2-methyl-3-phenylbutane. Liu et al reported that Ni catalysts were converting toluene to gas product more efficiently and that higher surface area of catalyst support resulted in an increase of toluene decomposition. It was also showed, when studying the place of the catalyst in the system, that toluene decomposition was more efficient in the plasma zone. The highest conversion of toluene was obtained for Ni/ZSM-5 catalyst, 86.5%, whereas the conversion without catalyst in the system was around 64%. (Liu et al., 2017)

Liu et al. used a DBD system and nickel supported on alumina catalyst to study steam reforming of toluene as a tar model compound for biomass gasification. Different Ni loading, from 5-20 wt.%, were analysed. and compared to plasma reaction without catalyst. In this experiment, plasma-catalysis enhanced the conversion of toluene, the yield of hydrogen and the energy efficiency of the process. The plasma-catalytic process was further improved by increasing the Ni loading. With a 20 wt.% Ni-alumina catalyst, the conversion of toluene and the hydrogen yield were at their highest, 52% and 32% respectively. The presence of Ni-alumina catalyst in the process reduced significantly the formation of organic by-products. Moreover, its presence shifted the toluene destruction pathway: instead of dehydrogenation or oxygenation of a methyl group, the primary reaction pathway became a direct cleavage of toluene ring. A wide range of hydrocarbons were detected, including xylenes, styrene, propylbenzene, ethylbenzene, benzenes and oxygenated hydrocarbons. This was demonstrated by the increased yield of hydrogen and  $C_2H_2$ . However, this mechanism was conducted within an argon environment as Ar is used as a gas carrier. The mechanism could change in a different atmosphere, as it will create different reactive species inside the plasma. (Liu et al., 2017)

### **2.5.2.3 Reduction of other single model tar compounds**

Apart from toluene, removal of single tar compounds has been intensively studied for alcohols, such as formaldehyde, or aromatic compounds, such as benzene, styrene or

naphthalene. These examples are presented in this section for low-temperature plasma-catalysis systems.

Activation of Cu/ZrO<sub>2</sub> catalysts for dehydrogenation of alcohols by low-temperature oxygen and hydrogen plasma has been studied by Pylinina et al, using 2-butanol as a model compound. The presence of Cu resulted in an increase in catalytic activity of alcohol dehydrogenation when placed in a plasma, hydrogen or oxygen plasma. (Pylinina and Mikhaleenko, 2013) Formaldehyde removal in a plasma-catalytic system has also been investigated by Zhu et al using a DBD reactor and Cu-Ce catalysts. The highest removal efficiency and CO<sub>2</sub> selectivity were obtained for Cu-Ce binary oxide catalysts with 94.7% and 97.3% respectively. The plasma-catalysis enhanced the reaction performance when a Cu-Ce binary oxide catalyst was used and was shown to have a negative effect on the formaldehyde removal when CuO or CeO were used. The binary oxide catalyst resulted in a larger surface area, larger pore volume, and greater formation of adsorbed oxygen on the catalyst surface, favouring formaldehyde oxidation in plasma-catalysis systems. It also facilitated the formation of more active oxygen atoms, contributing to oxidation reactions in plasma-catalysis system. (Zhu et al., 2015)

Kim et al. studied the decomposition of benzene in a plasma-driven catalyst reactor using Ag/TiO<sub>2</sub> and the influence of electrode configuration and Ag loading amount on benzene decomposition. Modifying the ground electrode to reduce void between dielectrics and the ground electrode improved the energy efficiency of the plasma by reducing the irregular corona discharges. Using silver paste instead of aluminium tape or copper mesh electrodes resulted in the highest energy efficiency. The larger the Ag-loading on TiO<sub>2</sub> catalyst, the better the benzene decomposition, leading to improved carbon balance and CO<sub>2</sub> selectivity. (Kim et al., 2004)

The destruction of styrene in air stream by packed DBD reactors was studied by Chang et al., comparing packed and non-packed DBD reactors and using glass, Al<sub>2</sub>O<sub>3</sub> or Pt-Pd supported on Al<sub>2</sub>O<sub>3</sub> catalysts. CO<sub>2</sub> was the major product of styrene removal with higher concentration for packed bed reactors compared to non-packed reactors. Increasing the styrene input quantity resulted in a decreasing removal efficiency and increase in solid by-product, containing carbon. With packed-beds, efficiency of styrene removal was improved, a higher CO<sub>2</sub> selectivity and a lower ozone

concentration were obtained with Pt-Pd supported on Al<sub>2</sub>O<sub>3</sub> catalysts. Increasing the bed length led to a decrease of carbon by-products. (Chang et al., 2005)

Wu et al. investigated the oxidation of naphthalene in a DBD plasma-catalytic system over TiO<sub>2</sub>/diatomite catalyst. Combining TiO<sub>2</sub>/diatomite catalyst with plasma resulted to higher naphthalene conversion and CO<sub>2</sub> selectivity compared to plasma-only processes, up to 40% and 92% respectively. It also reduced aerosol formation and secondary volatile compounds, up to 90 and 100% respectively. Plasma-catalysis was suggested to intensify electron energy, from which energised electrons activated TiO<sub>2</sub> catalysts. Interaction between the plasma and the catalyst resulted in synergetic effect, improving naphthalene oxidation. (Wu et al., 2018)

#### **2.5.2.4 Mixture of tar compounds**

To the best of the author's knowledge, very few publications were accessible for the removal of complex mixture of tar model compounds in plasma-catalytic systems. Moreover, few scientific publications investigated the removal of mixture of tar model compounds in plasma systems. This section presents the steam reforming of mixture of toluene and naphthalene in gliding arc discharge reactors. In a first example, Nunnally et al. simulated a syngas containing toluene and naphthalene as vapours, going through a gliding arc plasma to be reformed. At low tar concentration, 30 g/m<sup>3</sup>, over 90% of conversion of naphthalene and toluene was reached; whereas for a higher tar concentration, 75 g/m<sup>3</sup>, 70% of conversion was obtained. Higher energy efficiencies for both tar model compounds at higher tar concentration were the result of effective gas mixing and plasma chemistry, including fast reaction kinetics from active species, radicals and ions. (Nunnally et al., 2014) Recently, Zhang et al. investigated steam reforming of naphthalene and toluene as model tar compounds in a gliding arc reactor, more specifically the effect of carbon dioxide and steam on the performance of the reaction. Increasing the quantity of steam improved the conversion of toluene and naphthalene, increasing the amount of hydroxyl radicals generated by water dissociation which reacted with tar model compounds and their intermediary products. Introducing carbon dioxide to the system resulted in a decrease of conversion and energy efficiency. Finally, the process showed traces of monocyclic and bicyclic aromatic by-products, alongside H<sub>2</sub>, C<sub>2</sub>H<sub>2</sub> and CO as major compounds. The model tar compounds removal could be originating from collisions of tar model

compounds with energetic electrons, nitrogen excited species or oxygen and hydroxyl radicals. (Zhang et al., 2019) Besides, as Zhang et al. underlined, due to complexity of tar compounds, the use of non-thermal plasma on a practical gasifier for tar removal will have a lower removal efficiency than the processes used for individual tar model compound in laboratory research.

## **Chapter 3: Materials and Methods**

In this chapter, the studied biomass materials and experimental procedure used to prepare the catalysts used in this study are described. The techniques used to analyse the products obtained from the experiments and to characterise the materials in use are presented. The procedures used to investigate the performance of different plasma-catalytic systems for tar reduction and syngas production are also discussed. A fixed bed reactor was used to analyse the pyrolysis products from different biomasses. A two-stage fixed bed reactor, with different second stage plasma-catalytic reactors, was used to investigate tar reduction and syngas production for non-thermal plasma catalytic systems.

This chapter is divided in two parts: first the materials, then the methods. The ‘Materials’ section describes the raw materials and the different researched catalysts. The ‘Methods’ section describes the experimental setup and procedures, as well as the different analytical techniques used to characterise the initial materials or products. Additionally, the reproducibility of the analytical methods and the experimental techniques are presented.

### **3.1 Materials**

In this section, the characteristics of the biomass samples used in this study, as well as the catalyst preparation and catalyst characteristics are described.

#### **3.1.1 Biomass samples**

Different biomass compounds were used as feedstock for these experiments. First, to analyse the different tar compounds present in biomass pyrolysis vapours, four different biomasses – wood pellet, corn stalk, peanut shell and coconut shell – were used. Then, the wood pellet sample was used as the main feedstock to investigate tar reduction and syngas production for two types of non-thermal plasma catalytic systems. In order to further understand the mechanisms in place in the plasma-catalytic system, model compounds, such as toluene, cellulose, hemi-cellulose and lignin, were used. All these materials are described in this section.

### 3.1.1.1 Different biomasses used as feedstocks

Four different biomasses – wood pellet, corn stalk, peanut shell and coconut shell – were studied. The waste biomass used as the feedstock for pyrolysis was in the form of waste wood sawdust which was compressed into wood pellets and was obtained from Liverpool Wood Pellets Ltd, Liverpool, UK. Corn stalk and peanut shell were obtained from Nigeria whereas Coconut shell was from Ghana. The biomasses were separately shredded and sieved to produce biomasses with a particle size in the range of 1 – 2.8 mm.

**Table 3.1-1: Feedstock analysis of different biomasses**

<b>Biomass type</b>	<b>Wood pellet</b>	<b>Corn stalk</b>	<b>Peanut shell</b>	<b>Coconut shell</b>
Thermogravimetric Analysis (TGA)				
Dehydration end (°C)	93	112	106	105
Pyrolysis start(°C)	350	320	298	323
Pyrolysis end (°C)	618	612	618	622
Proximate analysis				
Moisture (%)	7.3	8.0	8.9	10.0
Volatile (%)	75.5	67.7	64.1	67.3
Fixed carbon (%)	15.2	16.7	21.6	21.2
Ash (%)	2.0	7.6	5.5	1.5

Sample characterisation was obtained through proximate and ultimate analysis, methods presented in section 3.3.1. The results for the different feedstocks are represented in Table 3.1-1. These results are close to those reported in the literature (ECN Phyllis Classification, 2012) for proximate analysis and close to experimental start and end of pyrolysis through TGA results.

The results, presented in Table 3.1-2, are very close to the reported literature values. (ECN Phyllis Classification, 2012) Wood pellet had the highest carbon content. Corn stalk was the feedstock with the highest oxygen content and the highest ash content.

Coconut shell had the highest moisture content, carbon content, hydrogen content and the highest heating value.

**Table 3.1-2: Ultimate analysis (as received) of different biomasses**

<b>Ultimate analysis (wt. %)</b>	<b>Wood pellet</b>	<b>Corn stalk</b>	<b>Peanut shell</b>	<b>Coconut shell</b>
<b>Moisture</b>	7.3	8.0	8.9	10.0
<b>Carbon</b>	46.1	34.7	40.5	47.6
<b>Hydrogen</b>	5.7	4.4	5.1	6.0
<b>Nitrogen</b>	0.1	1.1	1.2	0.6
<b>Sulphur</b>	0	0	0	0
<b>Ash</b>	2.0	7.6	5.5	1.5
<b>Oxygen</b>	38.8	44.3	38.9	34.2
<b>Total</b>	100	100	100	100
<b>Heating value MJ/kg (Friedl et al., 2005)</b>	18.4   19.8 (dry)	14.2   15.5 (dry)	16.0   17.6 (dry)	19.3   21.5 (dry)

### **3.1.1.2 Components of biomass: cellulose, hemi-cellulose and lignin**

In order to further understand the mechanisms in place in the plasma-catalytic system, model compounds representative of the main biopolymer components of biomass, i.e. cellulose, hemi-cellulose and lignin, were used. These compounds were obtained from Sigma-Aldrich UK, (now Merck), for cellulose and lignin. Hemi-cellulose was obtained from Macklin Ltd. UK in the form of Xylan from corncob. These compounds were used in powder form.

Sample characterisation was obtained through proximate and ultimate analysis, the analytical methods are presented in section 3.3.1. The results for the different model biopolymer compounds are represented in Table 3.1-3. These results are close to literature (ECN Phyllis Classification, 2012) for proximate analysis. The results of ultimate analysis, presented in Table 3.1-4, are very close to the literature values.

(ECN Phyllis Classification, 2012) These analyses showed the main differences between the compounds: Lignin is a heavy carbonated compound with a high carbon content and relatively low oxygen content. Cellulose had the highest volatile content and hemi-cellulose had the highest carbon, hydrogen and oxygen content, linked to its lowest moisture content.

**Table 3.1-3: Feedstock analysis of the components of biomass (wood pellet)**

<b>Biomass type</b>	<b>Biomass</b>	<b>Cellulose</b>	<b>Hemi-cellulose</b>	<b>Lignin</b>
Thermogravimetric Analysis (TGA)				
Dehydration end (°C)	93	103	115	90
Pyrolysis start(°C)	350	290	200	180
Pyrolysis end (°C)	618	605	622	722
Proximate analysis				
Moisture (%)	7.3	6.4	4.0	4.3
Volatile (%)	75.5	82.4	80.1	56.2
Fixed carbon (%)	15.2	10.0	15.1	35.7
Ash (%)	2.0	1.2	0.8	3.8

### **3.1.1.3 Toluene**

In order to validate the plasma-catalytic system used in this study with the results from the literature, a widely used model compound, toluene, was used. (Whitehead, 2010) Toluene was supplied in liquid form by SLS (Scientific Laboratory Supplies) from Honeywell Riedel-De-Haen in a 2.5 L bottle.

### **3.1.2 Researched catalysts**

Different catalysts were used in these experiments. First, working on a two-stage fixed bed reactor using a Dielectric Barrier Discharge (DBD) plasma-catalytic reactor, presented in section 3.2.2, nickel supported on alumina catalysts were studied for different particle sizes. Metal promoters were then added to the nickel supported alumina catalyst. In addition, nickel supported catalyst supported on titanium oxide

and Y-zeolite catalyst as an alternative support, was investigated in order to study the effect of the catalyst properties on the plasma-catalytic system. Finally, barium titanate and alumina were used as packing in a two-stage fixed bed reactor using a packed-bed Dielectric Barrier Discharge (DBD) plasma-catalytic reactor, presented in section 3.2.3. These catalysts are all described in this section.

**Table 3.1-4: Ultimate analysis (as received) of the components of biomass (wood pellet)**

<b>Ultimate analysis (wt. %)</b>	<b>Biomass</b>	<b>Cellulose</b>	<b>Hemi-cellulose</b>	<b>Lignin</b>
<b>Moisture</b>	7.3	6.4	4.0	4.3
<b>Carbon</b>	46.1	41.8	42.6	60.5
<b>Hydrogen</b>	5.7	6.6	7.5	6.1
<b>Nitrogen</b>	0.1	0.1	0.1	1.0
<b>Sulphur</b>	0	0	0	0.5
<b>Ash</b>	2.0	1.2	0.8	3.8
<b>Oxygen</b>	38.8	43.9	45.0	23.9
<b>Total</b>	100	100	100	100
<b>Heating value MJ/kg (Friedl et al., 2005)</b>	18.4   19.8 (dry)	16.6   17.7 (dry)	16.9   17.6 (dry)	25.4   26.5 (dry)

### 3.1.2.1 Ni/Alumina with different particle diameter sizes

The alumina catalyst used, was in the form of beads, with a particle size of 1 mm diameter. Ni-based catalysts are widely used in industry to catalyse steam and dry reforming. Steam reforming of hydrocarbons and methane for an increase of hydrogen and carbon monoxide content can be achieved by using Ni-catalysts at high temperature, above 740°C. (Yang et al., 2015)

Different sizes of alumina support were used. From the original support size of 1 mm diameter bead obtained from Nankai University, China, alumina beads were blended and sieved to achieve size ranges between a 1 mm sieve, a 500 µm sieve and a 212 µm sieve. The supports were separated into 4 categories. 1 mm diameter support, 1-0.5 mm diameter support and 500- 212 µm diameter support were labelled and used for nickel impregnation. The particles smaller than 212 µm were kept for future work and not used in this study.

Nickel supported on alumina was prepared by impregnation method. With 10% weight of Ni,  $\text{Ni}(\text{NO}_3)_2 \cdot 6\text{H}_2\text{O}$  were dissolved in deionised water. Alumina support was added to the mixture and heated up. The temperature is then increased by 15 °C increments up to 95 °C until the mixture became viscous. It is then left to dry overnight at 110 °C. Calcination at 750 °C was carried out the following day with a heating ramp of 2 °C.min<sup>-1</sup>. The catalyst is then reduced using a 5% hydrogen mixture in nitrogen. With a gas flow of 200 mL.min<sup>-1</sup>, temperature reached 800 °C, at a heating ramp of 20 °C.min<sup>-1</sup>, and hold for an hour. The results for the characterisation of catalysts used in this section are presented in Table 3.1-5, using the method described in section 3.3.2.

**Table 3.1-5: Alumina catalyst characteristics for different diameter sizes**

<b>Diameter size</b>	<b>1 mm</b>	<b>1-0.5 mm</b>	<b>500-212 µm</b>
<b>Isotherm type (Sing, 1985; Donohue and Aranovich, 1998)</b>	Type IV (IUPAC 1985 Classification), hysteresis type H2: highly mesoporous	Type IV (IUPAC 1985 Classification), hysteresis type H2: highly mesoporous	Type IV (IUPAC 1985 Classification), hysteresis type H2: highly mesoporous
<b>BET surface area (Rouquerol et al., 1994)</b>	154.96 m <sup>2</sup> /g	143.83 m <sup>2</sup> /g	152.79 m <sup>2</sup> /g
<b>BJH pore volume data (adsorption) (Barrett et al., 1951)</b>	0.394 cc/g	0.386 cc/g	0.376 cc/g
<b>BJH pore volume data (desorption) (Barrett et al., 1951)</b>	0.415 cc/g	0.406 cc/g	0.398 cc/g
<b>BJH pore size (adsorption) (Barrett et al., 1951)</b>	3.234 nm	4.699 nm	3.848 nm
<b>BJH pore size (desorption) (Barrett et al., 1951)</b>	3.963 nm	3.952 nm	3.310 nm

An example of the isotherms obtained for the different catalyst sizes is presented in Figure 3.1-1. All catalysts were very similar, as expected, with a surface area around

150 m<sup>2</sup>/g and a pore size about 3.5-4 nm. This also confirmed the isotherm type IV, characteristic of mesoporous catalysts where pore size is between 1.5 and 100 nm.

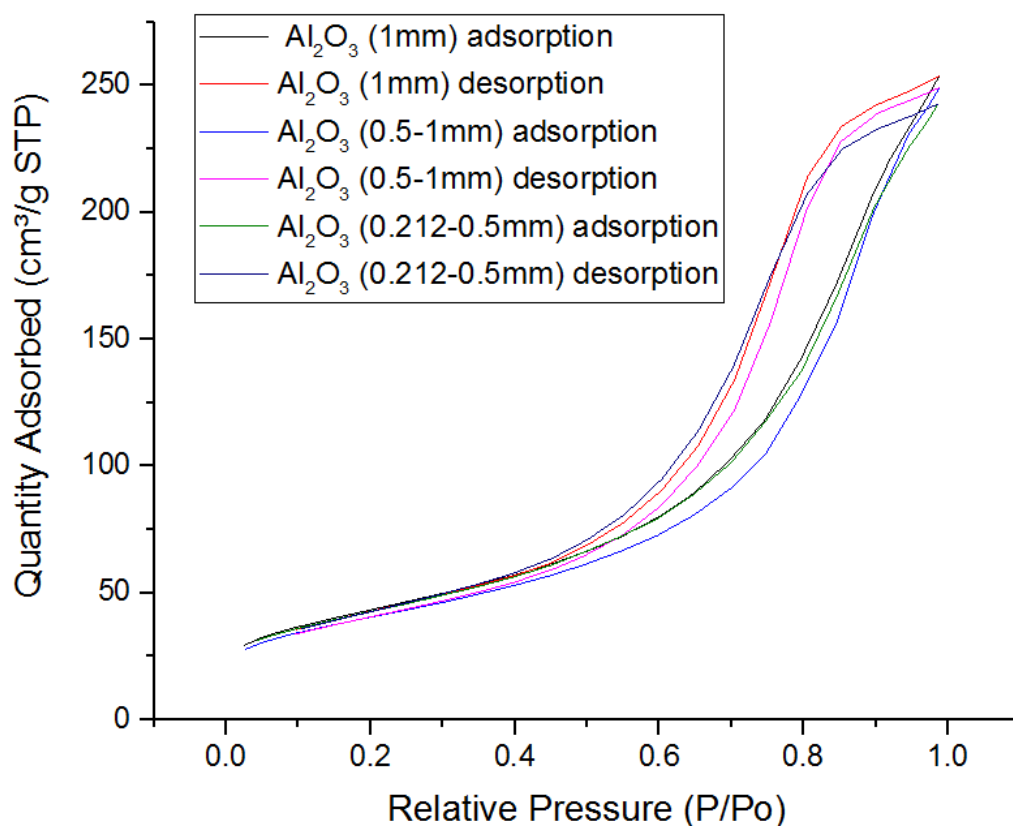


**Figure 3.1-1: Ni/Alumina catalyst BET isotherm for different particle diameter size**

### 3.1.2.2 Ni/Alumina with promoters

To study the effect of different metal promoters on plasma-catalysis, different metals were studied: Iron and copper have been intensively used for catalysing water gas shift reactions and thus could lead to higher hydrogen production (Rhodes et al., 1995); Cerium and magnesium have been shown to enhance the stability of catalyst performance in thermal catalytic processes (Özkara-Aydinoğlu et al., 2010; Alipour et al., 2014; Sengupta et al., 2015); Cobalt has demonstrated improved activity and stability of the catalyst when added on Ni-catalysts (Xu et al., 2009; Sengupta et al., 2015); and nickel, a traditional metal used in steam reforming processes for its good catalytic effect on hydrogen production and its comparatively low cost (Wu et al., 2010).

Nickel supported on alumina was prepared by impregnation method. With 5% weight of Ni and 5 wt.% of promoter,  $\text{Ni}(\text{NO}_3)_2 \cdot 6\text{H}_2\text{O}$  and the associated promoter ammonium salt ( $\text{Ce}(\text{NO}_3)_2 \cdot 6\text{H}_2\text{O}$ ,  $\text{Cu}(\text{NO}_3)_2 \cdot 3\text{H}_2\text{O}$ ,  $\text{Fe}(\text{NO}_3)_3 \cdot 9\text{H}_2\text{O}$  and  $\text{Ni}(\text{NO}_3)_2 \cdot 6\text{H}_2\text{O}$ ) were dissolved in deionised water. Alumina support was added to the mixture and heated up. The temperature is then increased by 15 °C increments up to 95 °C until the mixture became viscous. It is then left to dry overnight at 110 °C. Calcination at 750 °C was carried out the following day with a heating ramp of 2 °C.min<sup>-1</sup>. The catalyst is then reduced using a 5% hydrogen mixture in nitrogen. With a gas flow of 200 mL.min<sup>-1</sup>, temperature reached 800 °C, at a heating ramp of 20 °C.min<sup>-1</sup>, and hold for an hour.

### 3.1.2.3 Nickel on different catalytic supports

To study the effect of catalyst supports on plasma-catalysis, three different supports were studied: Alumina, a traditional support for thermal processes (Yang et al., 2015); titanium oxide, a catalyst activated by UV stimulation used in many plasma-catalysis studies (Tauster et al., 1978; Bartholomew et al., 1980); and Y-zeolite, a catalyst mainly used in oil refineries to crack tar and for gasoline production (Choi et al., 2006; Möller et al., 2013). Alumina and Y-zeolite were obtained from Nankai University, China and titanium oxide was obtained from Fischer Scientific Ltd., UK.

Nickel supported on alumina, Y-zeolite and titanium oxide were prepared by impregnation method, as they were in the previous sections. With 5% weight of Ni,  $\text{Ni}(\text{NO}_3)_2 \cdot 6\text{H}_2\text{O}$  were dissolved in deionised water. Alumina support was added to the mixture and heated up. The temperature is then increased by 15 °C increments up to 95 °C until the mixture became viscous. It is then left to dry overnight at 110 °C. Calcination at 750 °C was carried out the following day with a heating ramp of 2 °C.min<sup>-1</sup>. The catalyst is then reduced using a 5% hydrogen mixture in nitrogen. With a gas flow of 200 mL/min, temperature reached 800 °C, at a heating ramp of 20 °C.min<sup>-1</sup>, and hold for an hour.

The different catalyst supports were analysed by BET to obtain surface and pore size characteristics. Their properties are reported in Table 3.1-5 and the BET isotherm for each support is presented in Figure 3.1-2. Titanium oxide, Y-zeolite and alumina all had a similar isotherm type. The BET surface was around 150 m<sup>2</sup>.g<sup>-1</sup> for both alumina and titanium oxide, whereas Y-zeolite had a surface area of 423 m<sup>2</sup>.g<sup>-1</sup>. Y-zeolite had

the biggest pore size (13.4 nm), followed by titanium oxide (9.7 nm) and alumina had the smallest pore size (3.2 nm). The properties of Y-zeolite has made the catalyst commonly used in industry for oil cracking and refining because of its large surface area and structured pore size makes it a perfect candidate for heavy tar breakdown.(Choi et al., 2006; Möller et al., 2013) Finally, TiO<sub>2</sub> had the highest dielectric constant, followed by alumina and Y-zeolite, which is expected as titanium oxide is mainly used as a photocatalyst in industry and plasma chemistry (Tauster et al., 1978; Bartholomew et al., 1980).

**Table 3.1-5: Characteristics of different catalyst supports**

<b>Diameter size</b>	<b>TiO<sub>2</sub></b>	<b>Y-zeolite</b>	<b>Alumina</b>
<b>Isotherm type (Sing, 1985; Donohue and Aranovich, 1998)</b>	Type IV (IUPAC 1985 Classification), hysteresis type H2: highly mesoporous	Type IV (IUPAC 1985 Classification), hysteresis type H3: mesopores& micropores	Type IV (IUPAC 1985 Classification), hysteresis type H2: highly mesoporous
<b>BET surface area (Rouquerol et al., 1994)</b>	150.9 m <sup>2</sup> /g	423.3 m <sup>2</sup> /g	154.96 m <sup>2</sup> /g
<b>BJH pore volume data (adsorption) (Barrett et al., 1951)</b>	0.454 cc/g	0.252 cc/g	0.394 cc/g
<b>BJH pore volume data (desorption) (Barrett et al., 1951)</b>	0.453 cc/g	0.249 cc/g	0.415 cc/g
<b>BJH pore size (adsorption) (Barrett et al., 1951)</b>	9.688 nm	13.405 nm	3.234 nm
<b>BJH pore size (desorption) (Barrett et al., 1951)</b>	9.293 nm	13.917 nm	3.963 nm
<b>Dielectric constant</b>	10 – 85 (AZOMaterials, n.d.)	1.5 – 5 (Kuronen et al., 2000; Li et al., 2006)	7.8 – 11.1 (AZOMaterials, n.d.)

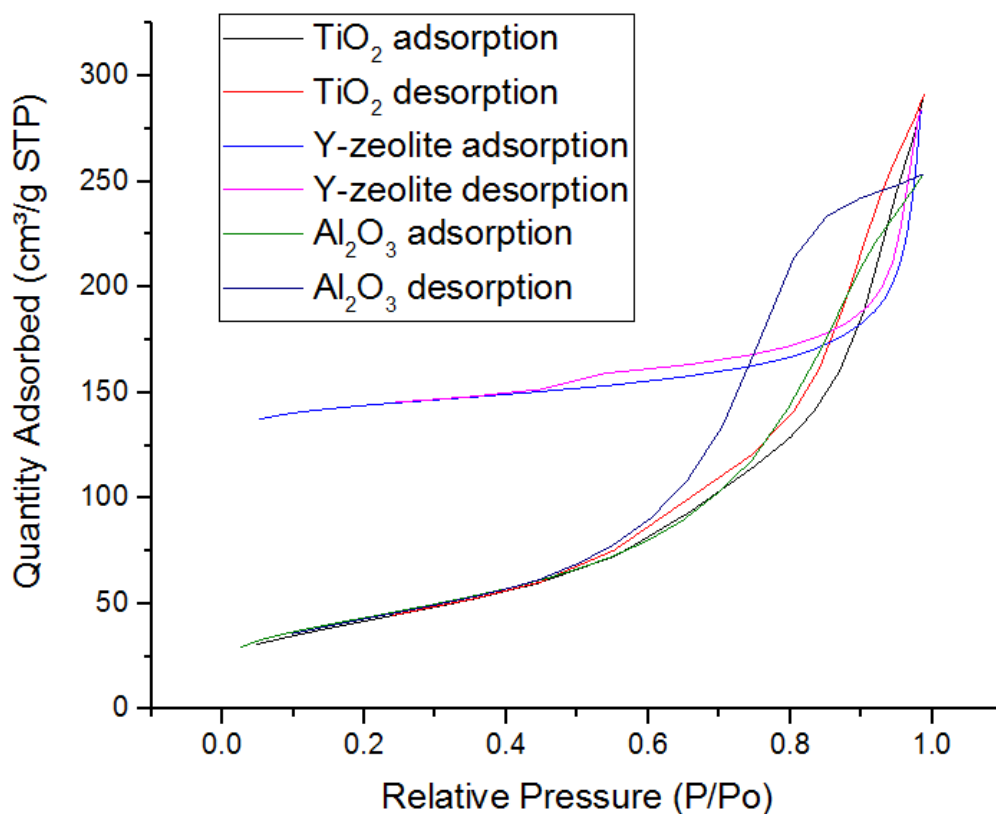


**Figure 3.1-2: BET isotherm for different supports – titanium oxide, Y-zeolite and alumina**

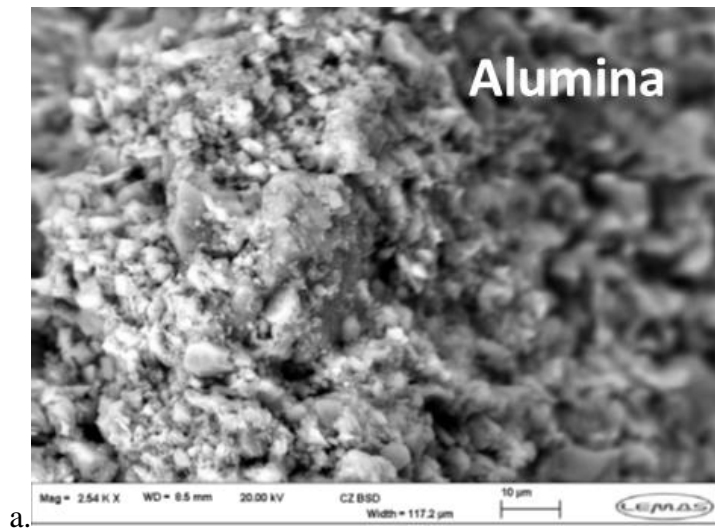
The SEM images of these supports are represented in Figure 3.1-3. These images showed the differences between the structures of the three catalysts supports studied. They further confirmed the results from BET isotherms determining the mesoporous or meso and microporous surface of the catalyst supports. The structure of Y-zeolite was less homogeneous than the structure of  $\text{TiO}_2$  which is to be expected considering the complexity of Y-zeolite compared to  $\text{TiO}_2$ . The shown roughness of alumina can be explained by the fact that alumina was manually grounded before being studied. The XRD of the different supports, alongside the nickel supported catalysts before and after reduction, are shown in Figure 3.1-4. Figure 3.1-4(a) represented the three catalyst supports whereas Figure 3.1-4(b) represented the effect of reduction, seen in an additional peak at  $50^\circ$  – representing the presence of Nickel on the catalyst with most intense peaks of Ni:  $2\theta$  at  $44.5^\circ$ ,  $51.8^\circ$  and  $76.4^\circ$  (JCPDS 65-2865) – for Alumina and Y-zeolite catalyst. Each peak represents either a specific element or a specific phase of a given compound. As expected, Y-zeolite structure is very complex as such support is a silicate mineral mainly containing Al, Si, O, Na, Ca and Mg. It is however

very similar to what can be found in the literature as showed by Wang et al. (Wang et al., 2016)  $\alpha$ -Alumina is shown on Figure 3.1-4 with its main peaks: 25.6, 35.1, 43.2, 52, 58, 62, 66 and 68° (Li et al., 2017). The reduction of titanium oxide leads to a different reduction graph, indicating a possible change of configuration for titanium oxide, going from the anatase phase (main peaks at 25, 38, 49, 54,55, 68 and 70°) to the rutile phase (main peaks at 27, 36, 42 and 63°) after reduction, as shown by the disappearance of a peak at around 38°, characteristic to the anatase phase, and the appearance of a large peak around 54° and 37°, characteristic of the rutile phase. (White et al., 2013; Ijadpanah-Saravy et al., 2014)

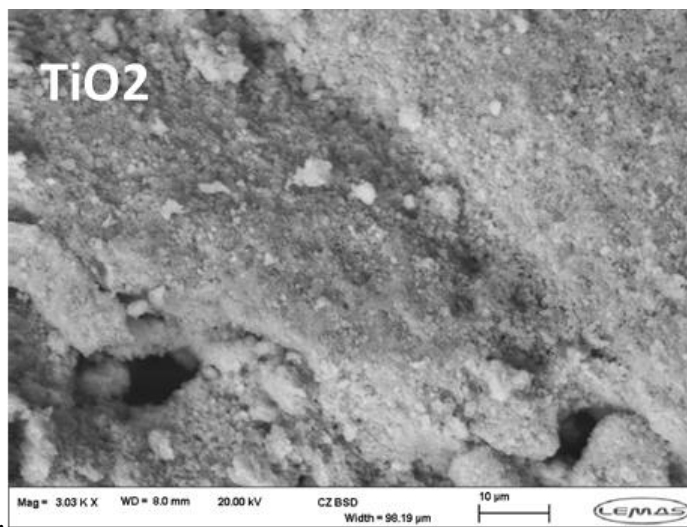
#### **3.1.2.4 Barium Titanate for packed-bed Dielectric Barrier Discharge plasma-catalytic reactor**

Barium titanate was used as packing material in the packed-bed Dielectric Barrier Discharge (DBD) plasma-catalytic reactor. Barium titanate is the packing that is the most commonly used for packed-bed dielectric barrier discharges (DBD) as described in the literature review. (Mei et al., 2015). It was also the packing which allowed a better study of the packed-bed Dielectric Barrier Discharge (DBD) plasma-catalytic reactor, enabling the study of different parameters in similar operating conditions than for the Dielectric Barrier Discharge (DBD) plasma-catalytic reactor. Barium titanate was obtained from CATAL UK in the form of bead of a 2 mm diameter size.

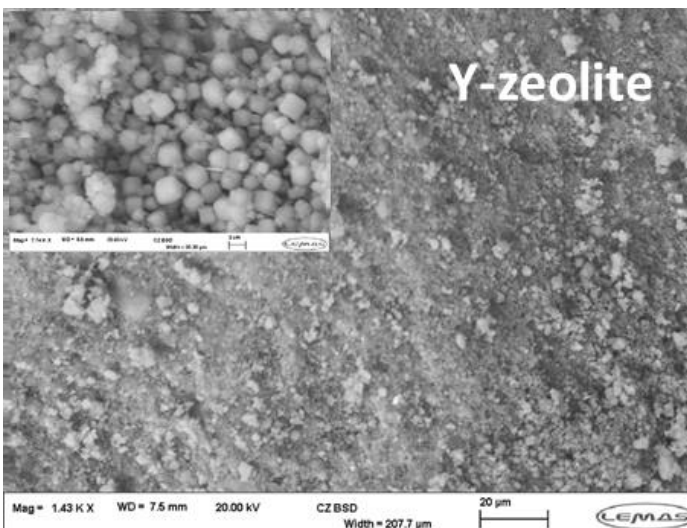
Barium titanate packing was characterised using the analytic methods described in section 3.3.2. The results are reported in Table 3.1-6 and the BET isotherm is represented in Figure 3.1-5. Table 3.1-6 indicated that BaTiO<sub>3</sub> was a microporous support with a very small surface area. This was further supported by the BET isotherm showing a very irregular isotherm, without much absorption nor desorption onto the support. XRD and SEM were used to identify the topography of Barium titanate and are represented in Figure 3.1-6 SEM pictures support the analysis conducted from Table 3.1-6 whereas the XRD plot on Figure 3.1-6 highlighted the XRD structure for further studies in Chapter 7.



a.

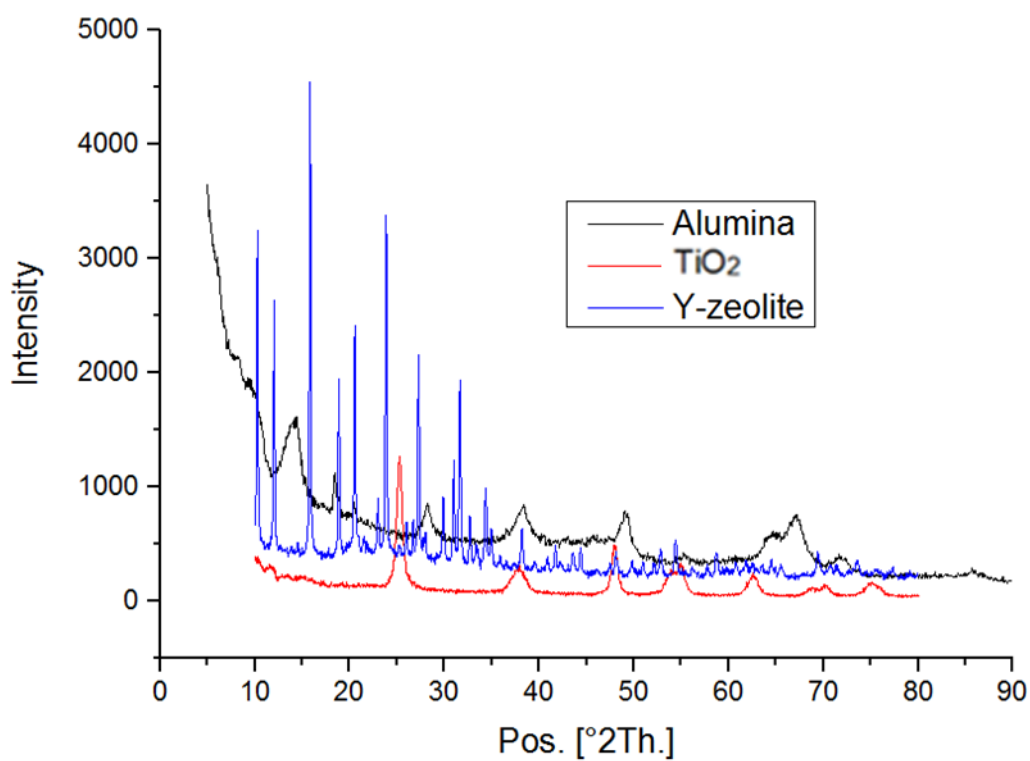


b.

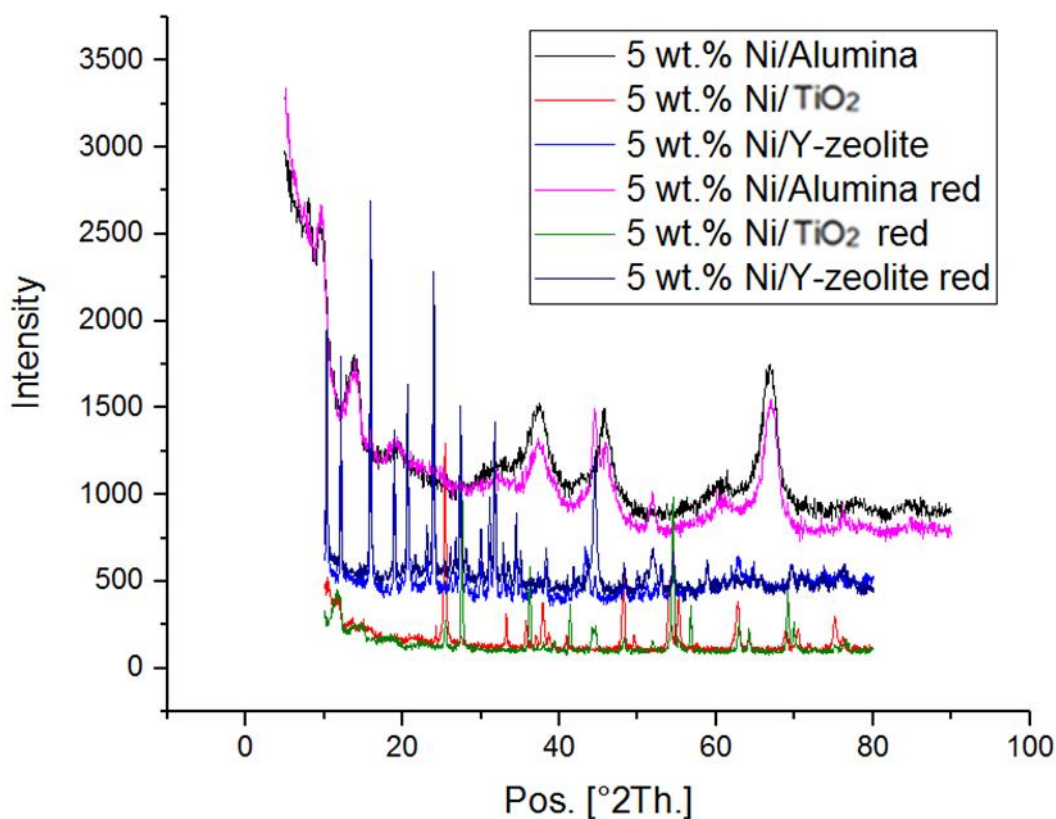


c.

**Figure 3.1-3: SEM images of Nickel supported on a. Alumina, b. TiO<sub>2</sub> and c. Y-zeolite**



a.



b.

**Figure 3.1-4: XRD graph of a. different fresh catalyst supports – alumina, titanium oxide and y-zeolite – and b. Nickel supported catalyst on different supports for reduced and non-reduced catalysts**

**Table 3.1-6: Characteristics of different packings for DBD plasma-catalytic reactor**

	<b>BaTiO<sub>3</sub></b>
<b>Bead size (mm)</b>	~2
<b>Isotherm type (Sing, 1985; Donohue and Aranovich, 1998)</b>	Type I (IUPAC 1985 Classification), hysteresis type H4: microporous
<b>BET surface area (Rouquerol et al., 1994)</b>	0.496 m <sup>2</sup> /g
<b>BJH pore volume data (adsorption) (Barrett et al., 1951)</b>	0.387.10 <sup>-3</sup> cc/g
<b>BJH pore volume data (desorption) (Barrett et al., 1951)</b>	N.A.
<b>BJH pore size (adsorption) (Barrett et al., 1951)</b>	11.636 nm
<b>BJH pore size (desorption) (Barrett et al., 1951)</b>	N.A.

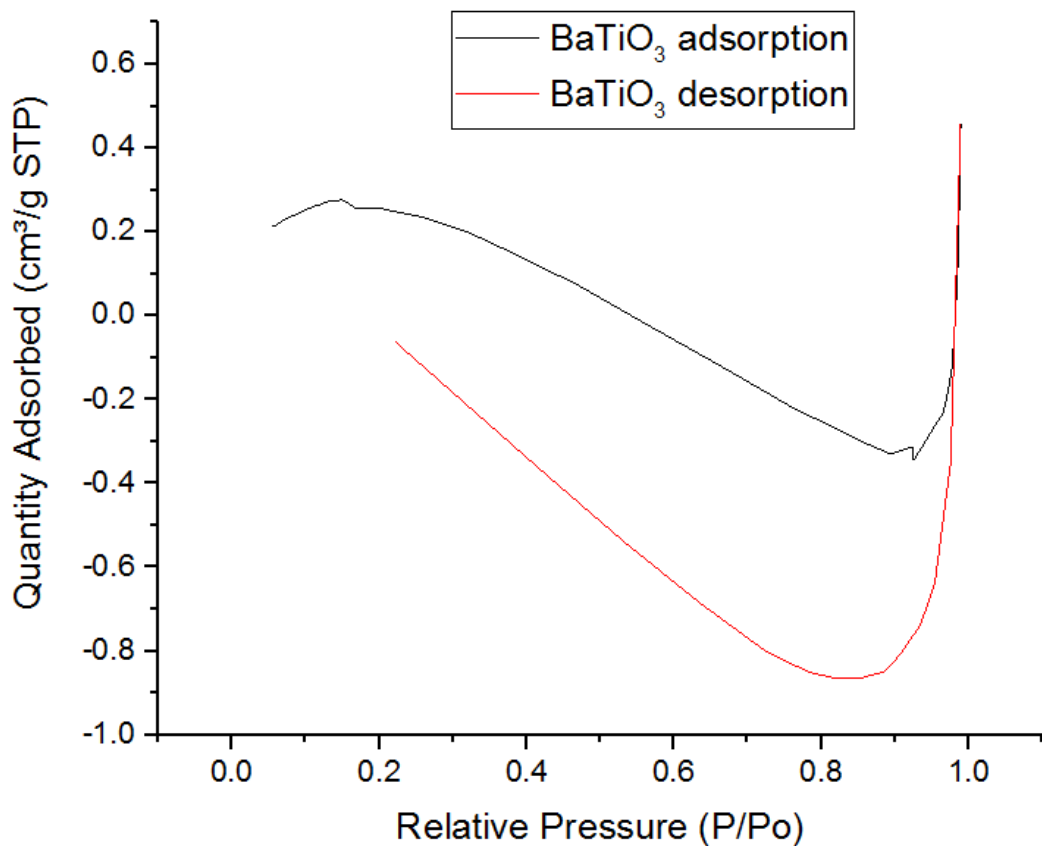
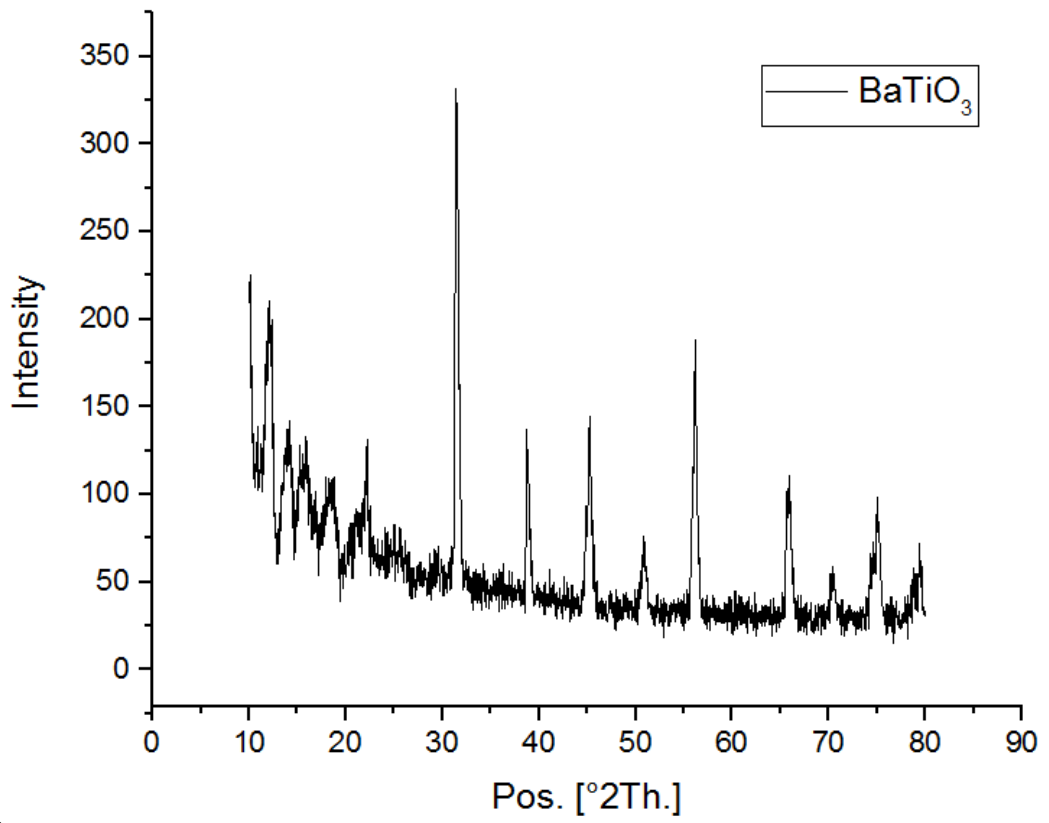
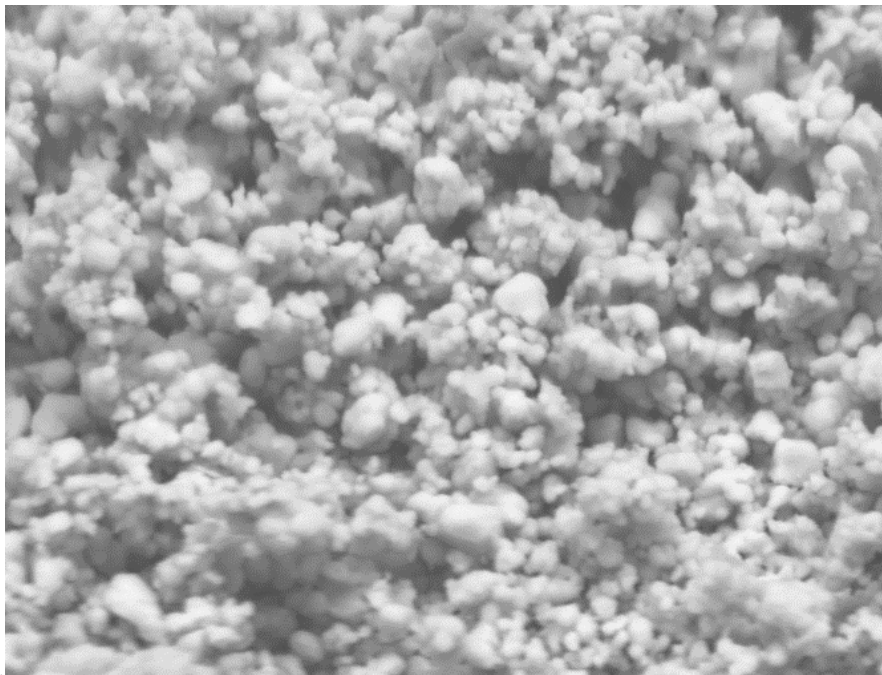


**Figure 3.1-5: Barium titanate support – BET isotherm**



a.



b.

**Figure 3.1-6: (a) XRD graph and (b) SEM picture of Barium titanate**

## **3.2 Experimental methods**

In this section, the different reactors used in this research are described. The reactor set-up, experimental procedure and reproducibility are detailed, along with the design choices and commissioning of the reactors, when applicable.

### **3.2.1 Pyrolysis system**

Four different biomasses – wood pellet, corn stalk, peanut shell and coconut shell – were used to study the yield and composition of pyrolysis oils in a pyrolysis system described below.

#### **3.2.1.1 Reactor set-up and procedure**

Pyrolysis of biomasses was carried out in a fixed bed reactor, 550 mm in length by 40 mm internal diameter, made from stainless steel. A schematic diagram of the pyrolysis system is shown in Figure 3.2-1 and a picture of the pyrolysis system is shown in Figure 3.2-2. Furnace temperature control and biomass temperature was monitored throughout the experiments using thermocouples. Gas flow and gas control used mass flow meters enabling the control and monitoring of process parameters during the experiments. A stainless steel crucible was used to hold the biomass feedstock (4 g) in the reactor, which was heated up to 600 °C via a furnace, at a heating rate of 20 °C min<sup>-1</sup>, and held at the final temperature of 600 °C for 30 minutes. A flow rate of Nitrogen of 200 mL.min<sup>-1</sup> was used as a gas carrier, in order to provide an inert atmosphere, to guide the pyrolysis vapours out of the hot reactor as well as to minimise secondary reactions such as thermal cracking, repolymerisation or condensation of pyrolysis vapours (Katyal et al., 2003). To trap the pyrolysis vapours as the condensable liquid fraction, a condenser system consisting of an air-cooled condenser, followed by two dry-ice cooled condensers was used. Non-condensable gases were passed through the condenser system and into a 25 L Tedlar™ gas sample bag. The furnace was then switched off and the gas kept being collected for a further 20 minutes. After closing the gas bag, the gas and liquid fractions were collected to be analysed. The liquid products were diluted into 10 mL of Methanol for further analysis.

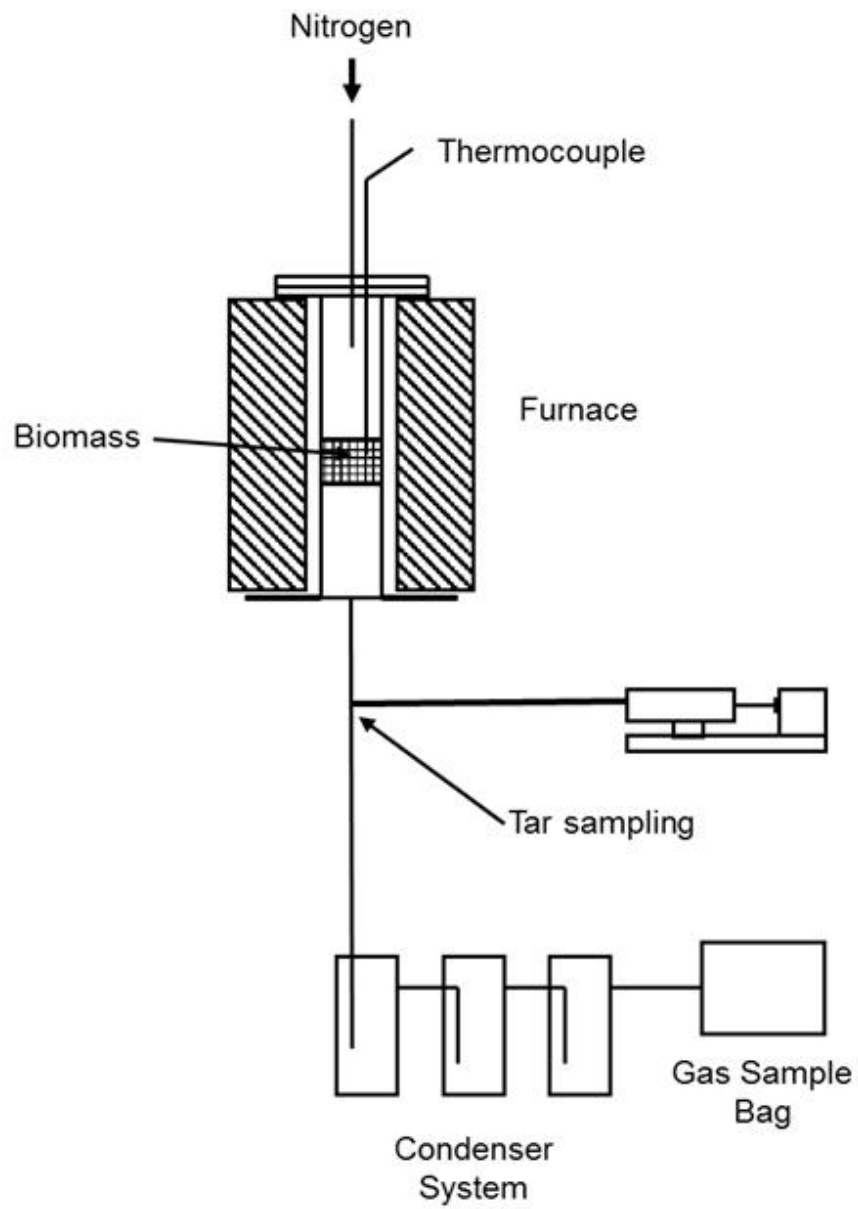


**Figure 3.2-1: Schematic diagram of the experimental setup for pyrolysis**



**Figure 3.2-2: Photograph of the pyrolysis system**

### **3.2.1.2 Tar sampling**

Tar sampling was conducted by following the SPA (Solid Phase Absorption) method developed by Brage et al. (Brage et al., 1997) This consists of two minute gas sampling at 50 mL/min. A needle of 5 cm long from Henke Sass Wolf and a filter in a 1 mL tube of polypropylene from Supelco were used to collect the tars. Three samples were taken for this experiment: at the beginning, the middle and the end of the experiment, at different temperatures. The beginning of the experiment was when pyrolysis started and vapours could be seen through the first condenser. The second sample was taken when the reactor temperature reached 600 °C. The third sample was taken when the furnace was switch off. To collect the tars, the pump was activated for two minutes, pumping the product gas at the bottom of the second stage of the reactor at 50 mL/min. As the pumped gas went through the needle and the filter, tar compounds were accumulated in the filter, whereas smaller particles went through the filter and pumped out. After two minutes of pumping, the filter is recovered and 2 mL of DCM (Dichloromethane) were passed through, to dilute and collect the tars accumulated into the filter. The recovered tars were then analysed by gas chromatography-mass spectroscopy.

### 3.2.1.3 Experiment reproducibility

Before running optimisation experiments and modifying parameters to understand their impact on an experiment, an experiment has been repeated at least twice. These repeat experiments helped to identify the repeatability of a particular setup and the errors which could be generated in an experiment when using the experimental setup. For example, three experiments were conducted with the pyrolysis reactor using woody biomass to analyse the mass balance product results and detailed gas composition in the gas outlet. These results were quite homogeneous, as shown in Table 3.2-2. The repeatability of the experiment could be estimated via the relative standard deviation. An excellent reproducibility with minimal errors is indicated by a relative standard deviation of less than 10%. The relative standard deviation was in the range of 0 – 9.12%, showing excellent reproducibility of this gas analysis method.

**Table 3.2-1: General and gas analysis summary for validation of the pyrolysis reactor**

Experiment	1	2	3	Average concentration	Standard Deviation	Relative Standard Deviation
Gas (g)	0.57	0.64	0.57	0.59	0.03	6.81
Liquid (g)	2.39	2.39	2.39	2.39	0	0
Char (g)	0.85	0.85	0.85	0.85	0	0
Mass Balance (%)	95.55	97.31	95.41	96.09	0.87	1.10
<b>Composition in mmol/g of feedstock</b>						
CO	1.73	1.69	1.68	1.7	0.02	1.56
H <sub>2</sub>	0.42	0.49	0.42	0.44	0.03	9.12
CO <sub>2</sub>	1.65	1.69	1.65	1.66	0.02	1.39
CH <sub>4</sub>	0.82	0.82	0.82	0.82	0	0

### 3.2.1.4 SPA reproducibility

For the oil analysis, three samples have been analysed twice and are presented in Table 3.2-2. The repeatability of the experiment could be estimated via the relative standard deviation. The relative standard deviation of oxygenated compounds was in the range of 0 – 17%, showing good reproducibility of this SPA analysis method.

**Table 3.2-2: SPA analysis summary for validation of the pyrolysis reactor with A.C. Average Concentration, Std. Dev. Standard Deviation and Re.Std.Dev. Relative Standard Deviation**

Experiment		Sample 1 (% of peak area)					Sample 2 (% of peak area)					Sample 3 (% of peak area)				
		1	2	A.C.	Std. Dev.	Re. Std. Dev.	1	2	A.C.	Std. Dev.	Re. Std. Dev.	1	2	A.C.	Std. Dev.	Re. Std. Dev.
<b>Oxygenated compounds</b>	chains	52.25	52.74	52.50	0.25	0.66	28.55	36.38	32.47	3.92	17.05	57.82	62.22	60.02	2.2	5.18
	1 ring	47.76	47.26	47.51	0.25	0.74	64.12	63.62	63.87	0.25	0.55	42.18	37.78	39.98	2.2	7.78
	2 rings	0	0	0	0	0	0	0	0	0	0	0	0	0	0	
	3 rings	0	0	0	0	0	0	0	0	0	0	0	0	0	0	
<b>Non-oxygenated compounds</b>	chains	0	0	0	0	0	0	0	0	0	0	0	0	0	0	
	1 ring	0	0	0	0	0	0	0	0	0	0	0	0	0	0	
	2 rings	0	0	0	0	0	7.33	0	3.67	3.67	81.61	0	0	0	0	
	3 rings	0	0	0	0	0	0	0	0	0	0	0	0	0	0	

### **3.2.2 Dielectric Barrier Discharge (DBD) plasma-catalytic system**

To reduce tar compounds from biomass pyrolysis-gasification and produce higher quality syngas, a Dielectric Barrier Discharge (DBD) non-thermal plasma-catalytic system was designed. The system used in this study is described in the following section.

#### **3.2.2.2 Design choices**

As described in the literature review section, plasma systems are of interest for some chemical applications as they involve greater temperatures and higher energy density as well as very high concentration of active species. (Fridman, 2008) To combine the high selectivity of the catalysis reaction and the advantages of the plasma technique, plasma-catalysis have been of interest for the scientific community. The interest in plasma-catalysis increased due to its possible application to environment such as destruction of pollutant in the waste gas stream or minimisation of unwanted products like nitrogen oxides or carbon dioxide. (Whitehead, 2010) Even though the mechanisms of these kind of processes are hardly understood, plasma-catalysis presents many advantages compared to thermal catalysis such as a lower temperature. (Neyts et al., 2014)

Single-stage plasma catalysis processes are mostly suitable for non-thermal plasmas whereas the two-stage plasma-catalysis system are suitable for both thermal and non-thermal plasmas. (Neyts et al., 2014) Dielectric barrier discharges, also known as DBD, were first introduced in 1857 by Siemens to generate ozone, determining the direction for DBD investigations and applications for many years. (Fridman et al., 2011) The main advantage of DBD plasmas compared to other discharges is the possibility to use atmospheric non-thermal and their relatively easiness to scale-up. (Conrads et al., 2000)

The DBD plasma-catalytic reactor chosen, represented in Figure 3.2-3, was used downstream of a fixed bed pyrolysis reactor to study the effect of this second stage on the product fractions obtained from biomass pyrolysis, studied using the reactor presented in 3.2.1. This was conducted in order to reduce tar compounds produced from biomass pyrolysis and produce high quality syngas.

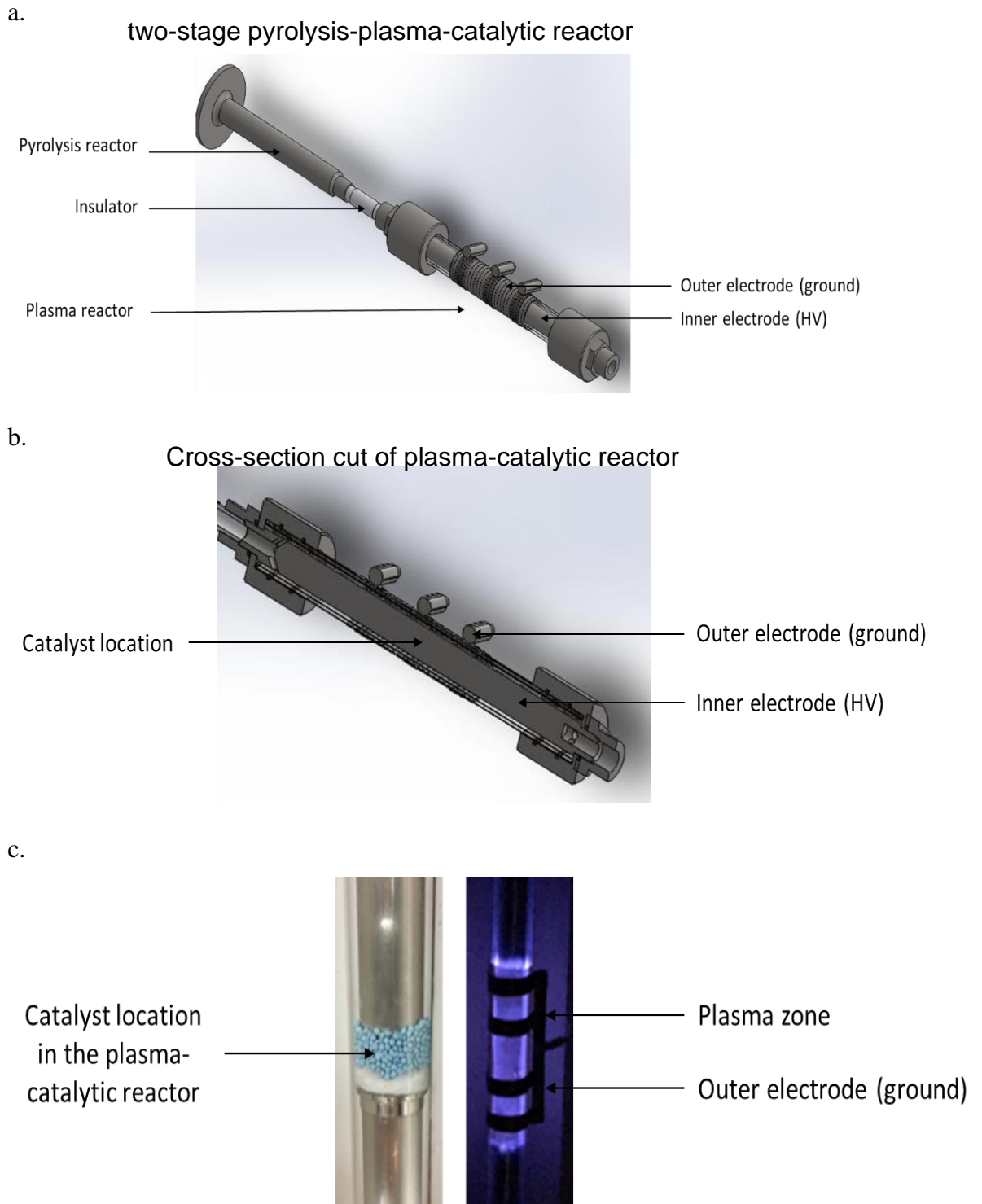


**Figure 3.2-3: Reactor description (a) drawing of the two-stage reactor (b) drawing of cross section cut of the plasma-catalytic reactor; (c) picture of the plasma-catalytic stage without the outer electrode and picture of the plasma zone**

### 3.2.2.2 Reactor set-up and procedure

The experimental system for the biomass pyrolysis-plasma-catalysis was comprised of a two stage reactor system shown in Figure 3.2-4, as a schematic diagram, and in Figure 3.2-5 as a photograph. The first stage was the pyrolysis stage which was a fixed bed reactor, 250 mm in length by 20 mm internal diameter, made from stainless steel and heated using a temperature controlled electric furnace. The evolved biomass pyrolysis gases were directly transferred to a second stage quartz reactor where non-thermal plasma and plasma-catalytic reactions took place. The pyrolysis and plasma-catalysis reactor were separated using an electrically insulating ceramic transfer tube. The feedstock (1 g) was weighed into a stainless steel crucible in the pyrolysis reactor and heated to 600 °C at a heating rate of 50 °C.min<sup>-1</sup> from ambient to the 600 °C pyrolysis temperature. The 2<sup>nd</sup> stage pyrolysis-catalytic reactor was a coaxial Dielectric Barrier Discharge (DBD) plasma reactor which consisted of an 80 mm long copper mesh wrapped on a quartz tube of 25 mm o.d. and 22 mm i.d. An 18-mm stainless steel rod was used as the inner electrode placed centrally within the quartz tube. Thus, the discharge region was ~80 mm with a discharge gap of 2 mm. The DBD plasma reactor was connected to an AC high-voltage power supply with a frequency of 1500 Hz and a maximum peak-to-peak voltage of 20 kV. The inner electrode was connected to the high voltage output whereas the outer electrode was grounded. A digital oscilloscope monitored the discharge. One gram of the Ni/Al<sub>2</sub>O<sub>3</sub> catalyst was placed at the centre of the discharge zone and held in place by quartz wool. The reactor system was continuously purged with nitrogen at a flow rate of 100 mL.min<sup>-1</sup>. The 2<sup>nd</sup> stage plasma reactor was maintained at a temperature of 250 °C using a temperature controlled electric furnace. Steam for the pyrolysis gases reforming reactions was generated from distilled water and injected into the second stage plasma reactor. Product gases were passed through a condenser system comprised of a series of dry-ice cooled glass condensers which condensed the product liquid products and non-condensable gases were passed to a 25 L Tedlar™ gas sample bag.

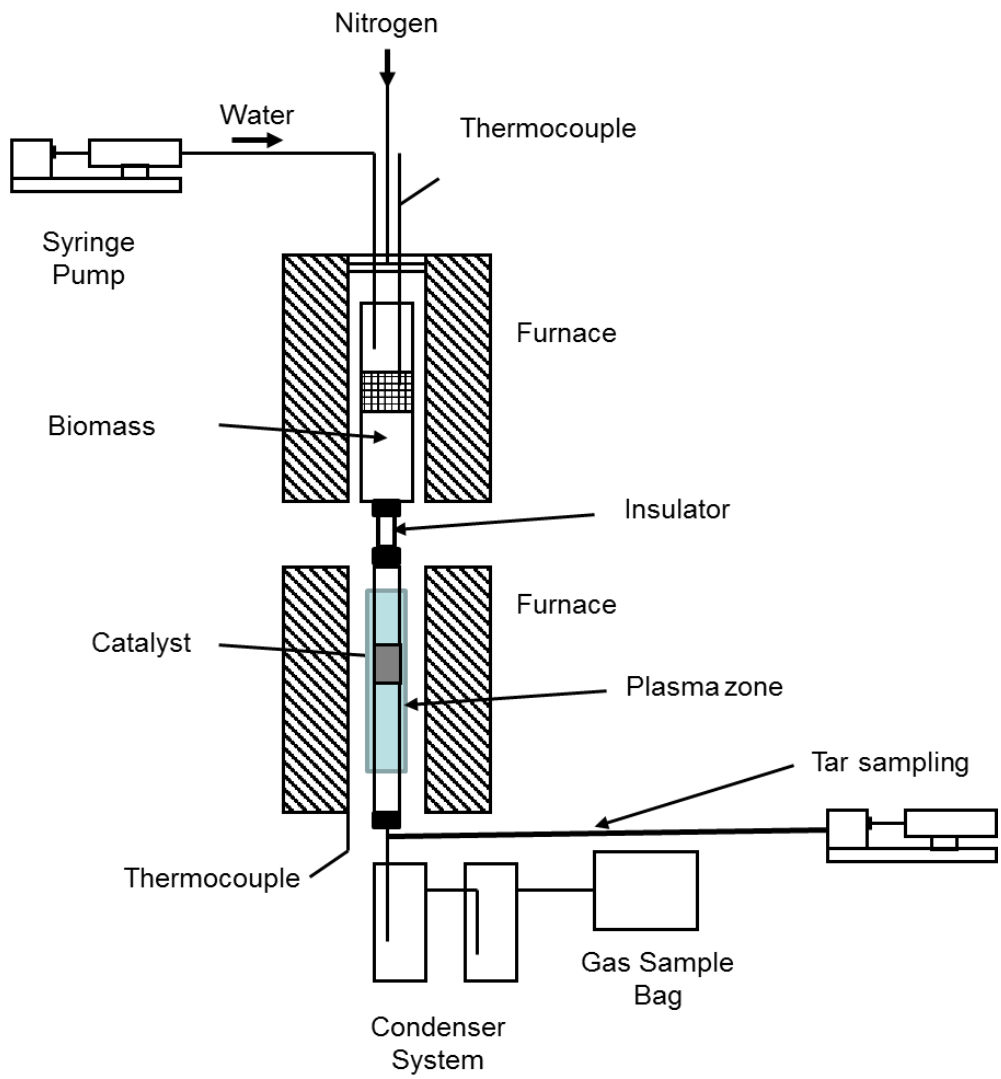
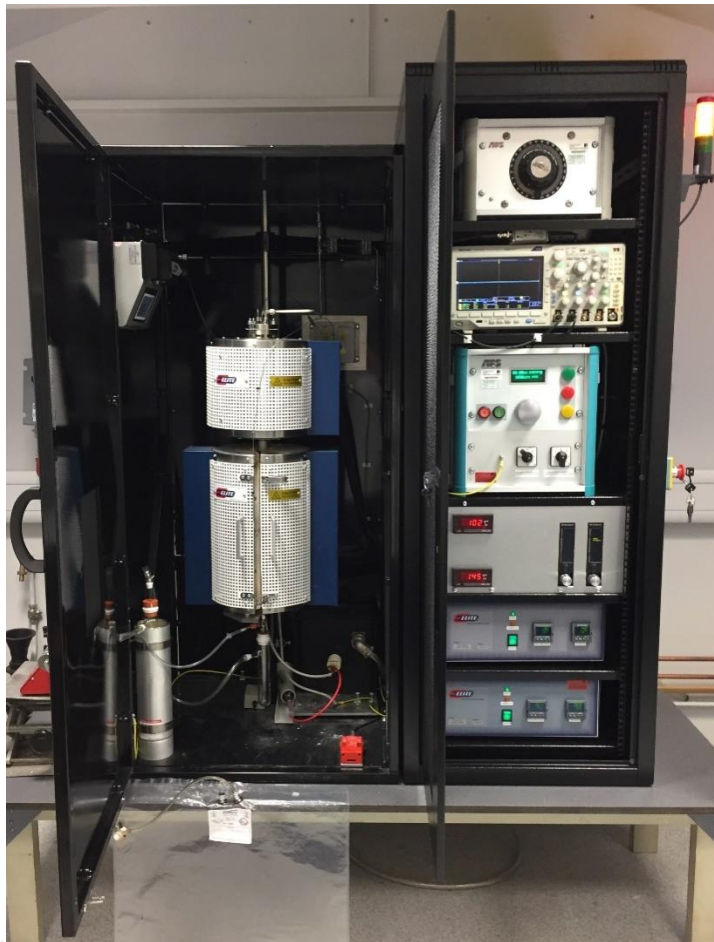
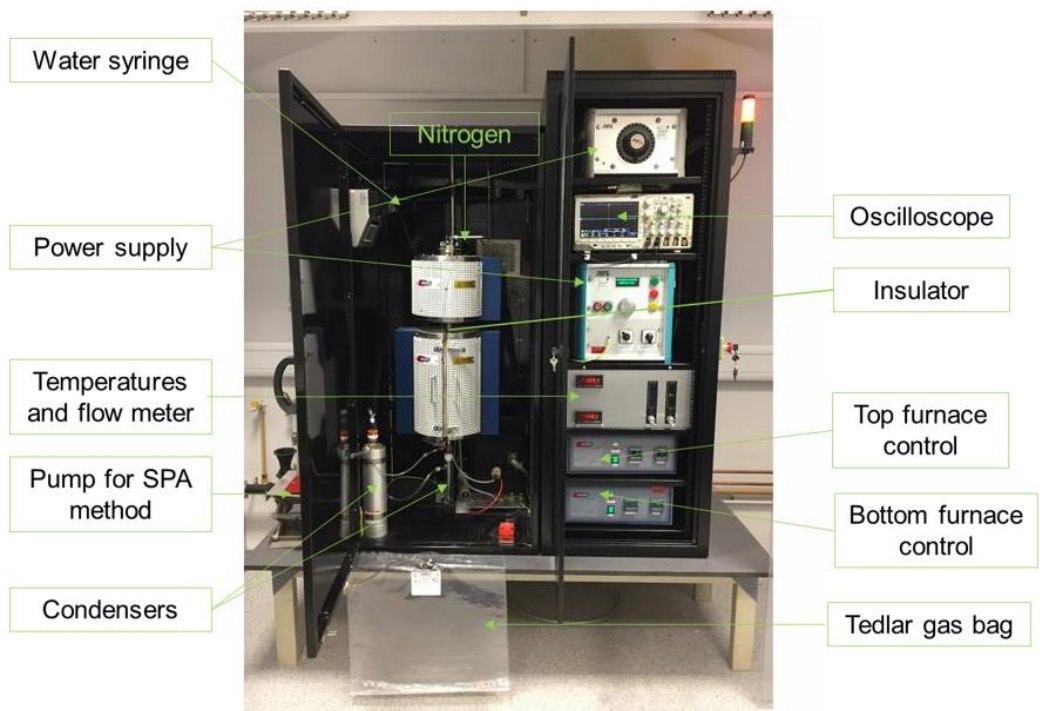


**Figure 3.2-4: Plasma-catalysis experimental setup – Dielectric Barrier Discharge**



a.



b.

**Figure 3.2-5: Photograph of the pyrolysis-plasma-catalysis experimental setup – Dielectric Barrier Discharge (a) and annotated picture (b)**

The experimental procedure consisted of pre-heating the second stage plasma reactor to 250 °C, and the pyrolysis first stage furnace to 120 °C. The plasma was then generated, and the pyrolysis of the biomass started by heating the biomass to 600 °C with a heating rate of 50 °C per minute. Once the pyrolysis reactor had reached 600 °C, the temperature was maintained for 10 minutes, then the furnace was switched off and the product gas was continued to be collected for a further 20 minutes. Gases were analysed later by gas chromatography analysis to identify the product gas composition. The condensed liquid product containing both condensed hydrocarbons and water were recovered from the condensers using methanol. The recovered liquid was analysed for water content and analysis of the tar using coupled gas chromatography-mass spectrometry.

### **3.2.2.3 Experiment reproducibility**

General analysis and gas analysis were conducted for three experiments on the DBD reactor, as shown in Table 3.2-3 for plasma-catalysis using 10 wt.% Ni/Alumina and woody biomass as a feedstock for a power input of 40 W. Oil analysis was conducted and represented in Table 3.2-4 for two experiments. These results showed the consistency of the products composition obtained when using the DBD plasma-catalytic reactor. The repeatability of the experiment could be estimated via the relative standard deviation. An excellent reproducibility with minimal errors is indicated by a relative standard deviation of less than 10%. The relative standard deviation was in the range of 0 – 7.4%, showing excellent reproducibility of the experiment using the DBD plasma-catalytic system.

**Table 3.2-3: General and gas analysis summary for validation of the DBD plasma-catalysis reactor**

Experiment	1	2	3	Average concentration	Standard Deviation	Relative Standard Deviation
Gas (g)	0.34	0.34	0.36	0.35	0.01	3.33
Liquid (g)	1.57	1.72	1.82	1.70	0.10	7.39
Char (g)	0.24	0.23	0.23	0.23	0.01	2.47
MB (%)	96.62	99.04	97.11	97.59	1.05	1.31
<b>Composition in mmol/g of feedstock</b>						
CO	3.31	3.33	3.07	3.24	0.12	4.47
H <sub>2</sub>	3.94	3.47	3.53	3.65	0.21	7.01
CO <sub>2</sub>	3.46	3.40	3.05	3.30	0.18	6.70
CH <sub>4</sub>	1.11	1.10	0.98	1.06	0.06	6.80

**Table 3.2-4: Oil analysis summary for validation of the DBD plasma-catalysis reactor**

Experiments	1	2	Average concentration	Standard Deviation	Relative Standard Deviation
Total tar (g/m <sup>3</sup> of N <sub>2</sub> )	0.157	0.14	0.149	0.01	8.09
<b>Selected tar compounds (ppm)</b>					
Phenol	11.29	10.56	10.925	0.37	4.72
o-cresol	5.52	5.554	5.537	0.02	0.43
p/m-cresol	13.87	12.49	13.18	0.69	7.40
2,4-dimethylphenol	6.571	6.443	6.507	0.06	1.39
4-ethylphenol	6.014	5.86	5.937	0.08	1.83
Benzene	0	0	0	0	0
4-isopropylphenol	4.983	4.921	4.952	0.03	0.89
2-methoxy-4-propylphenol	6.47	6.364	6.417	0.05	1.17

### 3.2.3 Packed-bed Dielectric Barrier Discharge (DBD) plasma-catalytic system

To improve the reduction of tar compounds and the quality of syngas produced, the DBD plasma-catalytic system needed to be modified. To do so, the easiest way was

to increase the electric field, which could be done by using a packed-bed DBD plasma-catalytic system. In fact, high voltage is applied to the packed bed and a non-equilibrium plasma will be created in the void space between the dielectric pellets of catalyst. By refracting of the electric field on the pellets, the electric field becomes non-uniform and stronger with an intensity dependent on the porosity, shape and dielectric constant of the pellets (Fridman et al., 2011). The first stage reactor from the system described in 3.2.2 was used to minimise the building work conducted.

To build the new plasma reactor, different constraints needed to be considered. First, the design itself of the reactors electrodes was challenging: the gas flow needed to travel through the reactor without back pressure when reaching the packed bed area. Electrodes had to be conductive, covering the whole reactor horizontal surface, in order to enable the whole packed-bed to be subject to plasma conditions and adjustable to enable different packing lengths to be trialled.

### **3.2.3.1 Non-heated reactor trials**

The first reactor design was obtained and can be seen in Figure 3.2-6.

The key feature of this reactor was the presence of a spring within an electrode, to allow different packing lengths and to avoid gas leaks by maintaining the two parts of the electrode to remain sealed through pressure from the top reactor weight. After passing the leak tests, different packings were tried for a cold setup to verify the possible ignition of plasma and the stability of the plasma itself.

These non-heated experiments were conducted to study the conditions for plasma ignition in the new plasma-catalytic reactor. As plasma is generated in the void between the dielectric beads of packing material, the dielectric properties and the type of packing material is highly important. Once plasma is ignited, the system needed to be maintained for a minimum of 30 minutes in order to be relevant for our study, as the procedure for this section intended to be similar of the one in 3.2.2.2. A summary of these experiments can be found in Table 3.2-5 for an approximate length 3 cm. More information on specific cases can be found below the table.

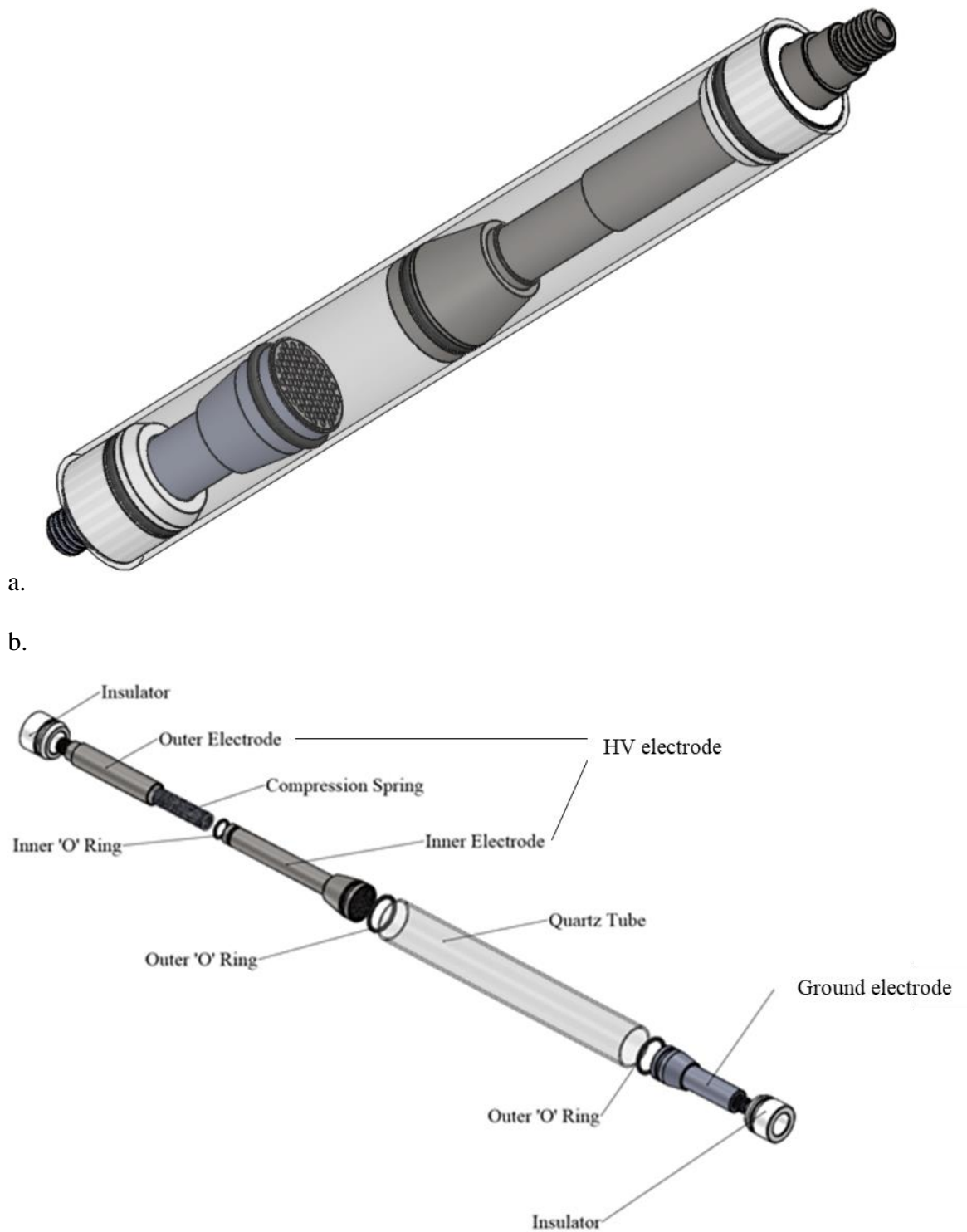


**Figure 3.2-6: Reactor description before experiment trials (a) drawing of the packed bed plasma-catalytic reactor (b) drawing of the packed bed plasma-catalytic reactor assembly**

**Table 3.2-5: Results of non-heated reactor trials**

<b>Packing used</b>	<b>Bead diameter (mm)</b>	<b>Supplier</b>	<b>Power (W)</b>	<b>Spark (Y/N)</b>	<b>Stability duration (min)</b>	<b>Notes</b>
<b>BaTiO<sub>3</sub></b>	~ 3	Catal UK	60	Y	N.A.	Sparks and unstable plasma for power > 20 W
			40	Y	N.A.	
			20	N	45	
<b>BaTiO<sub>3</sub></b>	~ 2	Catal UK	20	Y	45	Small sparks but generally stable
<b>Al<sub>2</sub>O<sub>3</sub></b>	~ 3	Alfa Aesar	40	Y	20	Small sparks but generally stable
			20	Y	45	
<b>Quartz</b>	~ 2		<12	Y	N.A.	No plasma ignition but loud noise and sparks from 12 W
<b>Ru/Ni-Al<sub>2</sub>O<sub>3</sub>(5/15wt.%)</b>	2 - 3	Catal UK	60	Y	N.A.	Unstable plasma leading to flame within the reactor
			20	Y	~ 5.	
<b>Ni/Al<sub>2</sub>O<sub>3</sub></b>	2 – 2.5	Catal UK	40	Y	~ 5	Non-homogeneous and unstable plasma leading to sparks
			25	Y	~ 5	

When using an input of 40W, the reactor seemed able to sustain a higher power input. This was controlled by the use of an oscilloscope as it can be seen in Figure 3.2-7(a), showing in yellow the voltage collection and in blue the intensity collection. The power was increased after a minute to 60W, as shown in Figure 3.2-7(b). After a couple of minutes, the power decreased dramatically to 33W for stability, even when trying to increase or decrease the power input. The shape of the intensity plot, shown in Figure 3.2-7(c) in blue, was different to the previous intensity plots in Figure 3.2-7(a) and Figure 3.2-7(b). This non-sinusoidal shape materialised as a change in plasma

structure: the plasma became non-homogeneous with only sparks at the top, followed by a visible flame inside the quartz tube as shown in Figure 3.2-7(d). The plasma was again ignited at 20W and stable for a few minutes with a sinusoidal intensity curve, until the plasma changed to flames and intensity plot took a similar shape to the intensity plot (in blue) in Figure 3.2-7 (c).

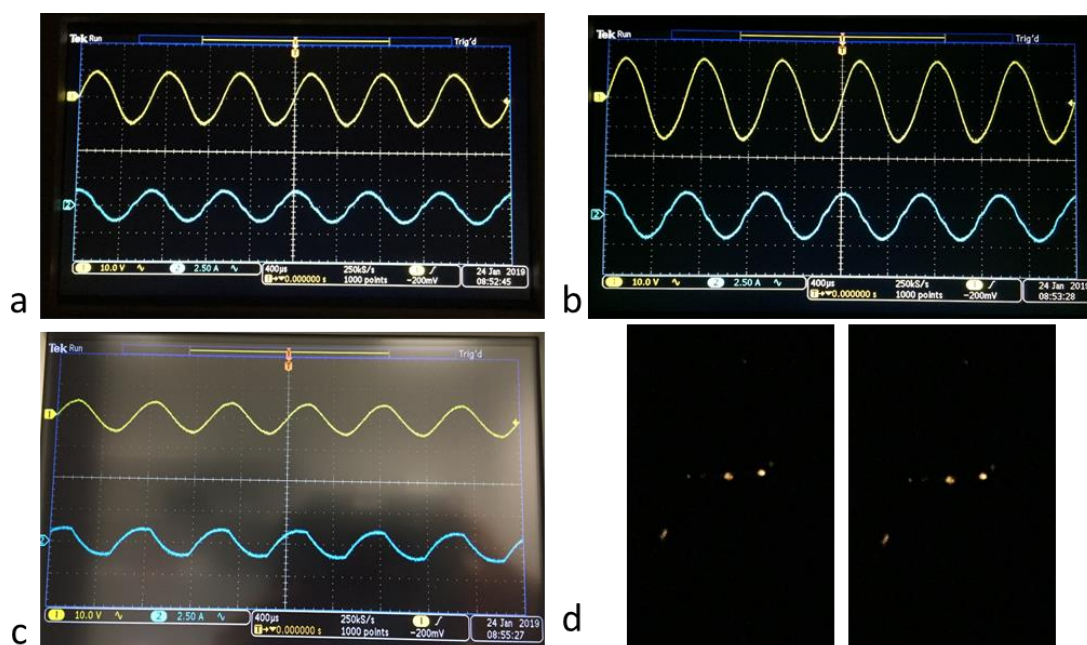


**Figure 3.2-7: Illustrations of usage of Ru/Ni-  $\text{Al}_2\text{O}_3$  (a) at 40 W, (b) at 60 W, (c) at 30 W and (d) flame pictures in the bed.**

When using a power input of 42W, the plasma was stable for few minutes. Plasma started to divide into three zones, with the middle one not lit up, as shown in Figure 3.2-8 (b). The power input then increased independently to 50W and sparks appeared, as represented in Figure 3.2-8 (a). These sparks showed the instability of the plasma in this condition, which leads to the plasma being unusable for the experimental study. An unstable plasma will not enable stable production of gas fraction and liquid fraction and thus lead to inconsistent syngas production, which does not permit the technology to be commercialised. The plasma was shut down and the power input was turned back on again at 25W. Plasma was only generated at the top of bed, as seen in Figure 3.2-8(c), and sparks were heard after few minutes, leading to an unstable generated plasma. Another issue with these uncontrolled sparks are the fact that they can interfere with electrical compounds and could damage the equipment used to control the experiment.

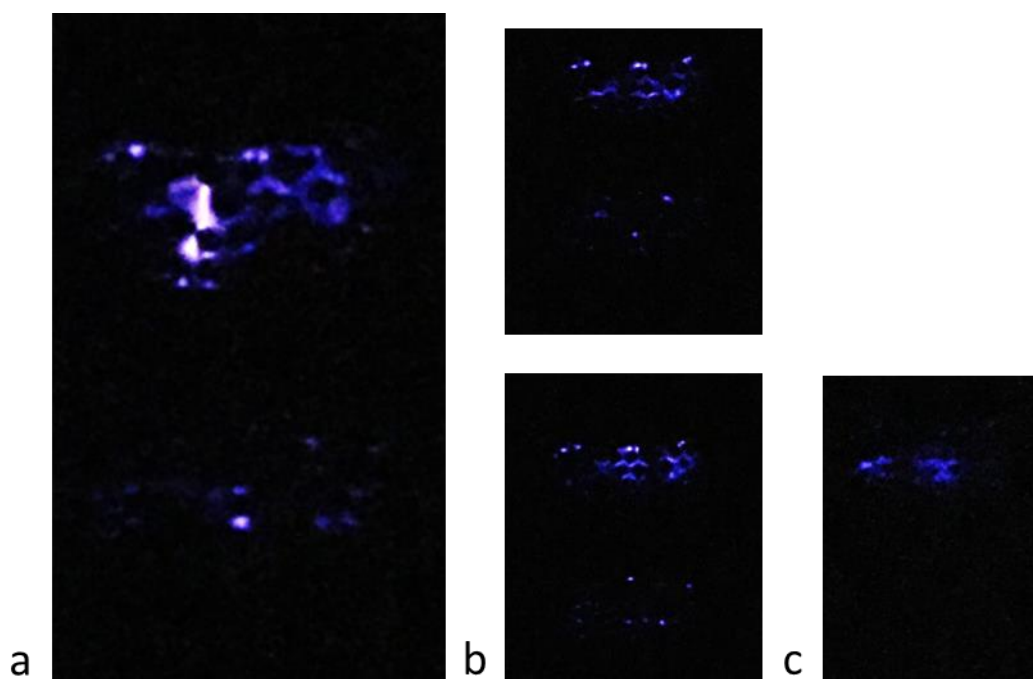


**Figure 3.2-8: Illustrations of usage of Ni/Al<sub>2</sub>O<sub>3</sub> (a) at 50 W, (b) at 40 W and (c) at 25 W**

From the different packings tried in the cold reactor trials, two packings were considered to continue trials: Alumina and Barium Titanate. Barium titanate is also the packing that is the most commonly used for packed-bed dielectric barrier discharges (DBD) as described in the literature review. (Mei et al., 2015) Alumina is also convenient to compare the packed bed DBD with the first DBD reactor described in section 3.2.2. Both packings were used as they could be used to higher power to sustain stable plasma.

### 3.2.3.2 Heated reactor trials

To further the commissioning of the reactor, the experiment protocol as described in section 3.2.2.2 was followed: the top pyrolysis reactor was heated up to 600 °C, the bottom reactor (packed bed DBD reactor) was heated up to 250°C and steam was injected at a rate of 2 g/h. This was conducted in order to have the biomass in a fixed bed pyrolysis reactor. Its produced fractions were carried through the plasma-catalytic reactor stage, heating at 250°C to avoid condensation of tar compounds within the reactor. Alumina and barium titanate were used as packing in the bottom reactor. Different packing lengths were tried to verify the feasibility of plasma. The results are reported in Table 3.2-6.

**Table 3.2-6: Results of heated reactor trials**

Packing support	Bead size (mm)	Packing length (cm)	Stable plasma (Y/N)
Alumina (Al <sub>2</sub> O <sub>3</sub> )	3	2.5	N
		3.5	
		4.5	
Barium Titanate (BaTiO <sub>3</sub> )	2	2.5	N
		3.5	
		4.5	

For every packing length at 20W, plasma will be ignited for a few minutes and turned into sparks after a few minutes. The sparks occasionally lead to disrupted furnace temperature controls, making the furnace unusable. To avoid these interferences, power should be turned down to 15 W to avoid sparks, even though there was no plasma ignition. In order to ignite plasma in the second reactor, it was decided not to heat the plasma reactor and start new trials in this condition.

### 3.2.3.3 Heated first reactor and non-heated second reactor trials

Following the previous trials, a different procedure to the one used in section 3.2.2.2 was used. The top pyrolysis reactor was heated up to 600°C, the bottom packed bed DBD reactor was kept at room temperature and steam was injected at a rate of 2 g/h. As before, alumina and barium titanate were used as packing in the plasma reactor. Different input powers and packing lengths were tried to verify the feasibility of plasma.

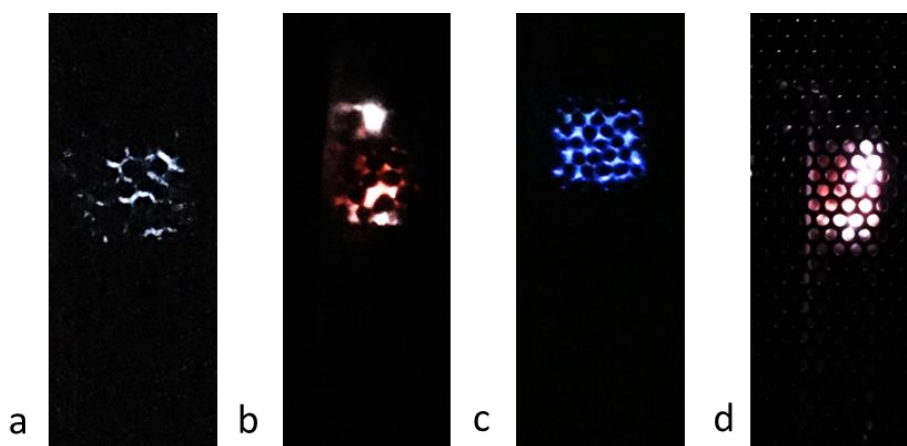
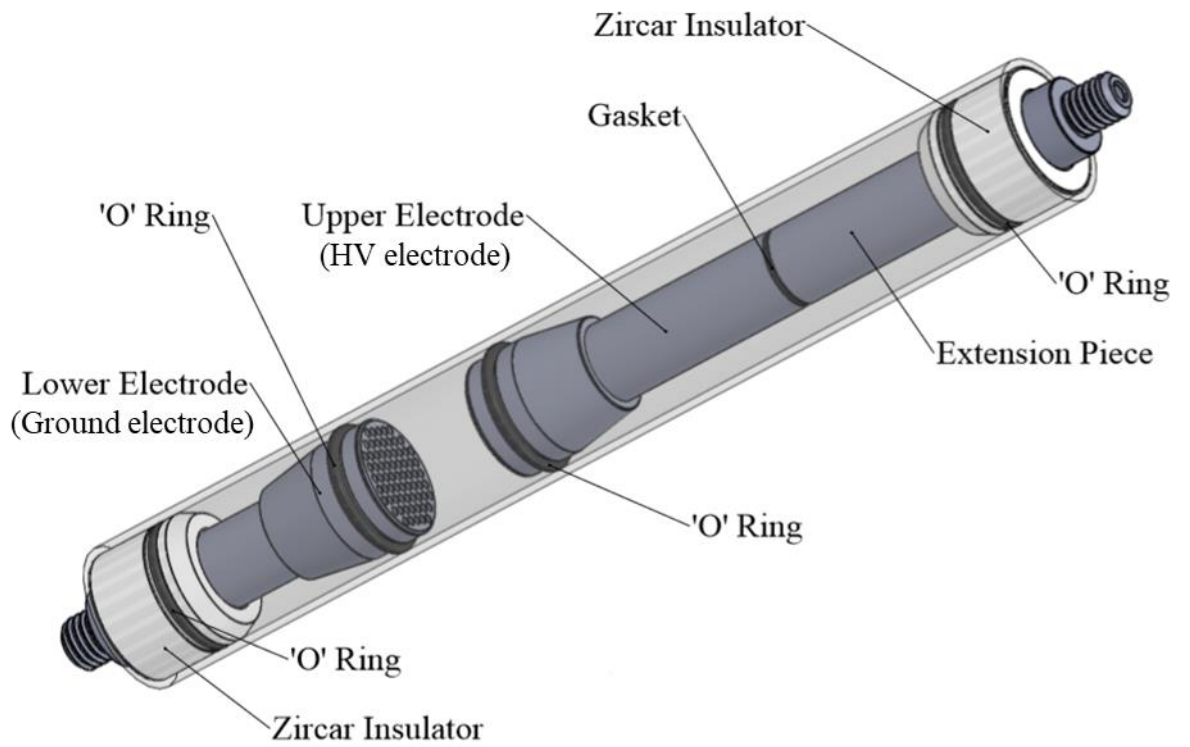


**Figure 3.2-9: Pictures of plasma for Alumina packing (length: 2.5 cm) (a) for 20 W after a minute, (b) for 20 W when steam reached the bottom reactor, (c) for 40 W after a minute, (d) for 40 W when steam reached the bottom reactor.**

Alumina packing was first used for a packing length of 2.5 cm and a power input of 20W and 40W. The plasma was first stable Figure 3.2-9(a) and Figure 3.2-9(c) until steam reached the bottom reactor. When steam was in contact with the plasma zone, the plasma shut itself down and tried to re-ignite itself with intense sparks as shown in Figure 3.2-9(b) and Figure 3.2-9(d). After a few seconds, the plasma came back to its stable state (Figure 3.2-9(a) and Figure 3.2-9(c)), until steam reached the plasma reactor again. It was decided that it was not safe to use alumina packing for further study and the focus was put on barium titanate.

Barium titanate was trialled at different lengths and different input power successfully. However, some issues were observed for the top electrode of the plasma reactor. With the spring heated up by heat diffusion from the top reactor, the pressure maintaining the reactor without leak was too weak to prevent leaks. Thus, the whole top electrode was changed into interchangeable stainless tubes of different lengths to provide different packing lengths, as well as to be conductive for enabling plasma ignition. In addition, excess condensation was observed around the seal of the two-part electrode. This was improved by using an O-ring to enable better sealing. The details of the changes in the reactor design can be found in Figure 3.2-10.

a.



b.

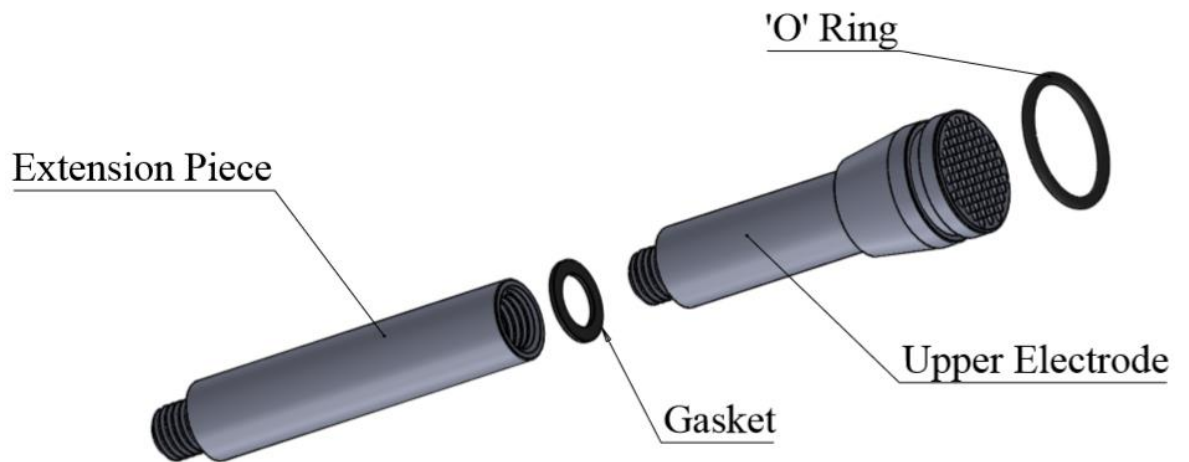


**Figure 3.2-10: Final Reactor description (a) drawing of the reactor (b) drawing of the upper electrode assembly**

### 3.2.3.4 Reactor set-up and procedure

The experimental system for the biomass pyrolysis-plasma-catalysis was comprised of a two-stage reactor system shown in Figure 3.2-11, as a schematic diagram. A photograph of the second stage plasma-catalytic reactor is represented in Figure 3.2-12. The first stage was the pyrolysis stage which was a fixed bed reactor, 250 mm in length by 20 mm internal diameter, made from stainless steel and heated using a temperature controlled electric furnace. The evolved biomass pyrolysis gases were directly transferred to a second stage quartz reactor where non-thermal plasma and plasma-catalytic reactions took place. The pyrolysis and plasma-catalysis reactor were separated using an electrically insulating ceramic transfer tube. The feedstock (1 g) was weighed into a stainless steel crucible in the pyrolysis reactor and heated to 600 °C at a heating rate of 50 °C.min<sup>-1</sup> from ambient to the 600 °C pyrolysis temperature. The 2<sup>nd</sup> stage pyrolysis-catalytic reactor was a packed-bed Dielectric Barrier Discharge (DBD) plasma reactor which consisted of a 248 mm length quartz tube of 30 mm o.d. and 33.5 mm i.d. A 87.5-mm long stainless steel rod was used as the lower electrode and a upper two-part electrode was used with a 235.8 ± 10 mm. The DBD plasma reactor was connected to an AC high-voltage power supply with a frequency of 1500 Hz and a maximum peak-to-peak voltage of 20 kV. The inner electrode was connected to the high voltage output whereas the outer electrode was grounded. A digital oscilloscope monitored the discharge. The barium titanate packing was introduced to obtain the desired packing length and plasma discharge length – between 25 and 45 mm length with a total mass between 30 and 60 g of catalyst. The reactor system was continuously purged with nitrogen at a flow rate of 100 mL.min<sup>-1</sup>. The 2<sup>nd</sup> stage plasma reactor was maintained at room temperature. Steam for the pyrolysis gases reforming reactions was generated from distilled water and injected into the second stage plasma reactor. Product gases were passed through a condenser system comprised of a series of dry ice cooled glass condensers which condensed the product liquid products and non-condensable gases were passed to a 25 L Tedlar™ gas sample bag.

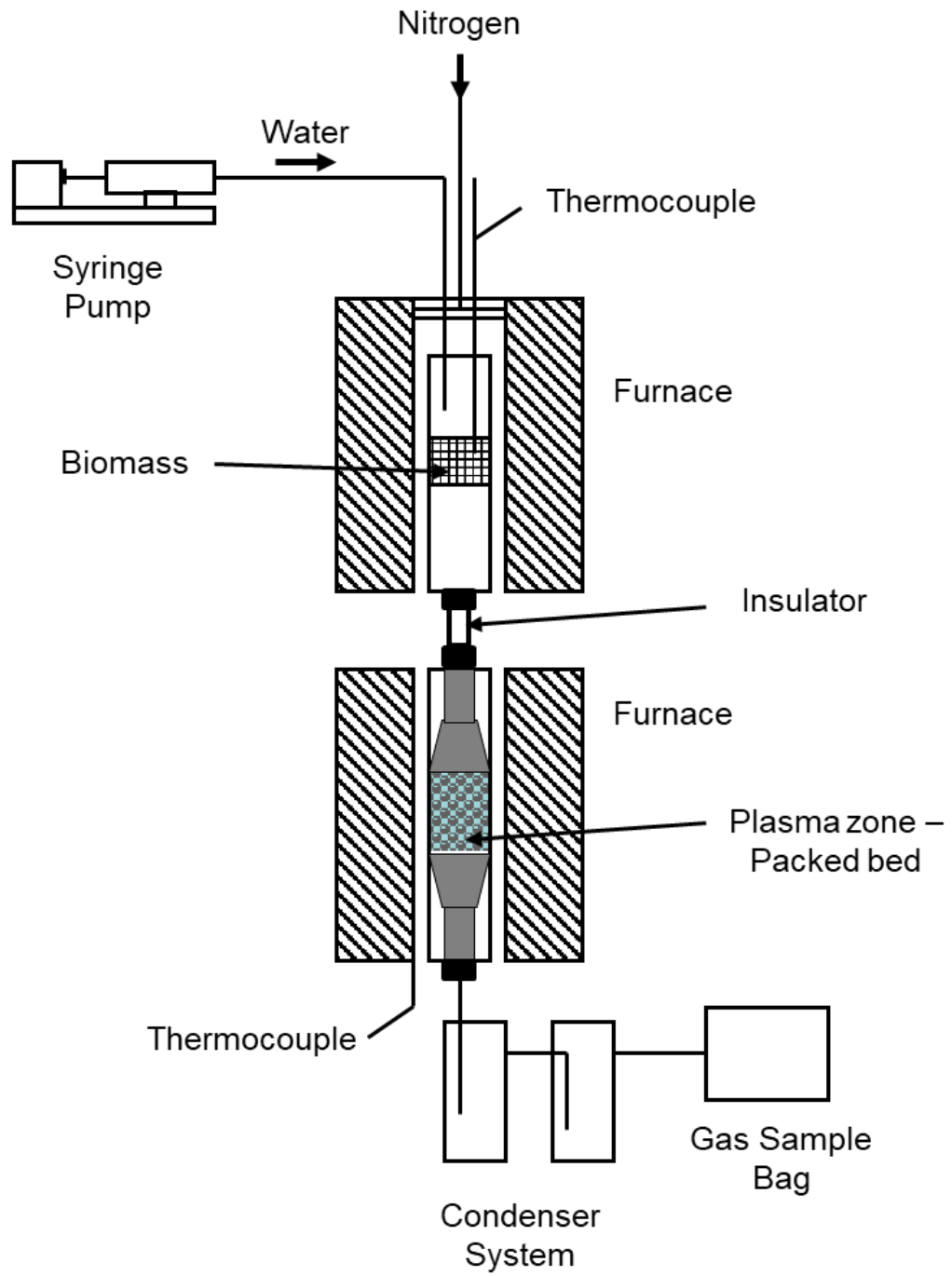


**Figure 3.2-11: Plasma-catalysis experimental setup - Packed-bed Dielectric Barrier Discharge**



**Figure 3.2-12: Photograph of the packed-bed DBD plasma-catalytic reactor**

The experimental procedure consisted of pre-heating the pyrolysis first stage furnace to 120 °C. The plasma was then generated, and the pyrolysis of the biomass started by heating the biomass to 600 °C with a heating rate of 50 °C per minute. Once the pyrolysis reactor had reached 600 °C, the temperature was maintained for 10 minutes, then the furnace was switched off and the product gas was continued to be collected for a further 20 minutes. Gases were analysed later by gas chromatography analysis to identify the product gas composition. The condensed liquid product containing both condensed hydrocarbons and water were recovered from the condensers using methanol. However, in this experimental setup, the main focus was on the product gas. Therefore, the liquid products were not analysed in the sections using the Packed-bed DBD reactor.

#### **3.2.3.5 Experiment reproducibility**

General analysis and gas analysis were conducted for three experiments on the Packed-bed DBD reactor, as shown in Table 3.2-7 for plasma-catalysis using barium titanate and woody biomass as a feedstock for a power input of 20 W. The repeatability of the experiment could be estimated via the relative standard deviation.

An excellent reproducibility with minimal errors is indicated by a relative standard deviation of less than 10%. The relative standard deviation was in the range of 0 – 15.8%, showing an excellent to good reproducibility of the experiment using the packed-bed DBD plasma-catalytic system.

**Table 3.2-7: General and gas analysis summary for validation of the packed-bed DBD plasma-catalysis reactor**

Experiment	1	2	3	4	Average concentration	Standard Deviation	Relative Standard Deviation
Gas (g)	0.25	0.27	0.21	0.2493	0.243	0.025	12.56
Liquid (g)	-	-	-	-	-	-	-
Char (g)	0.22	0.22	0.22	0.22	0.22	0	0
M.B. (%)	71.87	87.24	87.91	87.15	82.34	7.41	11.02
<b>Composition in mmol/g of feedstock</b>							
CO	2.35	2.43	2.16	2.46	2.31	0.11	5.99
H <sub>2</sub>	2.88	2.78	2.57	2.91	2.74	0.13	5.77
CO <sub>2</sub>	3.35	3.07	2.44	3.45	2.95	0.38	15.78
CH <sub>4</sub>	0.97	0.93	0.85	1.1	0.92	0.05	6.67

### 3.3 Characterisation of materials and products

From the experiments, different products were obtained, including gas, liquid and solid fractions. All products were in correlation, giving different information about general yield of the process, its efficiency or the feedstock used. Therefore, all obtained products were analysed following different analysis procedures, as described below.

#### 3.3.1 Sample characterisation

To characterise the biomass samples used as feedstocks in the experiments and described in section 3.1.1, feedstocks were analysed using thermal gravimetric analysis, proximate analysis and ultimate analysis. These analyses are described in the following section.

### 3.3.1.1 Thermal Gravimetric Analysis (TGA)

TGA on the different feedstocks was conducted using a Shimadzu TGA 50, represented in Figure 3.3-1. This technique enabled an analysis of the feedstocks within a pyrolysis reactor, as well as a study of the feedstock composition via the obtention of the proximate analysis of the feedstocks. The main components of the TGA equipment were a controlled ceramic furnace, coupled to a balance and a data recorder. This analysis showed the thermal stability of the feedstock during pyrolysis experiments and thus, indicated when the pyrolysis reaction started and ended. The sample (about 30 mg) was weighted in an alumina pan and heated up from room temperature to 800 °C, under nitrogen flow of 50 mL min<sup>-1</sup> with a heating ramp of 10 °C.min<sup>-1</sup>. After reaching the final temperature, the gas carrier was switched to air to remove the residual ashes. An example thermogram of the TGA for woody biomass is shown in Figure 3.3-2.



**Figure 3.3-1: TGA equipment**

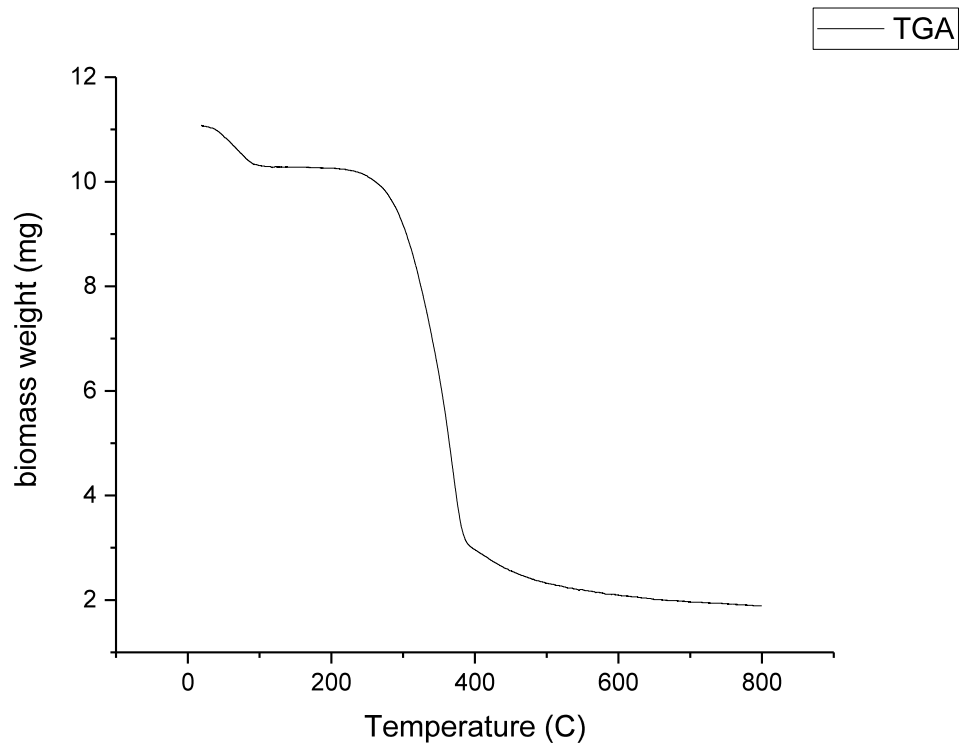


**Figure 3.3-2: Example of thermogram using TGA for woody biomass**

### 3.3.1.2 Proximate analysis

The proximate analyses of the biomass samples were conducted using the Shimadzu described in the previous section, to obtain a measure of their moisture, volatile matter, fixed carbon and ash content. The sample (about 30 mg) was weighed in an alumina pan and first heated under nitrogen, with a flow of  $50 \text{ mL min}^{-1}$ , to  $110 \text{ }^\circ\text{C}$  and held for 10 minutes at this temperature. The measured weight loss corresponded to the moisture content. Secondly, the sample was heated to  $900 \text{ }^\circ\text{C}$  and held for 20 minutes. At this stage, the reported weight loss represented the volatile content. The temperature was increased to  $900 \text{ }^\circ\text{C}$  and held for 20 minutes under nitrogen. Finally, the carrier gas was switched to air for 20 minutes to burn-off the fixed carbon, leaving only ash in the alumina pan. An example thermogram for the proximate analysis of woody biomass is shown in Figure 3.3-3.

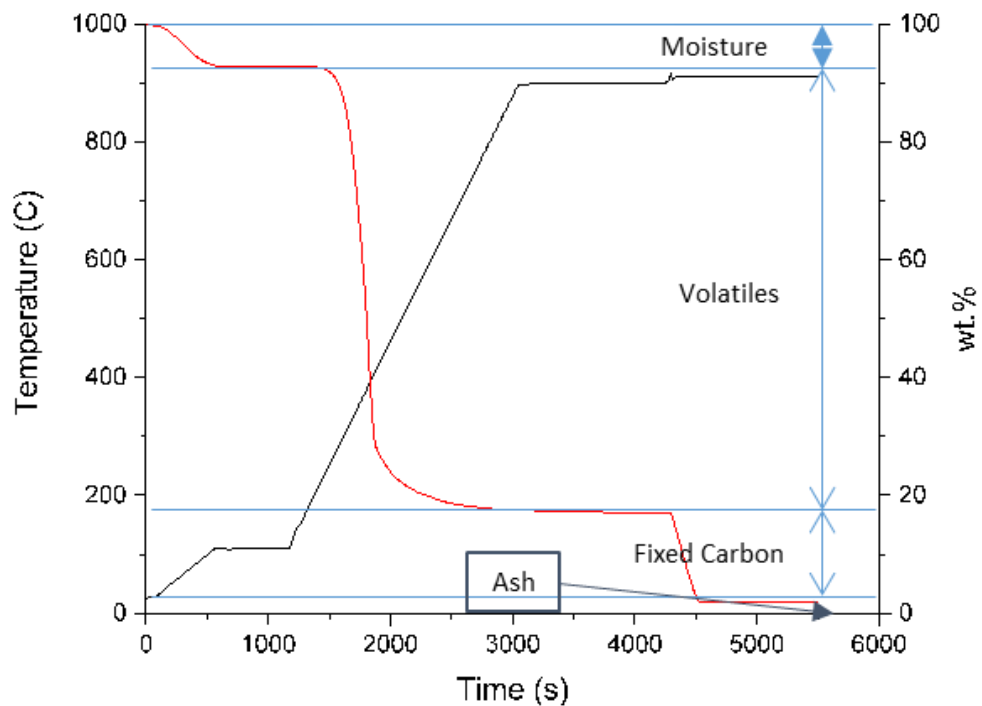


**Figure 3.3-3: Example thermogram for the proximate analysis of woody biomass**

### 3.3.1.3 Ultimate analysis

Ultimate analysis has been conducted on the feedstocks using an elemental analyser (CHNS-O) – Thermo EA2000. This equipment enabled to determine the carbon, nitrogen, hydrogen, sulphur and oxygen content (by difference) of a sample using a flash combustion method. (Technical Committee CEN/TC 335, 2011) From this analysis, the heating value can be calculated according to the literature. (Friedl et al., 2005)

Around 3 mg of sample is weighted and sealed in an aluminium capsule. Each sample was prepared at least in duplicate. The capsules were then placed into an auto-sampler, introducing them into a combustion chamber kept at 900-1000 °C. A fixed amount of oxygen is then injected into the chamber with a helium gas carrier. When the tin capsules reacted with oxygen, an exothermic reaction followed, leading to a temperature increase to 1800 °C and consequently, oxidation of the sample. The gases produced by combustion are sent to a reduction chamber, where CO<sub>2</sub>, NO<sub>2</sub>, H<sub>2</sub>O and SO<sub>2</sub> are formed. A chromatography column then separated the gases, which were

detected by thermal conductivity detector (TCD). This detector was calibrated using standards with known elemental composition. Gases were finally converted into weight percentages of carbon (C), hydrogen (H), nitrogen (N) and sulphur (S) via computer software.

### 3.3.2 Catalyst characterisation

To characterise the researched catalysts and packings described in section 3.1.2, the materials were analysed using different analytic procedures described in the following section. These analyses were conducted on both fresh and reacted catalyst, when applicable.

#### 3.3.2.1 Determination of surface area by Brunauer-Emmet-Teller (BET) method

The porous properties and surface area of the prepared catalysts were determined through nitrogen adsorption at liquid gas temperature, 77K.

The Brunauer-Emmet-Teller (BET) method is used to analyse porous materials. The surface area is determined by using the general BET linear equation below. (Sing, 1985; Lowell et al., 2004) A linear trend can be obtained using point-by-point adsorption data from the multipoint analysis. The solid-gas interactions, the temperature and the relative pressure ( $P/P^0$ ) are related to the amount of gas adsorbed.

#### Equation 3.1

$$\frac{1}{V\left(\frac{P^0}{P} - 1\right)} = \frac{1}{V_m C} + \frac{(C - 1)}{V_m C} \times \left(\frac{P}{P^0}\right)$$

With V, the amount of gas absorbed at the determined  $P/P^0$  pressure,  $P^0$  the saturation pressure,  $V_m$  the monolayer capacity and C an empirical constant.

The surface area analysis was carried out on a Tristar 3000 automated gas sorption system from Micromeritics, for non-alumina supported catalysts, and a Quantrachrome NOVA 2000 automated gas sorption system, for alumina supported catalysts. Prior to the analysis, previously physisorbed material from the adsorbent surface are being removed through degassing. (Sing, 1992) Around 200 mg of each sample was degassed for 4 hours (or overnight) under inert gas – nitrogen - at 400 °C using FlowPrep™ equipment from Micromeritics. The adsorption and desorption isotherms were obtained using the multipoint data described previously at different

relative pressure. An example of BET isotherm for alumina is represented in Figure 3.3-4, with a calculated surface area of  $154.96 \text{ m}^2 \cdot \text{g}^{-1}$ .

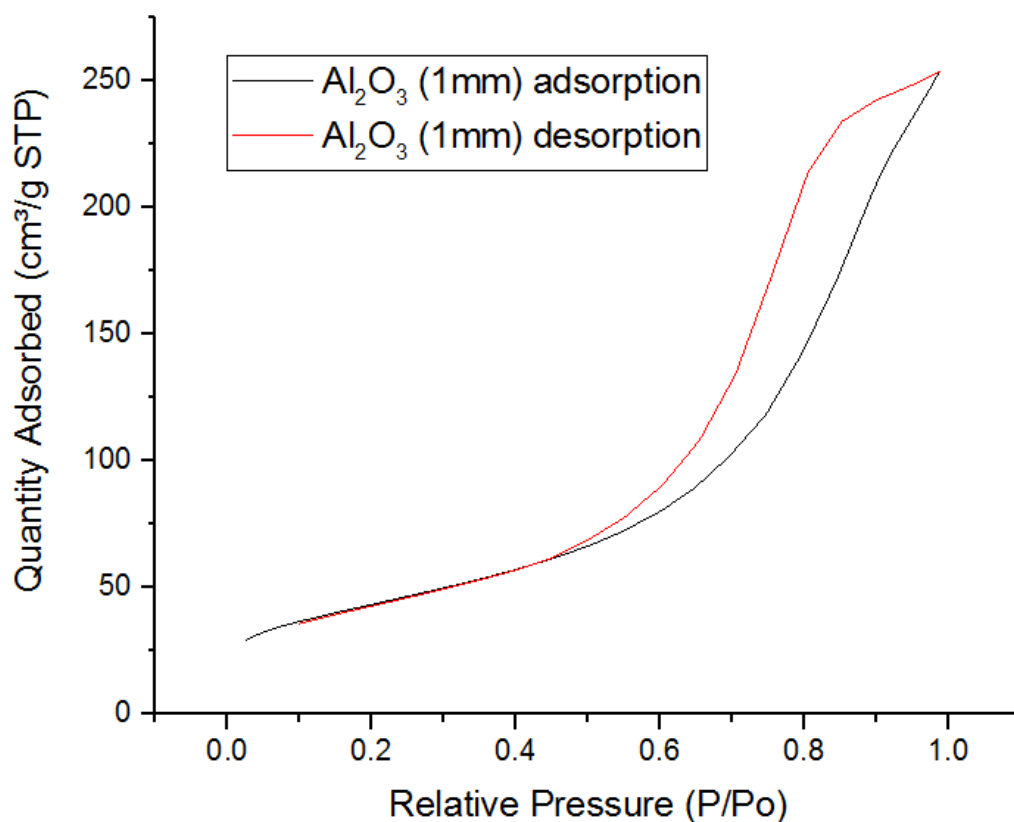


**Figure 3.3-4: Example of BET isotherm for alumina catalytic support of 1 mm diameter beads**

### **3.3.2.2 Determination of pore volume and pore size by Barrett, Joyner and Halenda (BJH) method**

Using the method of Barret, Joyner and Halenda (BJH) enabled to obtain information about the total pore volume and pore diameter, as it is intended to obtain information on porous adsorbents with a wide range of pores. This method considers capillary condensation in pores, used to calculate the pore size distribution from the Kelvin model of pore filling, linking the pore size to the adsorbate amount removed from the catalyst pores depending with respect to the relative pressure ( $P/P_0$ ). The Kelvin equation is described below. (Barrett et al., 1951; Gelb et al., 2002)

### Equation 3.2

$$r_c = r \times t(P)$$
$$\ln \frac{P}{P^0} \geq \frac{-2\gamma V_L}{RT} \times \frac{1}{r_c}$$

With  $t(P)$  the surface layer thickness,  $r$  the radius of the pore,  $V_L$  the molar volume,  $\gamma$  is the surface tension and  $P^0$  is the vapour pressure.

From this equation, the pore volume and pore size could be determined for each catalyst described in section 3.1.2.

#### 3.3.2.3 Temperature programmed oxidation (TGA-TPO)

The characteristics of the coke deposited on the catalyst can be identified by analysing the catalyst through a thermogravimetric method known as Temperature Programmed Oxidation (TPO). TPO's principle is to oxidise the carbon deposited on the reacted catalyst in order to know the quantity of coke deposited onto the catalyst after an experiment. To do so, about 25 mg of used catalyst is placed into an alumina crucible, using the TGA equipment described in 3.3.1.1. Under air flow, the temperature inside the crucible goes up to 800 °C at a heating rate of 15 °C per minute, with 10 minutes hold at 800 °C. The weight loss is recorded during the whole experiment. In the meantime, oxygen present in the air flow reacted with the coke deposited on the catalyst to form either CO<sub>2</sub> or CO as all volatile matter is vaporised at 800 °C. The recovered catalyst was cleaned of the dark matter recovering it before the TPO, underlining the total reaction of the coke during the TPO.

Through this experiment, the catalyst weight loss due to coke oxidation and produced compound volatilisation can be determined. The quantity of coke deposited on the catalyst for an experiment corresponds to the weight loss reported during the TPO experiment. Two main stages could be identified: around 100°C was vaporisation of the moisture within the catalyst, (Akande et al., 2005) and around 400 °C was identified with the combustion of the carbon deposited on the catalyst. (Wu et al., 2010) An example of TPO thermogram is represented in Figure 3.3-5, for a catalysis experiment using the DBD plasma-catalytic setup.

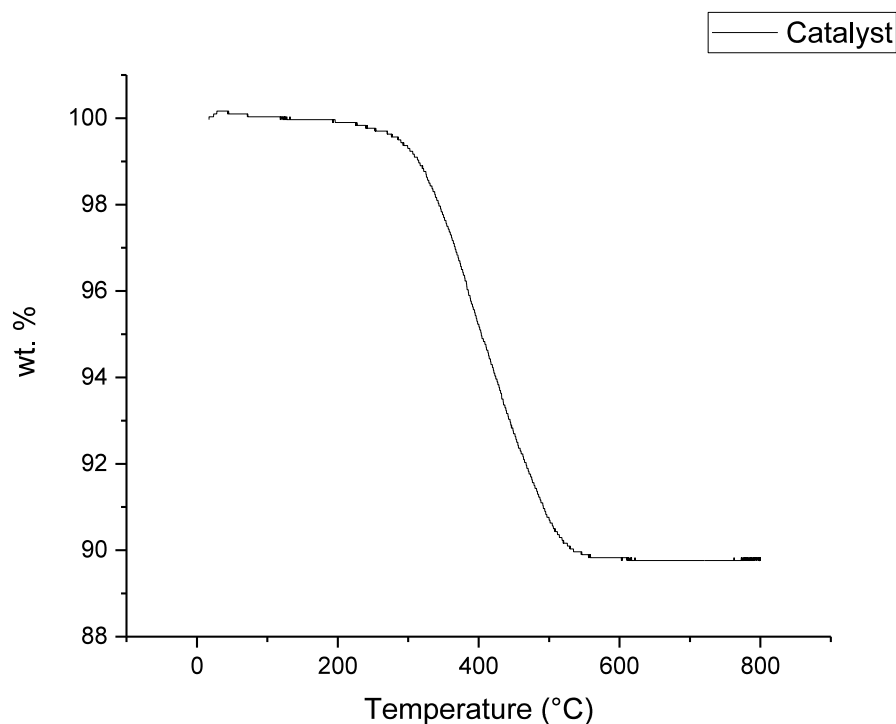


**Figure 3.3-5: Example of a TPO thermogram a catalysis experiment using the DBD plasma-catalytic setup**

### 3.3.2.4 X-ray Diffraction (XRD)

The fresh catalyst and the used catalysts after plasma-catalysis reaction were analysed by XRD (X-Ray Diffraction). The XRD spectra were obtained from a XRD Bruker D8 diffractometer using Mg-K $\alpha$  radiation.

According to Bragg's law, diffraction patterns of a crystal lattice generate different reflections at a specific angular position ( $2\theta$ ) and an angular wavelength ( $\lambda$ ). (Cole, 1970) Diffraction patterns inform on the structure of a sample: the shape and size of the crystal are related to the angular position, whereas the lattice symmetry and electron density are related to the pattern intensity. (Perego, 1998) The crystal size of a sample can be determined following Scherrer's method, from the thickness of the peak. (Langford et al., 1978) Approximately 500 mg of catalyst was put onto an inert sample holder and placed onto a support plane. Analysis was conducted within a range of 10 to 80° using a step size of 0.25° and a counting time of 0.35 s. The XRD identification was conducted using HighScore Plus by comparing the obtained XRD patterns with the corresponding JCPDS (Joint Committee on Powder Diffraction Standards) cards. An example of XRD graph for fresh reduced Ni/Alumina is

presented in Figure 3.3-6. The analysis has been repeated four times here to show its reproducibility.

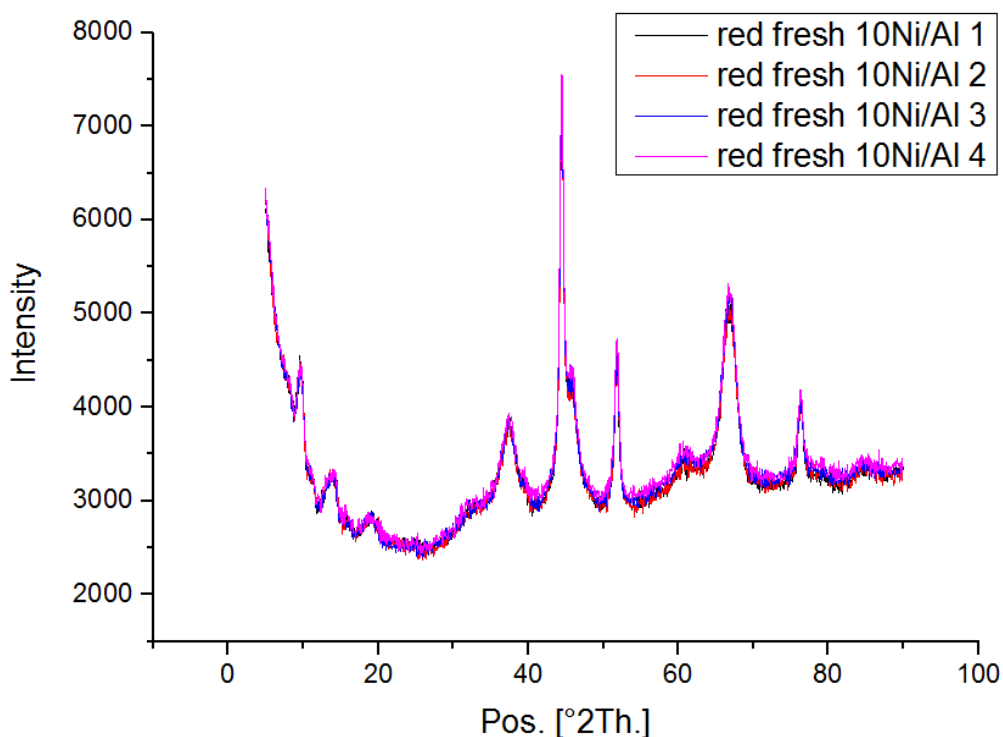


**Figure 3.3-6: Example of XRD graph for fresh reduced Ni/Alumina**

Scherrer's equation is used to identify the crystallite size of a studied catalyst, from its XRD data. For a given angle  $\theta$ , the crystallite size can be described as follow (Borchert et al., 2005):

**Equation 3.3**

$$d(2\theta) = \frac{K\lambda}{w\cos\theta}$$

With  $w$ , the peak width of the associated angle  $\theta$ ;  $d$  the crystallite size;  $K$  the Scherrer constant and  $\lambda$  the wavelength of the radiation.

The constant of proportionality  $K$ , also called the Scherrer constant, was chosen 0.9 as a good estimation when lacking shape information. (Holzwarth et al., 2011)

**3.3.2.5 Scanning Electron microscope (SEM) and Energy Dispersive X-ray (EDX)**

Scanning Electron Microscopy (SEM), operating at 20kV and working distance of 3 mm, can be conducted to characterise and examine the catalyst surface morphology

of the prepared catalysts. Energy Dispersive X-ray (EDX) was conducted in parallel to SEM to indicate the metal content in these catalysts. The analysis consists into X-ray detection by the EDX, X-ray produced when the electron beam interacted with the sample. The Aztec software was used to collect EDX spectra and to determine the sample elemental composition. Each energy peak on the EDX spectra corresponds to a specific element within the sample. The equipment used was Carl Zeiss EVO MA15 (variable pressure W SEM) with Oxford Instruments Aztec Energy EDX system with 80mm X-Max SDD detector. A SEM consists of an electron gun, lenses, detector and a sample chamber.

Before analysis, the catalysts were attached to a sampler holder with carbon conductive paste, then coated with 20 nm of Iridium using an Agar High resolution sputter coater using 99.95% Ir target. This helped to improve conductivity of the samples, minimising charging, and to increase the number of electrons recovered from the sample, enabling a better signal to noise ratio and improve the SEM image quality. The samples were then placed onto the specimen stand inside the sample chamber of the machine and analysed. An example of a SEM-EDX spectrum for barium titanate packing is shown in Figure 3.3-7.

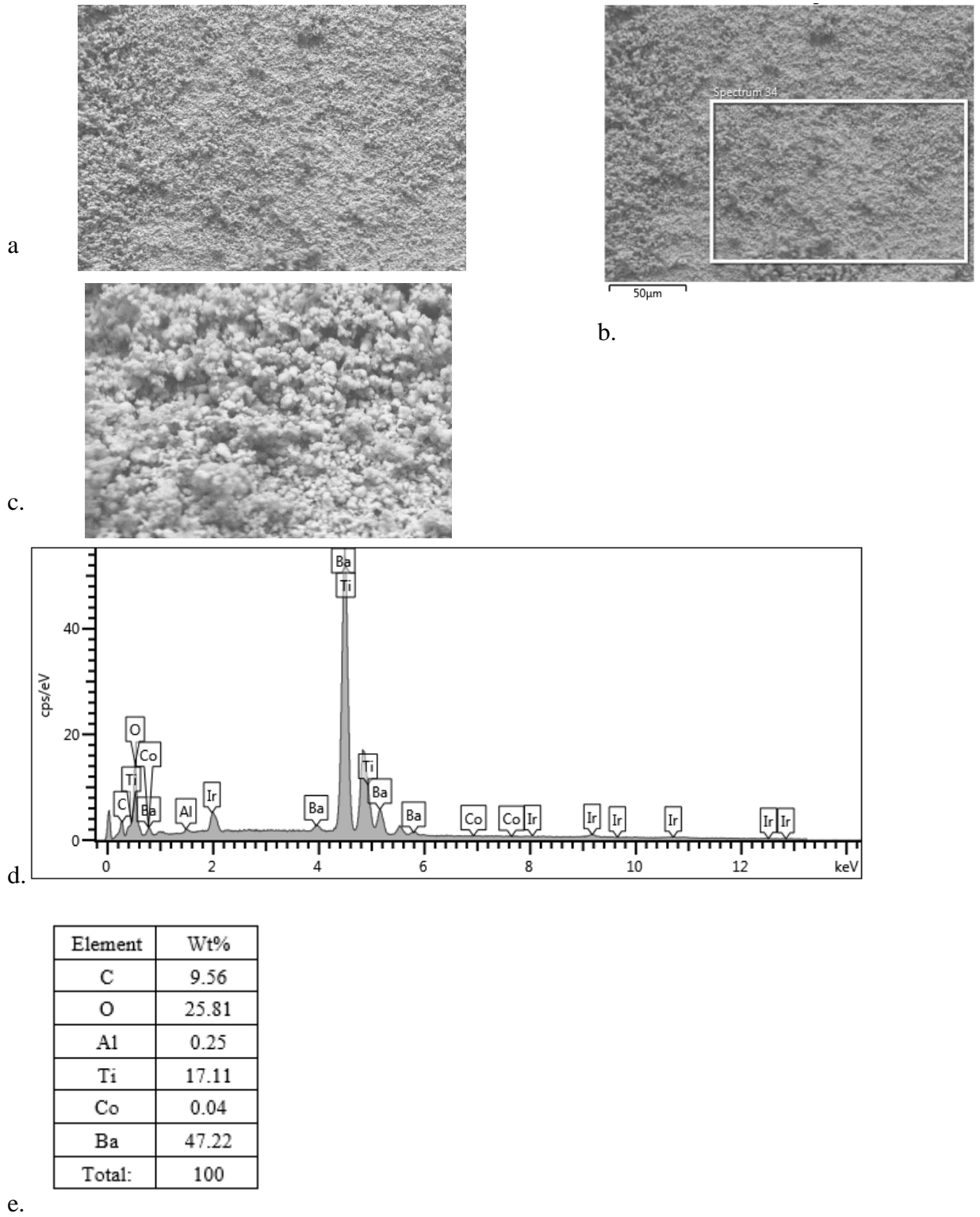


**Figure 3.3-7: An example of a SEM-EDX spectrum for barium titanate a. picture with a magnification of 1.25K, b. picture with a magnification of 5.14K, c. EDX spectrum obtained from the map in d. and e. elemental content (wt.%) of the highlighted zone**

### 3.3.3 Gas product analysis

The exhaust gas composition was analysed by gas chromatography. Using different columns, the concentrations of the permanent gases (hydrogen, carbon monoxide, nitrogen, oxygen), hydrocarbons and carbon dioxide are determined. A Schematic representation of a Gas Chromatography equipment is represented in Figure 3.3-8.

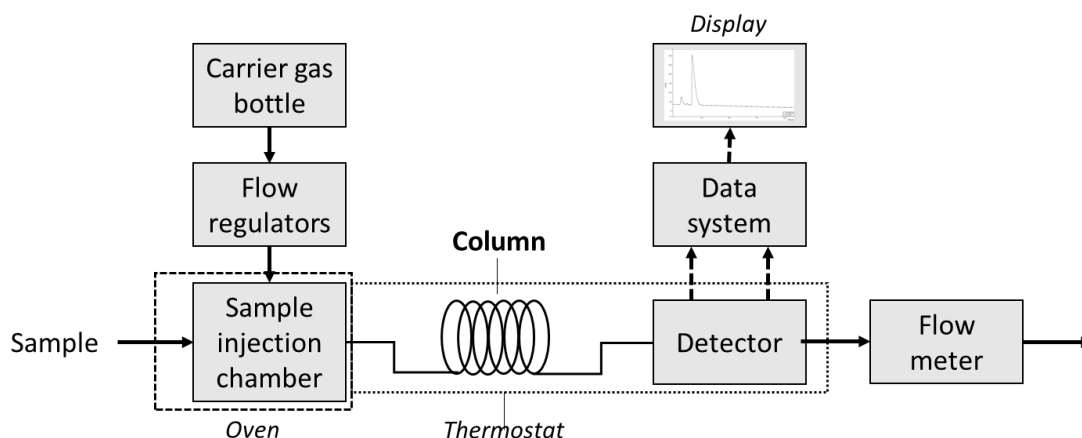


**Figure 3.3-8: Schematic GC system**

#### 3.3.3.1 Permanent Gas Chromatography (GC) analysis

To analyse the permanent gases, a Varian CP-3380 with two packed columns and two thermal conductivity detectors (GC-TCD) were used. Argon was the carrier gas. On one hand, carbon dioxide was analysed using a 2-metre-long and 2-millimetre inner diameter column with HayeSep 60-80 mesh molecular sieve. On the other hand, nitrogen, oxygen, carbon monoxide and hydrogen were analysed using another column with the same characteristics. The procedure was similar for both columns: the detector and injector were held at 120 °C, the column at 30 °C and the filament was at 160 °C for the analysis.

#### 3.3.3.2 Hydrocarbon Gas Chromatography (GC) analysis

The hydrocarbon from C<sub>1</sub> to C<sub>4</sub> were analysed using a Varian CP-3380 gas chromatography with a Flame Ionisation Detector (GC-FID). Nitrogen was the carrier gas. The 2-metre long column made of stainless steel had an inner diameter of 2 millimetre packed with 80-100 mesh HayeSep. The temperature programme started at 60 °C for 3 min and increased at 20 °C per minute up to 120 °C and held for 10 minutes. The detector temperature was 200 °C and the injector at 150 °C.

The chromatographic peaks were integrated thanks to the software Harley Peakmaster Integration. To obtain the compounds proportion in the outlet gas, the GC devices were calibrated before use. To calibrate the machines, standards were injected once a week. Using the calibration data, the gas composition was determined through comparison of each gas area obtained with the calibration gas area followed by the calculation of the percentage of each gas inside the outlet gas. The quantity of nitrogen was not considered as it was the experimental carrier gas and none was produced during the experiment.

### 3.3.3.3 Gas Chromatography (GC) calibration method

Calibration was done once a week to ensure accurate molar concentration calculations. To calibrate the gas chromatography system, precision standard gas mixtures (permanent gas, alkane and alkene mixtures) were used in 20-litre compressed cylinders at 300 psi. The permanent gas mixture contained 1 vol.% of each constituent: oxygen, hydrogen, carbon dioxide and carbon monoxide, overall balanced by nitrogen. The alkane cylinder contained 1 vol.% of methane, ethane, propane and butane gases balanced by nitrogen. The alkene cylinder contained 1 vol.% of ethene, propene, butene and butadiene, also balanced by nitrogen.

### 3.3.3.4 Determination of gas composition

To determine the gas composition in terms of volume, moles and weight, those values were calculated from the values associated to nitrogen as it is a constant and known value. The production of nitrogen during the experiment was assumed inexistent. In order to exclude the air contamination into the syringe during sampling, the data was adjusted. All the calculations were conducted in a spreadsheet.

The percent volume of each compound was calculated through the chromatograph peak area given, after each injection and for each gas, for the gasification experiments and the standards.

#### Equation 3.4

$$\frac{\text{Area of produced gas (A)}}{\text{Area of calibrated gas (A)}} \times \text{Volume percent in calibration mixture of gas A} = \text{Volume percent of gas A in pyrolysis gas}$$

Three injections minimum are taken and the average volume percent of gas across the injections is considered. These volume concentrations are then adjusted so that the total concentration is equal to hundred percent.

The molar concentration for each component was calculated as follow, assuming the molar volume at standard pressure and temperature (1 atm, 273°C) at 22.4 L/mol:

**Equation 3.5**

$$\text{Mole of gas (A): } n_A = \frac{\text{Vol}_A \times Q \times t}{22400}$$

With  $Q$   $N_2$  flowrate in L/m<sup>3</sup>,  $t$  gas collection time in minutes and  $\text{Vol}_A$ : the volume fraction of gas (A)

From the gas quantity, the total weight of gas produced could be obtained by:

**Equation 3.6**

$$\text{Mass of gas (A): } m_A = \frac{n_A}{M_A}$$

**Equation 3.7**

$$\text{Total mass of gas produced} = \sum_i m_i$$

The volume and gas yield percent of each component ( $\text{Vol}_A\%$  and  $Y_A$  respectively) could then be calculated as follow:

**Equation 3.8**

$$\text{Vol}_A\% = \frac{\text{Vol}_A}{\sum_i \text{Vol}_i - \text{Vol}_{N_2}} \times 100$$

**Equation 3.9**

$$Y_A = \frac{m_A}{m_{feed}} \times 100$$

With  $m_{feed}$  the initial mass of biomass introduced.

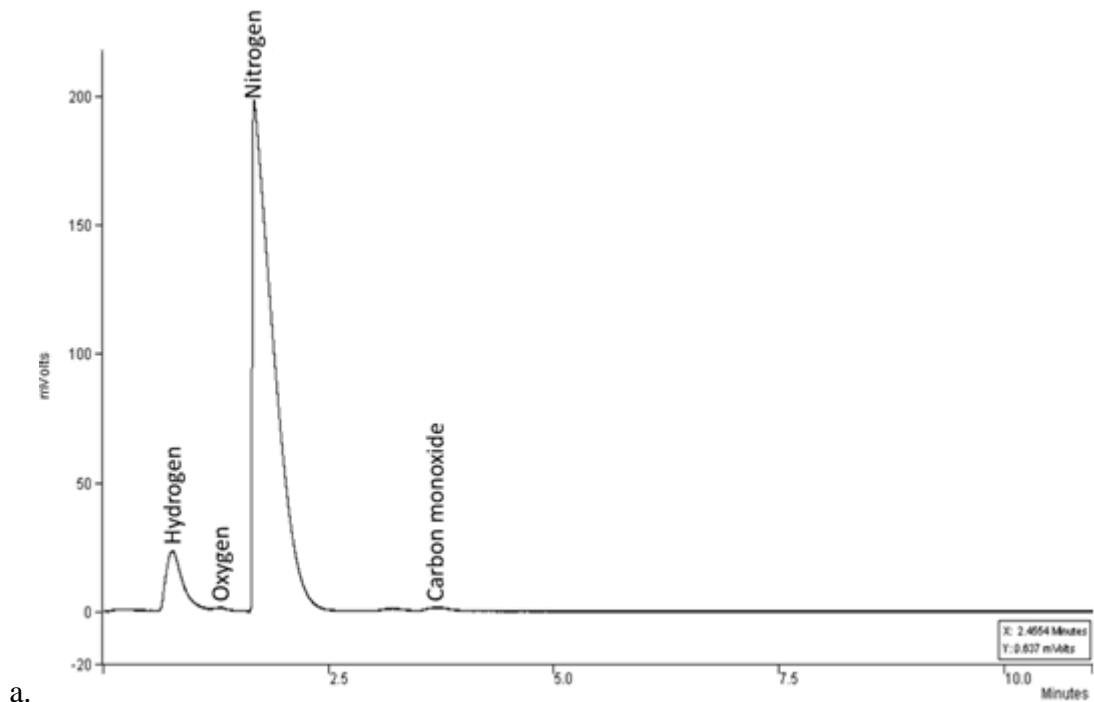
Finally, the quantity of each component per gram of feedstock introduced,  $y_A$ , was calculated as follow:

**Equation 3.10**

$$y_A = \frac{n_A}{m_{feed}}$$

### 3.3.3.5 Reproducibility of gas analysis

To evaluate the reproducibility of the procedure for gas analysis, injections were repeated using the gas sample collected in the same gas bag. Sample injections had each a volume of 1 mm<sup>3</sup>. An example of the obtained chromatograms, with voltage signals as a function of time, can be found in Figure 3.3-9. As shown in the examples, the detector transmitted voltage signal to the digital integrator, which converted the voltage value as into area values used to calculate the volume and molar percentage of each gas, as described in the previous section 3.3.3.4. These obtained area values are labelled as “area of produced gas” in Equation 3.4. The reproducibility of the analysis can be found in Table 3.3-1. The area of produced gas is compared to the area of the calibrated gas to determine the volume and molar percent of said gas in the product gas, following the method indicated in the previous section 3.3.3.4. The repeatability of the experiment could be estimated via the relative standard deviation. An excellent reproducibility with minimal errors is indicated by a relative standard deviation of less than 10%. The relative standard deviation was in the range of showing excellent reproducibility of this gas analysis method. However, it is worth noting the high relative standard deviation for oxygen, around 17 %. This was mainly due to possible air contamination when moving the syringe from the gas bag to the GC instruments.



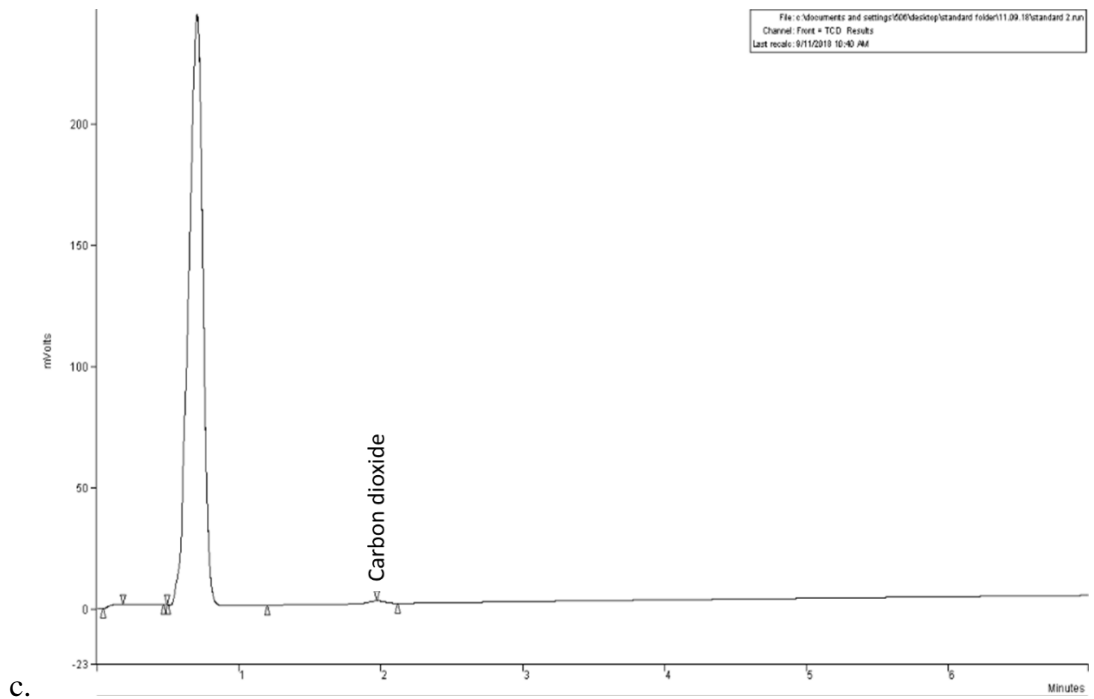
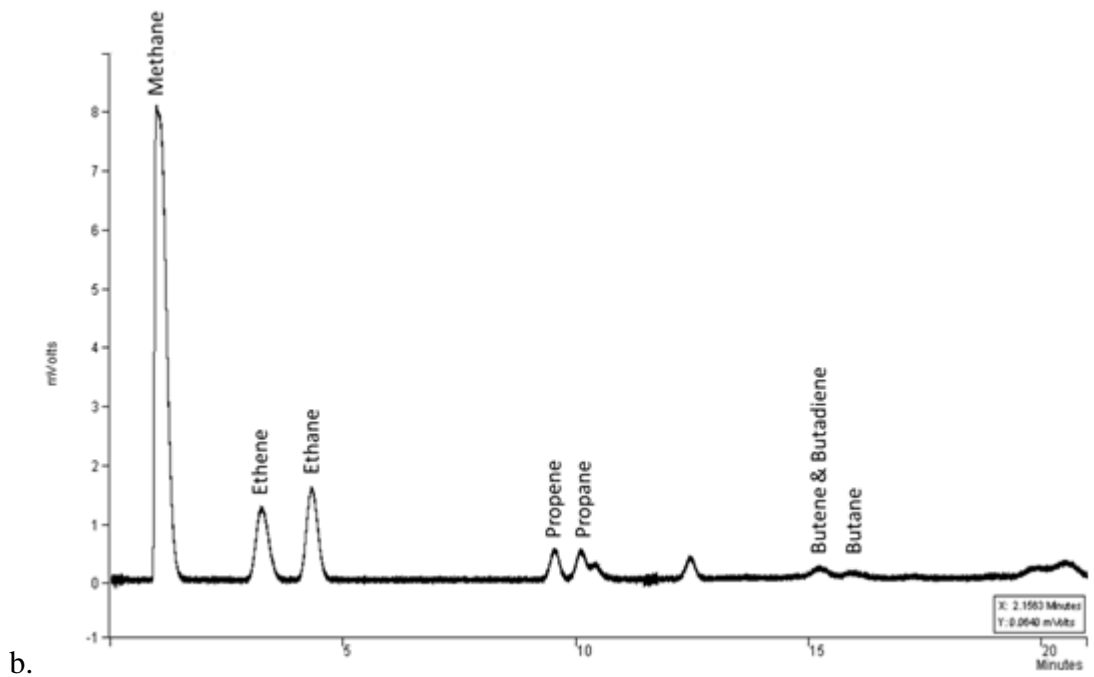


**Figure 3.3-9: Example of obtained chromatograms using gas chromatography for a. permanent gases, b. hydrocarbon gases and c. carbon dioxide**

**Table 3.3-1: Reproducibility of GC analysis**

Gas	Peak area of calibrated gas	Peak Area sample 1	Concentration (vol%)	Peak Area sample 2	Concentration (vol%)	Peak Area sample 3	Concentration (vol%)	Average concentration	Standard Deviation	Relative Standard Deviation
CO	48619	60186	1.238	64145	1.319	58993	1.213	1.257	0.055	4.413
H <sub>2</sub>	583109	774549	1.328	774651	1.328	739802	1.269	1.309	0.034	2.633
O <sub>2</sub>	70279	38478	0.548	27973	0.398	29220	0.416	0.454	0.082	17.996
N <sub>2</sub>	49353.5	4641163	94.039	4895464	99.192	4671383	94.651	95.961	2.815	2.933
CO <sub>2</sub>	12239	15681	1.281	15809	1.292	15627	1.277	1.283	0.008	0.595
CH <sub>4</sub>	781252	320560	0.410	330567	0.423	322618	0.413	0.415	0.007	1.628
C <sub>2</sub> H <sub>4</sub>	1524560	13622	0.009	13884	0.009	13530	0.009	0.009	0.000	1.343
C <sub>2</sub> H <sub>6</sub>	1490238	52523	0.035	53814	0.036	52911	0.036	0.036	0.000	1.628
C <sub>3</sub> H <sub>6</sub>	2211346	7399	0.003	8385	0.004	9032	0.004	0.004	0.000	1.343
C <sub>3</sub> H <sub>8</sub>	2233568	27649	0.012	29292	0.013	29913	0.013	0.013	0.001	1.248
C <sub>4</sub> H <sub>8</sub>	2742750.5	3651	0.001	2625	0.001	3864	0.001	0.001	0.000	9.941
C <sub>4</sub> H <sub>10</sub>	3012824	4756	0.002	3568	0.001	4419	0.001	0.001	0.000	4.041

### 3.3.4 Oil sample characterisation

To characterise the liquid fraction obtained as a product of experiments, the fraction was analysed using different analytic procedures described in the following section.

#### 3.3.4.1 Water content analysis by using Karl-Fischer Titration

The water content from the oil produced was first determined by using dehydration technique represented in Figure 3.3-10.a. The Metrohm apparatus 890 Titrande with the Karl Fischer Titration determination method running through the software tiamo™ 2.3 gave directly the water in weight percent inside the produced liquid. Represented in Figure 3.3-10.b, about 12 g of sodium sulphate was used to absorb the water in the produced liquid, using a filtration method.

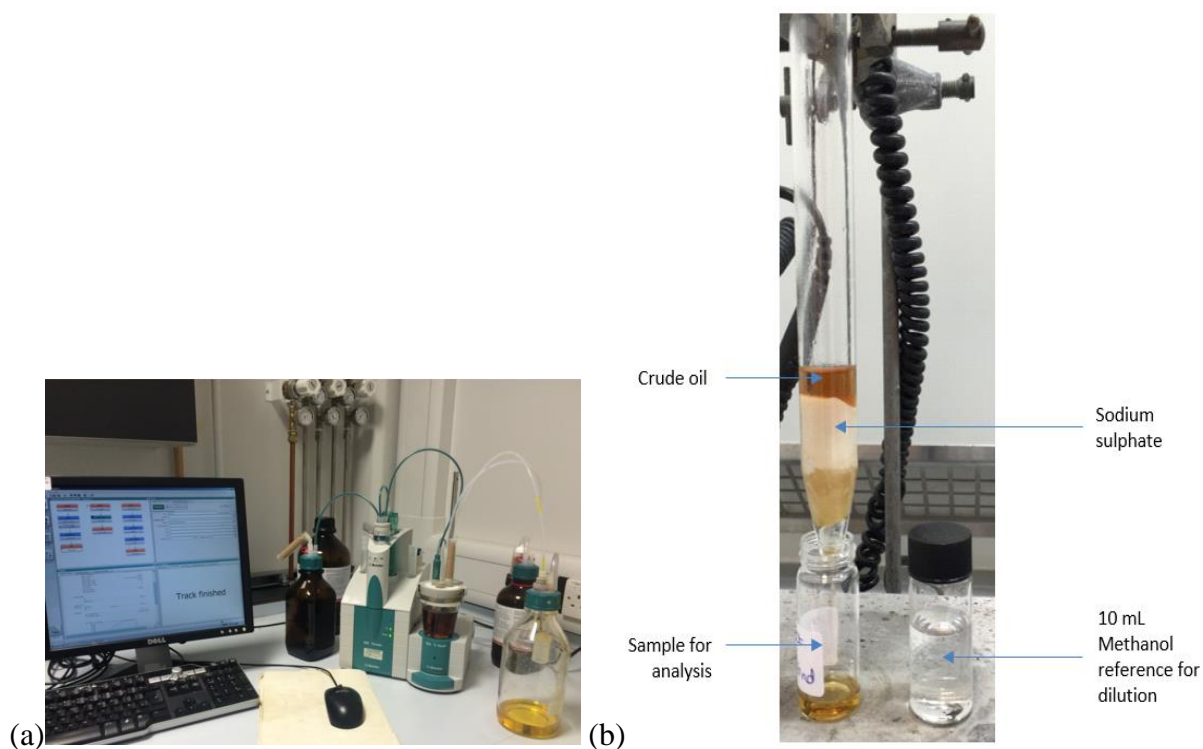


**Figure 3.3-10: Water content and dehydration of the liquid produced. (a) Measurement of the water content. (b) Dehydration of the liquid produced.**

#### 3.3.4.2 Gas Chromatography/Mass Spectroscopy (GC-MS)

The oil produced was analysed using a gas chromatography system coupled with a mass spectrometry detector (GC-MS), represented in Figure 3.3-11. The equipment

used were a Hewlett Packard 5280 gas chromatograph coupled with a HP 5271 ion trap detector and a Perkin Elmer Clarus 560 gas chromatograph coupled with a sealed long-life photomultiplier and a single Quadrupole as analyser. The chromatographic column characteristics are 30-metre long and 0.25-millimetre internal diameter Restek RTX-5MS column fitted with fused silica 95% dimethyl polysiloxane and 5% diphenyl of 25  $\mu\text{m}$  film thickness. Helium was the gas carrier used. The sample was placed directly on the sample tray for automatic dilution before analysis. The same apparatus and method were used for tar samples through SPA method, although using a different solvent. The injection temperature of the sample was 290  $^{\circ}\text{C}$ . The oven programme temperature was kept at 40 $^{\circ}\text{C}$  for 5 minutes, then heated up to 80  $^{\circ}\text{C}$  with a heating rate of 5  $^{\circ}\text{C min}^{-1}$ , heated up to 140  $^{\circ}\text{C}$  with a heating rate of 3  $^{\circ}\text{C}\cdot\text{min}^{-1}$  and finally heated up to 280  $^{\circ}\text{C}$  with a heating rate of 5  $^{\circ}\text{C}\cdot\text{min}^{-1}$  and held for 2 minutes. The transfer line between the GC and the MS equipment was kept at 280  $^{\circ}\text{C}$ , and the ion trap was maintained at 200  $^{\circ}\text{C}$ .

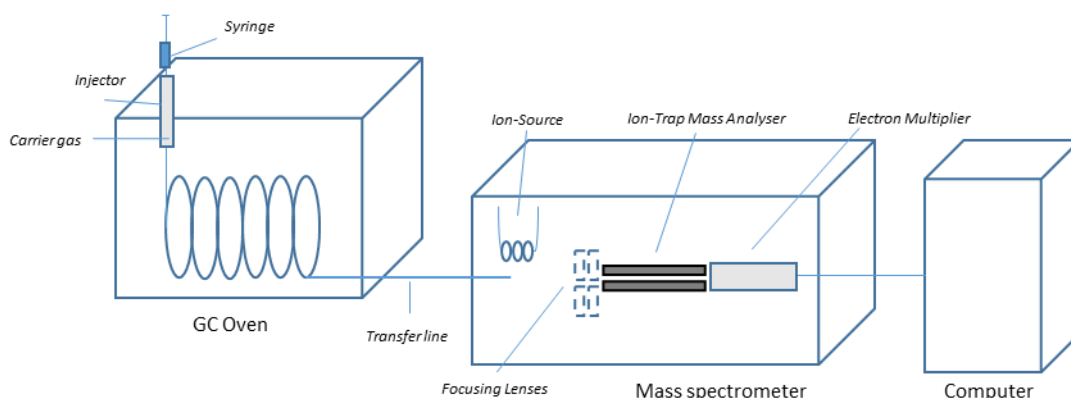
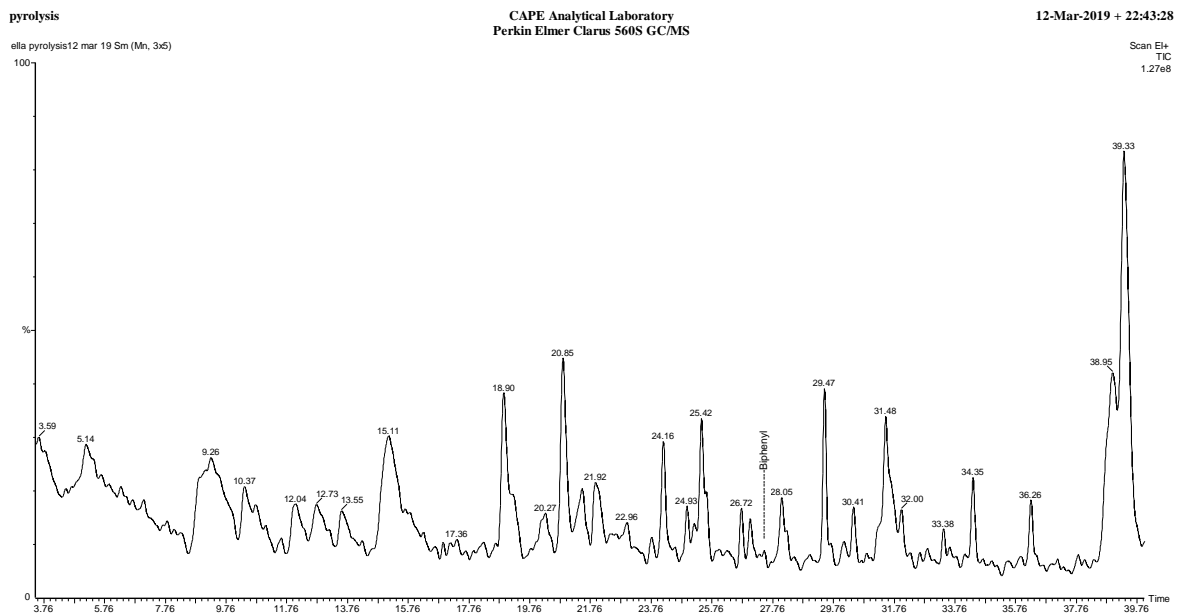


**Figure 3.3-11: Schematic diagram of Gas Chromatography-Mass Spectroscopy (GC-MS) equipment**

The peaks were analysed and attributed to a compound using the GC-MS software. The compounds were assigned looking at the probability and the closest mass spectrometer. Others, part of the most common tar compounds, have been calibrated and their concentration in the mixture can be obtained. An example of a chromatogram obtained via GC-MS is presented in Figure 3.3-12.

a.



b.

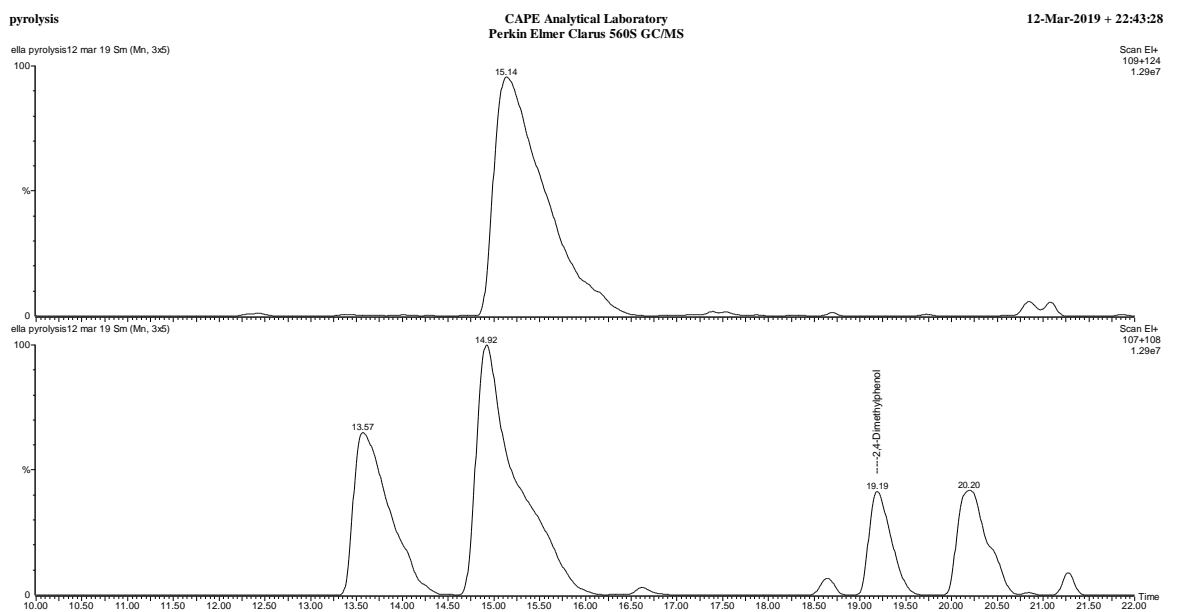


**Figure 3.3-12: Example of a. a full chromatogram and b. a zoom-in view of said chromatogram**

### 3.3.4.3 Calibration of Gas Chromatography/Mass Spectroscopy (GC-MS)

The GC-MS equipment was calibrated for aromatics and oxygenated compounds in DCM (Dichloromethane) and in Methanol for both the liquid and tar sampling analysis. Standard solutions with a mixture of different oxygenated and aromatic compounds were created, based on the most common tar compounds reported in the literature for tar/oil samples from thermal processing of solid wastes. (Kinoshita et al., 1994; Li et al., 2009) About 100 mg of each standard compound was weighted and dissolved into 10 mL of desired solvent, obtaining a concentration of 10,000 ppm for each compound. In a 50 mL flask for each standard mixture, 0.5 mL of each compound was added and dissolved into a 50 mL of desired solvent to finally get a final concentration of 100 ppm. Further dilutions were obtained using the general equation for dilution, presented below, to make 20, 40, 80 and 100 ppm solutions of each mixture in both solvents.

#### Equation 3.11

$$C_1 \times V_1 = C_2 \times V_2$$

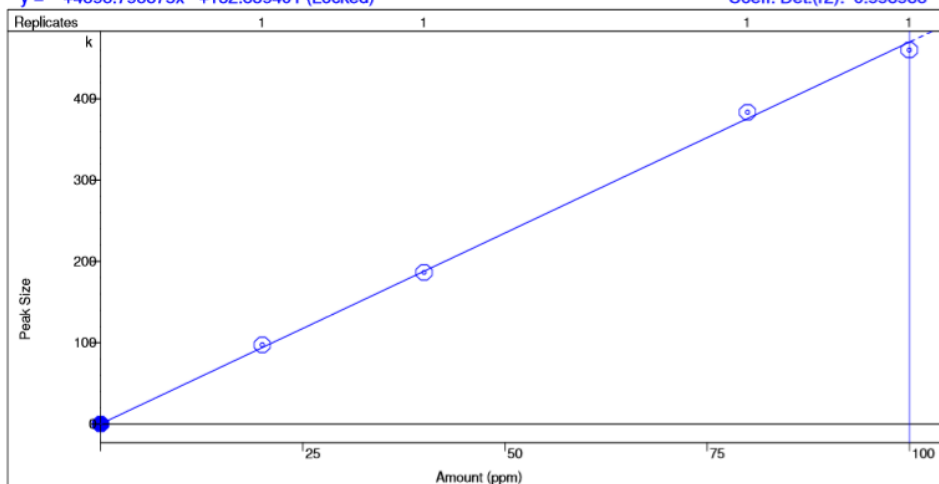
With  $C_1$  the original concentration,  $C_2$  the desired concentration,  $V_2$  the final desired volume and  $V_1$  the unknown volume. The list of the selected standard compounds can be found in Table 3.3-2.

For each compound, quantum ions were determined, and a calibration line could be drawn on a peak area against concentration graph. Thus, for any of the selected tar compounds, the quantity of this compound in the sample can be determined thanks to this calibration curve. Example of calibration curves for Toluene, o-Xylene and Naphthalene are presented in Figure 3.3-13.

**Table 3.3-2: List of selected compounds used as standards for GC-MS calibration**

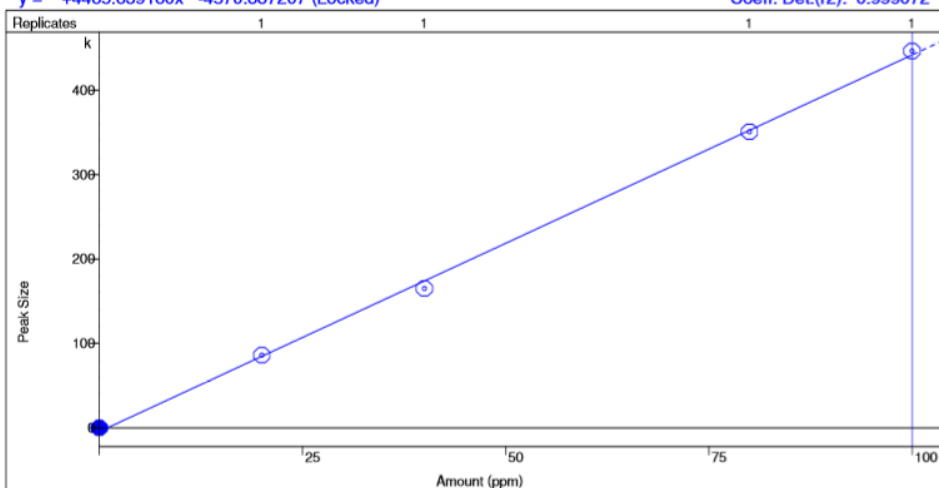
	<b>Oxygenates Calibration</b>	<b>bp</b>	<b>Aromatics Calibration</b>	<b>bp</b>
<b>1</b>	Furfural	161.7	Benzene	80.1
<b>2</b>	Anisole	153.8	Cyclohexane	80.7
<b>3</b>	Solketal	82.5	Toluene	110.6
<b>4</b>	Phenol	181.7	Ethyl Benzene	136.0
<b>5</b>	p-cresol	201.8	p-Xylene	138.4
<b>6</b>	o-cresol	191	m-Xylene	139.0
<b>7</b>	m-cresol	203	o-Xylene	144.0
<b>8</b>	Guaiacol	205	Limonene	176.0
<b>9</b>	2,6-Xylenol	203	Styrene	145.0
<b>10</b>	3,5-dimethylanisole	193	p-methyl styrene	172.5
<b>11</b>	2,3-dimethylanisole	195	1,2-dihydro naphthalene	204.9
<b>12</b>	3,4-dimethylanisole	200.5	Naphthalene	218.0
<b>13</b>	2,4-dimethylphenol	211.5	2-methyl Naphthalene	241.5
<b>14</b>	4-ethylphenol	218.5	2-Ethyl Naphthalene	251.5
<b>15</b>	2,4,6-trimethylphenol	220	2,6-dimethyl Naphthalene	262.0
<b>16</b>	4-isopropylphenol	212.5	1,4-dimethyl Naphthalene	263.0
<b>17</b>	2-methoxy-4-propylphenol	125.5	Acenaphthene	279.0
<b>18</b>	Biphenyl	255	o-terphenyl	389.0
<b>19</b>	Furoin	310	Phenanthrene	340.0
<b>20</b>	3-Methyl pyrazole	204	Pyrene	404.0
<b>21</b>			m-terphenyl	389.0
<b>22</b>			p-terphenyl	389.0
<b>23</b>			1,3,5-triphenylbenzene	460.0
<b>24</b>			Indene	182.4
<b>25</b>			Acenaphthylene	280
<b>26</b>			Dibenzofuran	285
<b>27</b>			Fluorene	295
<b>28</b>			Xanthene	310
<b>29</b>			Fluoranthene	375

Curve Fit: Linear, Origin: Include, Weight: 1/X  
 $y = +4696.796875x + 132.839401$  (Locked)      Resp. Fact. RSD: 2.598%  
 Coeff. Det.(r2): 0.998986



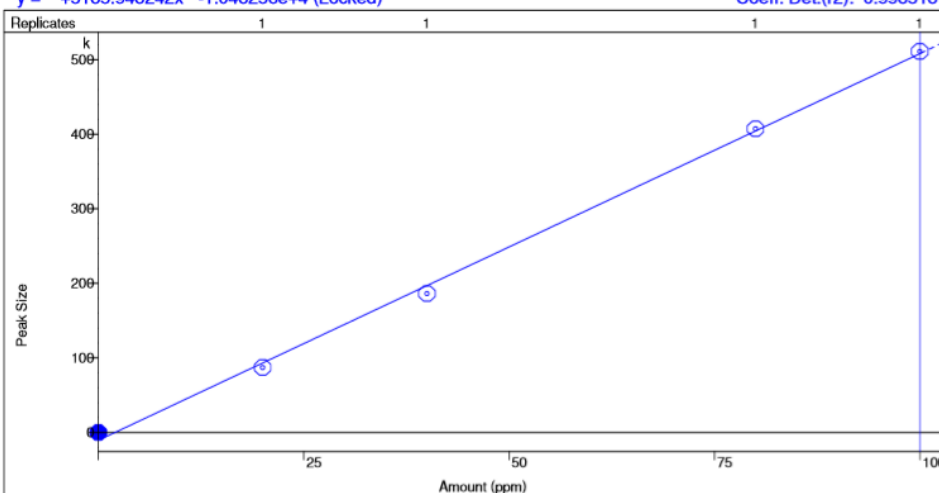
a.

Curve Fit: Linear, Origin: Include, Weight: 1/n  
 $y = +4465.639160x - 4570.887207$  (Locked)      Resp. Fact. RSD: 3.349%  
 Coeff. Det.(r2): 0.999072



b.

Curve Fit: Linear, Origin: Include, Weight: 1/n  
 $y = +5185.948242x - 1.048256e+4$  (Locked)      Resp. Fact. RSD: 7.517%  
 Coeff. Det.(r2): 0.998518



c.

**Figure 3.3-13: Calibration curves for example compounds a. Toluene b. o-Xylene c. Naphthalene**

### 3.3.4.4 Determination of tar content from Gas Chromatography-Mass Spectroscopy (GC-MS)

From those selected compounds concentrations [A] in ppm, the total tar content, [tar], can be calculated as follow: from the concentration in the GC sample, followed by the concentration in the liquid recovered from each experiment to finally obtained the concentration of tar per m<sup>3</sup>.

#### Equation 3.12

$$[tar]_{GCsample} = \sum_{aromaticcompounds} [A] + \sum_{oxygenatedcompounds} [A] \text{ (ppm)}$$

#### Equation 3.13

$$m(tar)_{10\text{ mLofMeOH}} = [tar]_{GCsample} \times \frac{0.010\text{ L}}{1000}$$

With 1 g/L = 1000 ppm

#### Equation 3.14

$$[tar]_{total} = \frac{m(tar)_{10\text{ mLofMeOH}}}{Q \times t} \text{ (g.m}^{-3}\text{)}$$

With Q:  $N_2$  flowrate in m<sup>3</sup>/min

t: gas collection time in minutes

### 3.3.4.5 Size Exclusion Chromatography (SEC)

To further analyse the produced oil, size exclusion chromatography (SEC, shown in Figure 3.3-14) was used to determine the molecular mass distribution of the condensed hydrocarbon tar. The system incorporated a 300 mm length and 7.5 mm diameter column with a Polymer Laboratories 3  $\mu$ m GPC/SEC 100A type packing, which was maintained at 30 °C. Tetrahydrofuran (THF) was used as a solvent for the mobile phase with a flow rate of 1 mL min<sup>-1</sup>. The calibration system used was based on polystyrene standards in the Mw range of 100-9000 Da. The detector measuring the elution of all compounds was a refractive index detector from Perkin Elmer. The output from the detector was given in millivolts and transmitted to a software, Total Chrom Navigator. The Mw distribution was determined as a molecular weight average (Mw). The samples for analysis were prepared using approximately 0.25 mL of the condensed hydrocarbon liquid with a dilution of 1/100 in the solvent, THF.



**Figure 3.3-14: Size Exclusion Chromatography (SEC) equipment**

An example of a Molecular weight (Mw) range obtained using the SEC for a pyrolysis experiment is represented in Figure 3.3-15-15.

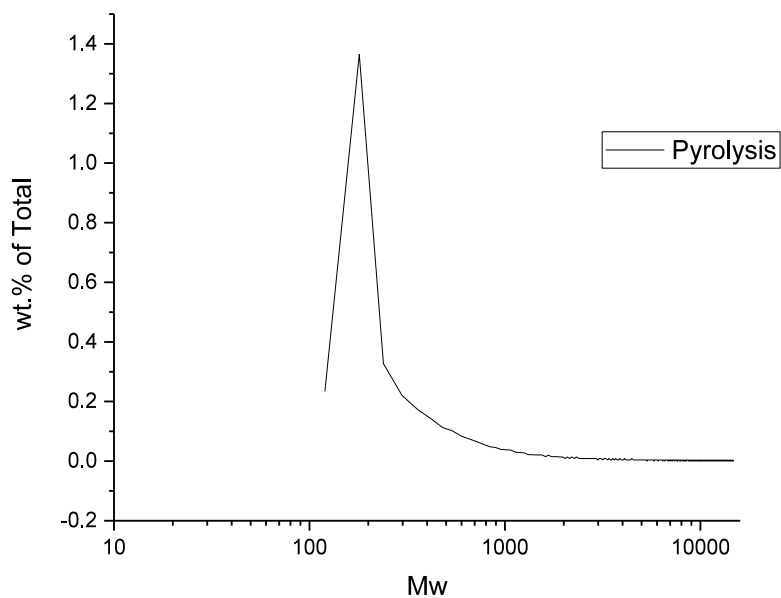


**Figure 3.3-15: Example of a Molecular weight (Mw) range obtained using the SEC for a pyrolysis experiment**

## **Chapter 4: Pyrolysis of different feedstocks.**

This chapter consists of two sections, focusing on the products resulting from biomass pyrolysis, liquid and gaseous, and their analyses. Four biomasses – wood pellet, corn stalk, peanut shell and coconut shell described in Chapter 3, section 3.1.1.1 – were studied in this chapter. The experiments were conducted in a fixed bed pyrolysis reactor as presented in section 3.2.1. The different sections of this chapter are described below.

Section 4.1 focuses on the gas composition produced from the pyrolysis of these feedstocks. The product gas yield and composition from pyrolysis of wood pellet, corn stalk, peanut shell and coconut shell were compared to one another and to the literature. This will enable to determine suitable biomasses to use in the pyrolysis-plasma-catalysis systems to produce high quality hydrogen-rich syngas.

Section 4.2 describes the study of tar composition from tar sample collected by Solid Phase Adsorption (SPA) method for the four different biomasses. The tar composition obtained from the SPA methods was analysed and discussed in this section in order to identify which high molecular weight hydrocarbons are produced during pyrolysis by these different biomasses.

### **4.1 Gas composition**

The results in terms of product yield and gas composition and yield, in relation to the different feedstocks, are represented in Table 4.1-1. More gas products were obtained from corn stalk compared to other feedstocks, producing about 30 wt.% of gas, compared to other biomasses, which all produced similar weight of product gas – around 17 wt.%. Depending on the nature of the different feedstock, the quantity of char was dependent on the feedstock nature, being the lowest for wood pellet with 21 wt.%, and the highest for peanut shell, with 29 wt.% of char. This is most probably due to a higher lignin content in biomasses, which might lead to higher char yields and lower bio-oil yields for corn stalk and peanut shell, compared to wood pellets and coconut shell (Mohan et al., 2006; Gani et al., 2007).

**Table 4.1-1: General product composition after pyrolysis at T=600 °C**

Biomass	Wood pellet	Corn stalk	Peanut shell	Coconut shell	% error
Gas (wt.%)	16	31	17	17	6.8
Liquid (wt.%)	60	47	49	56	0
Char (wt.%)	21	27	29	25	0
Mass Balance (%)	97.31	104.43	95.19	97.98	1.1
Composition in mmol/g of feedstock					
CO	1.69	2.14	1.61	1.39	1.6
H <sub>2</sub>	0.49	0.41	0.60	0.61	9.1
CO <sub>2</sub>	1.69	4.83	2.17	2.21	1.4
CH <sub>4</sub>	0.82	0.82	0.74	0.68	0

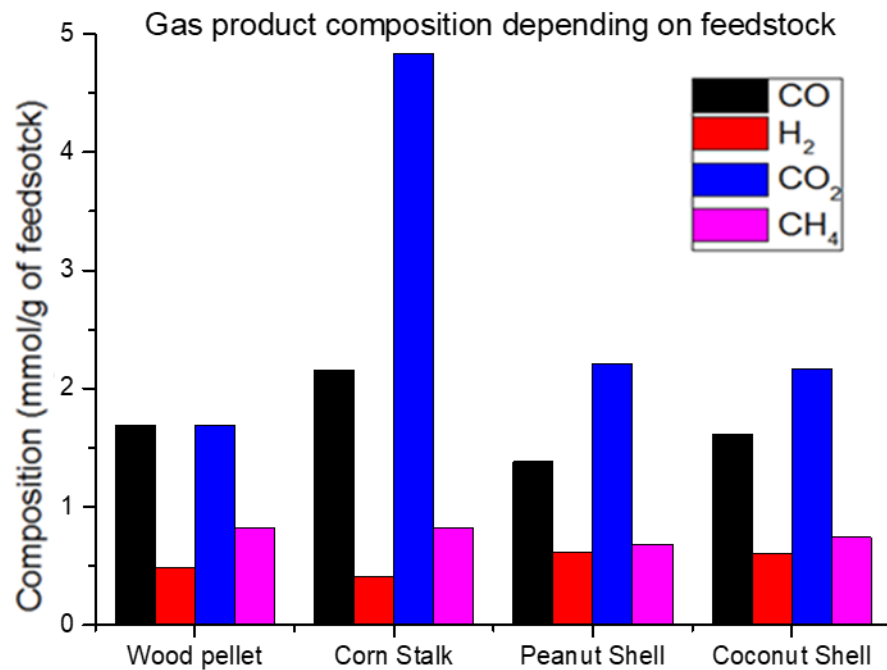


**Figure 4.1-1: Gas product composition after pyrolysis experiment for different feedstocks**

The product gas composition for the different feedstocks are represented in Figure 4.1-1. For most feedstock, the production of carbon dioxide is higher than any other gas, ranging from  $4.83 \text{ mmol.g}^{-1}_{\text{biomass}}$  for corn stalk, around  $2.2 \text{ mmol.g}^{-1}_{\text{biomass}}$  for the biomass shells, and  $1.69 \text{ mmol.g}^{-1}_{\text{biomass}}$  for wood pellets. The production of methane and hydrogen were similar between biomasses, at around  $0.75 \text{ mmol.g}^{-1}_{\text{biomass}}$  and  $0.5 \text{ mmol.g}^{-1}_{\text{biomass}}$  respectively. The product gas from corn stalk resulted in a very high production yield of carbon dioxide, which made it unlikely to be used as a preferred biomass due to its high content of carbon dioxide. The two highest syngas productions were obtained for wood pellets and corn stalk, respectively with  $2.18 \text{ mmol.g}^{-1}_{\text{biomass}}$  and  $2.55 \text{ mmol.g}^{-1}_{\text{biomass}}$ .

However, when observing the proportion of hydrogen within the syngas, wood pellet resulted in a higher hydrogen content, with approximately 22% of syngas, compared to corn stalk, with a hydrogen content of about 16% of syngas. Thus, the most interesting feedstock for this study is wood pellet as the proportion of hydrogen and the proportion of syngas produced from the total produced gas was higher than for corn stalk. Its high heating value presented in the previous section, 3.1.1.1, in addition to the high syngas production makes wood pellet a good candidate as biomass for energy purpose.

In the case of the pyrolysis of coconut shell at different pyrolysis temperatures, Wang et al. (2018) demonstrated that the production of CO and CO<sub>2</sub> followed similar patterns, with the release of CO<sub>2</sub> higher than the release of CO. Methane production was maximum around 550 °C. The high methane content could be attributed to the higher content of aromatic ring and O-CH<sub>3</sub> functional groups in biomasses. The production of CO and CO<sub>2</sub> was attributed to the content of higher carbonyl and carboxyl groups respectively (Wang et al., 2018). This has been demonstrated before for carbon monoxide, which may be generated during the decarbonylation process through the aromatic condensation of lignin (Fu et al., 2009). Thus, depending on the biomass composition and chemical group content, different gas yield could be produced in our study.

Yu et al. (2016) studied the pyrolysis of corn stalk and rice husk in a auger pyrolysis reactor for different temperatures, from 350 °C to 600 °C. They demonstrated that for an increasing temperature, molar fractions of combustible gases such as CO and CH<sub>4</sub>

increased, whereas the molar fraction of CO<sub>2</sub> decreased. The release of light hydrocarbons was associated with the cracking and reforming of heavier hydrocarbons present in the pyrolysis vapours. For pyrolysis temperatures higher than 500°C, H<sub>2</sub> became detectable and increased with increasing temperature, leading to an increase in heating value of the product gas. Hydrogen could be produced by hydrocarbon cracking at higher temperatures (Yu et al., 2016). This can explain the high content of combustible gases and the low content of hydrogen within the product gas obtained from pyrolysis of corn stalk.

## **4.2 Solid Phase Adsorption (SPA)tar sampling method results**

The SPA method was used to determine the quantity of tar compounds present in the gas outlet at three different times during the experiment: the first sample when the pyrolysis started (around 400 °C), the second sample when the pyrolysis reactor reached 600 °C, and the third sample when turning off the pyrolysis reactor. The results are presented in Table 4.2-1. Most tar compounds reported by GC-MS analysis for the different biomasses were straight chain oxygenated compounds, such as 2-hexyl-1-octanol, and oxygenated aromatic compounds, with one aromatic ring such as methyl-phenols.

Different feedstocks generated different tar compounds: tar compounds from wood, which presented a high carbon content, were a mix straight chain oxygenated compounds and aromatic compounds, with an increasing proportion of chain compounds by the end of the pyrolysis. Corn stalk derived tars were mainly oxygenated aromatics, with an increase of their proportions as the reaction time increased. This was not a surprise considering the main component of corn stalk was oxygen as presented in Chapter 3, in the characterisation section 3.1.1.1. Tar compounds from peanut shell were mainly aromatics, as were these derived from coconut shell.

The different SPA samples for a given feedstock resulted in different chemical composition trends. For wood pellets, the second SPA sample, when the reactor temperature reached 600 °C, was the sample with the highest content of aromatic compounds, about 66%, including one ring oxygenated and two ring aromatic compounds. A similar outcome could be observed for peanut shell, with about 90%

of aromatic compounds within the SPA sample. Other SPA samples from the pyrolysis of wood pellets and peanut shell presented a high proportion of alkyl compounds, up to 60% for woody biomass after holding the reactor temperature at 600 °C for 10 minutes. SPA samples obtained from corn stalk followed the following trend: as the reactor temperature increased and the longer the highest temperature was maintained, the more aromatic compounds were detected, with about 90% of oxygenated aromatic compounds and as low as 9% of alkyl compounds. The samples from pyrolysis of coconut shell on the other hand showed an inverse trend: the aromatic content was the lowest for the third SPA sample, after holding at 600 °C. However, all SPA samples for coconut shell were shown to have high content of aromatic and oxygenated aromatic compounds, over 82% for both contents.

Optimum pyrolysis temperature from different studies resulted into an optimal range of pyrolysis temperature, between 500 °C and 600 °C, for maximising the bio-oil yield. (Uzun et al., 2009; Guo et al., 2015) For coconut shell, this maximum has been demonstrated at 575 °C (Rout et al., 2016). Furthermore, Elliott described the relationship between the temperature and the chemical compounds presents within the bio-oil from biomass pyrolysis. With an increasing temperature, alkyl chemical groups cleaved from aromatics. Aromatics condensed into polycyclic aromatic hydrocarbons (PAHs) at higher temperatures (Elliott, 1986). In the temperature range considered in this study through SPA samples, the relationship is described as the following: at 400 °C, the liquid fraction is a mixture of oxygenates; at 500 °C, it is mainly composed of phenolic ethers; and at 600 °C, it is mostly constituted of alkyl phenolic compounds. (Elliott, 1986) This breakdown and evolution could be observed for all biomasses across the three SPA samples.

According to Fardhyanti, pyrolysis of coconut shell at low temperature, between 300 °C and 350 °C, resulted in a high content of phenolic compounds within the product bio-oil (Fardhyanti et al., 2017). This has also been demonstrated for higher pyrolysis temperature by Rout et al. For a pyrolysis temperature of 575 °C, the aliphatic and phenolic content within a bio-oil were about 6% and 69% respectively (Rout et al., 2016). Guo et al. (2015) conducted a series of experiments analysing the content of the bio-oil, depending on the pyrolysis temperature of corn stalk. Higher pyrolysis temperature leads to more bio-oil cracking, resulting in higher syngas yield and higher

bio-oil yield. The oxygen content of the bio-oil was lower than the one of the original feedstock. With increased pyrolysis temperature, the heavy oil content (asphaltene) in the product oil was increased, most likely due to higher energy to pyrolyse macromolecules from the biomass feedstock. (Guo et al., 2015) This could explain the increase of the proportion of aromatic compounds within the SPA sample, as the temperature at which the sample was taken, increased.

**Table 4.2-1: Tar analysis via SPA method**

Experiment Sample number (1-start of pyrolysis stage, 2- temperature reaching 600 °C, 3- after holding 600 °C for 10 min)		Wood pellet (% of peak area)			Corn stalk (% of peak area)			Peanut shell (% of peak area)			Coconut shell (% of peak area)		
		1	2	3	1	2	3	1	2	3	1	2	3
Oxygenated compounds	chains	56.42	33.48	60.02	30.40	16.51	6.65	24.24	8.81	42.94	3.86	3.62	17.56
	1 ring	43.59	62.85	39.98	55.40	72.57	87.53	75.66	83.75	55.76	95.16	93.79	81.86
	2 rings	-	-	-	10.27	2.38	2.03	-	-	-	0.27	-	-
	3 rings	-	-	-	-	-	-	-	-	-	-	1.17	-
Non-oxygenated compounds	chains	-	-	-	-	3.41	1.96	-	-	-	0.71	-	-
	1 ring	-	-	-	0.21	4.72	0.12	0.10	4.70	-	-	1.23	-
	2 rings	-	3.67	-	3.71	0.40	1.64	-	2.50	1.30	-	0.19	0.58
	3 rings	-	-	-	-	-	0.07	-	0.24	-	-	-	-
Total peak area		241701	673511	304877	353507	1372240	2074585	1838175	258824	237242	14887269	4119044	356907

### 4.3 Summary

In conclusion, the pyrolysis of different feedstocks was studied in this section to determine suitable biomasses to use in the pyrolysis-plasma-catalysis systems to produce high quality hydrogen-rich syngas, as well as to identify which high molecular weight hydrocarbons are produced during pyrolysis by these different biomasses. The gas products and the tar content using SPA method were analysed for four feedstocks: wood pellet, corn stalk, peanut shell and coconut shell. Corn stalk led to a higher production of gas in wt.%, a higher production of carbon dioxide, syngas and carbon monoxide. However, wood pellet presented the proportion of syngas produced from the total gas production was the highest, due to a smaller carbon dioxide production. Wood pellet also resulted in the highest hydrogen content within the syngas produced, compared to the other biomasses. The tar analysis for wood pellet showed that the analysis might be less complex if wood pellet is used as a feedstock in the following experiments. Moreover, wood pellet lead to the highest calorific value out of all feedstocks considered.

As different feedstock lead to different tar compounds and gas composition, the choice of feedstock is going to have an important impact on the plasma-catalytic system used to reduce tars.

Therefore, wood pellet was considered the most interesting feedstock for further study in plasma-catalytic reactors and will be used as the reference feedstock in the following chapters. These results will enable a better understanding of the biomass pyrolysis products, when looking at the product gas and tar composition, obtained from the SPA methods, and comparing them with results from the outlet of the plasma-catalytic reactor, to better understand the effect of plasma on tars.

## **Chapter 5: Dielectric barrier discharge (DBD) plasma-catalysis to produce high-quality syngas and reduce tar compounds**

This chapter consists of three sections, focusing on the use of a dielectric barrier discharge (DBD) plasma-catalytic reactor to produce high-quality syngas and reduce tar compounds. The experiments conducted for this chapter were using a two stage fixed bed reactor coupled with a DBD plasma catalytic system described in Chapter 3, section 3.2.2. The different sections of this chapter are described below.

Section 5.1 examines the effect of plasma-catalysis compared to pyrolysis (no plasma, no catalyst), pyrolysis-catalysis (no plasma) and pyrolysis-plasma (no catalyst) systems downstream of the fixed bed reactor. The effect of plasma-catalysis on gas production, tar reduction and reacted catalyst are discussed in this section.

Section 5.2 focuses on understanding the tar decomposition mechanism and the syngas production in the DBD plasma-catalytic, by using tar model compounds. Toluene and the constitutive compounds of biomass – cellulose and lignin – were investigated.

Section 5.3 describes the study of the influence of parameters on produced gas composition, tar reduction and reacted catalyst. The influence of power input, steam flow rate, catalyst size and catalyst to feedstock ratio on products is reported.

## 5.1 Plasma effect

In this section, the production of gases and tar compounds from two-stage biomass pyrolysis with plasma-catalysis, as well as the reacted catalysts, were investigated via comparison of two stage pyrolysis-pyrolysis (no plasma, no catalyst), pyrolysis-catalysis (no plasma), pyrolysis-plasma (no catalyst) and pyrolysis-plasma-catalysis for the steam reforming of the biomass pyrolysis gases. The experiments used the equipment and procedure described in section 3.2.2.2. a power input of 40 W to sustain the plasma discharge and an input steam flow rate of 2 g/h to stimulate the steam reforming process.

### 5.1.1 Plasma effect on gas production

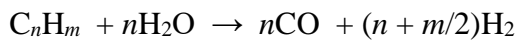
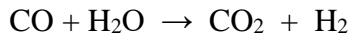
The results of the effect of plasma, in terms of product yield, gas composition and yield, via comparison of pyrolysis-pyrolysis, pyrolysis-catalysis, pyrolysis-plasma and pyrolysis-plasma-catalysis, are presented in Table 5.1-1. The quantity of products in wt.% is detailed for each of the four experiments, along with the detailed composition of the produced gas. The quantity of gas produced during the experiments was about 10 wt.% of feedstock for pyrolysis-pyrolysis and pyrolysis-catalysis experiment, lower than the 15 wt.% obtained for pyrolysis-plasma or pyrolysis-plasma-catalysis. A similar quantity of liquid was obtained after each experiment, with plasma-catalysis leading to a lower liquid production. The quantity of char produced for each experiment was stable as the char was produced during the first stage, where conditions remained unchanged throughout the experiments.

The yield of gas produced in relation to pyrolysis-catalysis, pyrolysis-plasma and pyrolysis-plasma-catalysis is presented in Figure 5.1-1 (a) and the detailed composition of the product gas is shown in Figure 5.1-1 (b) Pyrolysis-pyrolysis and pyrolysis-catalysis produced a product gas yield of  $3 \text{ mmol.g}^{-1}_{\text{biomass}}$ . However, with the introduction of the plasma in the pyrolysis-plasma process (no catalyst) a product gas yield of  $\sim 7 \text{ mmol.g}^{-1}_{\text{biomass}}$  was produced. With the introduction of the catalyst together with plasma, the consequent plasma-catalytic process produced only a very small increase in total gas yield above that for the plasma alone. However, a more detailed compositional analysis of the produced gas shows that the individual gas yields were changed in the presence of the plasma-catalytic steam reforming system compared to plasma alone (Figure 5.1-1(b)). Decreased  $\text{CH}_4$  yields in the presence of

plasma and plasma-catalysis suggests steam reforming of the CH<sub>4</sub>, but also the higher molecular weight hydrocarbon gases, which produced an increased yield of H<sub>2</sub> (Equation 5.1). The plasma-catalytic process produced increased H<sub>2</sub> and CO<sub>2</sub> and reduced CO yields, which suggests that the catalyst promotes not only the steam reforming of the pyrolysis hydrocarbons but also the water gas shift reaction (Equation 5.2) (Kumar et al., 2014). The nickel catalyst is a known material for breaking down tar compounds in gasification processes, by steam reforming leading to a higher hydrogen gas production (Brock et al., 1999). In plasma-catalysis, compared to the plasma process, the higher H<sub>2</sub> production was most likely the result of reduction of tar hydrocarbons by the Ni-catalyst.

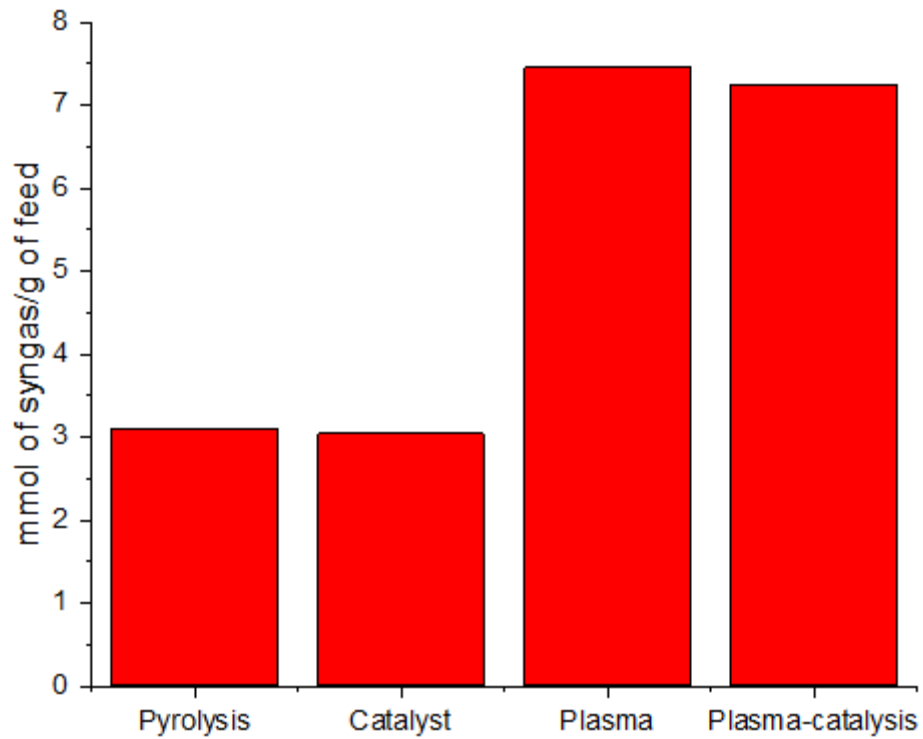
**Table 5.1-1: Experimental summary for identifying the effect of plasma**

Experiment – results in relation to biomass and reacted water	Pyrolysis- Pyrolysis	Pyrolysis- Catalysis	Pyrolysis- Plasma	Pyrolysis -Plasma- Catalysis	% Error
Gas (wt.%)	10.24	10.72	15.63	15.20	3.3
Liquid wt.%)	76.68	76.27	71.69	69.47	7.4
Char (wt.%)	11.21	9.75	10.50	10.62	2.5
Mass Balance (%)	98.14	97.16	99.19	96.62	1.3
Composition in mmol/g of feedstock					
CO	1.87	1.91	3.6	3.31	4.5
H <sub>2</sub>	1.23	1.13	3.48	3.94	7.0
CO <sub>2</sub>	2.33	2.06	3.20	3.46	6.7
O <sub>2</sub>	1.62	2.79	2.16	2.10	-
CH <sub>4</sub>	0.75	0.71	1.1	1.1	6.8

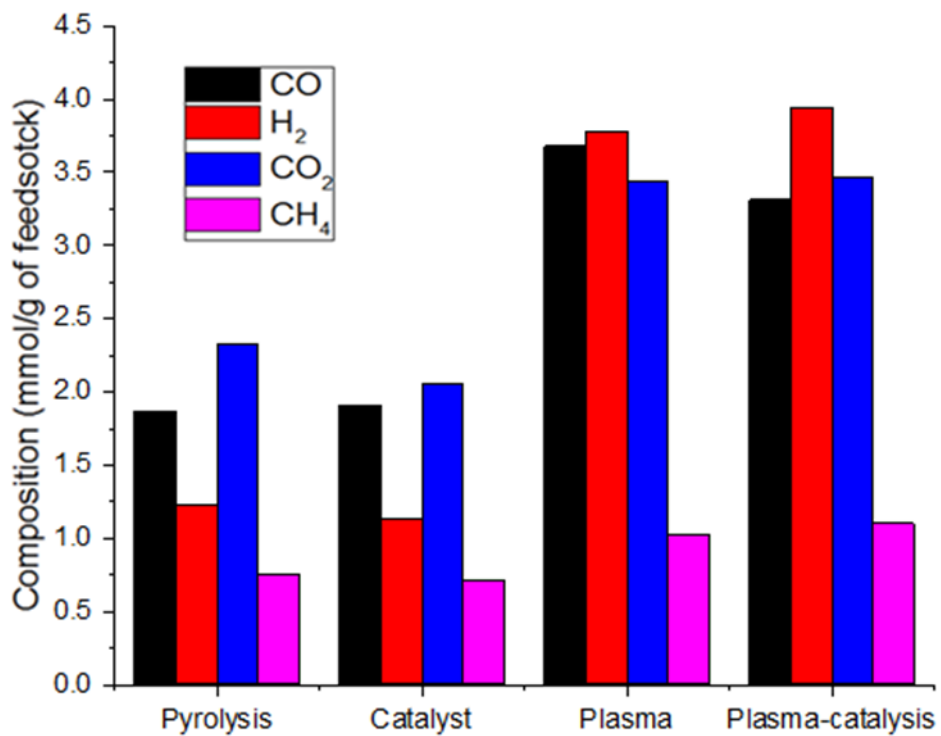
**Equation 5.1****Equation 5.2**

The reaction of CO<sub>2</sub> to produce excited CO\* and O<sub>2</sub>\* species, has been reported to take place in the plasma reaction zones (Brock et al., 1999; Zheng et al., 2003), the recombination of the excited O<sub>2</sub>\* species, is likely to lead to oxygen production which was observed in the product gases for the plasma and plasma-catalytic systems. Considering the slight increase of oxygen in the plasma-catalytic system, where the carbon monoxide concentration was the highest, the combination of both reactions could explain the differences between the plasma and plasma-catalytic system.

It is important to note that the Ni/Al<sub>2</sub>O<sub>3</sub> catalyst is typically used for high temperature steam reforming at temperatures of ~ 800 °C (Czernik, et al, 2002) and not low temperature plasma-catalysis at temperatures of ~250 °C. Therefore, the catalyst may have low catalytic activity at the operating temperature used in this work. However, it has been reported that the water gas-shift reaction can occur at temperatures of 200-300 °C (Hilaire, et al., 2004; Smith, 2010). The temperature inside the second stage plasma reactor was maintained at 250 °C, but temperature inside the plasma reactor zone may be higher than this, also the Ni/Al<sub>2</sub>O<sub>3</sub> catalyst may show some activity, particularly if the plasma promotes surface catalytic reactions.



a.



b.

**Figure 5.1-1: Effect of plasma on the quantity of syngas produced (a) and its effect on the detailed produced gas composition (b) for DBD rig**

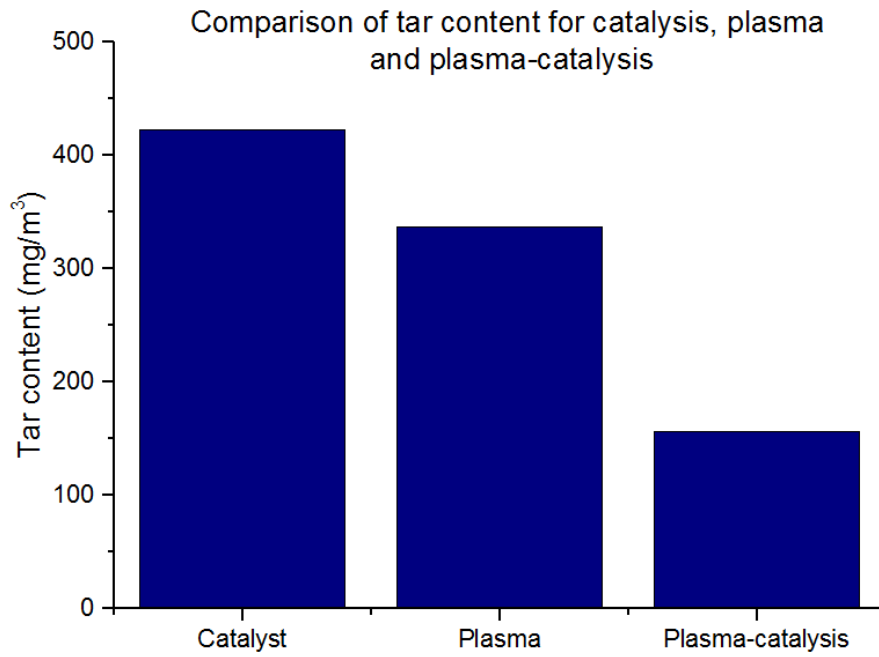
### 5.1.2 Plasma effect on tar reduction

The two-stage biomass pyrolysis with plasma-catalysis was also used to investigate the effect of plasma and plasma-catalysis on the steam reforming process for the reduction of the higher molecular weight hydrocarbon tar species in produced liquid. Figure 5.1-2 (a) shows the total hydrocarbon tar content of the product gas in relation to the pyrolysis-catalysis, pyrolysis-plasma and pyrolysis-plasma-catalysis systems for the steam reforming of the biomass pyrolysis tars. The total hydrocarbon tar content was determined from the analysis of the total hydrocarbons condensed in the reactor condensation system and detected using the GC-MS analytical system. The results were then converted to  $\text{mg tar m}^{-3}$  of gas based on the total gas throughput. Figure 5.1-2 (b) shows the detailed analysis of the tars for selected tar hydrocarbons in relation to process conditions. The selected hydrocarbons represented the range of molecular weights found in light tars with molecular weights from benzene (M.Wt.78) to higher molecular weight compounds with molecular weights over 160 MW units. The selected hydrocarbons were, alkylated-phenols or aromatic compounds: benzene, phenol, o-cresol, p/m-cresol, guaiacol, 2,4-dimethylphenol, 4-ethylphenol, 4-isopropylphenol and 2-methoxy-4-propylphenol. The product gas total tar content was  $420 \text{ mg m}^{-3}$  for the pyrolysis-catalysis system, but was reduced to  $335 \text{ mg m}^{-3}$  for the pyrolysis-plasma system. However, with the introduction of the catalyst into the plasma zone, the hydrocarbon tar content in the product gas was markedly reduced to  $150 \text{ mg m}^{-3}$ . Compared to the hydrocarbon tar content in the absence of the plasma (pyrolysis-catalysis) the pyrolysis-plasma system represents a reduction in hydrocarbon tar content of 21% and 64% reduction for the pyrolysis-plasma-catalysis system.

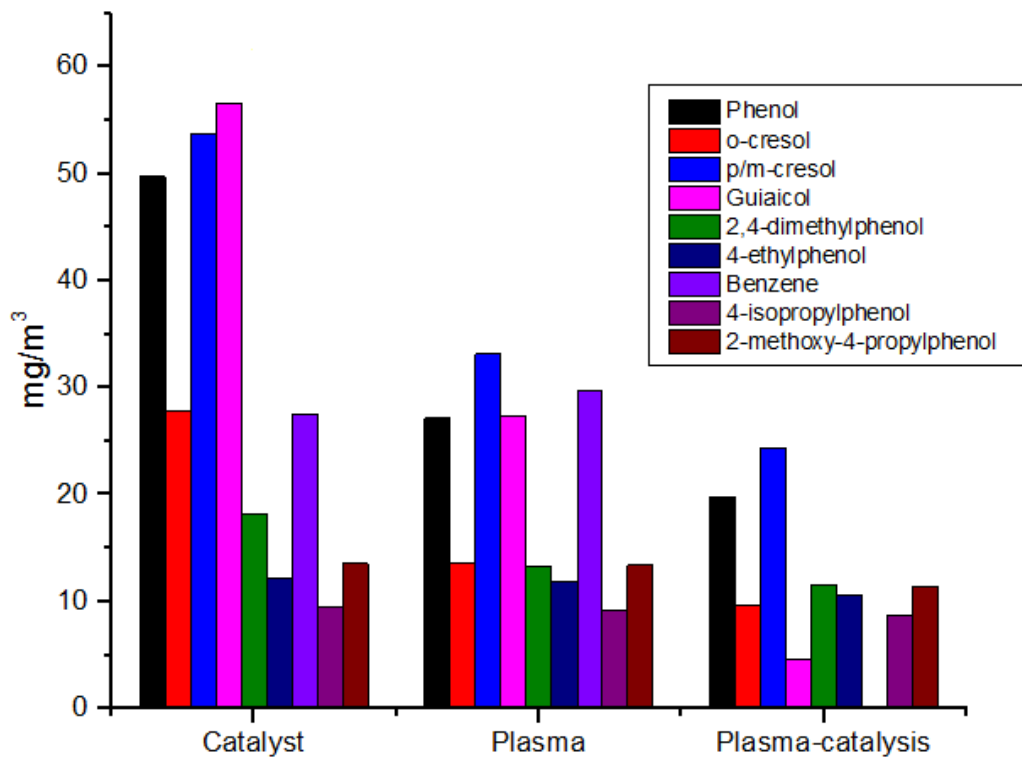
The detailed comparison of the selected hydrocarbons in the hydrocarbon tar in the product syngas shown in Figure 5.1-2 (b) shows that the individual aromatic and oxygenated aromatic hydrocarbons are reduced in concentration in the plasma and plasma-catalytic processes. The plasma-catalytic process producing the highest reduction in concentration of the selected hydrocarbons. In addition, the larger hydrocarbon tar molecules with very high boiling points will also be reduced in concentration. Figure 5.1-3 shows the average molecular weight and the molecular weight range of the condensed hydrocarbons determined using size exclusion chromatography in relation to the influence of plasma on the process. Figure 5.1-3 (a)

shows that the pyrolysis hydrocarbons had a very wide molecular weight range from ~100 to over 1000 Mw units. The introduction of the Ni/Al<sub>2</sub>O<sub>3</sub> catalyst to the system produced a marked decrease in the molecular weight range of the hydrocarbon tars, as was also shown by the pyrolysis-plasma process. However, the pyrolysis-plasma-catalysis process showed that the product hydrocarbon tars were reduced to produce a low molecular weight range tar. Figure 5.1-3 (b) for the average molecular weight of the hydrocarbon tars shows that the pyrolysis only system produced the highest average molecular weight of 885 Mw compared to pyrolysis-catalysis at 169 average Mw and pyrolysis-plasma at 126 average Mw systems. The lowest average molecular weight was obtained for the pyrolysis-plasma-catalysis system (102 Mw). The marked decrease in average molecular weight showing that the post-pyrolysis processing of the biomass pyrolysis gases using catalyst, plasma or plasma-catalysis produces a major decrease in the high molecular weight hydrocarbon tar content of the product gas. Such high molecular weight hydrocarbon tars are the problematic tar species that are the main cause of blockages of gas fuel transfer lines, fuel injectors, etc.

In the plasma process, the plasma produces high energy electrons which activate the reactants initiating radical reactions (Tao et al., 2013). The reduction in tar yield for the plasma and plasma-catalytic systems may be attributed to the reactive plasma species including high energy electrons, the free radicals such as OH<sup>\*</sup>, O<sup>\*</sup> and N<sup>\*</sup> and excited N<sub>2</sub><sup>\*</sup> species reacting with the biomass pyrolysis products (L. Liu, Wang, Song, et al., 2017). These short-life species can breakdown the tar compounds through collision, generating smaller molecular weight species (Eliasson et al., 1991).

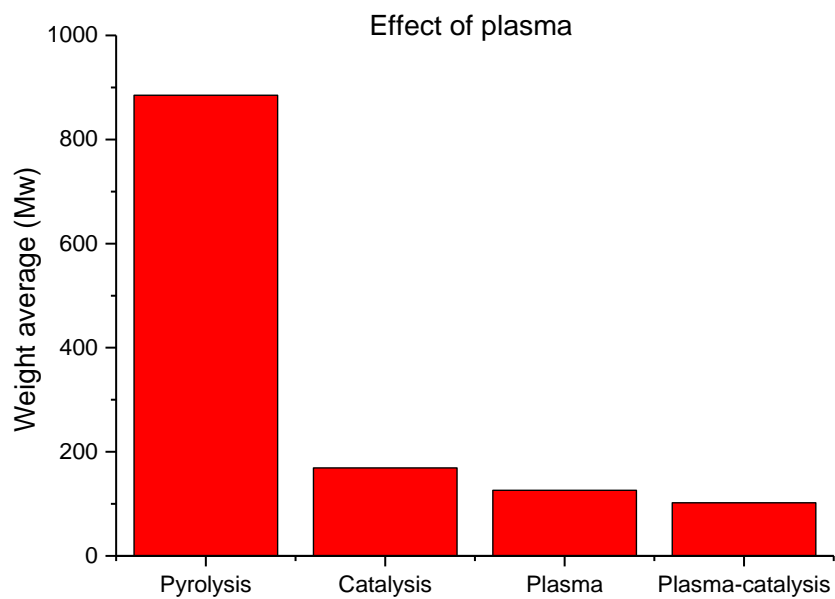


a.

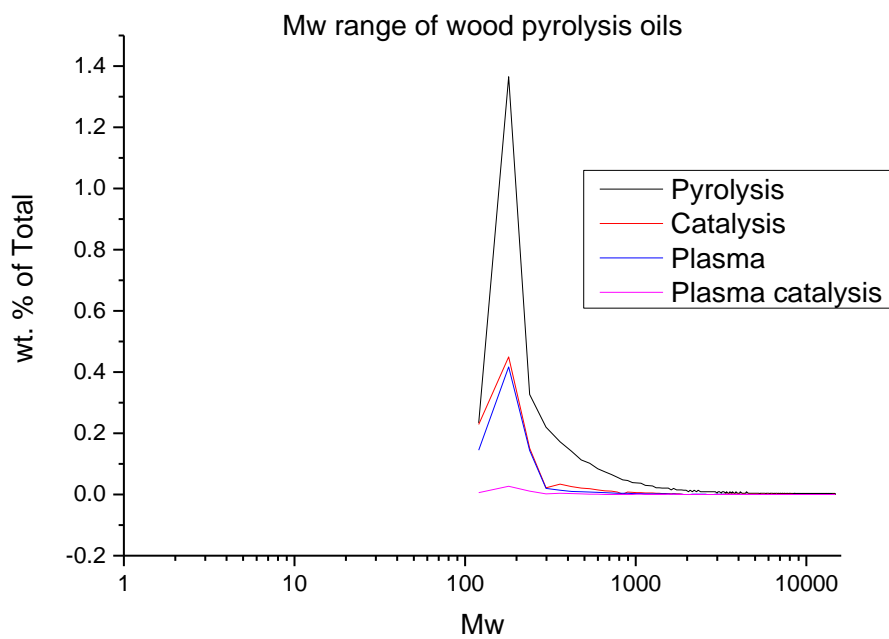


b.

**Figure 5.1-2: Effect of plasma on the tar production (a) and on selected tar compounds (b) of produced liquid for DBD rig**



a.



b.

**Figure 5.1-3: Effect of plasma on the weight average (Mw) (a) and on the Mw range (b) of produced liquid for DBD rig**

The marked reduction in hydrocarbon tar content in the product gas from the plasma-catalytic process involves the interaction of the plasma with the catalyst enhancing tar reduction reactions. The presence of the catalyst particles in the discharge gap will enhance charge accumulation on the particle surface, resulting in increased local or average electrical field and thereby the number of high energy electrons and reactive species (Liu et al., 2017). In addition to this physical effect of the particles, the presence of electrically conductive nickel particles on the catalyst surface will also increase the plasma development and provide nickel metal sites for the catalysed decomposition of the biomass thermal degradation species. The plasma-catalysis system enables plasma generated, high energy electrons, ions, radicals and excited species to interact with the catalyst, which will not be the case for thermal catalysis (Neyts et al., 2014). The presence of the catalyst within the plasma zone enables both plasma induced reactions and also catalytically promoted reactions to occur. The plasma will activate the pyrolysis gases to produce a complex mixture of molecules, free radicals, excited species, atoms, ions and electrons which will both interact in the gas phase and on the catalyst surface (Neyts et al., 2014). In addition, the catalyst surface characteristics, metal species content and dielectric properties will modify the plasma properties on the catalyst, enhancing decomposition of the pyrolysis products. The presence of the plasma may also alter the physicochemical properties of the catalyst surface. It should also be noted that the presence of the packing material particles of the  $\text{Al}_2\text{O}_3$  support may have dielectric properties which act as a physical effect on the plasma-solid interaction which induces the chemical effects that enhances pyrolysis product degradation. This effect is in addition to the presence of the active nickel species present in the catalyst which enhances selective reforming and cracking reactions. The pore size distribution of the catalyst will also influence pyrolysis product decomposition where it has been reported that strong electric fields are produced due to micro-discharges in the catalyst pore volume (Neyts et al., 2014).

Comparison of the hydrocarbon tar reduction results from biomass may be compared to model compound work reported in the literature. For example, Liu et al. (Liu et al., 2017) used a dielectric barrier discharge system to study the non-thermal plasma-catalytic steam reforming of toluene as a tar model compound using a range of different catalysts. The catalysts used were Ni and Fe based catalysts with different support materials. They reported that the Ni catalysts were more effective in

converting the toluene to product gas and that the surface area of the support influenced toluene decomposition, with higher surface area support material increasing decomposition. They also investigated the location of the catalysts in the reactor system and showed that placing catalyst within the plasma zone was more effective for toluene decomposition. This was attributed to the reactive plasma species including the radicals  $\text{OH}^*$ ,  $\text{O}^*$  and  $\text{N}^*$  and excited species  $\text{N}_2^*$  reacting with the toluene on the surface of the catalyst. A maximum toluene conversion of 86.5% was achieved with the Ni/ZSM-5 catalyst, whereas in the absence of catalyst the conversion efficiency for the plasma only system was ~64%. Liu et al. (Liu et al., 2017) also used a dielectric barrier discharge system and a Ni/ $\text{Al}_2\text{O}_3$  catalyst to study the catalytic steam reforming of toluene as a model biomass gasification tar compound. They investigated the influence of different Ni catalyst contents on toluene decomposition. In the absence of catalyst, the toluene conversion was 39.5% but when the Ni-catalyst was added, conversion of toluene was increased and at the highest catalyst Ni content of 20 wt.% conversion reached 51.9%. The main product gases were  $\text{H}_2$ ,  $\text{CO}_2$  and  $\text{CH}_4$  and lower concentrations of  $\text{C}_1 - \text{C}_4$  hydrocarbons. In addition, the condensed hydrocarbons from the toluene decomposition in the absence of a catalyst (plasma only) produced a range of aromatic and oxygenated hydrocarbons which were significantly reduced in the plasma-catalytic process. Benzene and ethylbenzene were identified as reaction products from the plasma-catalytic reforming of toluene, but a wide range of other hydrocarbons were also detected, including xylenes, styrene, propylbenzene and oxygenated hydrocarbons (Liu et al., 2017).

The biomass pyrolysis products generated in the first stage pyrolysis process and passed to the plasma-catalytic system are highly complex and therefore the degradation mechanism is difficult to develop. Even simple single tar model compounds have been shown to generate a range of hydrocarbon and oxygenated hydrocarbon products. For example, Wang et al (Wang, et al., 2017) used a dielectric barrier discharge (DBD) plasma-catalytic reactor with  $\text{CeO}_2\text{-MnO}_x$  catalysts to study the decomposition of toluene. They identified, a range of aliphatic and aromatic hydrocarbons in the degradation products, including methyl- and dimethylbenzenes, benzaldehyde and methylbutanol. Liu et al (Liu et al., 2017) also used a DBD reactor to investigate the plasma-catalytic decomposition of toluene, using different Ni-based and Fe-based catalysts on different catalyst supports. They reported that benzene and

ethylbenzene were the main products of toluene decomposition with lower concentrations of xylene, styrene, cumene, propylbenzene, isobutylbenzene, 1,2-diphenylethane and 2-methyl-3-phenylbutane. Therefore, the biomass pyrolysis gases will undergo extensive reaction and decomposition in the plasma-catalytic system generating a wide range of hydrocarbon species as reflected in the molecular weight range of the hydrocarbon tars shown in Figure 5.1-3.

Based on experimental results presented in this section and published reaction mechanisms, mechanisms for tar removal can be drawn in the pyrolysis-plasma-catalytic system. First, it is worth mentioning that most reaction mechanisms for tar removal in plasma-catalytic systems are conducted for single tar compounds as reactions in plasma environment are known to be very complex. From these single tar compounds, the most extensively studied compounds are toluene and naphthalene. Liu et al (2017) studied the steam reforming of toluene in a gliding arc reactor and suggested a reaction mechanism reproduced below in Figure 5.1-5. Two possible pathways are shown for toluene removal. First, H-abstraction from the methyl group by nitrogen excited species or energetic electrons could initiate the breakdown of toluene, the dissociation energy of C-H in methyl being smaller than other dissociation energies in toluene. C-C bond between methyl and benzene could also be broken down by excited nitrogen species and energetic electrons, generating phenyl radicals which will react with other radicals – H, OH, NH<sub>2</sub> and CN – recombining into different single ring aromatics. Certain intermediary radicals could further be broken down to syngas. Secondly, oxidation of the aromatic ring was shown as the second pathway to remove toluene. This generates an unstable intermediary compound, forming a peroxide bridge radical and being a precursor to both carbonyl and epoxide pathways. Nevertheless, both pathways can be further broken down to syngas. (Liu et al., 2017)

The same two pathways have been presented by Wang et al (2019) for the plasma reforming of naphthalene, with or without steam, in Figure 5.1-5. Naphthalene dissociation was shown to include water dissociation in plasma through the recombination of one of the aromatic rings with OH radical forming highly reactive intermediary compounds in routes I and II. Route I represented the reaction between unstable intermediaries and peroxy radicals, producing indene, marked as compound

(c). Route II showed the generation of intermediaries through ring cleavage, cracking, dehydration or reaction with  $\text{CH}_2$  radicals. Furthermore, naphthalene removal can be initiated by its collision with energetic electrons and metastable nitrogen species. The route III led to the formation of mono-substituted benzene derivative through ring cleavage reactions. Route IV showed naphthalene breaking down to ethylene by step-wise oxidation process to form carbon oxides and water. (Wang et al., 2019)

Very few research publications investigate the reaction pathways and mechanisms for more than a tar model compound as very large number of chemical reactions happen simultaneously, resulting into a very complex process. Mei et al (2019) studied the enhanced steam reforming of toluene and naphthalene in a hybrid gliding arc plasma-catalytic process and studied the possible reaction mechanisms for tar removal, represented in Figure 5.1-6. The process is known to involve gas and surface reactions on the catalyst. The process is first most likely induced by the H-abstraction and cleavage of the aromatic rings by excited nitrogen species and energetic electrons, which have demonstrated a significant contribution to tar compounds removal in nitrogen plasmas. Aliphatic compound generation was the result of the dissociation of C-C and C=C bonds in tar compounds, as well as their fragment recombination. Polymerisation reaction could also occur at a very low occurrence in plasma reforming processes. Oxidations of tar compounds originated from water dissociation into OH radicals, breaking further down toluene and naphthalene via H-addition, recombination or dehydrogenation. In plasma-catalysis, molecules can be adsorbed on the catalyst surfaces and react with active species, providing additional reaction pathways for tar conversion, further enhancing hydrogen production and tar conversion. (Mei et al., 2019).

A more detailed reaction pathways for the steam reforming removal of toluene and naphthalene are presented in from a study by Mei et al. This reaction pathway, represented in Figure 5.1-7, was obtained through a complete analysis of gas and by-products, as well as optical emission spectroscopic diagnostics. Toluene tar compounds could be oxidised to benzaldehyde and further oxidised to benzoic acid by oxidative species, followed by the generation of carbon dioxide and phenyl radicals (which could form benzene). Unstable intermediary compounds could react with O radicals, forming a peroxide bridge radicals for carbonyl an epoxide routes, as

described previously. Toluene ring can be open through step-wised oxidation by OH and O radicals to form stable oxygenated compounds. Aromatic compounds from ring cleavage could be further broken down to generate syngas and water. As shown before, hydroxylation of naphthalene led to the formation of 1,4-naphthoquinone which, once oxidised, will break an aromatic ring to generate benzaldehyde and phthalic acid. Phthalic acid can also further react to produce dibutyl phthalate. This intermediates would be further oxidised by O and OH radicals to form carbon oxides and water. (Mei et al., 2019).

Therefore, the tar removal pathways during the pyrolysis-plasma-catalysis of biomass are suggested to be similar to the mechanisms previously presented for the mixture of naphthalene and toluene.



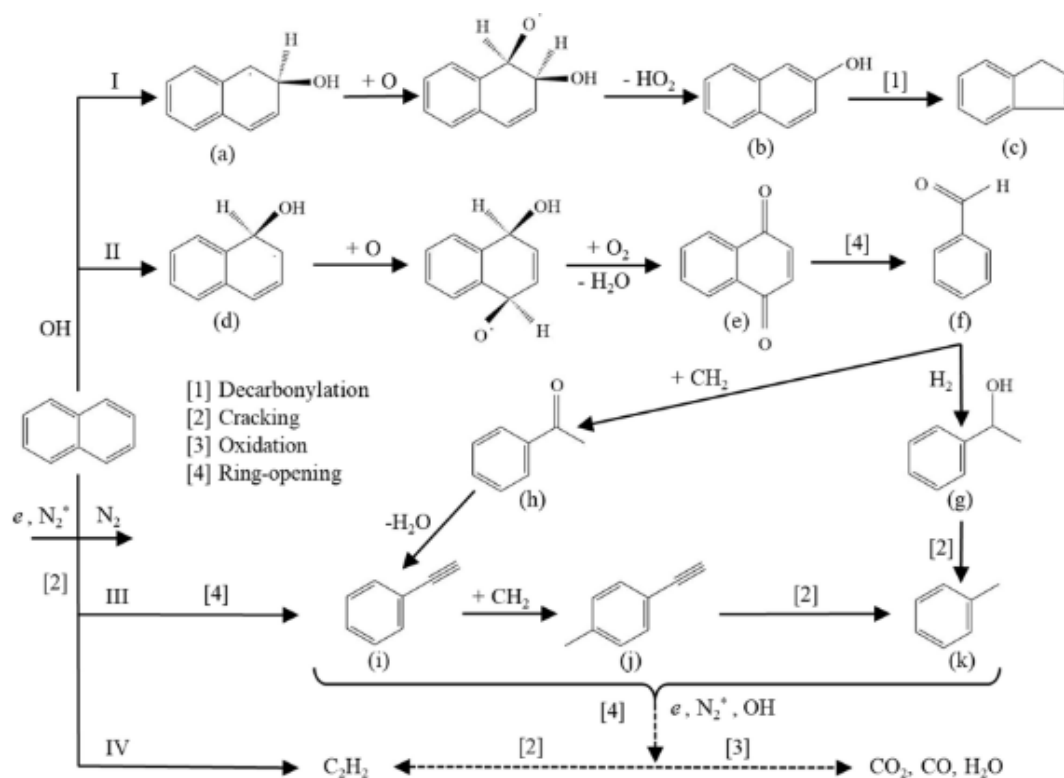


Figure 5.1-5: Possible reaction pathways of steam reforming of naphthalene (Wang et al., 2019)

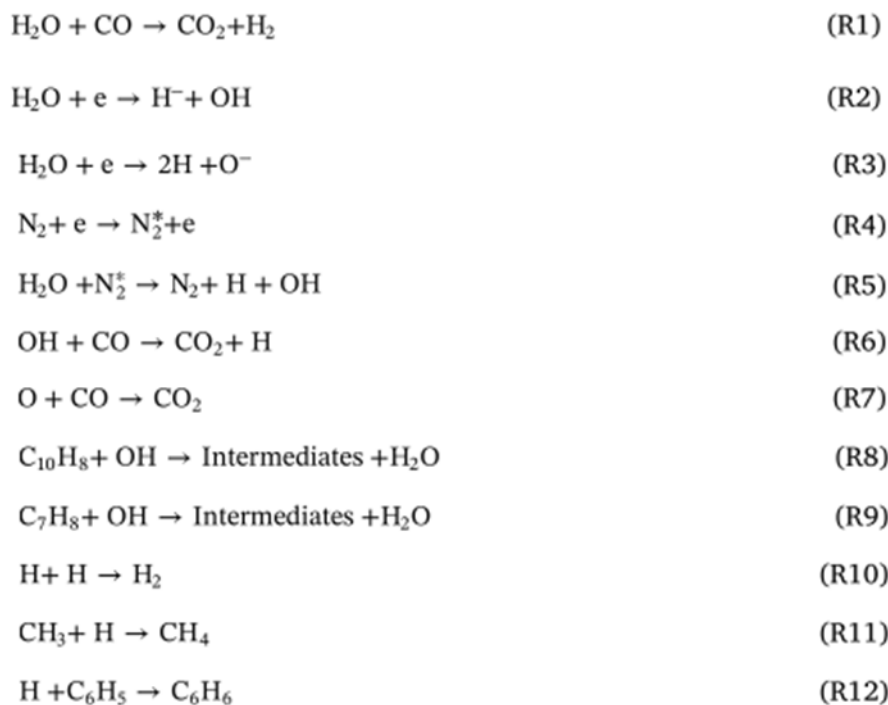


Figure 5.1-6: Possible reactions mechanisms for toluene and naphthalene removal in plasma-catalysis system (Mei et al., 2019)



### 5.1.3 Plasma effect on reacted catalyst

Temperature programmed oxidation was used to determine the amount of carbonaceous coke deposited on the catalysts for the pyrolysis-catalysis process and the pyrolysis-plasma-catalysis process. The associated results are presented in Figure 5.1-8. The pyrolysis-catalysis process resulted in a coke deposition of 10.2 wt.% compared to the coke deposition with the pyrolysis-plasma-catalysis process where coke deposition was significantly lower at 7.7 wt.%. Oxidation of the catalyst carbon was complete at oxidation temperatures below 550°C, which indicates that the carbon deposited on the catalyst surface was amorphous carbon (Yao et al., 2014). During plasma-catalysis, the environment is hotter than for catalysis due to the excited molecules colliding with energetic electrons and leading to a slight temperature increase by energy transfer between the electrons and the heavy molecules (Fridman, 2008). However, the Boudouard reaction indicates that CO is the most stable carbon oxide at high temperature (above 500 K). Thus, it is suggested that the contribution of the Boudouard reaction to plasma-catalysis leads to higher de-coking compared to catalysis only (Kameshima et al., 2015).

The fresh nickel supported alumina catalyst and the reacted catalysts after reaction were characterised by X-ray diffraction (XRD). Figure 5.1-9 shows the XRD spectra for the fresh prepared Ni/Al<sub>2</sub>O<sub>3</sub> catalyst, the Ni/Al<sub>2</sub>O<sub>3</sub> catalyst after reduction and the catalyst after reaction in the plasma-catalytic system. The XRD spectra shows that three diffraction peaks were observed around the most intense peaks of NiO/Al<sub>2</sub>O<sub>3</sub>: 2θ at 37.3°, 43.3° and 62.9° (JCPDS 78-0643). The diffraction peaks for the fresh catalyst were more intense than for the reduced fresh catalyst. This suggests that smaller nickel particles are produced after reduction (Yan et al., 2013). After reduction, a new XRD peak around 51° could be observed, which matched one of the most intense peaks of Ni: 2θ at 44.5°, 51.8° and 76.4° (JCPDS 65-2865). The diffraction spectra for the catalyst after reaction in the plasma-catalytic system were less intense compared with the peaks for the unreacted catalysts. This suggests that the nickel particles were smaller after processing in the plasma-catalytic system.

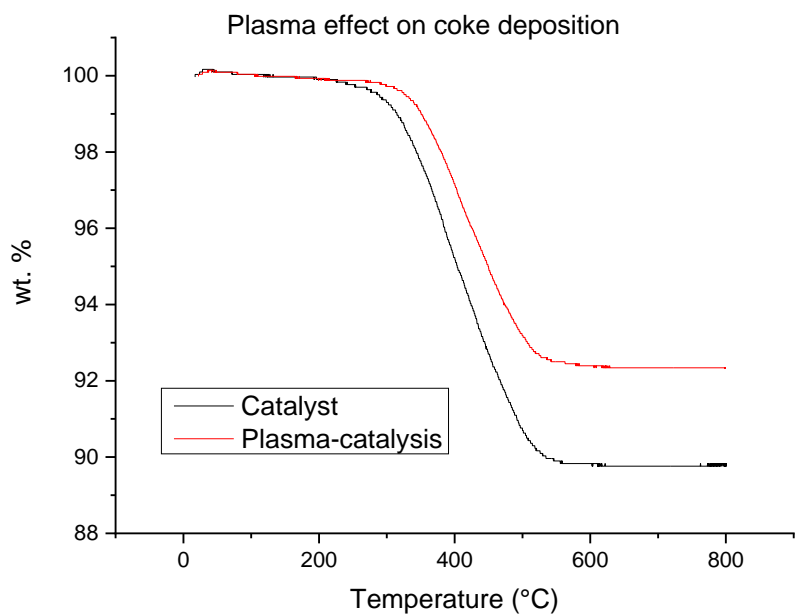


**Figure 5.1-8: Effect of plasma on coke deposition on the catalyst for pyrolysis-catalysis (black) and plasma-catalysis (red) systems**

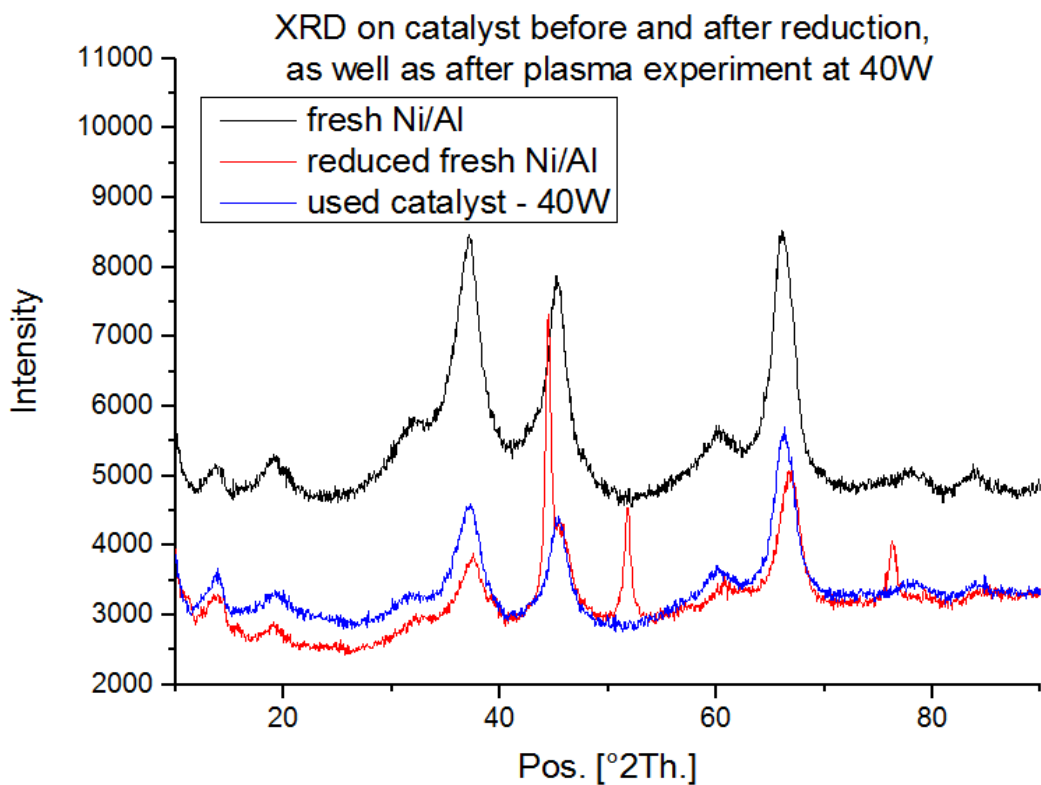


**Figure 5.1-9: XRD on catalyst before reduction (black), after reduction (red) and after plasma experiment at 40 W (blue)**

## **5.2 Tar model compounds and biomass components used as feedstock in the DBD plasma-catalytic reactor**

In section 5.1, the effect of plasma was studied on the different products of the two-stage biomass pyrolysis with plasma-catalysis system presented in section 3.2.2.2. Plasma-catalysis system was identified as the best system for higher syngas and hydrogen production, alongside high tar reduction. However, the experimental setup used cannot be compared to previous work, to the best of my knowledge, as the literature contained mainly single tar model compound in plasma-catalytic systems. In order to verify the reproducibility and synergy of published results to validate our setup, toluene was first used as feedstock of the two-stage biomass pyrolysis with plasma-catalysis system. To obtain some insights into the decomposition of biomass within a plasma-catalytic system, the different components of biomass – cellulose and lignin – were used as feedstocks. The resulting observations enabled a better comprehension of the mechanisms in place in the plasma-catalytic system.

### **5.2.1 Toluene**

The use of toluene as a tar model compound and the synergetic effect of plasma-catalysis was studied at an input power of 40 W. The influence of increasing power input to the plasma system was investigated to determine the influence on product gas yield and gas composition at input powers of 20, 40 and 60 W. The typical steam/carbon ratio used for steam reforming reactions is comprised between 2.5 and 3.5, according to Wukovits et al (Wukovits, , 2012). Thus, a steam to carbon ratio of 3|1 was used throughout the experiments, with a Toluene flow rate of 2 mL.h<sup>-1</sup> and a steam flow rate of 7.2 mL.h<sup>-1</sup>.

The experimental summary is represented in Table 5.2-1. The total product gas produced and the detailed gas composition of product gas are represented in Figure 5.2-1 (a) and Figure 5.2-1 (b) respectively. Confirming literature results of plasma-catalysis on model compounds such as toluene (Liu et al., 2017; Wang et al., 2017; Whitehead, 2009), plasma-catalysis technology enabled to destruct more toluene, leading to producing more syngas (Figure 5.2-1 (a)) and more hydrogen (Figure 5.2-1(b)) than catalyst cracking or non-thermal plasma (DBD). The tar content in the product liquid is shown in Figure 5.2-2. A higher tar content was observed for the

plasma-catalytic system than for the pyrolysis-plasma system, further showing the reduction of toluene in the plasma-catalytic system.

An increase of power input improved removal efficiency of toluene, as showed by an increase of syngas production showed in Figure 5.2-1 (a), an increase of hydrogen production represented in Figure 5.2-1 (b), and an increase in tar content showed in Figure 5.2-2, for increasing power input. These observations were similar to the observations from Wang et al (Wang et al., 2017). In their publication, the removal efficiency of toluene and the selectivity of carbon dioxide is improved with increase of input power, when using a plasma-catalytic system with CeO<sub>2</sub>-MnO<sub>x</sub> catalysts. Finally, the study of coke deposition on the catalyst in the plasma-catalytic system is represented in Figure 5.2-3. With increasing power input, the coke deposition increased, further confirming the enhanced decomposition of toluene with increasing power inputs.

**Table 5.2-1: Experimental summary for experiments using toluene as a tar model compound**

Experiment using Toluene – results in relation to biomass and reacted water	Plasma-Catalysis at 20 W	Plasma-Catalysis at 40 W	Plasma-Catalysis at 60 W	Pyrolysis-Plasma at 40W	Pyrolysis-Catalysis	% error
Gas (wt.%)	0.49	1.00	1.97	0.85	-	3.3
Liquid (wt.%)	90.73	90.06	88.95	91.50	85.47	7.4
Char (wt.%)	-	-	-	-	-	2.5
Mass Balance (%)	91.22	91.06	91.07	92.35	85.47	1.3
Composition in mmol/g of feedstock						
CO	-	0.66	1.19	-	-	4.5
H <sub>2</sub>	1.91	4.24	5.81	4.44	-	7.0
CO <sub>2</sub>	0.54	0.89	1.23	3.01	-	6.7
CH <sub>4</sub>	-	0.25	0.36	0.32	-	6.8

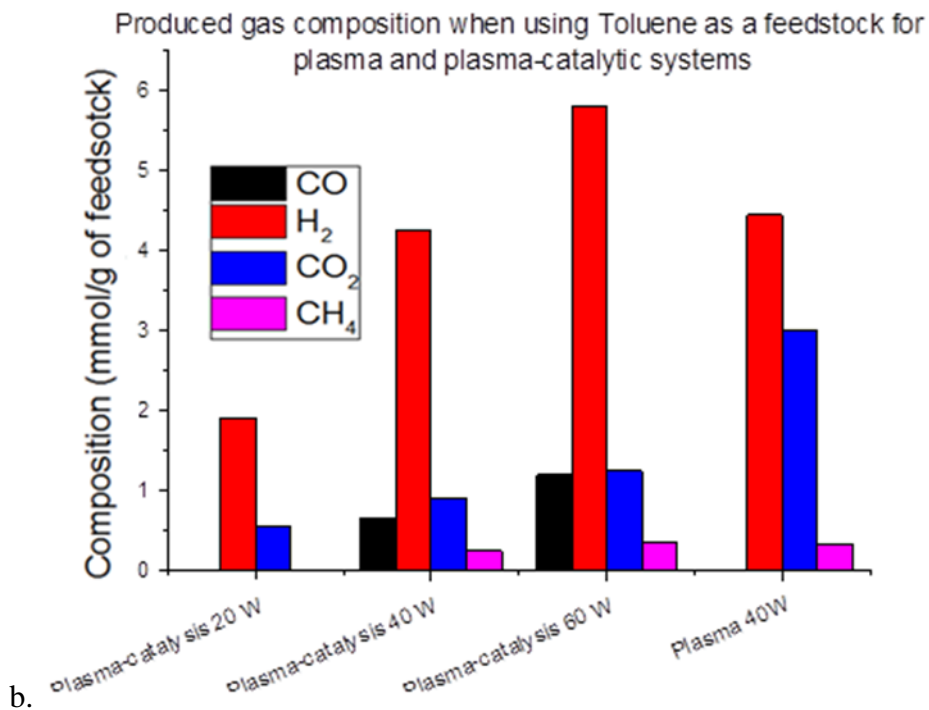
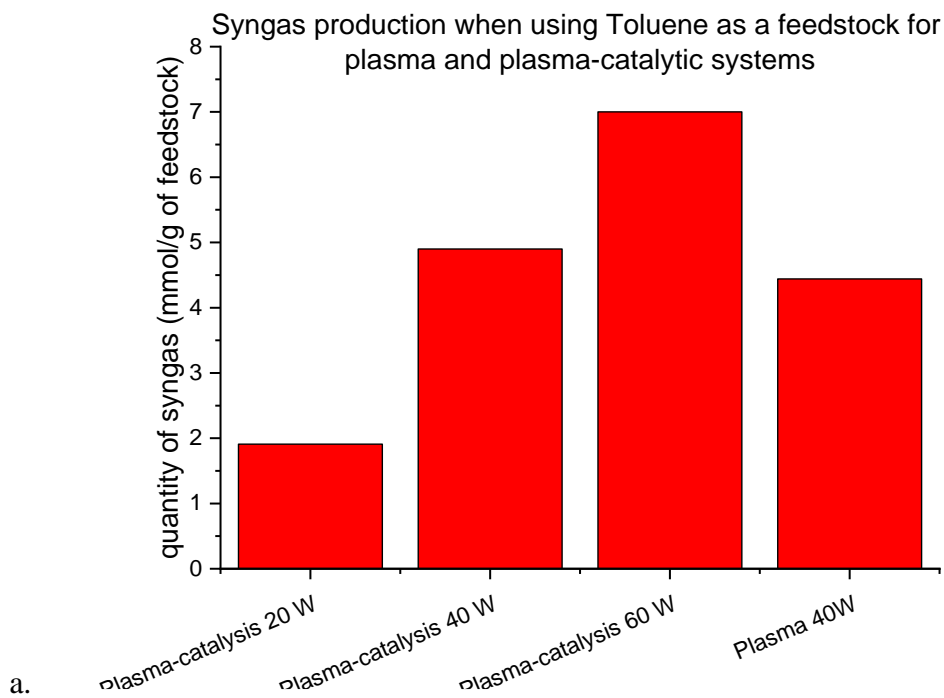


**Figure 5.2-1: Effect of plasma-catalysis and power increase on the quantity of syngas produced (a) and its effect on the detailed produced gas composition (b) for DBD rig when using Toluene as a feedstock**

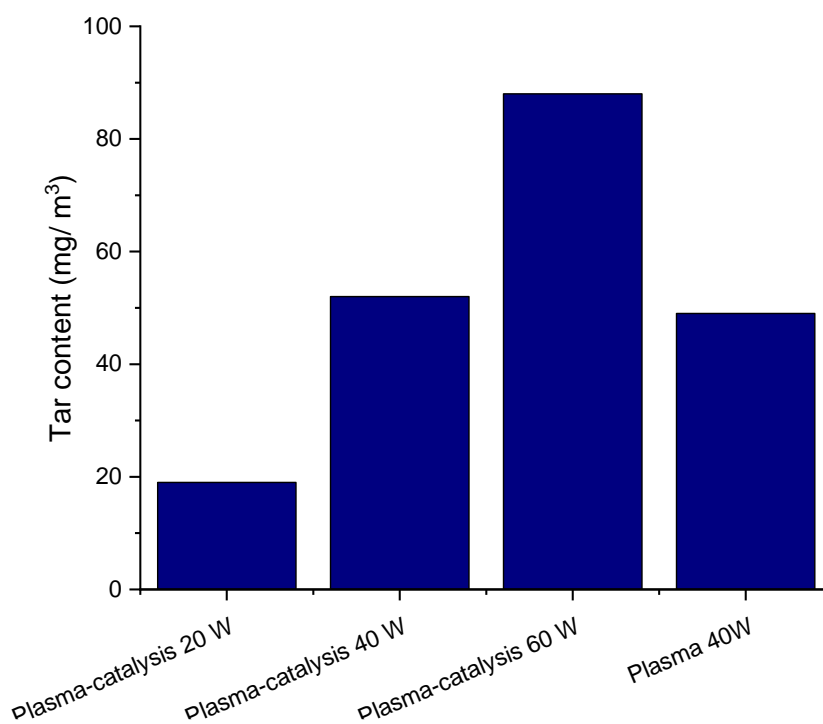


**Figure 5.2-2: Effect of plasma-catalysis and power increase on tar production for DBD rig when using Toluene as a feedstock**

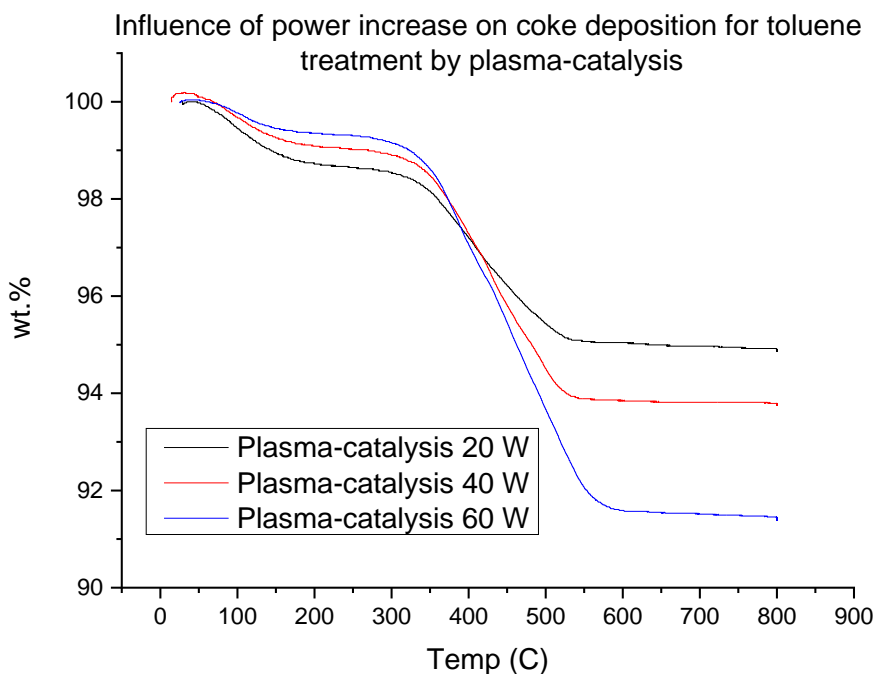


**Figure 5.2-3: Effect of plasma-catalysis and power increase on coke deposition for DBD rig when using Toluene as a feedstock**

## 5.2.2 Biomass components: cellulose and lignin

The production of gases and tar compounds from the two-stage biomass pyrolysis with plasma-catalysis, as well as the reacted catalysts, were investigated via the use of cellulose and lignin to better understand the breakdown mechanism of biomass in the plasma-catalytic system. The experiments used a power input of 40 W to sustain the plasma discharge and an input steam flow rate of 2 g/h. To support these experiments, the description of the components constituting biomass are described in Chapter 3, section 3.1.1.2.

### 5.2.2.1 Produced gas composition

The results for the different components of biomass in terms of product yield, gas composition and yield, are shown in Table 5.2-2, in Figure 5.2-4 for the total syngas produced and Figure 5.2-5 for the detailed gas composition. Each figure consists of a series of graphs including plasma-catalytic system (a), pyrolysis-plasma system (b) and pyrolysis-catalysis system (c). As presented in section 5.1, the use of plasma-catalysis system lead to a higher syngas and hydrogen production than the use of pyrolysis-plasma or plasma-catalysis systems, for cellulose and lignin.

First, the total product gas increased when switching from a pyrolysis-catalysis system to a pyrolysis plasma system, from 7.8 to 11.9 wt.% for cellulose and from 6.5 to 7.4 wt.% for lignin. Further gas was produced when introducing catalyst into the pyrolysis-plasma system, from 11.9 to 12.6 wt.% for cellulose and from 7.4 to 10.1 wt.% for lignin. The product gas obtained when using pyrolysis-plasma-catalysis was compared in Figure 5.2-4 (a) and Figure 5.2-5 (a) for three different feedstocks: biomass itself and its components. Cellulose used in plasma-catalysis system led to a higher syngas production with 7.2 mmol per gram of feedstock, due to a higher carbon monoxide production, 3.1 mmol.g<sup>-1</sup><sub>biomass</sub>. The use of lignin in plasma-catalysis system resulted into the highest hydrogen production and highest methane production, respectively 4.3 mmol.g<sup>-1</sup><sub>biomass</sub> and 2.5 mmol.g<sup>-1</sup><sub>biomass</sub>. When comparing the biomass components across the three systems – pyrolysis-catalysis, pyrolysis-plasma and pyrolysis-plasma-catalysis – the highest production of methane is obtained for lignin used in pyrolysis-plasma-catalysis, whereas the productions of carbon monoxide and carbon dioxide are the highest for cellulose used in pyrolysis-plasma and pyrolysis-

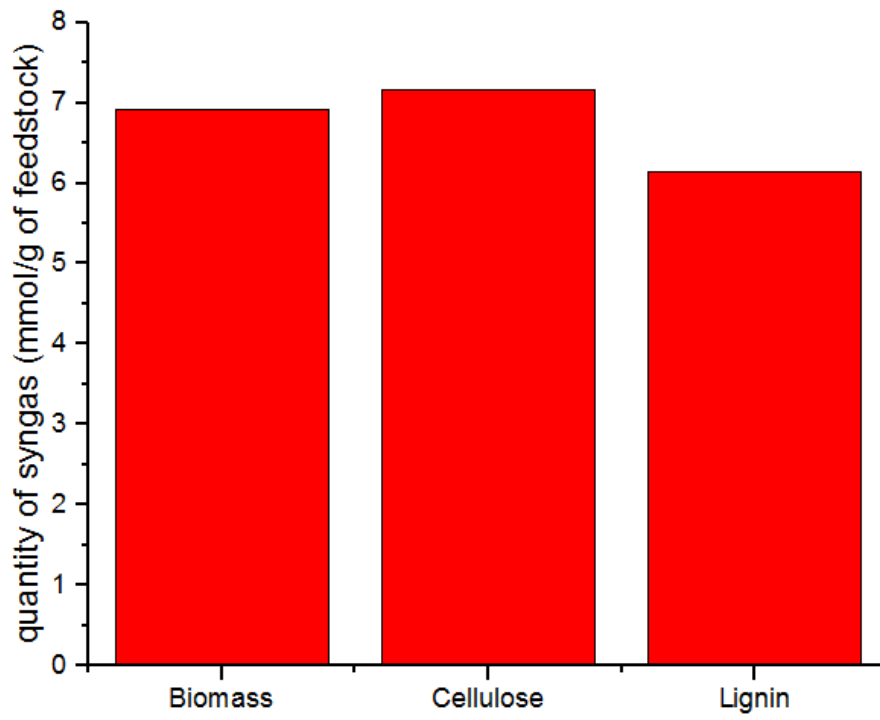
plasma-catalysis respectively. Hydrogen production is the highest for both biomass components when using pyrolysis-plasma-catalysis.

Supported by the feedstock characterisation (Section 3.1.1.2), the gas produced from lignin contained less oxygenated compounds and more methane than other product gases. This can be explained by its lower oxygen content and its higher carbon content compared to other feedstocks. The higher presence of moisture in biomass and cellulose compared to lignin could lead to a higher syngas concentration, as moisture will more easily be pyrolysed and thus, interact within the plasma-catalytic reactor. The higher hydrogen concentration from lignin product gas cannot be explained by the hydrogen content in all feedstocks, as they are very similar. This could be linked to the accessibility of hydrogen atoms in the polymer structures: in lignin, C-H chemical bond seemed easier to break down than C-O bond in all feedstocks, or C-H bond in cellulose or hemi-cellulose.

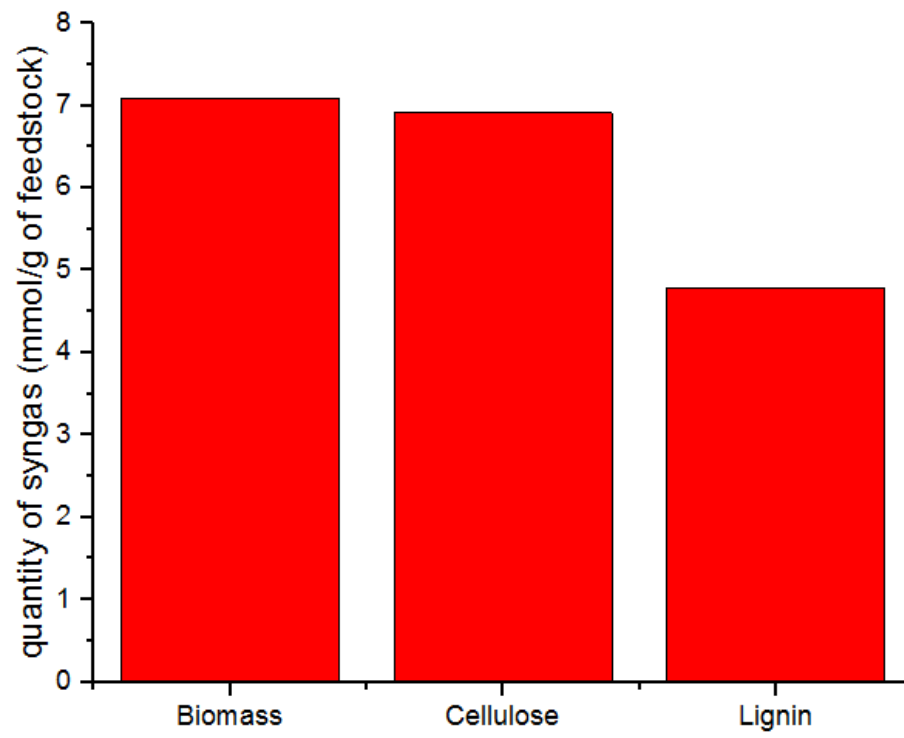
Yang et al. (Yang et al. 2007) studied the characteristics of hemicellulose, cellulose and lignin pyrolysis. The main gas products were dependent of the biomass components used as feedstock. Yang et. al observed that hemicellulose had higher carbon dioxide yield, cellulose higher carbon monoxide yield, and lignin higher hydrogen and methane yield. These observations could be explained by the molecular structure of the biomass components. During the pyrolysis process, the abundant presence of C-O Chemical groups in cellulose is suggested to promote the production of carbon monoxide. The numerous C=O chemical groups in hemicellulose might favour the production of carbon dioxide. Lignin is rich in methoxyl (O-CH<sub>3</sub>) containing compounds, which might promote the production of methane. ( Yang et al., 2007) Wu et. al (Wu, 2013) observed that the addition of nickel supported on alumina catalyst might promote reforming of oxygenated compounds, increasing the hydrogen production for lignin pyrolysis/gasification. High hydrogen production was also observed for catalytic steam pyrolysis/gasification of cellulose. (Wu et al., 2013)

**Table 5.2-2: Experimental summary for pyrolysis-catalysis, pyrolysis-plasma and plasma-catalysis experiments using biomass components**

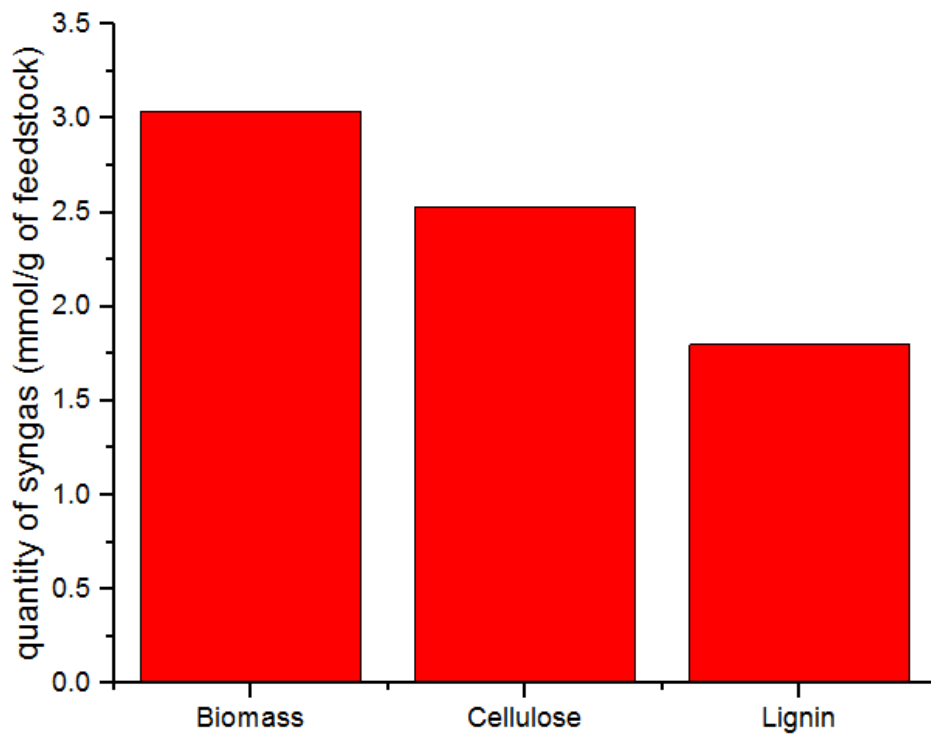
Experiment – results in relation to biomass and reacted water	Pyrolysis-Catalysis		Pyrolysis-Plasma 40 W		Plasma-Catalysis 40 W		% error
	Cellulose	Lignin	Cellulose	Lignin	Cellulose	Lignin	
Gas (wt.%)	7.84	6.54	11.89	7.37	12.63	10.13	3.3
Liquid (wt.%)	78.19	67.26	70.80	66.52	72.88	72.53	7.4
Char (wt.%)	8.23	23.01	8.85	22.61	9.75	21.46	2.5
Mass Balance (%)	95.08	97.25	91.53	96.50	95.26	104.12	1.3
Composition in mmol/g of feedstock							
CO	1.72	1.14	3.36	1.51	3.09	1.86	4.5
H <sub>2</sub>	0.81	0.69	3.55	3.28	4.07	4.29	7.0
CO <sub>2</sub>	2.57	1.71	2.89	1.83	3.81	2.24	6.7
O <sub>2</sub>	0.48	0.34	0.85	0.36	0.41	1.02	-
CH <sub>4</sub>	0.44	1.53	0.59	1.56	0.98	2.51	6.8



a.

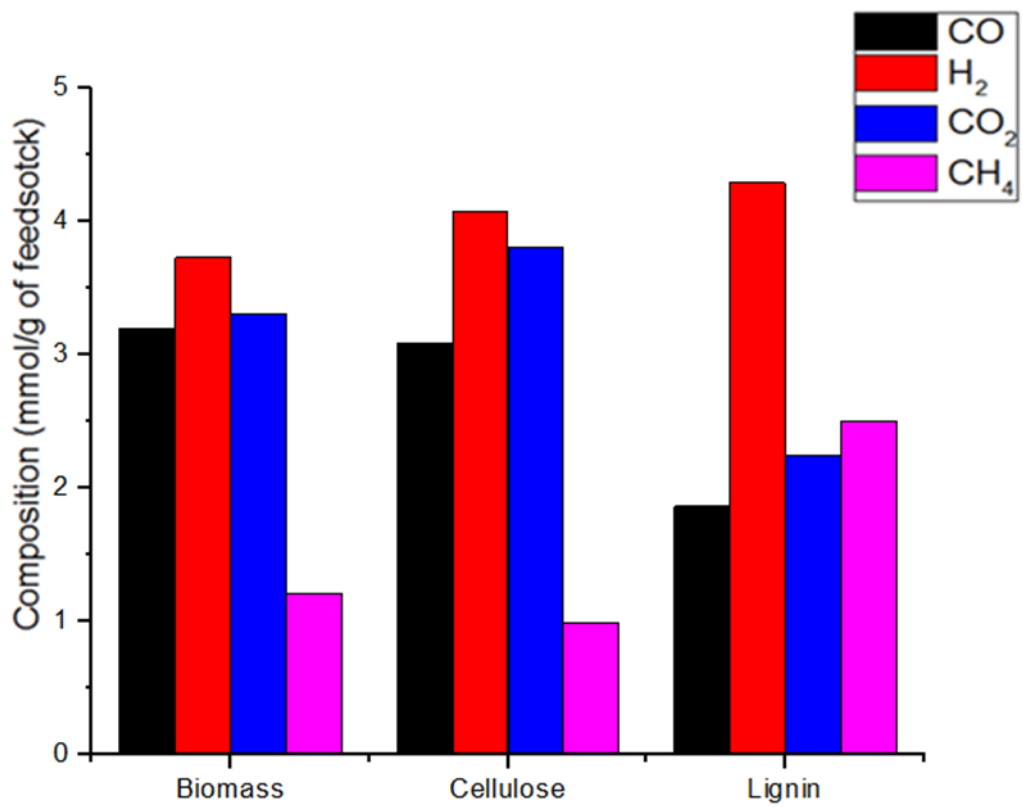


b.

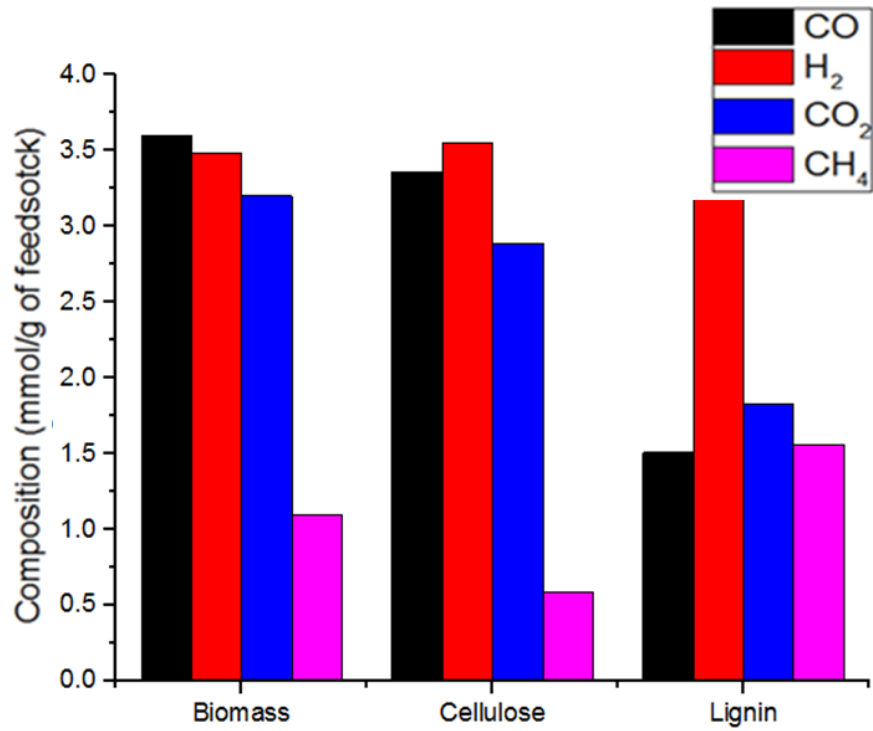


c.

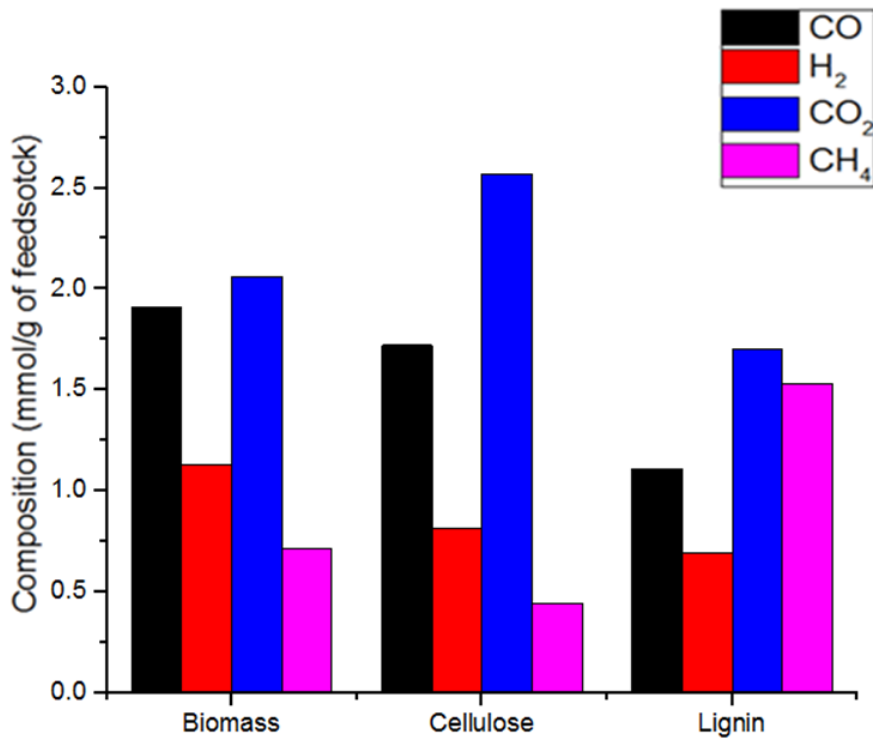
**Figure 5.2-4: Quantity of syngas produced for different biomass components in plasma-catalysis (a), pyrolysis-plasma (b) and pyrolysis-catalysis (c) systems**



a.



b.



c.

**Figure 5.2-5: Detailed composition of produced gas for different biomass components in plasma-catalysis (a), pyrolysis-plasma (b) and pyrolysis-catalysis (c) systems**

### 5.2.2.2 Tar content analysis

The biomass components were also used to investigate the effect of plasma and plasma-catalysis on the steam reforming process for the reduction of the higher molecular weight hydrocarbon tar species in produced liquid. Figure 5.2-6 shows the total hydrocarbon tar content of the product gas in relation to the pyrolysis-catalysis, pyrolysis-plasma and pyrolysis-plasma-catalysis systems for the steam reforming of the biomass pyrolysis tars. The total hydrocarbon tar content was determined from the analysis of the total hydrocarbons condensed in the reactor condensation system and detected using the GC/MS analytical system. The results were then converted to  $\text{mg tar m}^{-3}$  of gas based on the total gas throughput. This figure consists of a series of graphs including plasma-catalytic system (a), pyrolysis-plasma system (b) and pyrolysis-catalysis system (c).

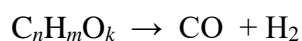
As presented in section 5.1.2, the use of plasma-catalysis system lead to a smaller tar content and higher tar reduction than the use of pyrolysis-plasma or plasma-catalysis systems. This was confirmed with the use of the components of biomass as shown in Figure 5.2-6. For example, in the case of the study of cellulose, the product gas total tar content was  $186 \text{ mg.m}^{-3}$  for the pyrolysis-catalysis system but, was reduced to  $126 \text{ mg.m}^{-3}$  for the pyrolysis-plasma system. However, with the introduction of the catalyst into the plasma zone, the hydrocarbon tar content in the product gas was markedly reduced to  $0.5 \text{ mg.m}^{-3}$ . For lignin, the product gas total tar content was  $255 \text{ mg.m}^{-3}$  for the pyrolysis-catalysis system but, was reduced to  $185 \text{ mg.m}^{-3}$  for the pyrolysis-plasma system and to  $62 \text{ mg.m}^{-3}$  for the plasma-catalysis system. Compared to the hydrocarbon tar content in the absence of the plasma (pyrolysis-catalysis) the pyrolysis-plasma system represents an average reduction in hydrocarbon tar content of 30% and 88% reduction for the pyrolysis-plasma-catalysis system, across the components of biomass.

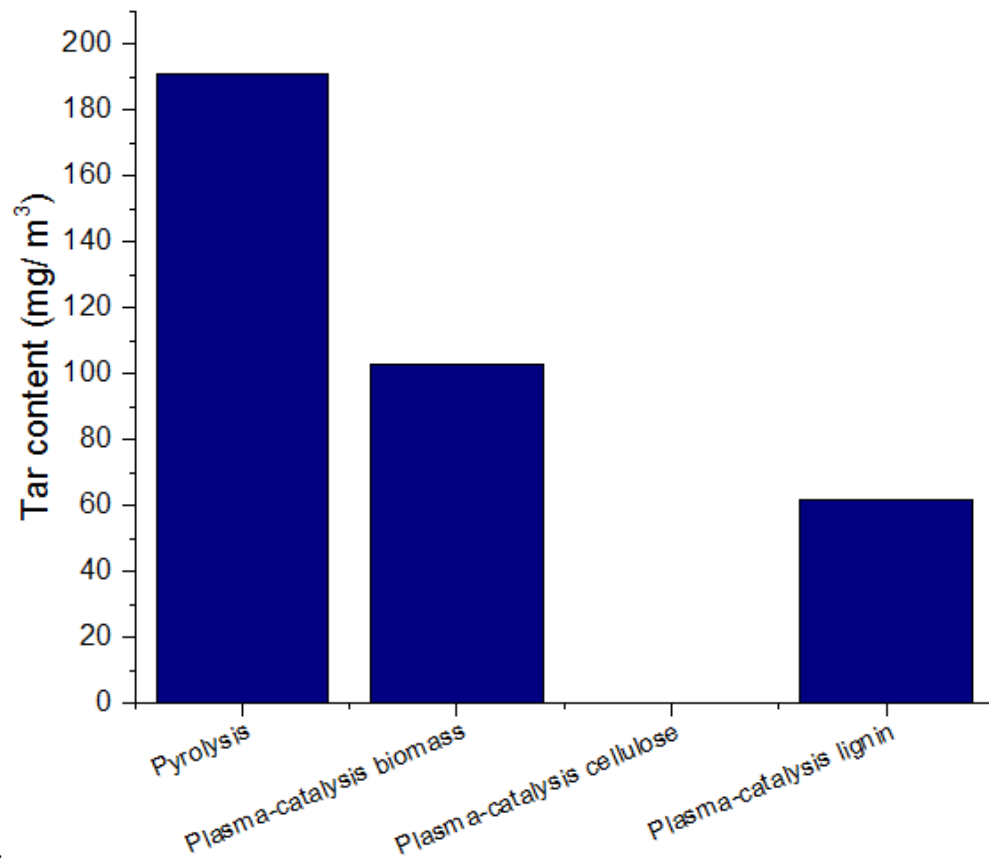
First, it can be observed that more tar compounds were recovered for experiments using lignin than cellulose, cellulose experiments containing the lowest tar content out of the components of biomass. This has also been demonstrated by Yu et. al (Yu et al., 2014) in different experimental conditions. For all components of biomass, the relative percentage of PAHs, in tar composition, increased with temperature. (Evans et al., 1987; Yu et al., 2014) According to Yu et. al (Yu et al., 2014), at higher

temperature, the tar content moved towards a higher molecular weight compounds, such as polycyclic aromatic hydrocarbons (PAHs). For lignin, PAHs originated from phenols and its derivatives. For cellulose and hemi-cellulose, they mainly derived from benzene, toluene, ethylbenzene and xylene isomers (BTEX) and miscellaneous hydrocarbons. Differences between components of biomass is linked to their molecular structures. Lignin is a phenolic macromolecule, containing electron-rich methoxy group which may react easily to form oxygenated compounds such as phenol and its alkyl derivatives. (Liu, 2008) Cellulose and hemi-cellulose are rich in glycosidic bonds, which will first break and dehydrate to generate small-molecule carbonyl derivatives, among others. These compounds will then separate into benzene and its derivatives, furan and toluene. (Nada et al., 2000) To further generate PAH, two main paths are considered: the use of benzene as a precursor, where propylene and butadiene in the decomposition products of cellulose and hemi-cellulose form benzene by diene synthesis reaction; or the use of phenol as a precursor, where the ether bond in lignin breaks to form phenol under acidic conditions and phenolic compounds lose a CO radical to form cyclopentadiene. (Yu et al., 2014) This mechanism could further explain the higher syngas production when using cellulose and hemi-cellulose as feedstock, compared to lignin.

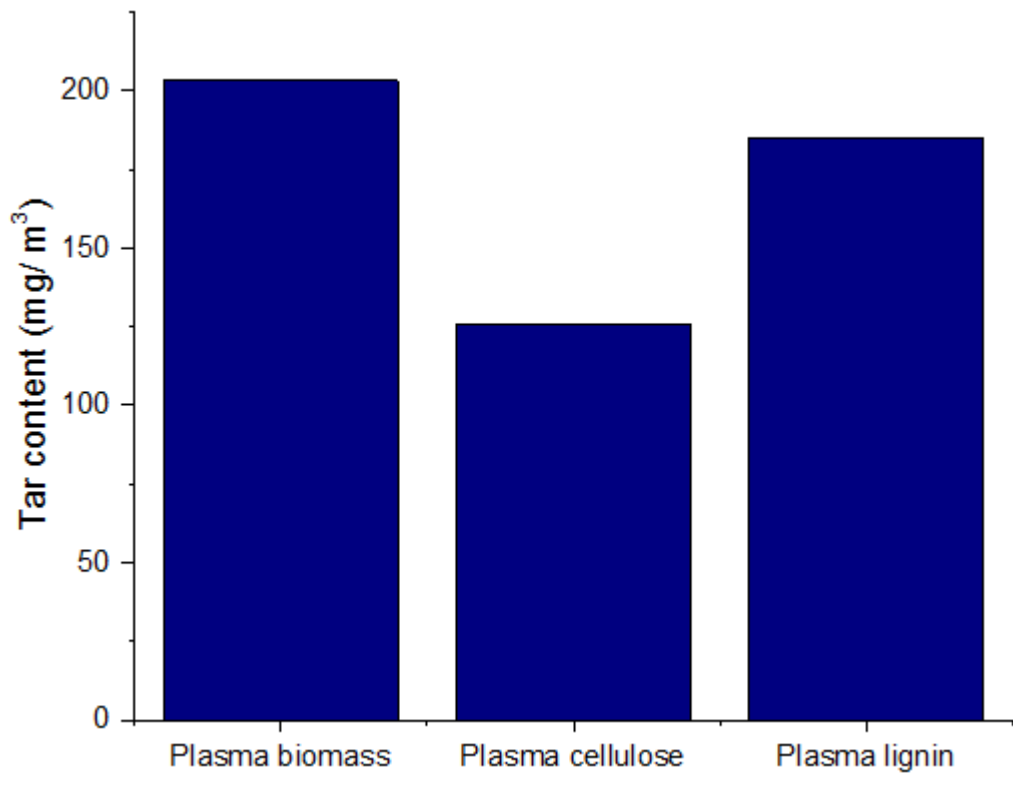
Wu et. al (Wu et al., 2013) observed that the addition of catalyst might promote steam reforming of hydrocarbon oils such as aromatics (Equation 5.1), but also the reforming of oxygenated compounds such as alcohols (Equation 5.3). Thus, Wu et. al suggested that oxygenated compounds are more dominant in derived hydrocarbons from lignin pyrolysis at the first reaction stage, compared with the use of cellulose or hemi-cellulose. (Wu et al., 2013)

### **Equation 5.3**

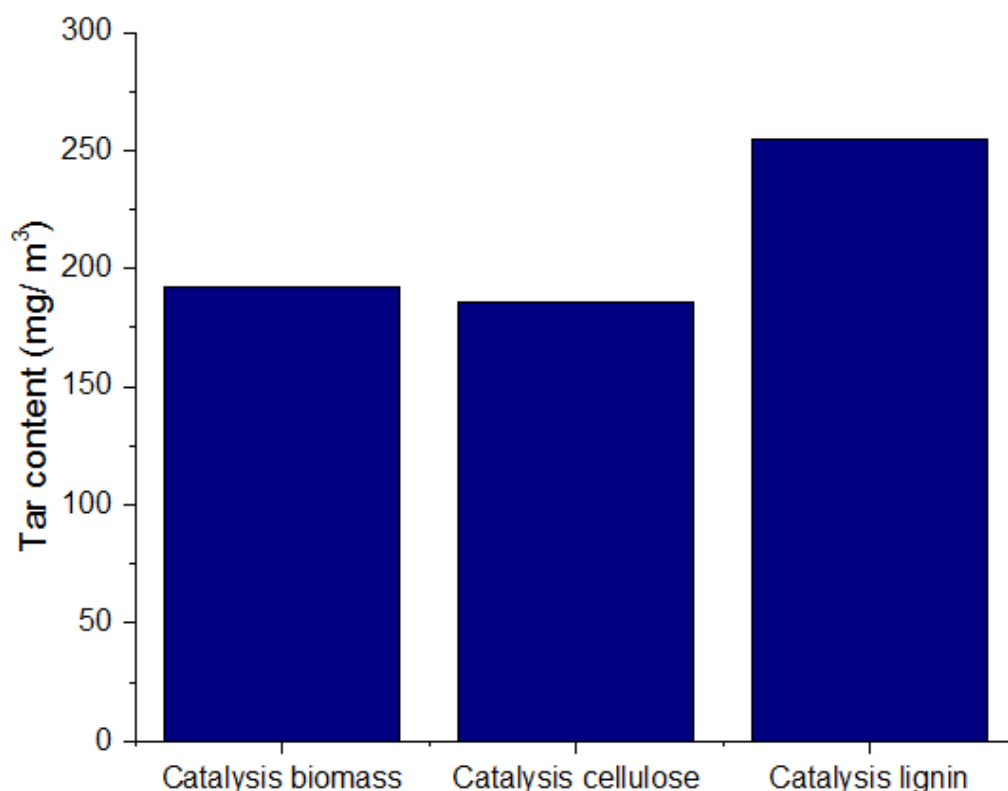




a.



b.

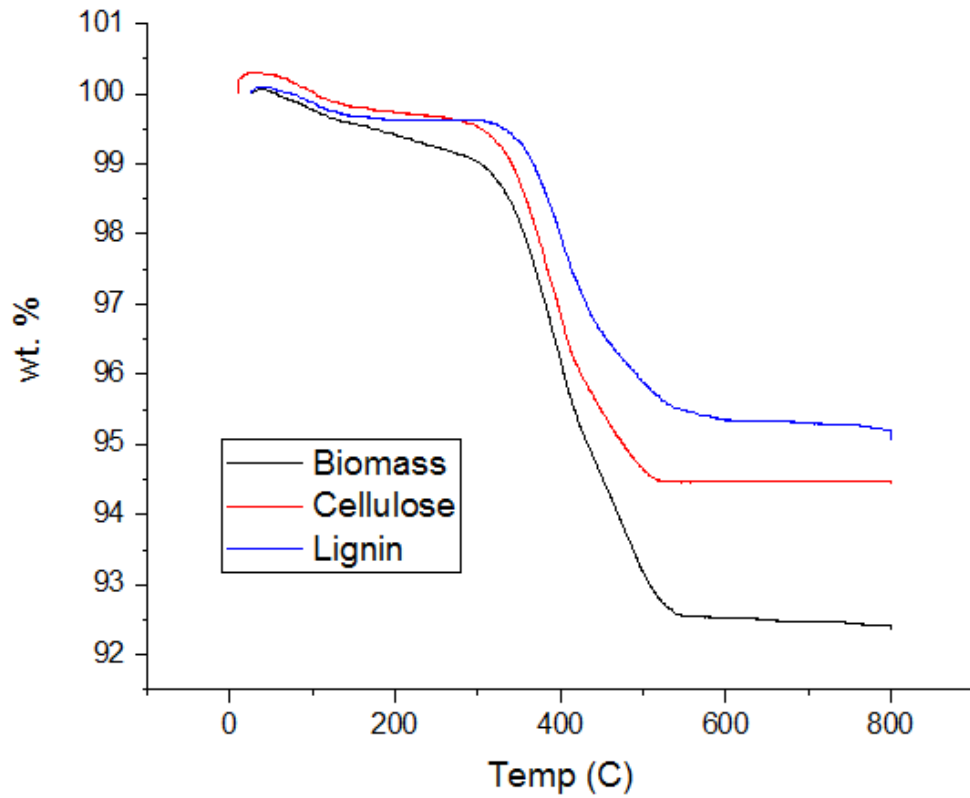


c.

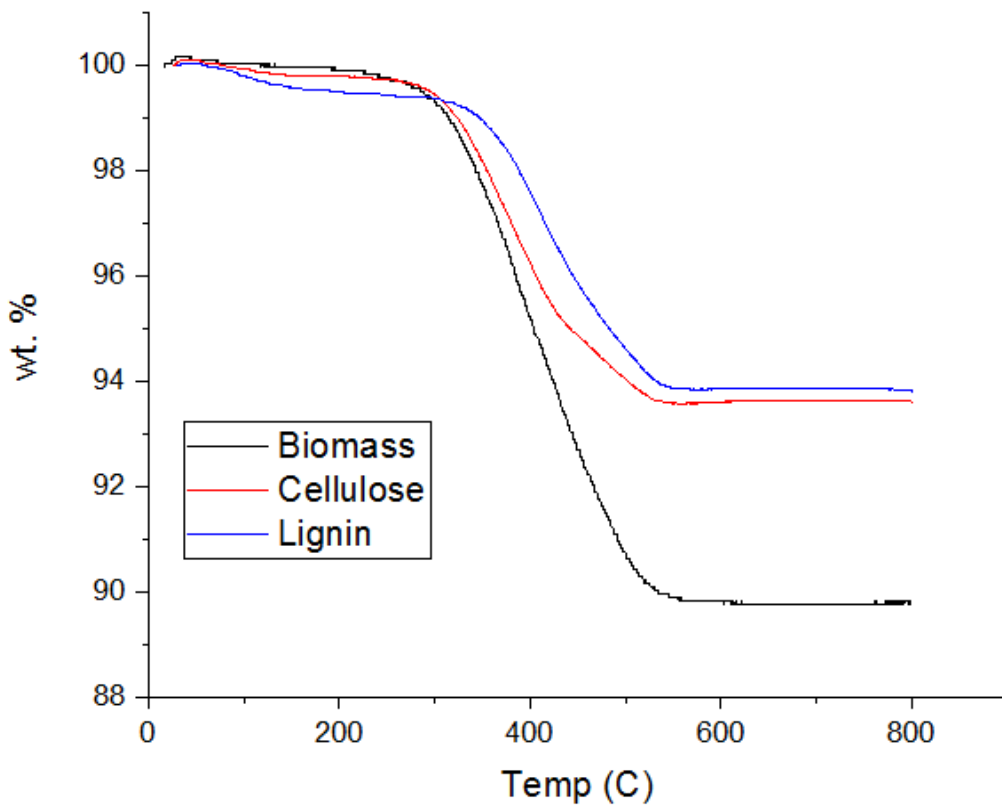
**Figure 5.2-6: Effect of plasma on the tar content for different biomass components in plasma-catalysis (a), pyrolysis-plasma (b) and pyrolysis-catalysis (c) systems**

### 5.2.2.3 Reacted catalyst analysis

Temperature programmed oxidation was used to determine the amount of carbonaceous coke deposited on the catalysts for the pyrolysis-catalysis process and the pyrolysis-plasma-catalysis process. The associated results are presented in Figure 5.2-7. The pyrolysis-catalysis process of biomass resulted in a higher coke deposition compared to the coke deposition with the pyrolysis-plasma-catalysis process. For the pyrolysis-catalysis system, the use of cellulose and lignin led to a coke deposition on the nickel supported on alumina catalyst of 6.38 and 6.18 wt. % respectively. The quantity of coke deposited on the catalyst surface is already quite negligible, as suggested by previous publications such as the one from Wu et al. (Wu, 2013) When used in the plasma-catalysis system, the coke deposition was reduced by approximately 1 wt.%, leading to a coke deposition of 5.52 and 4.93 wt. % when using cellulose and lignin respectively. Thus, the same conclusion could be observed for biomass than for the different components of biomass.



a.



b.

**Figure 5.2-7: Coke deposition on reacted catalyst for different biomass component in plasma-catalysis (a) and pyrolysis-catalysis (b) systems**

### 5.3. Study of different process parameters

In section 5.2, the two-stage biomass pyrolysis with plasma-catalysis system presented in section 3.2.2.2 has been shown to reproduce literature results, confirming the effect of plasma on the different products of the two-stage biomass pyrolysis with plasma-catalysis system, studied in section 5.1. Plasma-catalysis system was identified as the best system for higher syngas and hydrogen production, alongside high tar reduction. To optimise the experimental setup and better understand the effect of different parameters, the influence of power input, steam flow rate, catalyst size and catalyst/feedstock ratio were studied in this section.

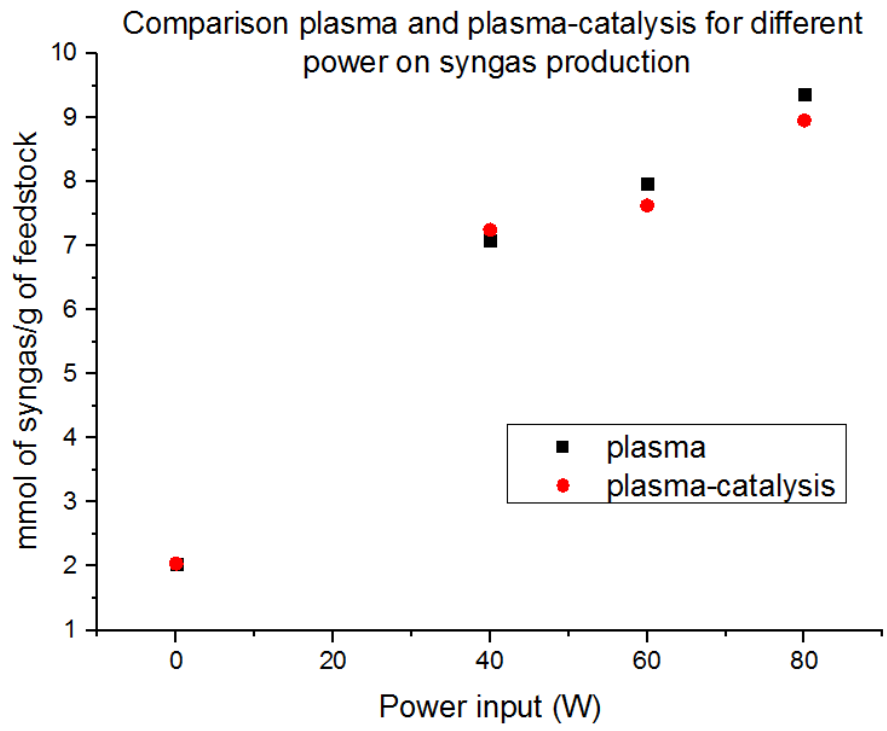
#### 5.3.1 Input power effect

The influence of increasing power input to the plasma system was investigated to determine the influence on product gas yield and gas composition at input powers of 40, 60 and 80 W. A steam flow of 2 g/h was used throughout the experiments. The experimental summary is represented in Table 5.3-1. The results in relation to product gas yield at increasing power input for plasma and plasma-catalytic systems are presented in Figure 5.3-1(a). For both plasma and plasma-catalysis the increase of power input led to an increase of product gas yield. However, when the power was 40 W, plasma-catalysis produced more product gas than the plasma process, but, when the power was higher than 40 W, the plasma system produced slightly more product gas than the plasma-catalytic system.

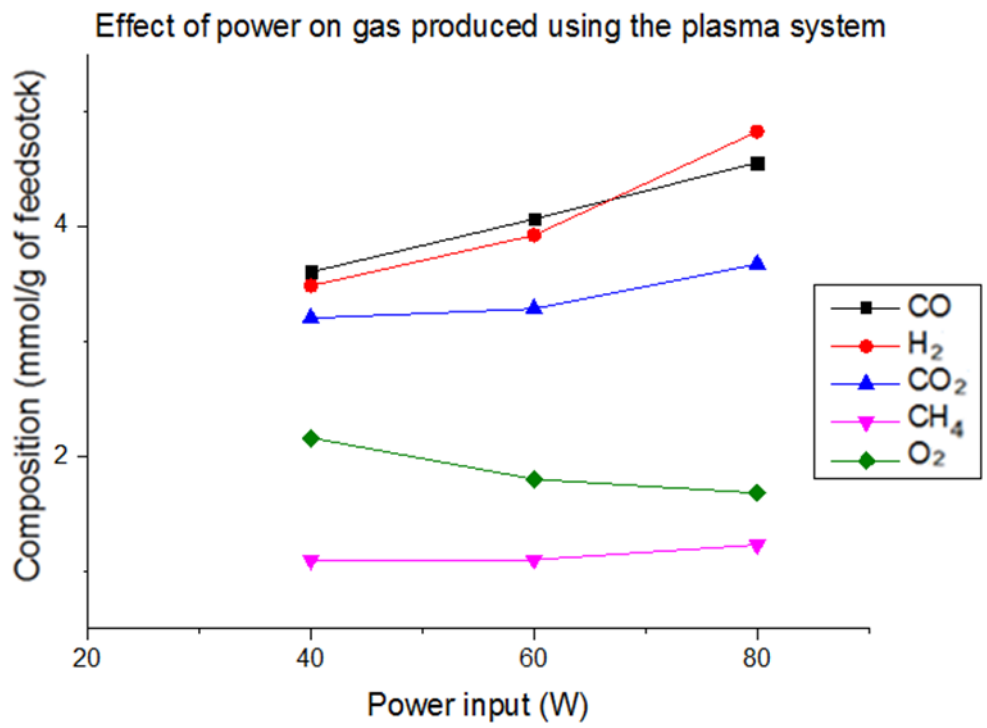
The detailed composition of the produced gas are shown in Figure 5.3-1 (b) for the pyrolysis-plasma process and in Figure 5.3-1 (c) for the pyrolysis-plasma-catalysis process. For each input power, more hydrogen was produced with the plasma-catalytic process compared to the plasma only process. For example,  $3.5 \text{ mmol H}_2 \text{ g}^{-1}_{\text{biomass}}$  feedstock was produced for the plasma system at 40W and  $4.0 \text{ mmol H}_2 \text{ g}^{-1}_{\text{biomass}}$  feedstock for the plasma-catalytic system. On the other hand, carbon monoxide production was higher for the plasma system compared to plasma-catalysis for each power input. Methane production for both systems and all powers were very similar, at around  $1 \text{ mmol g}^{-1}_{\text{biomass}}$ .

**Table 5.3-1: Experimental summary for different power input**

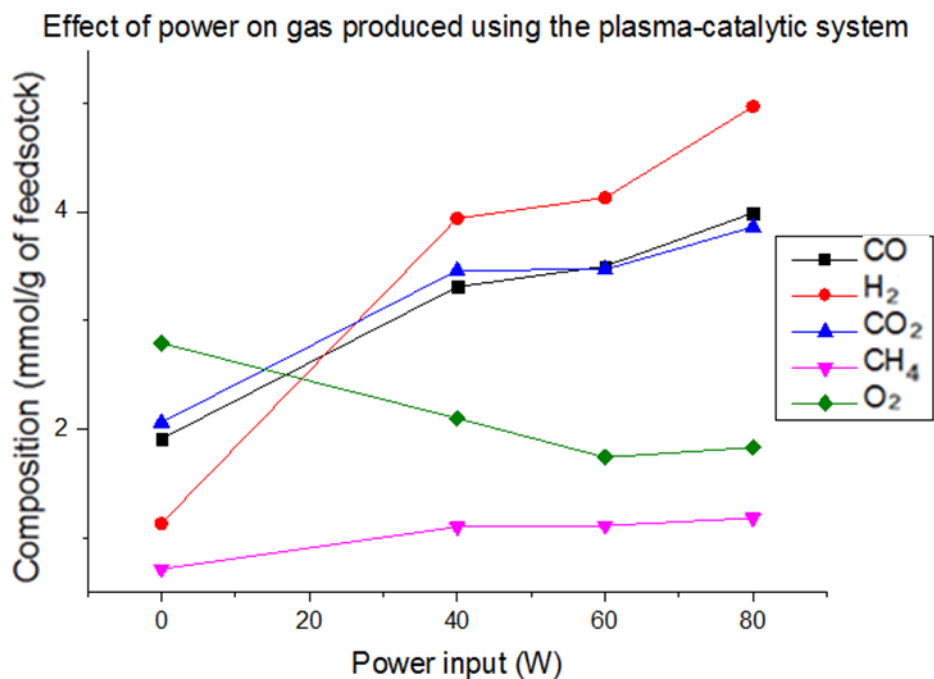
Experiment – results in relation to biomass and reacted water	Pyrolysis-Catalysis	Pyrolysis-Plasma 40 W	Pyrolysis-Plasma 60 W	Pyrolysis-Plasma 80 W	Plasma-Catalysis 40 W	Plasma-Catalysis 60 W	Plasma-Catalysis 80 W	% error
Gas (wt.%)	10.72	15.63	16.01	16.28	15.20	14.92	16.02	3.3
Liquid (wt.%)	76.27	71.69	70.64	73.50	69.47	70.49	65.96	7.4
Char (wt.%)	9.75	10.50	10.55	9.83	10.62	10.13	9.79	2.5
Mass Balance (%)	97.16	99.19	97.66	99.61	96.62	95.97	92.19	1.3
Composition in mmol/g of feedstock								
CO	1.91	3.60	4.06	4.55	3.31	3.50	3.99	4.5
H <sub>2</sub>	1.13	3.47	3.92	4.82	3.94	4.13	4.97	7.0
CO <sub>2</sub>	2.06	3.20	3.28	3.67	3.46	3.47	3.86	6.7
O <sub>2</sub>	2.79	2.16	1.80	1.68	2.10	1.74	1.83	-
CH <sub>4</sub>	0.71	1.1	1.1	1.23	1.1	1.11	1.18	6.8



a.



b.



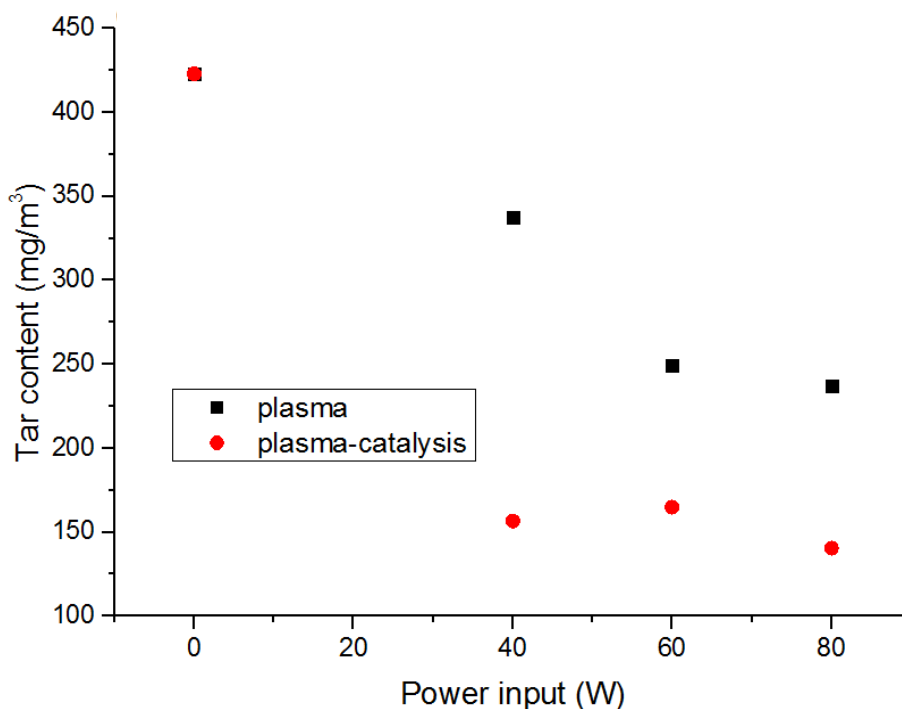
c.

**Figure 5.3-1: Effect of plasma power input on the quantity of syngas produced (a), its effect on the detailed produced gas composition for plasma system (b) and its effect on the detailed produced gas composition for plasma-catalytic system (c)**

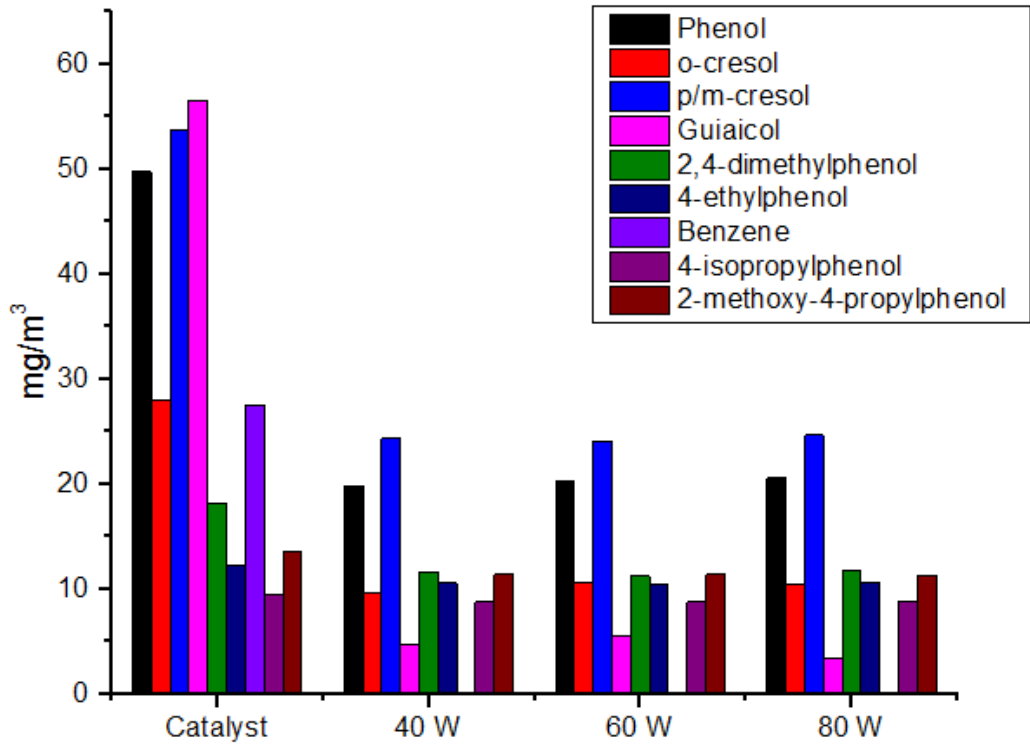
The influence of plasma discharge power in relation to hydrocarbon tar reduction was investigated for the plasma and plasma catalytic systems, different powers were studied, 40, 60 and 80 W. A steam flow of 2 g/h was also used to simulate the reforming process. The results are shown in Figure 5.3-1. The plasma-catalysis produced less hydrocarbon tar than the plasma alone process at all the power inputs investigated. The hydrocarbon tar content in the plasma system was approximately twice the hydrocarbon tar content in the plasma-catalytic system. Moreover, the higher the input power, the lower the product gas hydrocarbon tar content. The optimum result obtained was  $<135 \text{ mg.m}^{-3}$  product gas hydrocarbon tar content for a plasma-catalytic system with an input power of 80 W which produced a hydrocarbon tar reduction of 68% compared to the hydrocarbon tar produced with the pyrolysis-catalysis process. The evolution of hydrocarbon tar content and increased gas production may be attributed to an increase of electric field, electron temperature as well as the temperature of the discharge gas as the input power is increased. Thus, more energetic electrons and active species are created, leading to an easier

breakdown of molecules. This has been observed in the conversion of carbon dioxide in atmospheric DBD by Paulussen et al. (Paulussen et al., 2010).

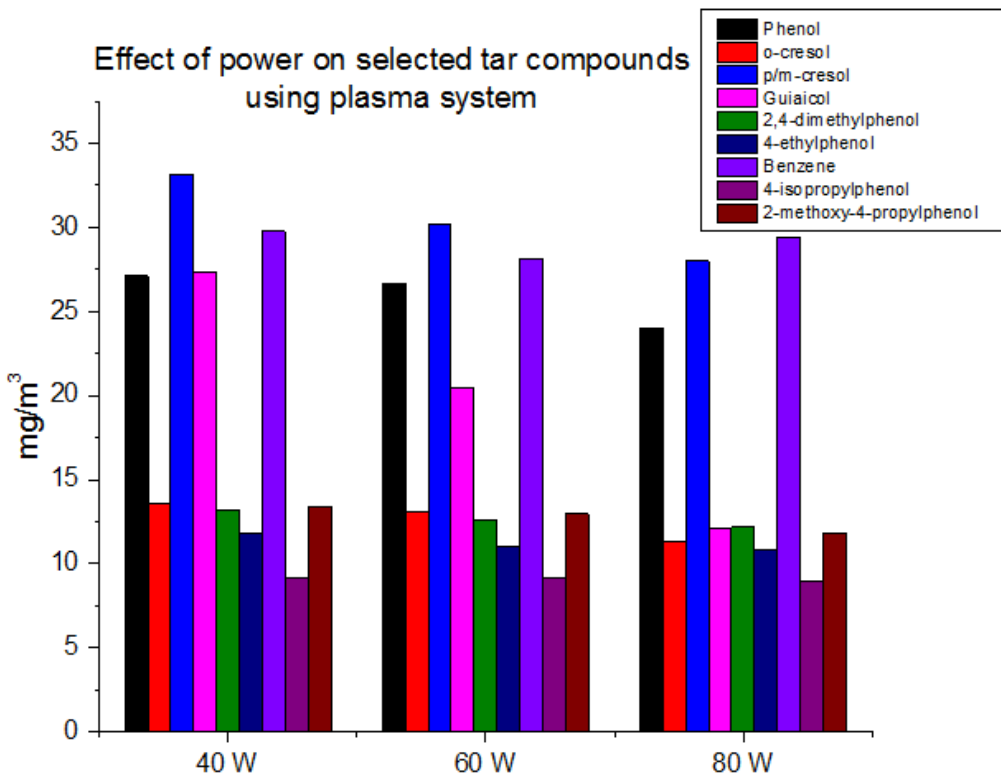
The used Ni-Al<sub>2</sub>O<sub>3</sub> catalysts after use in the plasma-catalytic system with different power inputs were also analysed by XRD and the resultant XRD spectra are shown in Figure 5.3-3. For the catalysts with a power input of 40 W, 60 W and 80 W, the diffraction peaks were more intense for a reaction with a power input of 60 W, with lower peak intensities found at power inputs of 40 W and 80 W. This relates to the nickel particle size suggesting a smaller nickel particle size for the catalysts used at 80 W input power, followed by 40 W and 60 W. It has been suggested that the rate of carbon formation increases with the particle size (Chen et al., 2005; Christensen, et al., 2006). Thus, the formation of carbon is less likely to occur with a power input of 80 W, confirmed by the results obtained with TPO analysis used to determine the carbon deposition on the reacted catalysts and shown in Figure 5.3-4.



a.



b.



c.

**Figure 5.3-2: Effect of plasma power input on tar content (a), its effect on the selected tar compounds for plasma system (b) and its effect on the detailed produced gas composition for plasma-catalytic system (c)**

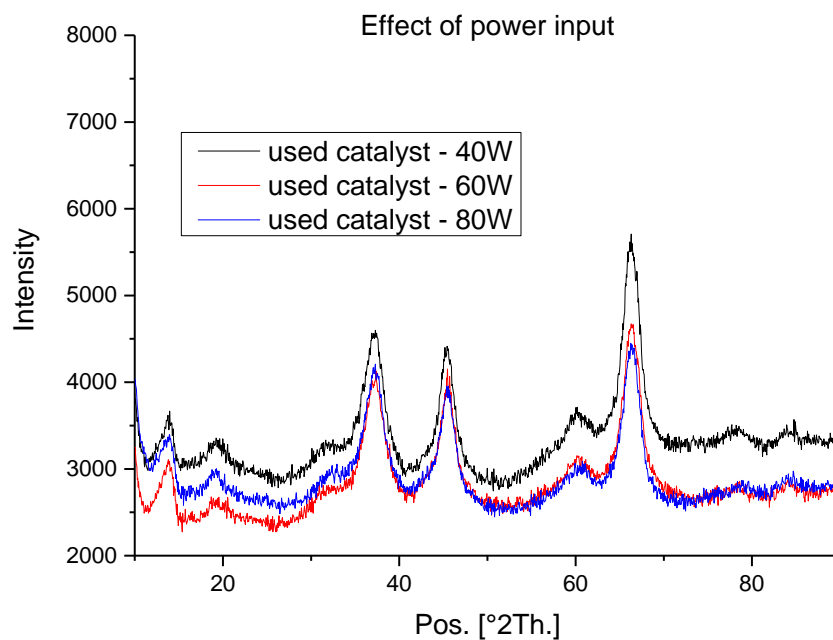


**Figure 5.3-3: Effect of plasma on XRD for reacted catalyst in plasma-catalysis system at different power input – 40 W (black), 60 W (red) and 80W (blue).**

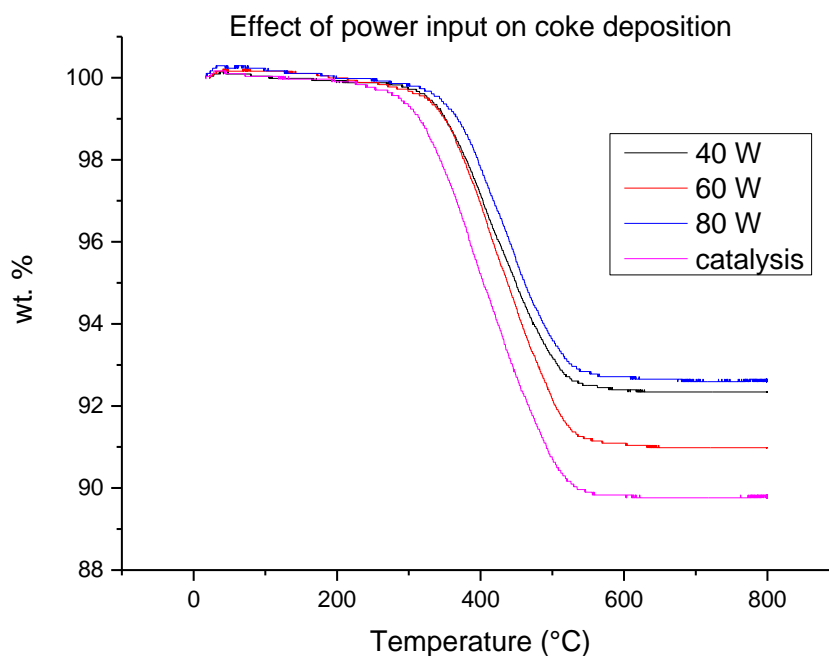


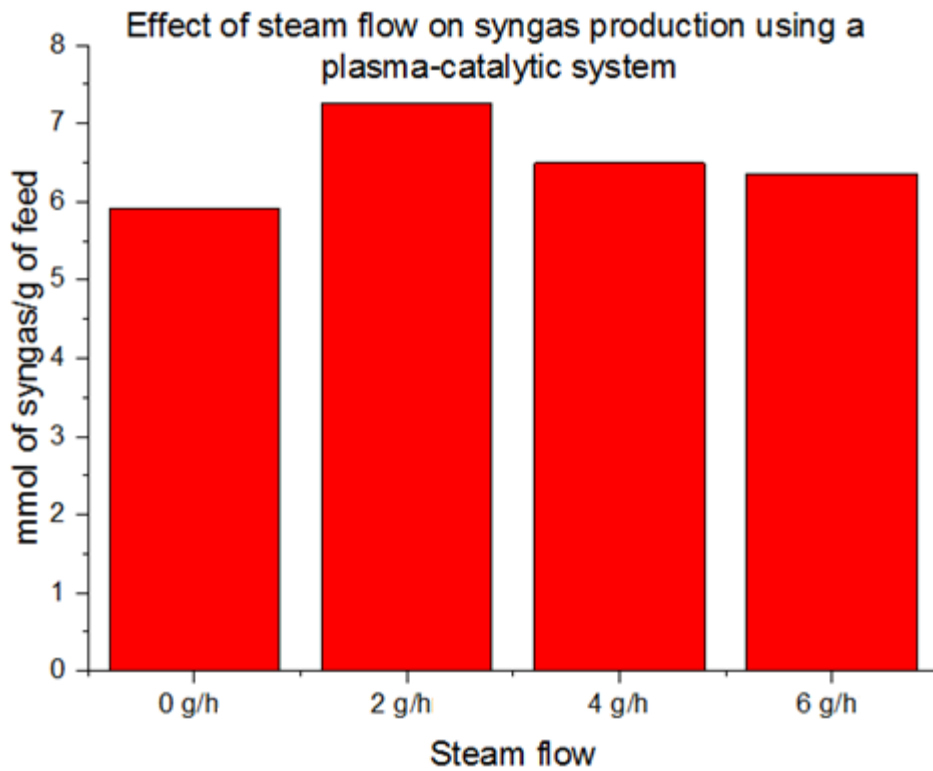
**Figure 5.3-4: Effect of plasma power input on coke deposition on the catalyst at 40 W (black), 60 W (red), 80W (blue) and 0 W/catalysis (pink)**

### 5.3.2 Steam effect

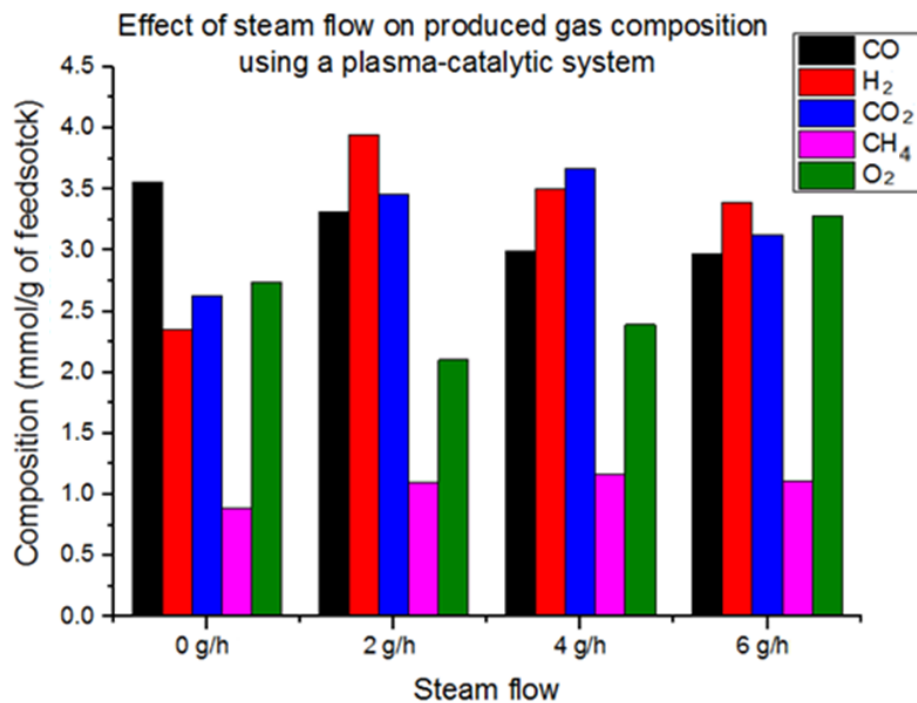
To study the effect of steam flow rate on the plasma-catalysis system for product gas yield, the plasma-catalytic system was investigated at a power input of 40W. These experiments were conducted for different steam (water) flow rates, from 0 to 6 g/h. The results are shown in Table 5.3-2 for the experimental summary, in Figure 5.3-5 (a) for the total product gas produced and Figure 5.3-5 (b) for the detailed gas composition. The production of gas was highest at 2 g/h steam flow rate as shown in Figure 5.3-5 (a). The absence of steam produced lowered gas production and hydrogen production (Figure 5.3-5 (b)). Without steam, the number of active OH<sup>\*</sup> radicals would be reduced and thus could not participate in the collisions and creation of active species leading to H<sub>2</sub> production. Water is a product of biomass pyrolysis, therefore it would be expected that OH<sup>\*</sup> radicals would be generated in the plasma zone, but the amount would be reduced in relation to additional steam input. At higher steam flows, the catalyst partially lost its activity and efficiency, the optimum steam flow in terms of the production of product gas was 2 g/h.

**Table 5.3-2: Experimental summary for different steam flows at a power input of 40 W**

Experiment at 40 W – Steam flow rate (g/h) – results in relation to biomass and reacted water	0	2	4	6	% error
Gas (wt.%)	32.98	15.20	8.17	6.68	3.3
Liquid (wt.%)	42	69.47	84.95	87.99	7.4
Char (wt.%)	23	10.62	5.32	4.32	2.5
Mass Balance (%)	98.98	96.62	98.45	99.17	1.3
Composition in mmol/g of feedstock					
CO	3.56	3.31	2.99	2.97	4.5
H <sub>2</sub>	2.35	3.94	3.50	3.39	7.0
CO <sub>2</sub>	2.63	3.46	3.67	3.12	6.7
O <sub>2</sub>	2.74	2.10	2.39	3.28	-
CH <sub>4</sub>	0.89	1.1	1.17	1.11	6.8



a.

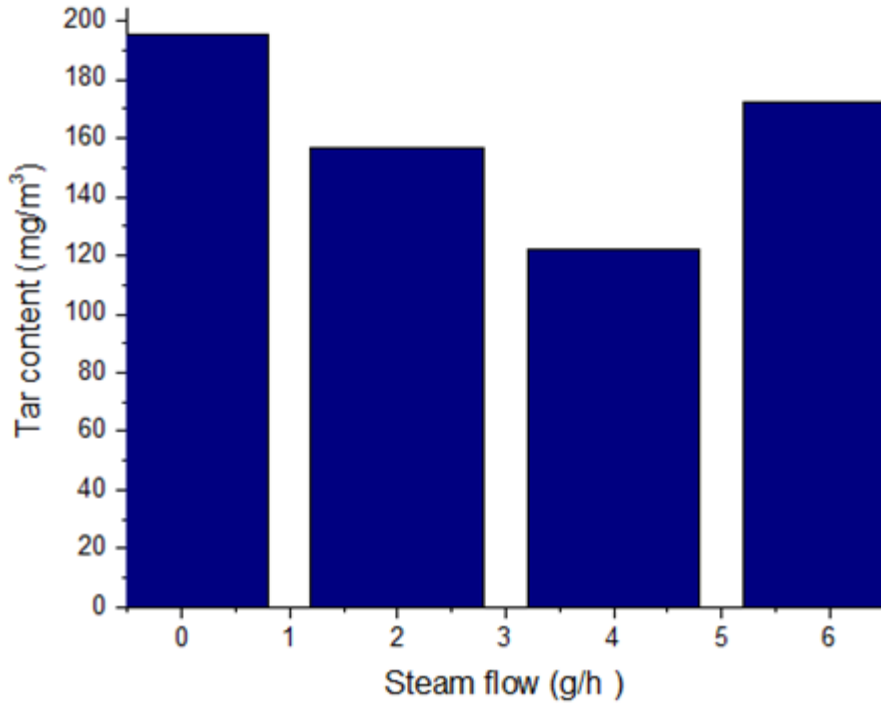


b.

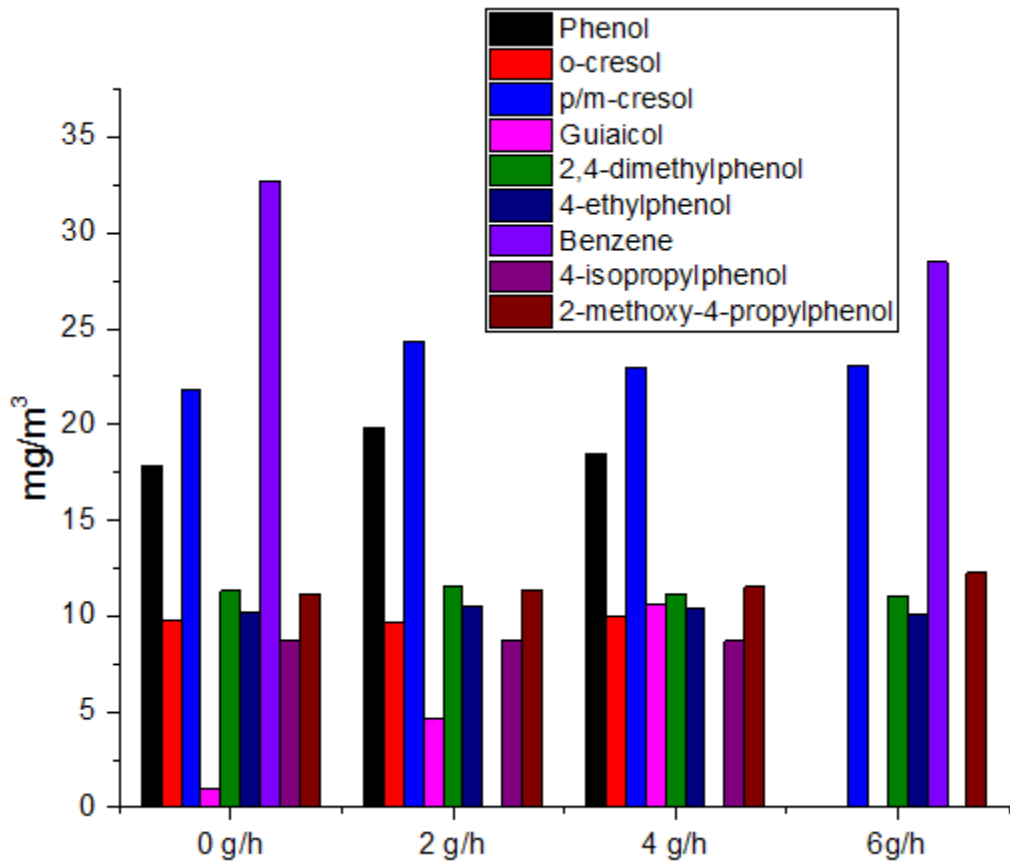
**Figure 5.3-5: Effect of steam flow rate on the quantity of syngas produced (a) and its effect on the detailed produced gas composition (b)**

The influence of input steam flow rate to the pyrolysis-plasma-catalytic process was investigated at 0, 2, 4 and 6 g/h steam (water) input for a fixed power input of 40 W. The results are shown in Figure 5.3-6. At zero steam input the hydrocarbon tar content of the product gas was  $195 \text{ mg.m}^{-3}$ , but as steam was introduced, the hydrocarbon tar content was reduced due to an increase in steam reforming reactions, decreasing to  $150 \text{ mg.m}^{-3}$  at 2 g/h steam input and further reducing to  $125 \text{ mg.m}^{-3}$  at 4 g/h steam input. Input of steam results in higher hydroxyl radical production generated by the radiolysis of water leading to reduction in hydrocarbon tar (Chun, , 2016; Lim et al., 2012). Nunnally et al. (Nunnally et al., 2014) have also emphasised the importance of plasma OH<sup>\*</sup> radical production in the steam reforming process. The OH<sup>\*</sup> formed either through electron interaction with H<sub>2</sub>O or with electrically excited interaction of O<sub>2</sub><sup>\*</sup> and N<sub>2</sub><sup>\*</sup> with H<sub>2</sub>O. The produced OH<sup>\*</sup> radicals readily react with the hydrocarbon tar compounds resulting in decomposition. However, at higher steam input hydrocarbon tar content increased to  $170 \text{ mg m}^{-3}$ , suggesting a lowering of the hydrocarbon tar reduction efficiency of the process. Chun et al (Chun et al., 2016) have also reported that at higher steam inputs the efficiency of benzene removal decreased due to the electronegative characteristics of water. High steam input generates a high number of water molecules which limit the electron density in the system and quenches the activated chemical species. Also, in experiments conducted by Van Durme et al (Van Durme et al., 2007) on toluene removal in humid air by a plasma-catalytic system, water formed mono or multi-layers on the catalyst surface, preventing access to the catalyst active sites.

Temperature programmed oxidation analysis of the reacted catalysts in relation to plasma-catalysis at different steam inputs, represented in Figure 5.3-7, showed that the carbonaceous coke deposits on the catalyst at zero steam input produced a coke deposit of 11.0 wt.% However, with the addition of steam at high water flow rates, the coke deposition was reduced to 6.0 wt.% at 4 g/h steam input.



a.



b.

**Figure 5.3-6: Effect of steam flow rate on the tar production (a) and on selected tar compounds (b)**

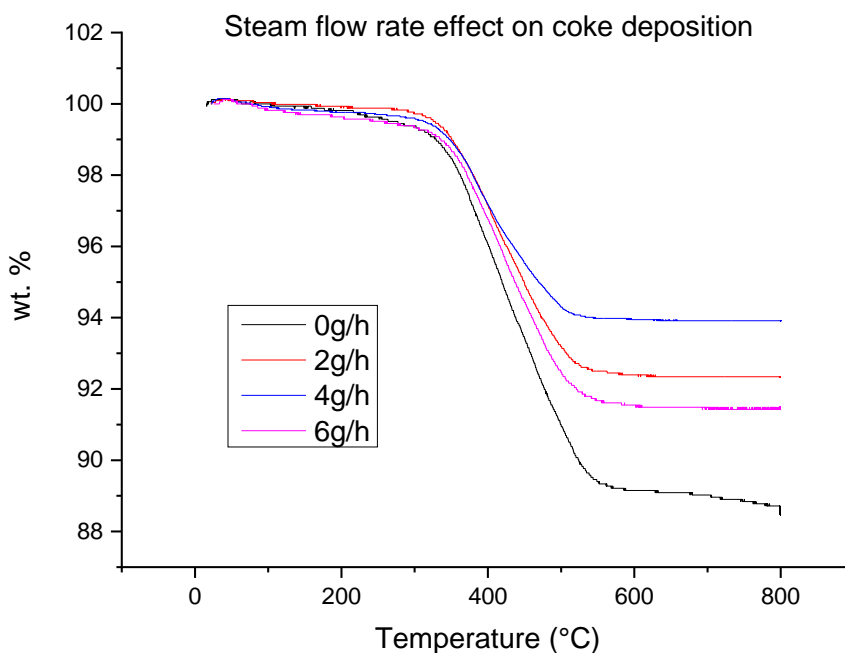


**Figure 5.3-7: Effect of steam flow rate on coke deposition on the catalyst**

To conclude, the study of the influence of the steam flow rate on experiments with a power input of 40 W showed the existence of an optimum flow rate for produce higher syngas and lower tar content. In order to confirm this conclusion, the same experiments were conducted for power inputs of 20 W and 60 W. The analysis of the quantity of syngas produced, shown in Figure 5.3-8, highlighted a similar result to the one previously presented in this section: for each power input, an optimal steam flow rate could be identify – 2 and 4 g/h for 20 W and 60 W respectively – and thus, the previous observation and discussion can be applied to any power input.

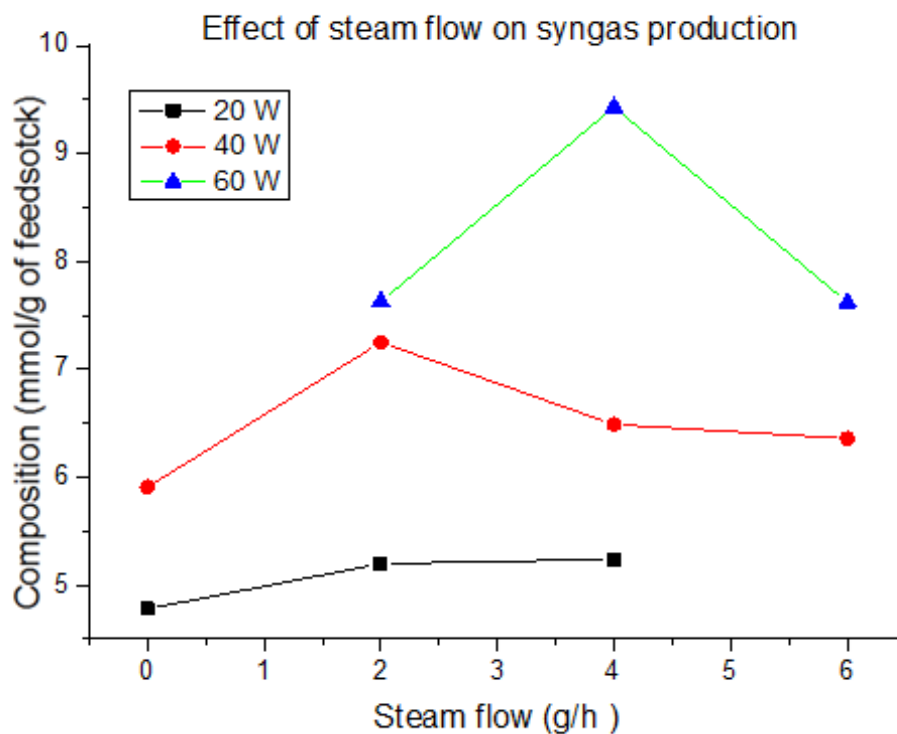


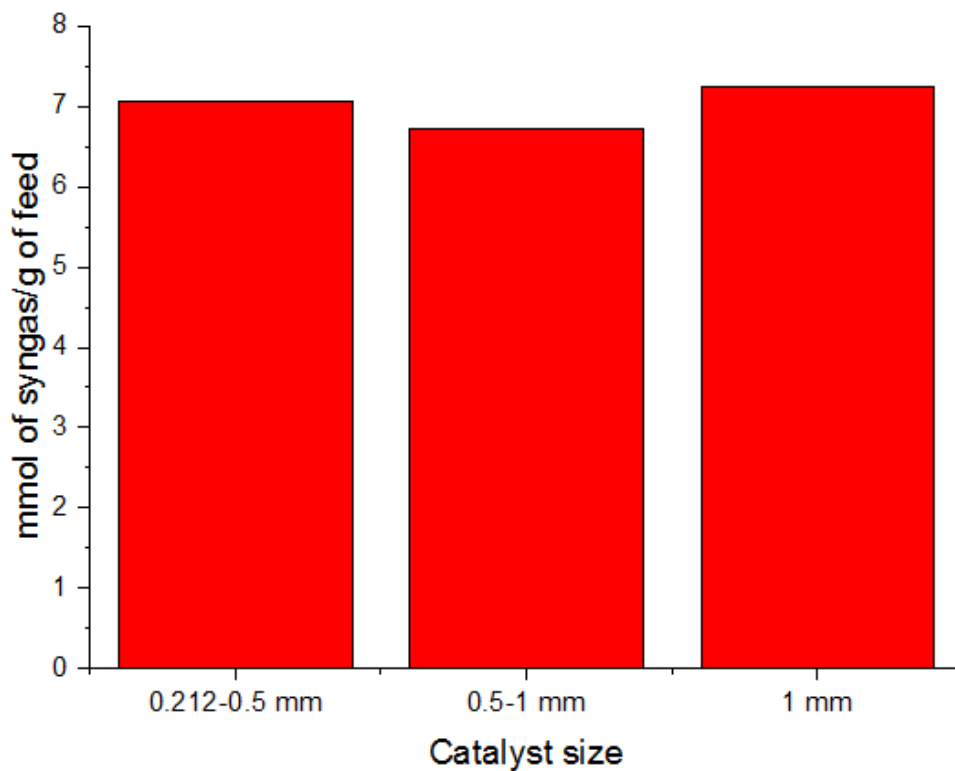
**Figure 5.3-8: Effect of steam flow rate on the quantity of syngas produced at a power input of 20 W (black), 40 W (red) and 60 W (green)**

### 5.3.3 Catalyst particle size effect

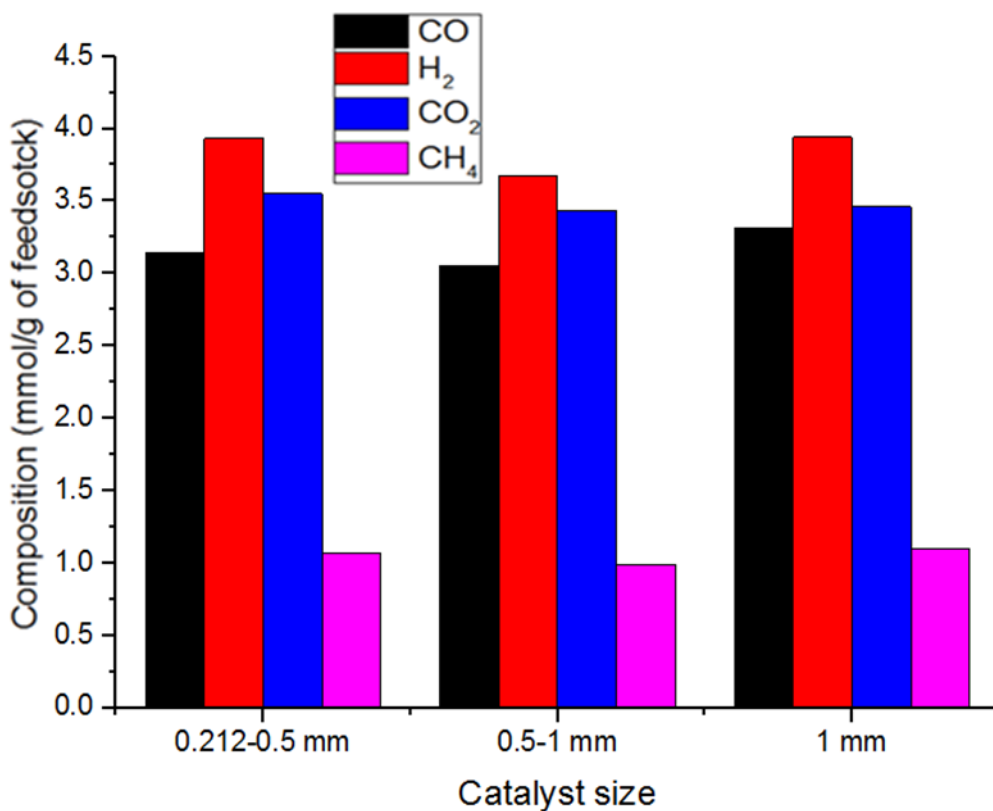
To study the effect of steam flow rate on the plasma-catalysis system for product gas yield, the plasma-catalytic system was investigated at a power input of 40W. These experiments were conducted for different catalyst particle sizes, from 1 mm to 0.212 mm in three categories – 1 mm, 0.5-1 mm and 0.212-0.5 mm. The results are shown in Table 5.3-3 for the experimental summary, Figure 5.3-9 (a) for the total syngas produced and Figure 5.3-9 (b) for the detailed gas composition. The production of syngas was slightly higher for the biggest particle size as shown in Figure 5.3-9 (a).

**Table 5.3-3: Experimental summary for different catalyst particle sizes**

Experiment at 40 W – catalyst particle size (mm) – results in relation to biomass and reacted water	1	1 – 0.5	0.5 – 0.212	% error
Gas (wt.%)	15.20	16.21	12.07	3.3
Liquid (wt.%)	69.47	71.87	72.05	7.4
Char (wt.%)	10.62	9.96	7.74	2.5
Mass Balance (%)	96.62	94	92.54	1.3
Composition in mmol/g of feedstock				
CO	3.31	3.05	3.14	4.5
H <sub>2</sub>	3.94	3.67	3.92	7.0
CO <sub>2</sub>	3.46	3.43	3.55	6.7
CH <sub>4</sub>	1.1	0.98	1.07	6.8

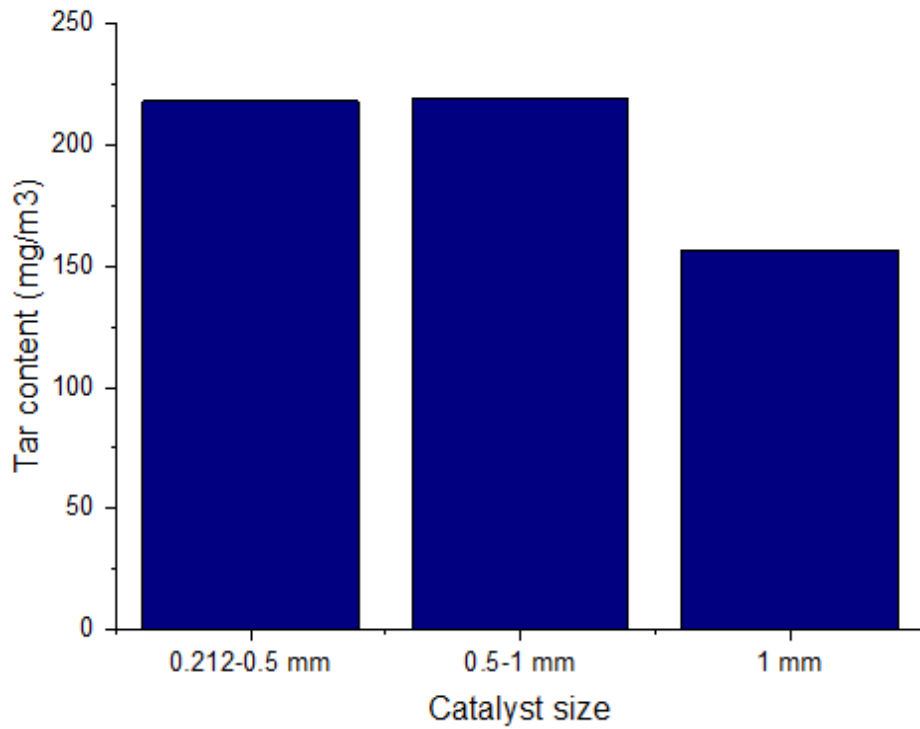


a.

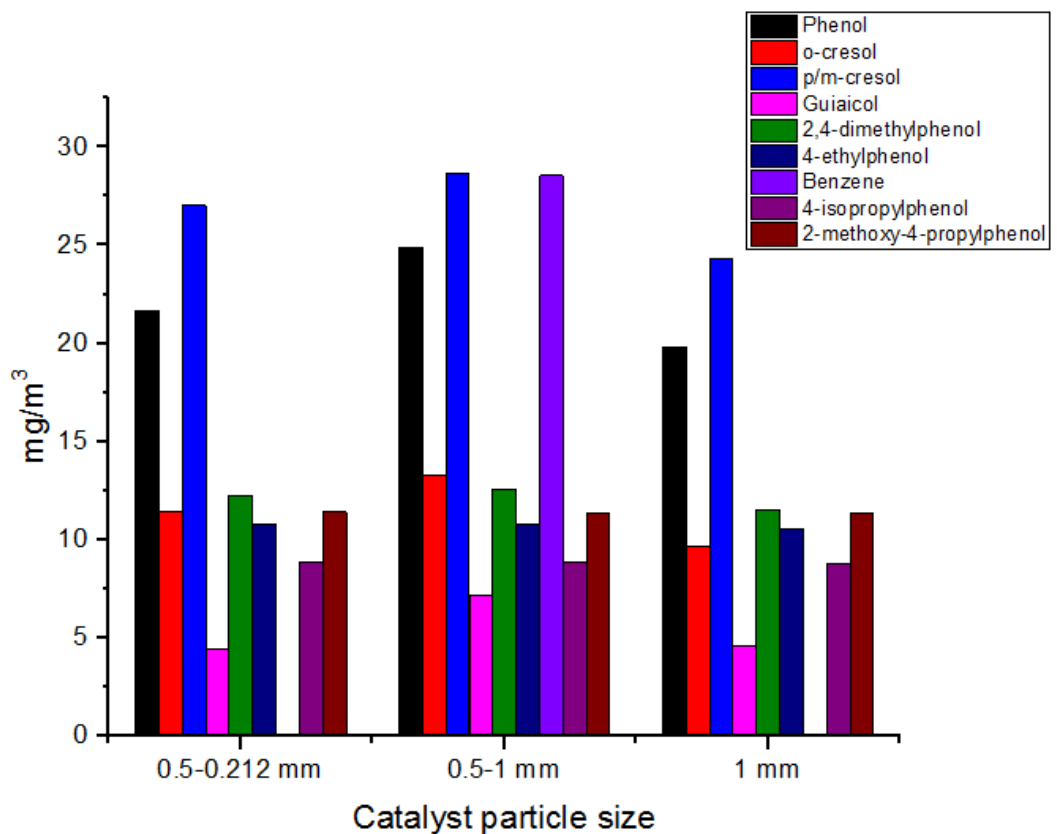


b.

**Figure 5.3-9: Effect of catalyst particle size on the quantity of syngas produced (a) and its effect on the detailed produced gas composition (b)**



a.



b.

**Figure 5.3-10: Effect of catalyst particle size on the tar production (a) and on selected tar compounds (b)**

The effect of catalyst size on the oil composition can be observed in Figure 5.3-10. These results showed that the tar content was smaller for the biggest catalyst size, 1mm diameter. Therefore, 1mm diameter was the optimum catalyst size. This can be explained by the fact that different particle size lead to different physical properties to the discharge: smaller particle size present not only filament discharge, as in traditional DBD, but also surface discharges in the catalyst. The suppression of filamentary discharges is a result of a weak interaction between the plasma and the catalyst. This phenomenon has been observed by Tu and Whitehead, when comparing a fully packed-bed DBD of Ni-catalyst with a packing method enabling more void space and filamentary discharges. (Tu et al., 2012) The same phenomenon can be observed for the results of coke deposition for the different catalyst sizes, represented in Figure 5.3-11. The particle size of 1 mm diameter had less coke deposited on the catalyst than other particle sizes, showing a better interaction between the plasma and the catalyst. The diameter of 1 mm for the catalyst particle size was thus considered optimum for our plasma catalysis study.

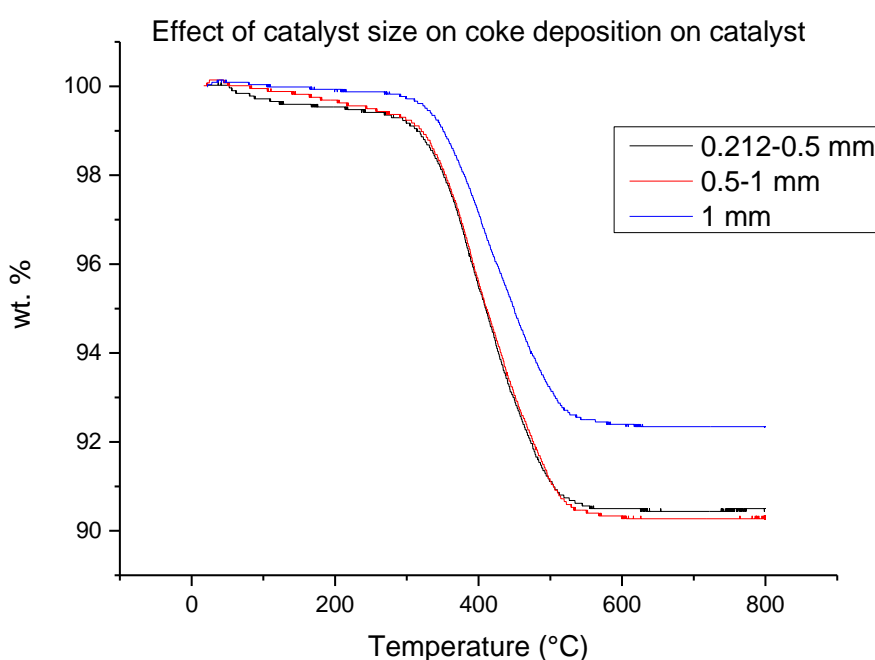


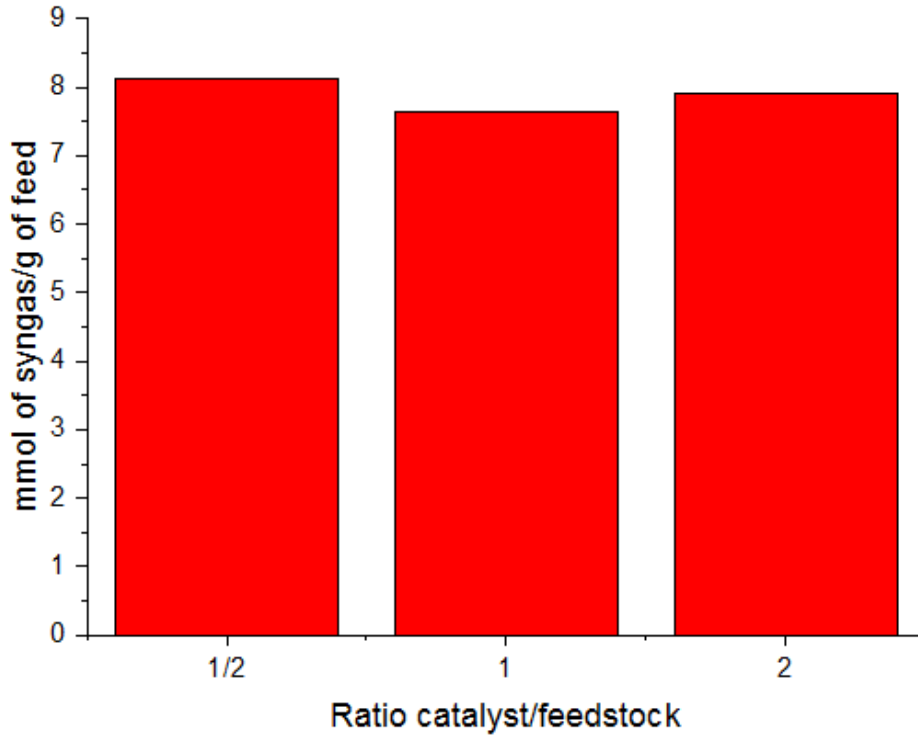
**Figure 5.3-11: Effect of catalyst particle size on coke deposition on the catalyst**

### 5.3.4 Ratio Catalyst/Feedstock effect

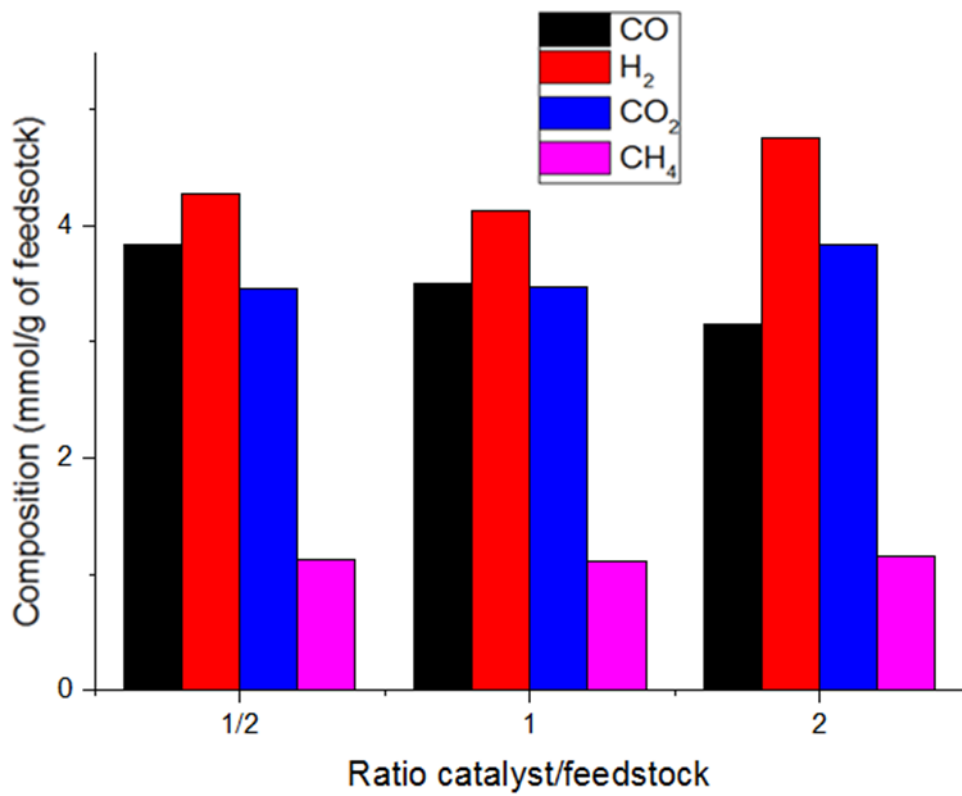
To study the effect of steam flow rate on the plasma-catalysis system for product gas yield, the plasma-catalytic system was investigated at a power input of 60W. These experiments were conducted for different ratio catalyst/feedstock, from 0.5 to 2. The results are shown in Table 5.3-4 for the experimental summary, Figure 5.3-12 (a) for the total product gas produced and Figure 5.3-12 (b) for the detailed gas composition. The production of syngas was slightly higher for the biggest particle size, as shown in Figure 5.3-12 (a). Looking into the detailed composition of the produced gas, presented in Figure 5.3-12 (b), methane production was kept stable for different ratios. The production of carbon dioxide increased whereas the production of carbon monoxide decreased when the ratio of catalyst/feedstock increased. The more catalyst is put into the plasma-catalytic system, the more hydrogen is produced. This is as expected as Nickel catalysts are commonly used in the gasification industry to enhance the hydrogen production. (Yang et al., 2015)

**Table 5.3-4: Experimental summary for different catalyst/feedstock ratios**

Experiment at 60 W – catalyst/feedstock ratio – results in relation to biomass and reacted water	0.5	1	2	% error
Gas (wt.%)	15.21	14.92	14.66	3.3
Liquid (wt.%)	69.83	70.49	67.81	7.4
Char wt.%)	9.91	10.13	10.73	2.5
Mass Balance (%)	95.38	95.97	94.49	1.3
Composition in mmol/g of feedstock				
CO	3.84	3.50	3.15	4.5
H <sub>2</sub>	4.28	4.13	4.75	7.0
CO <sub>2</sub>	3.46	3.47	3.84	6.7
O <sub>2</sub>	1.85	1.74	1.62	-
CH <sub>4</sub>	1.13	1.11	1.16	6.8

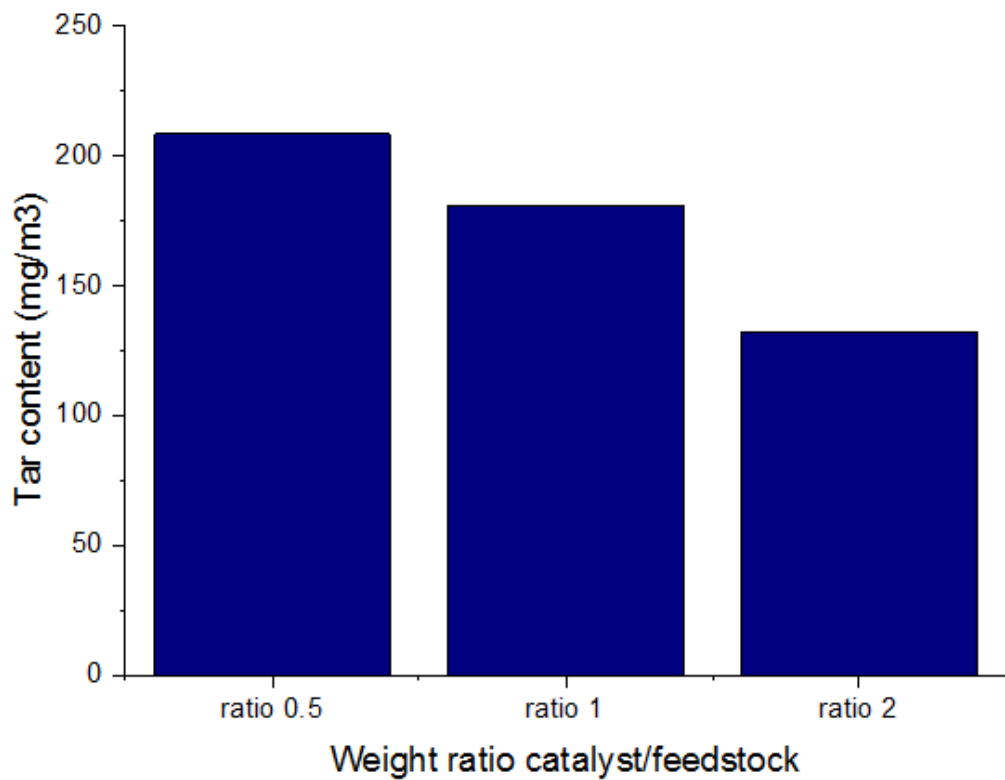


a.

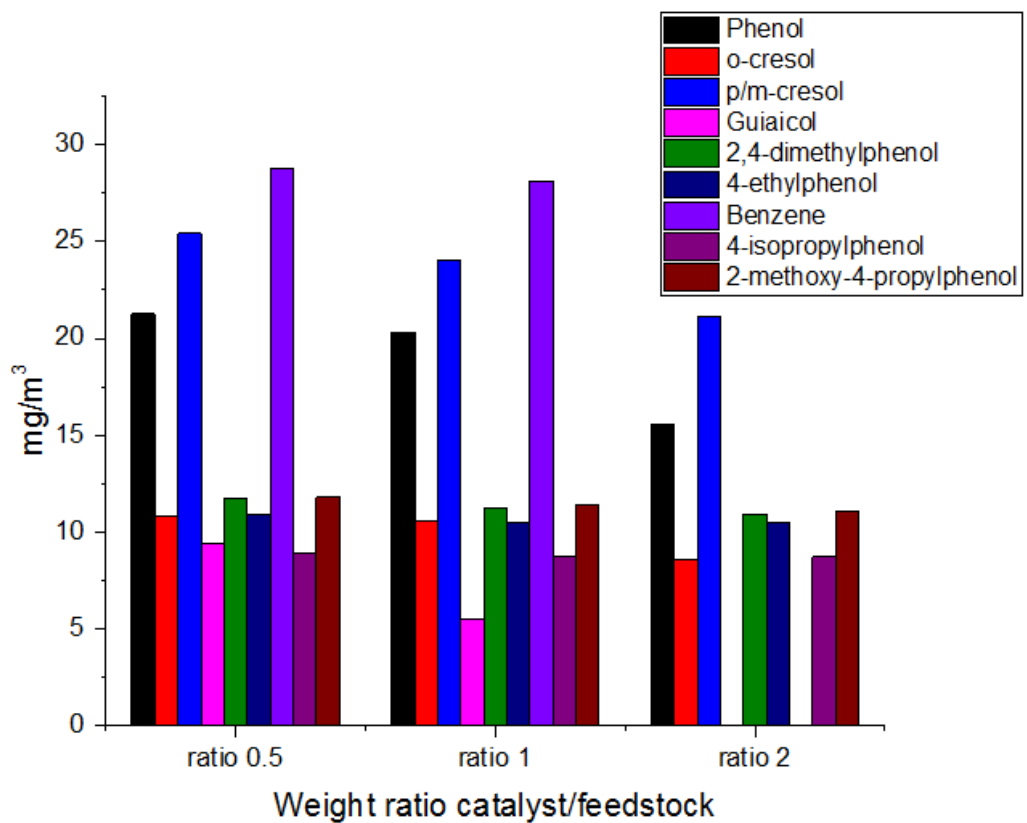


b.

**Figure 5.3-12: Effect of catalyst/feedstock ratio on the quantity of syngas produced (a) and its effect on the detailed produced gas composition (b)**



a.



b.

**Figure 5.3-13: Effect of catalyst/feedstock ratio on the tar production (a) and on selected tar compounds (b)**

The oil composition for the different catalyst/feedstock ratios are represented in Figure 5.3-13 through the tar content in  $\text{mg.m}^{-3}$  and the concentration in selected tar compounds. The tar content decreased as the quantity of catalyst in the plasma-catalytic system increased. Using from half a gram to two grams of catalyst reduced the tar content by more than 60%, from  $200 \text{ mg.m}^{-3}$  to  $125 \text{ mg.m}^{-3}$ . The same was observed for selected tar compounds. Similarly to the gas production results, as the more catalyst was put into the plasma-catalytic system, the more tar compounds will be reduced through the increased number of catalyst active sites. As expected with a higher quantity of catalyst, less coke was deposited during the experiment with the highest ratio, as presented in Figure 5.3-14.

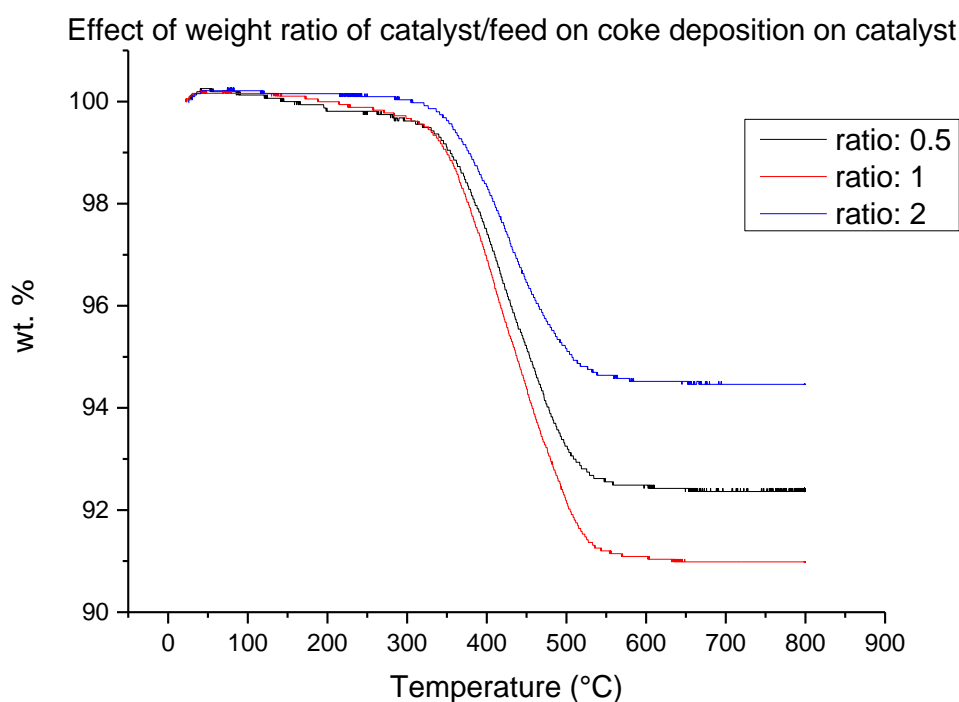


**Figure 5.3-14: Effect of catalyst/feedstock ratio on coke deposition on the catalyst**

## 5.4 Summary

The plasma-catalysis process has been investigated for the production of hydrogen-rich gas using real-world biomass as the feedstock. The process involves initial pyrolysis of the biomass to generate a wide range of hydrocarbon gases which are then passed directly to the plasma-catalysis steam reforming reactor. The influence of plasma alone and various process parameters were investigated. The results showed that plasma processing of the biomass pyrolysis gases in the absence of a catalyst resulted in a marked increase in total gas yield compared with catalytic steam reforming without plasma. Addition of catalyst (plasma-catalysis) produced only a small increase in total gas yield. The hydrogen yield in the product gases using pyrolysis-plasma reforming showed a three-fold increase compared to pyrolysis-catalysis and the hydrogen yield was further increased with the pyrolysis-plasma-catalysis.

A wide range of aromatic and oxygenated compounds were identified in the condensed hydrocarbon tar phase. Pyrolysis-catalysis (non-plasma) processing was shown to reduce the yield of tar but the introduction of non-thermal plasma to the process produced a decrease in tar content of the product gas by a further 64%. Even plasma alone (biomass pyrolysis-plasma) was found to be more efficient to remove tar from the product gas, with a 21% reduction in tar content compared to pyrolysis-catalysis. The reforming of the hydrocarbon tar compounds producing increased hydrogen content of the product gas.

As also demonstrated in the literature, the reduction of toluene was improved when using a plasma-catalytic system. Moreover, the increase of power input enhanced the removal efficiency of toluene. Comparing plasma-catalysis, pyrolysis-plasma and pyrolysis-catalysis for the different components of biomass, the same observation than for biomass could be made. Plasma-catalysis lead to higher syngas production, higher hydrogen production, lower tar content and lower coke deposition. A high content of lignin in the biomass might promote methane and tar production, whereas a high content of cellulose might favour the production of carbon monoxide and higher syngas production. The highest hydrogen production was obtained when using pyrolysis-plasma-catalysis, with very similar quantity produced for both components of biomass.

The influence of power input to the plasma system showed that increasing the power markedly increased total gas yield and hydrogen content of the product gas. There was a corresponding decrease in the tar produced for the pyrolysis-plasma system as well as a further slight tar reduction for the pyrolysis-plasma-catalytic system. The influence of the steam flowrate on the system showed that there was an optimum input rate of steam and at high steam inputs, the catalyst became saturated with water resulting in the plasma-catalytic process becoming less efficient resulting in a decrease in total gas and hydrogen production and consequent rise in tar content of the product gas. The influence of catalyst particle size demonstrated that the higher the particle size the better, as it led a stronger interaction between the plasma and the catalyst through the increase of void space and filamentous discharges. The influence of catalyst/feedstock ratio confirmed a result previously observed in catalytic cracking: the more catalyst in the system, the more hydrogen and syngas is produced and the more efficient is the reduction of tar compounds.

## **Chapter 6: Study of the catalytic effect on DBD plasma-catalysis**

This chapter consists of three sections, focusing on the study of the catalyst used in a dielectric barrier discharge (DBD) plasma-catalytic reactor to produce high-quality syngas and reduce tar compounds from biomass. The experiments conducted for this chapter were using the two stage fixed bed reactor coupled with a DBD plasma catalytic system previously used in Chapter 5, and described in Chapter 3, section 3.2.2. The different sections of this chapter are described below.

Section 6.1 examines the effect of metal promoters on 5 wt.% nickel supported on alumina catalyst on the quality of the syngas produced and the reduction of tar compounds from biomass pyrolysis when using the plasma-catalysis system. The influence of promoter by adding 5 wt.% Mg, Co, Ce, Cu, Fe and Ni to a 5 wt.% Ni-catalyst supported on alumina was investigated in this section.

Section 6.2 focuses on studying the effect of nickel loading on the quality of the syngas produced and the reduction of tar compounds when using the pyrolysis-plasma-catalysis system. The effect of different loadings of Nickel supported on our alumina support, for loadings of 0, 5 and 10 wt.%, is discussed in this section.

Section 6.3 describes the study of the influence of different catalyst supports on the the quality of syngas produced and the reduction of tar compounds when using the plasma-catalysis system for processing biomass. Three different supports were studied: Alumina, a usual support for thermal processes; titanium oxide, a catalyst activated by UV stimulation used in many plasma-catalysis studies; and Y-zeolite, a catalyst mainly used in oil refinery to crack tar. The effect of these three supports on the results from biomass gasification products after plasma-catalytic treatment was reported.

## **6.1 Effect of metal promoters on 5 wt.% Ni supported on alumina**

To study the effect of different metal promoters on the pyrolysis, plasma-catalysis of biomass, different metals were studied: Iron and copper have been intensively used for catalysing water gas shift reactions and thus could lead to higher hydrogen production (Rhodes et al., 1995); Cerium and magnesium have been shown to enhance the stability of catalyst performance in thermal catalytic processes (Özkara-Aydinoğlu et al., 2010; Alipour et al., 2014; Sengupta et al., 2015); Cobalt has demonstrated improved activity and stability of the catalyst when added on Ni-catalysts (Xu et al., 2009; Sengupta et al., 2015); and nickel, a traditional metal used in steam reforming processes for its good catalytic effect on hydrogen production and its comparatively low cost (Wu et al., 2010). These different promoters have been shown to be effective for thermal catalysis and are investigated in this section to identify their effects when used for plasma-catalysis processes.

The influence of promoter was studied by adding 5 wt.% Mg, Co, Ce, Cu, Fe and Ni to a 5 wt.% Ni-catalyst supported on alumina. The experiments used the equipment and procedure described in section 3.2.2.2. a power input of 40 W to sustain the plasma discharge and an input steam flow rate of 2 g/h to simulate the steam reforming process.

### **6.1.1 Metal promoter effect on gas production**

The results in terms of product yield and gas composition and yield, in relation to the pyrolysis, plasma-catalysis of biomass are presented in Table 6.1-1. The quantity of gas produced during the experiments using different promoters was comparable between all promoters. Whereas nickel and copper experiments produced about 12.3 and 12.5 wt.% respectively, of gas yield most promoters produced about 13 wt.% of gas per experiment.

First, the syngas production, represented in Figure 6.1-1 (a). was quite similar for all promoters, around  $7 \text{ mmol.g}^{-1}_{\text{biomass}}$ , with a slightly higher syngas production (over  $7.1 \text{ mmol.g}^{-1}_{\text{biomass}}$ ) for the Ce promoter, and a lower syngas production for the Cu promoter ( $6.6 \text{ mmol.g}^{-1}_{\text{biomass}}$ ). Looking into the more detailed gas production in Figure 6.1-1 (b), the carbon monoxide production is similar for all metal promoters, at around  $3.15 \text{ mmol.g}^{-1}_{\text{biomass}}$ . Co promoter resulted in the highest carbon monoxide

production with over  $3.25 \text{ mmol.g}^{-1}_{\text{biomass}}$ , and Cu promoter was the lowest with around  $3.1 \text{ mmol.g}^{-1}_{\text{biomass}}$ . The hydrogen production was the highest for the Ce promoter, at around  $4.2 \text{ mmol.g}^{-1}_{\text{biomass}}$ , and the lowest for the Cu promoter, at around  $3.6 \text{ mmol.g}^{-1}_{\text{biomass}}$ . Methane production was similar between most promoters, with a production between  $1.15$  and  $1.25 \text{ mmol.g}^{-1}_{\text{biomass}}$ , except Cu promoter with the lowest produced quantity, around  $0.8 \text{ mmol.g}^{-1}_{\text{biomass}}$ .

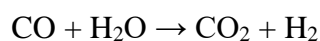
**Table 6.1-1: Experimental summary for identifying the effect of metal promoters**

Experiment – Metal promoter (5 wt.%) – results in relation to biomass and reacted water	Mg	Co	Ce	Cu	Fe	Ni	% error
Gas (wt.%)	13.04	12.84	12.87	12.55	13.07	12.27	3.3
Liquid (wt.%)	67.11	67.67	67.80	68.16	69.16	73.91	7.4
Char (wt.%)	10.96	10.78	10.59	11.21	11.01	8.70	2.5
Mass Balance (%)	91.11	91.29	91.26	91.92	93.25	94.88	1.3
Composition in mmol/g of feedstock							
CO	3.14	3.26	3.14	3.09	3.16	3.19	4.5
H <sub>2</sub>	4.00	4.02	4.22	3.58	3.84	3.73	7.0
CO <sub>2</sub>	3.65	3.58	3.75	3.39	3.60	3.31	6.7
O <sub>2</sub>	0.56	0.52	0.57	0.58	0.54	0.49	-
CH <sub>4</sub>	1.14	1.17	1.19	0.80	1.25	1.20	6.8

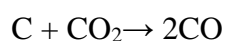
The ratio hydrogen: carbon monoxide (H<sub>2</sub>:CO) followed a similar trend to hydrogen production, categorised by a decreasing ratio for the following promoters: cerium, magnesium, cobalt, iron, nickel and copper resulting in the lower hydrogen to carbon monoxide ratio. The ratio H<sub>2</sub>:CO can be influenced by different reactions such as water gas-shift reaction (Equation 6.1), char gasification (Equation 6.2) or biogas reforming (Equation 6.3). The higher the H<sub>2</sub>:CO ratio, the more likely the catalyst

enhance the activity of water gas-shift reaction over char gasification or biogas reforming.

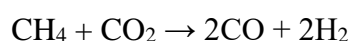
**Equation 6.1**



**Equation 6.2**



**Equation 6.3**



According to Rhodes et. al (Rhodes et al., 1995), copper supported on alumina catalysts have a very high catalytic activity, as they are able to convert virtually all the CO into product at the high temperature shift reaction, 240 °C, in thermal catalytic processes. Thus, water gas-shift reaction (Equation 6.1) will be enhanced for this Cu promoter, resulting into a lower production of methane and carbon monoxide. Moreover, metal active sites of copper supported on alumina catalysts can be oxidised if water dissociation occurs, at around 800 °C, in the presence of plasma hot spots, or in the presence of oxygen. This would lead to less active copper sites and smaller gas production of carbon dioxide and hydrogen. (Rhodes et al., 1995)

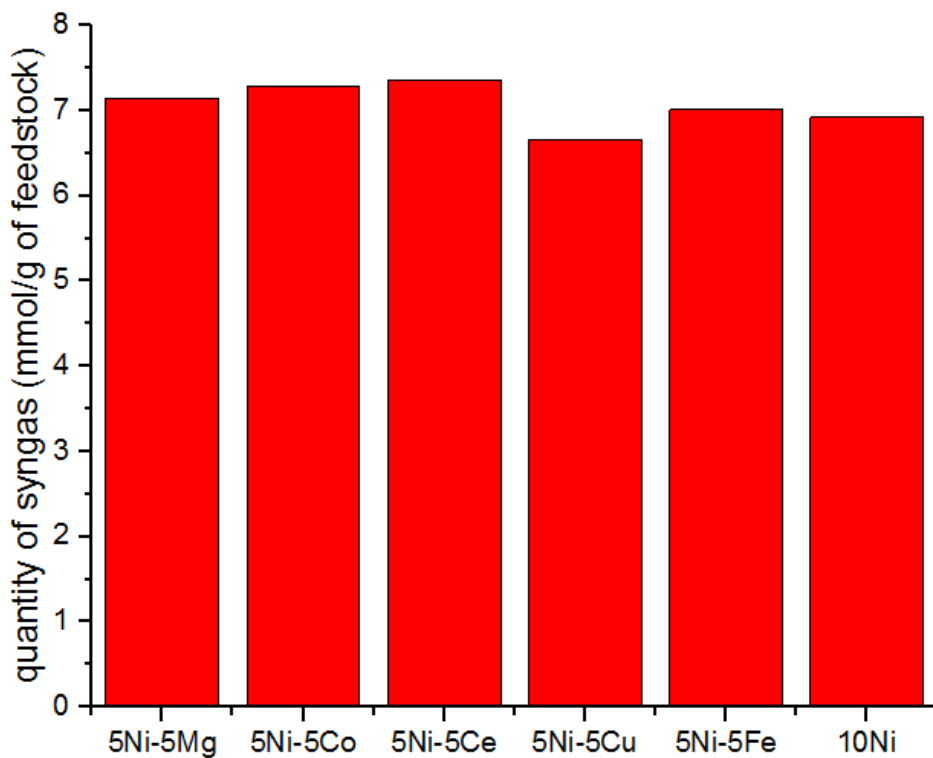
Özkara-Aydinoğlu et. al identified a superior catalytic performance with the addition of Ce onto a catalyst for methane reforming in thermal catalytic processes. (Özkara-Aydinoğlu et. al, 2010) Furthermore, Abedi et al. showed the addition of Ce onto nickel supported on alumina catalyst resulted in an increase of syngas yield during thermal biomass gasification experiments. This can be associated with an increase of catalyst metal dispersion as compared to an unpromoted catalyst, leading to an enhancement of catalytic activity. (Zou et al., 2017; Abedi et al., 2019)

However, it is worth noting that the plasma-catalytic process may have different temperature regimes within the catalyst due to the effect of the plasma, leading to different catalytic effects than the ones for thermal catalytic processes. The enhancement of catalytic activity in the pyrolysis-plasma-catalysis might be related to the formation of “hot spots” on the catalyst surface, regions where the local temperature is higher than the mean temperature due to formation of strong

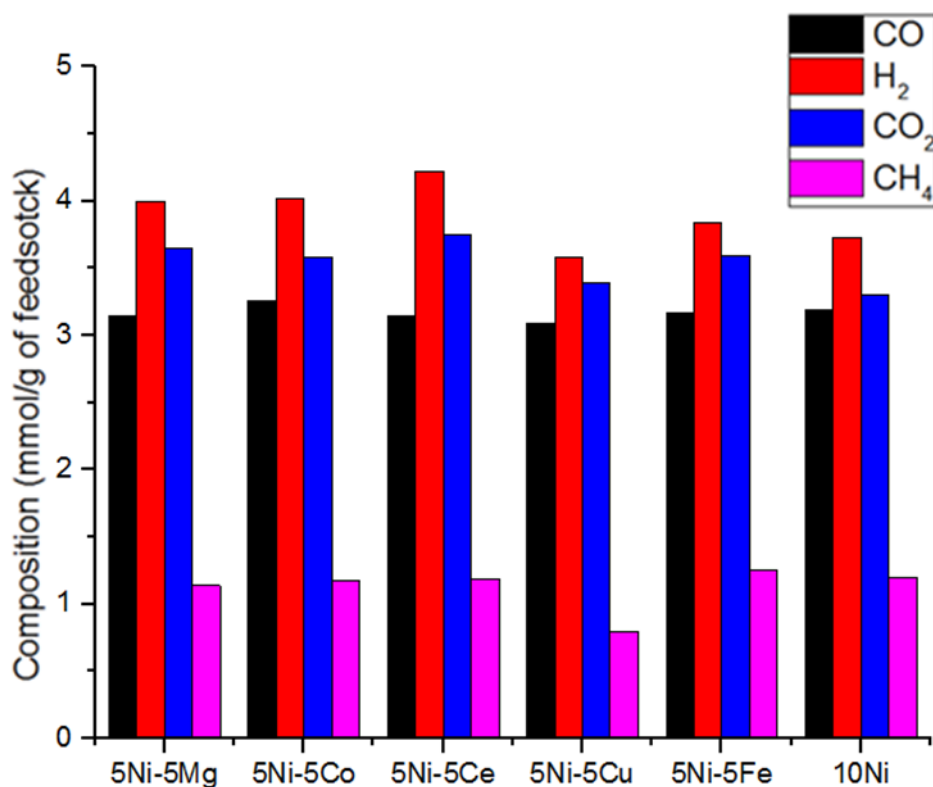
microdischarges in high-curvature areas such as catalyst pores (Van Durme et al., 2007). These “hot spots” are linked to the enhancement of electric field, which can modify the local plasma chemistry (Holzer et al., 2005) or locally thermally activate a catalyst, as shown by Kim et al. on Pt/Al<sub>2</sub>O<sub>3</sub> catalyst for benzene degradation (Kim et al., 2006). Using different promoters for plasma-catalytic biogas reforming (Equation 6.3), Zeng et al. (Zeng et al., 2018) identified some different behaviours, such as an increase of CO<sub>2</sub> conversion when using Mg promoter compared to Ce and K promoters in a thermal catalytic process; and a decrease in plasma-catalytic process. Nevertheless, these promoters enhanced the biogas reforming in the following order, Mg < Ce < K, confirming the previous observations in this study. More specifically, all promoters enhanced the conversion of methane and K and Ce promoters improved also the conversion of CO<sub>2</sub>. (Zeng et al., 2018)

### **6.1.2 Metal promoter effect on tar reduction**

The produced liquid from the metal promoted Ni-catalysts in relation to the pyrolysis, plasma-catalysis of biomass experiments were analysed by GC-MS and SEC, represented in Figure 6.1-2 and Figure 6.1-3 respectively. The tar content, represented in Figure 6.1-2 (a), shows that the smallest tar content was obtained for the cerium promoted nickel catalyst, at below 100 mg.m<sup>-3</sup> of tar within the recovered product liquid, and the highest for the iron promoter, at around 115 mg.m<sup>-3</sup> of tar within the recovered product liquid. Selecting specific compounds – phenol, o-cresol, guaiacol, 2,6-dimethylphenol, 1,4-dimethylnaphtalene, dibenzofuran, phenanthrene – are represented in Figure 6.1-2 (b), in mg.m<sup>-3</sup>. Less aromatic tar compounds were produced when using the catalysts with the iron and cerium promoters, with the disappearance of dibenzofuran and phenanthrene respectively, indicating a possible increase of the occurrence of opening of aromatic rings. The variation of concentrations of selected oxygenated tar compounds, between all promoters, were non-significant.



a.



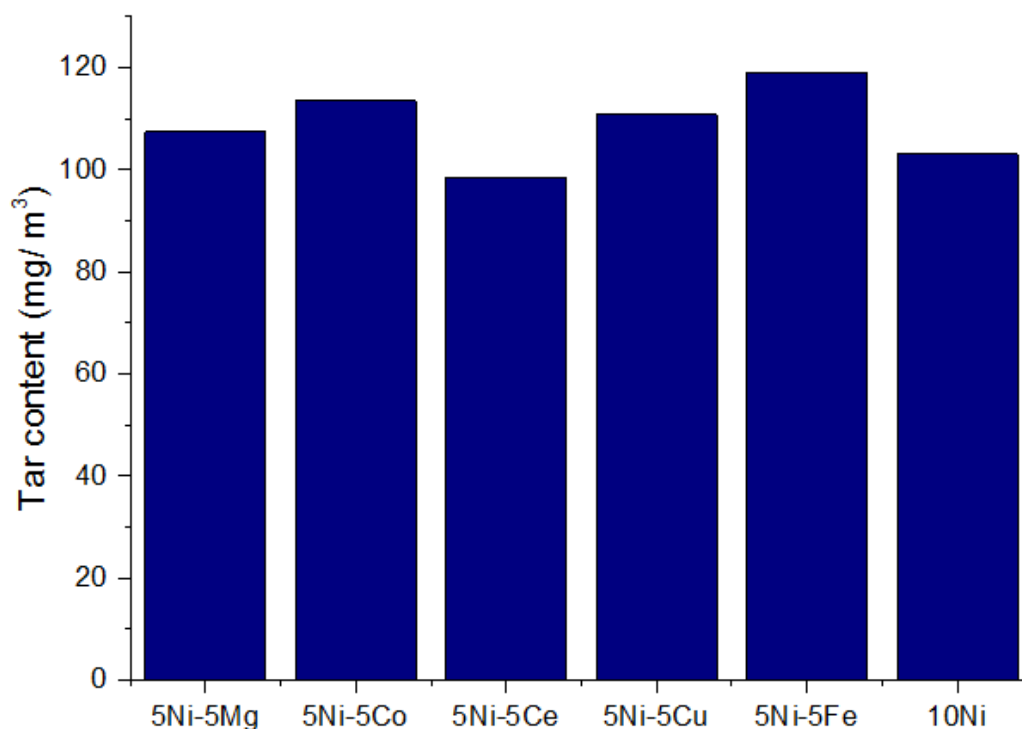
b.

**Figure 6.1-1: Effect of metal promoters on the quantity of syngas produced (a) and its effect on the detailed produced gas composition (b) in relation to the pyrolysis, plasma-catalysis of biomass with the DBD reactor**

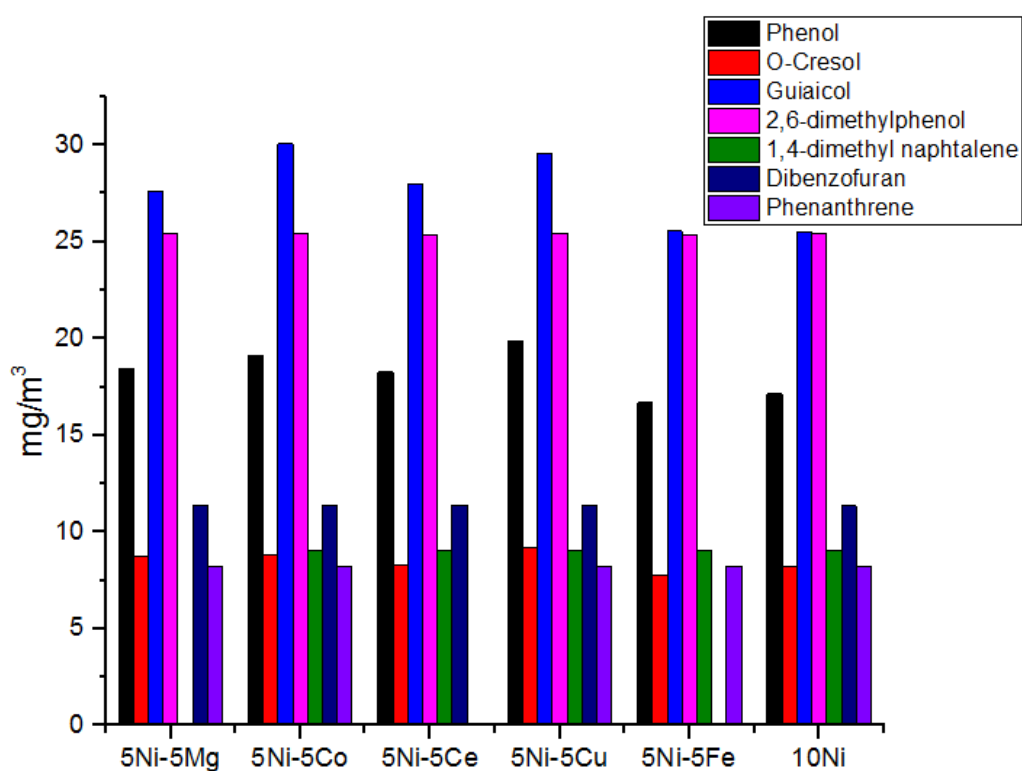
Figure 6.1-3 (a) shows the average molecular weight obtained by SEC for the four different promoters. The smallest average molecular weight, lower than 100 Mw, was obtained for both cerium and nickel promoters. Copper promoter presented the highest average molecular weight, showing the limited breakdown of tar compounds from copper as a promoter, compared to cerium or nickel.

Ce promoters on nickel supported on alumina catalyst have been reported to demonstrate higher reforming activity and to promote significantly the conversion of oxygenated compounds compared with nickel supported on alumina catalysts (Sánchez-Sánchez et al., 2007; Trane et al., 2012). Abedi et al. showed the addition of Ce onto nickel supported on alumina catalyst resulted in a decreased tar formation during thermal biomass gasification. This can be associated to an increase of catalyst metal dispersion as compared to an unpromoted catalyst. (Abedi et al., 2019)

Pylinina et al. (Pylinina et al., 2013) have studied the activation of Cu/ZrO<sub>2</sub> catalysts for dehydrogenation of alcohols by low-temperature oxygen and hydrogen plasma. In their work, copper was shown to increase the catalytic activity of the dehydrogenation of alcohols when placed in an oxygen or hydrogen plasma. Thus, copper is most likely to enhance the dehydrogenation of oxygenated tar compounds than steam reforming, leading to a high average molecular weight for the liquid product obtained from experiments using Cu promoters. The Cu metal in promoted catalysts could also be oxidised within the plasma into CuO. According to Zhu et al. (Zhu et al., 2015), CuO has demonstrated a negative effect on the removal of formaldehyde in a DBD reactor. This may be extended to most tar compounds, further contributing to the high average molecular weight in the produced liquid for Cu promoters.



a.



b.

**Figure 6.1-2: Effect of metal promoters on the tar production (a) and on selected tar compounds (b) of produced liquid in relation to the pyrolysis, plasma-catalysis of biomass with the DBD reactor**

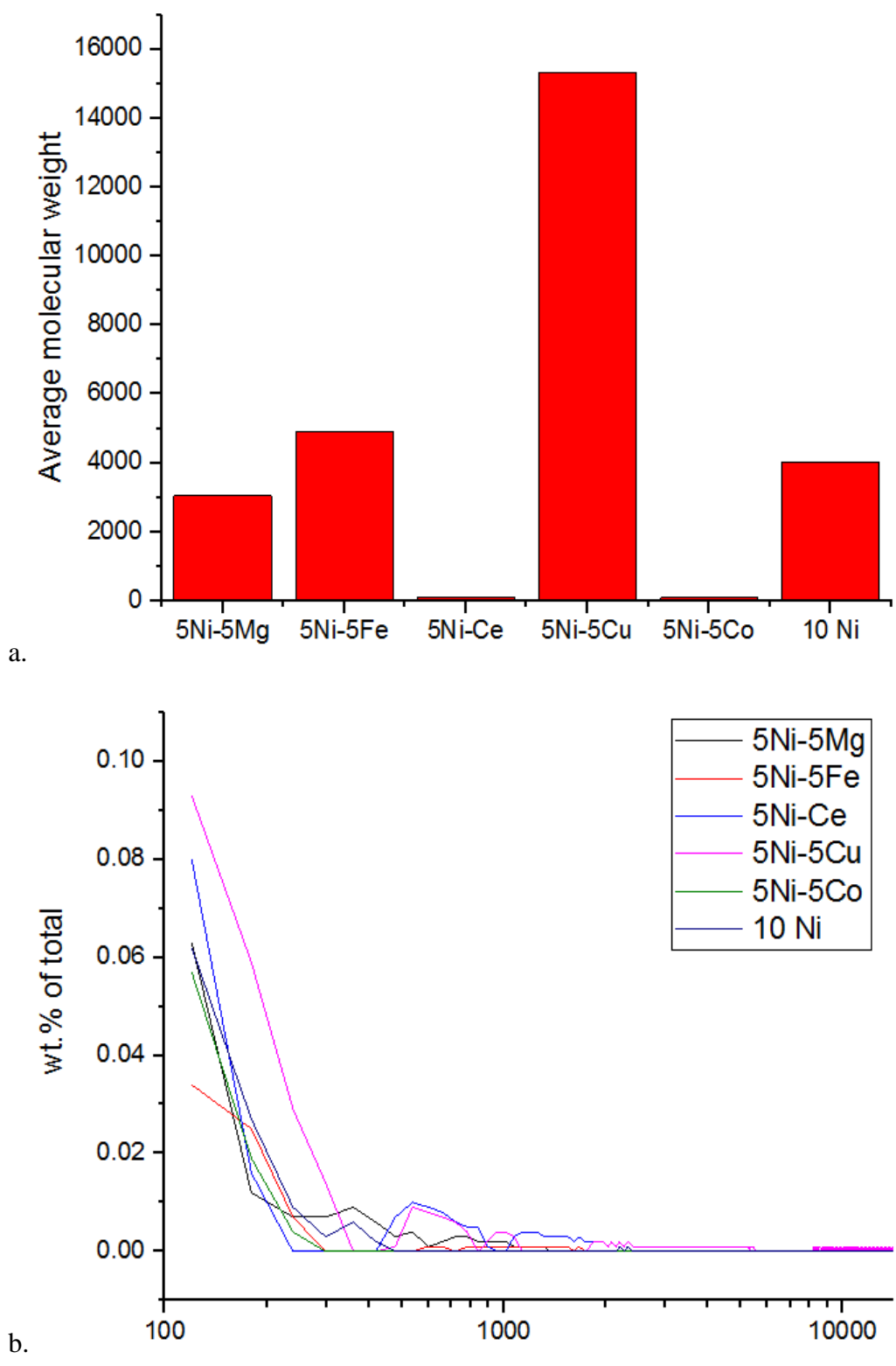


**Figure 6.1-3: Effect of metal promoters on the weight average (Mw) (a) and on the Mw range (b) of produced liquid in relation to the pyrolysis, plasma-catalysis of biomass with the DBD reactor.**

### 6.1.3 Metal promoter effect on reacted catalyst

The fresh nickel supported alumina catalysts with their promoters were characterised by X-ray diffraction (XRD). Figure 6.1-4 shows the XRD spectra for the fresh prepared Ni-Al<sub>2</sub>O<sub>3</sub> catalyst with promoters, 5 wt.% Mg, Co, Ce, Cu, Fe and Ni (producing 10 wt.% Ni) added to a 5 wt.% Ni-catalyst supported on alumina. The XRD spectra shows that three diffraction peaks were observed around the most intense peaks of NiO/Al<sub>2</sub>O<sub>3</sub>: 2 $\theta$  at 37.3°, 43.3° and 62.9° (JCPDS 78-0643). The most intense peaks of Ni could also be observed: 2 $\theta$  at 44.5°, 51.8° and 76.4° (JCPDS 65-2865). The diffraction peaks for the different promoters were the most intense for the Ni promoter, followed by, in decreasing order of intensity: Cu>Fe>Co>Mg>Ce promoters. This suggests that smaller nickel particles are produced for the Mg promoter than for the Ni promoter (Yan et al., 2013). The diffraction spectra for the catalyst after reaction in the plasma-catalytic system were less intense compared with the peaks for the unreacted catalysts. This suggests that the nickel particles were smaller after processing in the plasma-catalytic system, as it can be observed for most promoters in Table 6.1-2. The results in Table 6.1-2 are bigger particle size than most which can be found in the literature due to the big particle size of the studied catalysts.

**Table 6.1-2: Particle size for different metal promoters at 2 $\theta$ =51.8°**

Promoter	Particle size before plasma treatment (Å)	Particle size after plasma treatment (Å)
Mg	170	747
Co	749	145
Ce	345	256
Cu	101	112
Fe	749	293
Ni	262	948

Finally, Temperature programmed oxidation was used to determine the amount of carbonaceous coke deposited on the catalysts, as represented in Figure 6.1-5. All promoters lead to a coke deposition between 5 and 8 wt.% the highest being for the

nickel promoter (10 wt.% nickel), around 8 wt.%, followed by the cobalt promoter, iron promoter, cerium promoter, magnesium promoter and copper promoter, with a coke deposition of about 5 wt.% of the catalyst. This has been demonstrated before by Abedi et. al (Abedi et al., 2019), where the use of cerium promoters on a nickel supported on alumina catalyst led to a lower coke formation compared to the amount of coke deposited on nickel supported on alumina catalyst, for the thermal steam gasification of oat hull pellets. However, the higher coke deposition on Nickel supported catalyst might be due to a higher metal loading on the catalyst (i.e. 10 wt.% Ni/Al<sub>2</sub>O<sub>3</sub>). Özkara-Aydinoğlu et. al (Özkara-Aydinoğlu et al., 2010) showed that the incorporation of Ce and Mg promoters on Co supported on ZrO<sub>2</sub> catalyst led to a coke deposition of less than 3 wt.% for methane reforming experiments in thermal catalytic processes. This could be linked to the known high oxygen storage capacity of ceria, which, combined to other materials, led to a catalytic surface promoting the formation of oxygen vacancies and oxygen mobility through the lattice (Yao et al., 1997; Ji et al., 2001). The presence of Ce on the surface goes through cycles of reduction/oxidation and producing mobile surface oxygen during the reaction, enhancing oxygen transfer, making the active metal more resistant to coke deposition (Wang et al., 1998; Özkara-Aydinoğlu et al., 2009).

The Mg promoter on the nickel supported on alumina catalyst was shown to be a most effective catalyst in tar reduction, catalyst stability and high initial activity, compared to the nickel alone supported on alumina catalyst, when used in the thermal steam gasification of biomass (Garcia et al., 2002; Yao et al., 2014). This implies a lower coke deposition on Mg-Ni supported on alumina catalyst than for Ni supported on alumina catalyst. As previously highlighted from Rhodes et. al (Rhodes et al., 1995), Cu/Al<sub>2</sub>O<sub>3</sub> catalysts have a relatively high catalytic activity. They have also showed to improve the catalyst lifetime, reduce the likelihood of sintering, enhance the pellet strength and limit the pellet shrinkage occurring during reduction. (Rhodes et al., 1995) Thus, most carbon monoxide is consumed in the water gas shift reaction and not the Boudouard reaction (Equation 6.4), reducing the production of coke on the copper supported on alumina catalyst.

#### **Equation 6.4**



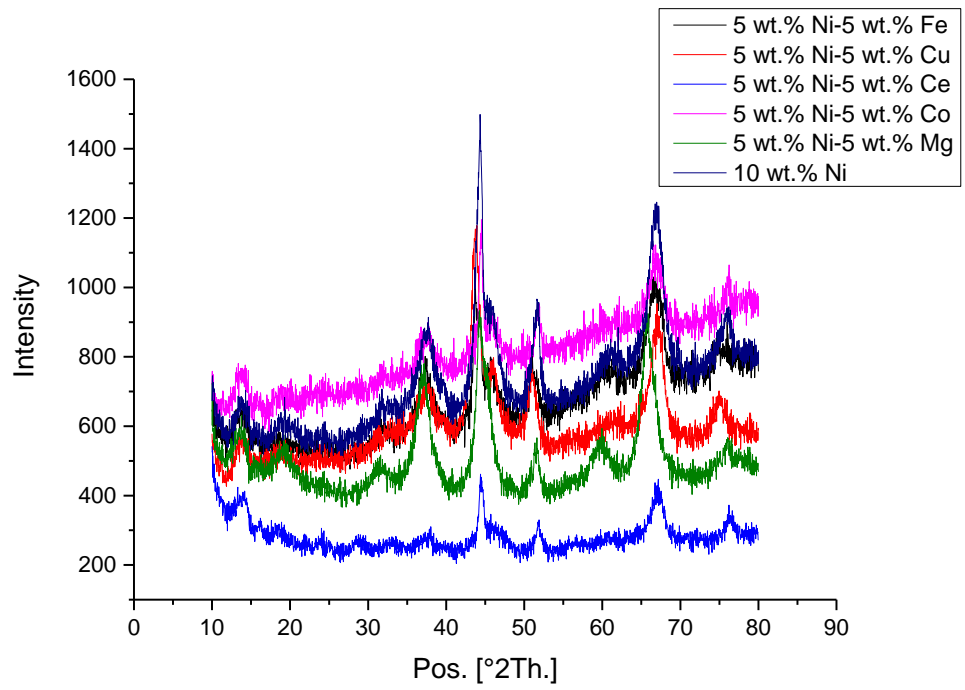


**Figure 6.1-4: XRD on the reduced metal promoted catalysts for different metal promoters**

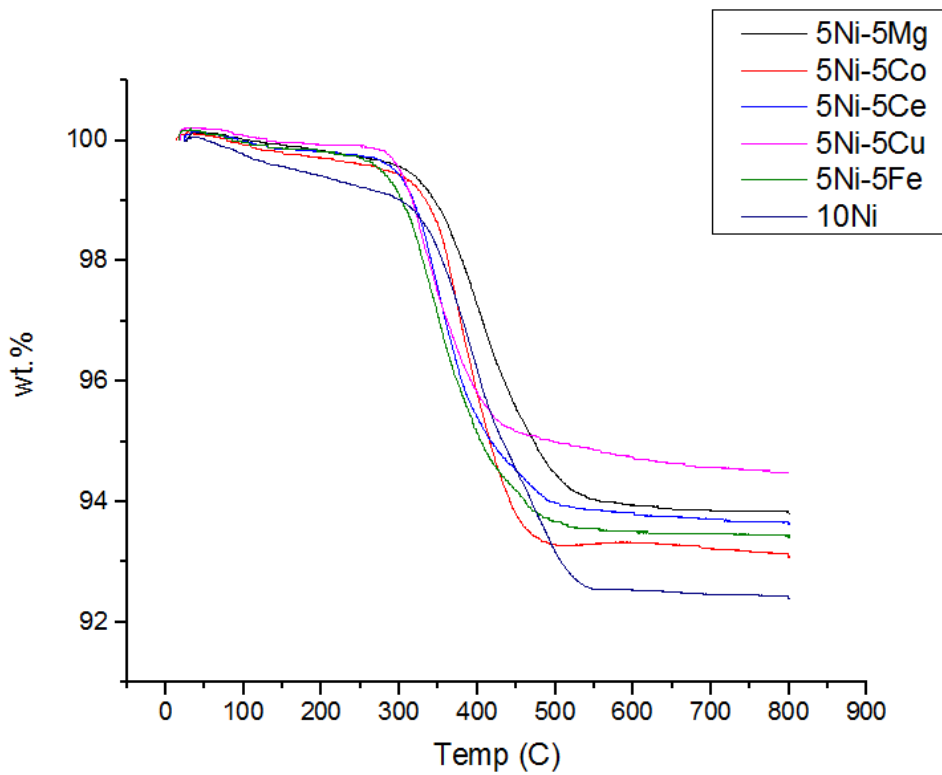


**Figure 6.1-5: Effect of metal promoters on coke deposition on the catalyst for plasma-catalysis system**

## 6.2 Effect of Nickel loading on plasma-catalysis

After the results in the previous section, no obvious promoter has significantly improved the high-quality syngas production and the tar reduction. Thus, without having a chosen promoter for this study, the loading of Nickel on alumina support was studied in this section, to see if increased metal concentration on alumina had an influence on the pyrolysis, plasma catalysis reforming of biomass. The loading of nickel supported on our alumina support, for a loading of 0, 5 and 10 wt.% was studied first to see the impact of the quantity of nickel catalyst on the system.

### 6.2.1 Nickel loading effect on gas production

The results of the effect of the amount of nickel loading on the alumina catalyst in terms of product yield and gas composition and yield, in relation to the pyrolysis, plasma-catalysis of biomass are presented in Table 6.2-1. The quantity of gas produced during the experiments using different nickel loadings was comparable between all experiments. The highest quantity of product gas, about 14 wt.%, was obtained for the 5 wt.% nickel supported on alumina catalyst. Alumina produced an intermediate 13 wt.% of gas per experiment, whereas the use of 10 wt.% supported on alumina catalyst resulted in 12 wt.%.

The gas product was analysed by GC-FID and GC-TCD as stated in the method section for gas analysis. The quantity of syngas produced when using the different nickel loading is represented in Figure 6.2-1 (a). All nickel loadings produced a similar quantity of syngas, approximately  $7 \text{ mmol.g}^{-1}_{\text{biomass}}$ , with a slightly higher syngas production for 5 wt.% of nickel and a slightly smaller syngas production for 10 wt.% of nickel supported on alumina catalyst (respectively  $7.27 \text{ mmol.g}^{-1}_{\text{biomass}}$  and  $6.92 \text{ mmol.g}^{-1}_{\text{biomass}}$ ). A more detailed composition of the gas product is represented in Figure 6.2-1 (b). Production of carbon monoxide for all nickel loading was observed between  $3.17 \text{ mmol.g}^{-1}_{\text{biomass}}$ , for alumina catalyst, and  $3.21 \text{ mmol.g}^{-1}_{\text{biomass}}$ , for 5 wt.% nickel supported on alumina catalyst. Hydrogen production is similar for all loading, with a slight increase (a difference of less than  $0.35 \text{ mmol.g}^{-1}_{\text{biomass}}$ ) for 5 wt.% nickel supported on alumina catalyst. Similarly, carbon dioxide production is slightly higher for 5 wt.% nickel on alumina, with a production of  $3.31 \text{ mmol.g}^{-1}_{\text{biomass}}$ , than for other loading, the smallest production being for 10 wt. % nickel supported on alumina, with a production of  $3.92 \text{ mmol.g}^{-1}_{\text{biomass}}$ . Production of methane for all

nickel loading was observed between 1.20 mmol.g<sup>-1</sup><sub>biomass</sub>, for 10 wt.% nickel supported on alumina catalyst, and 1.01 mmol.g<sup>-1</sup><sub>biomass</sub>, for alumina catalyst.

Similar results have been obtained and reported by previous publications, but for the reforming of methane or model tar compounds rather than for biomass, when using a plasma-catalytic system. Aziznia et al (Aziznia et al., 2012) showed that low temperature plasma-catalytic dry reforming of methane, when using a higher loading of nickel on alumina catalyst – 20 wt.% compared to 5 and 10 wt.% - placed in a corona discharge, led to higher carbon dioxide and methane conversions. Liu et al (S.Y. Liu et al., 2017) used toluene and different nickel loadings – from 5 to 20 wt.% - for nickel supported on alumina catalysts and showed that increasing the nickel loading increased the yield of hydrogen and carbon dioxide by 15% and 16% respectively. Similar results have also been obtained in thermal catalytic processes. For example, Wang reported a higher hydrogen production when the nickel loading was increased from 5 to 20 wt.% (Wang, 2013). Liu et al. (Liu et al., 2016) found an optimum of 10 wt.% of activated carbon on nickel catalysts for the thermal catalytic steam reforming of toluene.

**Table 6.2-1: Experimental summary for identifying the effect of Nickel loading**

Experiment – results in relation to biomass and reacted water	10 wt.% Ni supported on alumina	5 wt.% Ni supported on alumina	Alumina	% error
Gas (wt.%)	12.27	14.05	13.19	3.3
Liquid (wt.%)	73.91	71.30	74.03	7.4
Char (wt.%)	8.70	10.87	10.82	2.5
Mass Balance (%)	94.88	96.22	98.04	1.3
Composition in mmol/g of feedstock				
CO	3.19	3.21	3.17	4.5
H <sub>2</sub>	3.73	4.06	3.90	7.0
CO <sub>2</sub>	3.31	3.92	3.63	6.7
O <sub>2</sub>	0.49	0.98	0.87	-
CH <sub>4</sub>	1.20	1.05	1.01	6.8

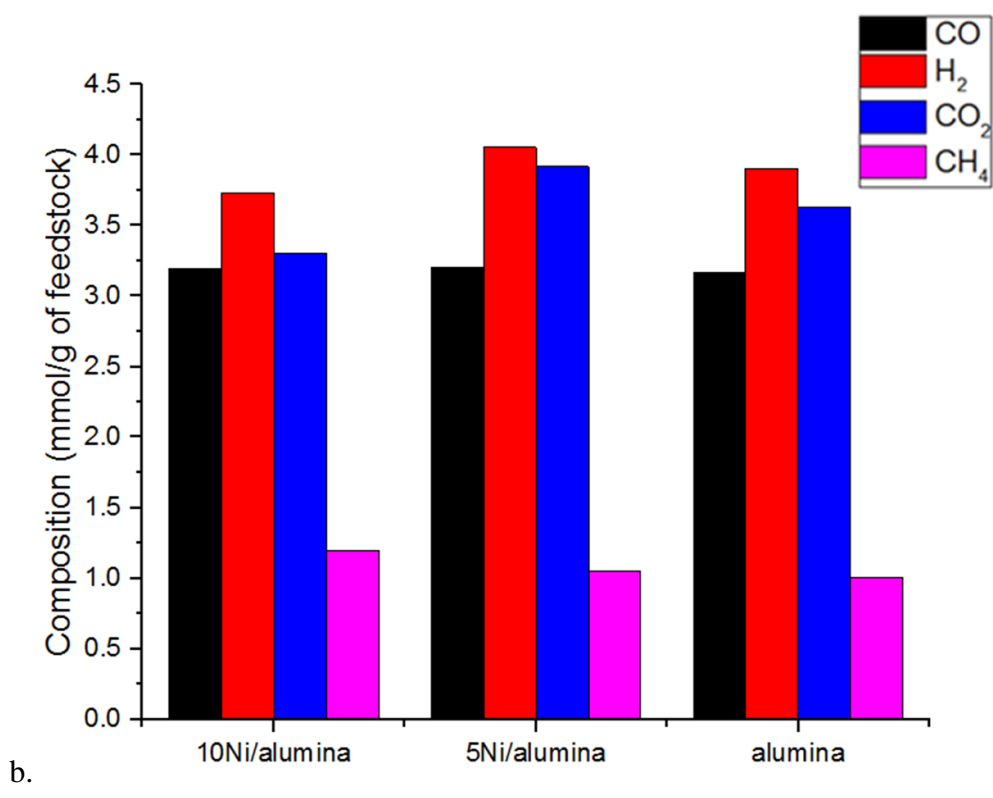
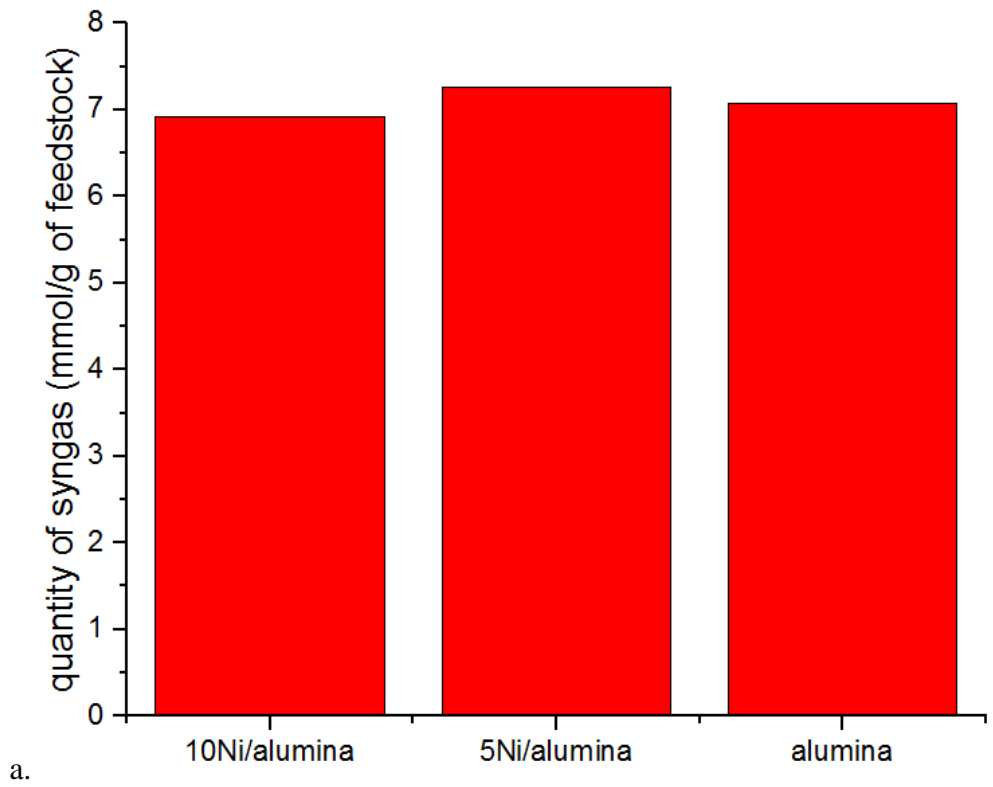


**Figure 6.2-1: Effect of Nickel loading on the quantity of syngas produced (a) and its effect on the detailed produced gas composition (b) in relation to the pyrolysis, plasma-catalysis of biomass with the DBD reactor**

## 6.2.2 Nickel loading effect on tar reduction

The produced liquid from the different amounts of nickel loading on the alumina catalyst experiments were analysed by GC-MS, represented in Figure 6.2-2. The tar content, represented in Figure 6.2-2 (a), shows that the smallest tar content was obtained for 10 wt.% nickel loading, below  $100 \text{ mg.m}^{-3}$  of tar within the recovered product liquid, and the highest for 5 wt.% nickel supported on alumina catalyst, around  $135 \text{ mg.m}^{-3}$  of tar within the recovered product liquid. As in the previous section, selected specific compounds – phenol, o-cresol, guaiacol, 2,6-dimethylphenol, 1,4-dimethylnaphtalene, dibenzofuran, phenanthrene – are represented in Figure 6.2-2 (b), in  $\text{mg.m}^{-3}$ . Less aromatic tar compounds were produced when using the alumina catalyst, with the disappearance of 1,4-dimethylnaphtalene, dibenzofuran and phenanthrene respectively indicating a possible increase of the occurrence of opening of aromatic rings. Furthermore, the quantity of oxygenated tar compounds, such as methyl-phenols, is smaller when using the alumina catalyst than for experiments involving nickel. Phenol, o-cresol and guaiacol quantities when using alumina catalyst have been halved compared to the quantities of the same tar compounds using 10 wt.% nickel supported on alumina catalyst; going from 17 to  $8 \text{ mg.m}^{-3}$ , 7 to  $3 \text{ mg.m}^{-3}$ , and 25 to  $13 \text{ mg.m}^{-3}$  respectively. The 5 wt.% nickel supported on alumina catalyst did not show the presence of the dimethyl compounds – 2,6-dimethylphenol and 1,4-dimethylnaphtalene – when studying the selected tar compounds in Figure 6.2-2 (b).

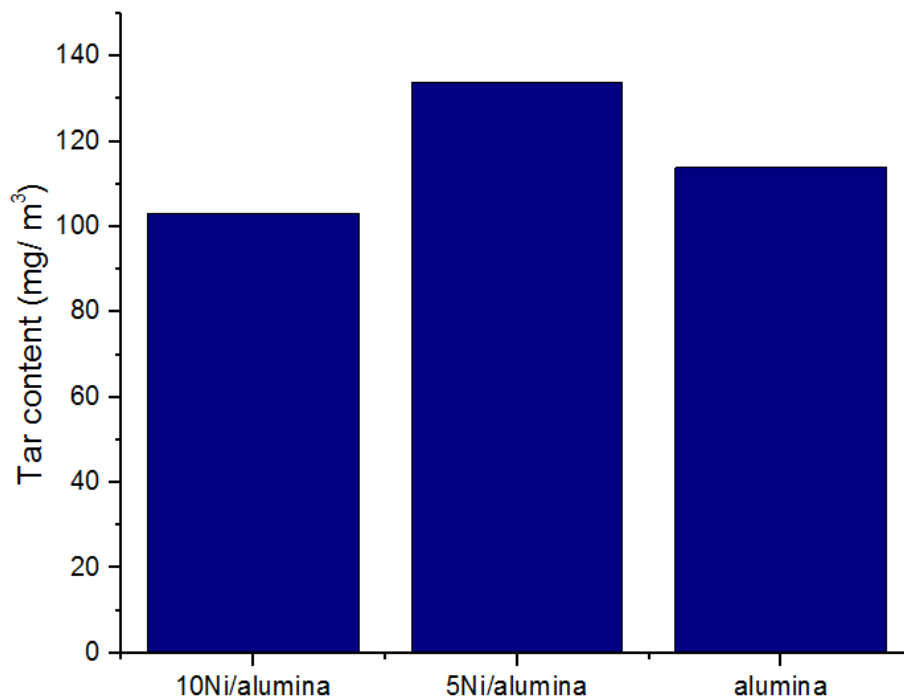
The average molecular weight for the liquid product has been analysed by SEC and is represented in Figure 6.2-3. 10 wt.% nickel loading lead to a smaller average molecular weight (inferior to 100 Mw), followed by alumina (about 200 Mw) and 5 wt.% nickel supported on alumina catalyst (about 750 Mw).

Liu et al (S.Y. Liu et al., 2017) used toluene and different nickel loadings – from 5 to 20 wt.% - for nickel supported on alumina catalysts and showed that increasing the nickel loading increased the toluene conversion and the energy efficiency of the plasma-catalysis. Furthermore, they found that the presence of 5 wt.% nickel supported on alumina catalyst in the plasma process significantly inhibited the formation of organic by-products. This could explain the decrease of selected

oxygenated tar compounds between 10 and 5 wt.% Ni supported on alumina catalyst. (S.Y. Liu et al., 2017)

In thermal steam reforming of acetic acid over nickel supported alumina catalyst, Zhang et al (Zhang et al., 2018) showed that the coke produced during the low nickel loading experiment contained more small aromatic rings and more oxygenated compounds. They argued that higher metal loading may have promoted catalytic cracking reactions whereas low nickel loading promoted polymerisation reactions. (Zhang et al., 2018) This could further explain the differences between the tar content of different nickel loading in this section.

Rhodes identified that dehydration reaction were catalysed by acidic oxides in catalytic processes. (Rhodes et al., 1995) In the case of alumina catalyst, the dehydration reaction was promoted, leading to a high syngas and hydrogen production, as shown in the previous section. However, without nickel promoting steam reforming reactions, the use of alumina catalyst resulted most likely into the production of tar compounds which could not be detected with our analytical method presented in Chapter 3.



a.

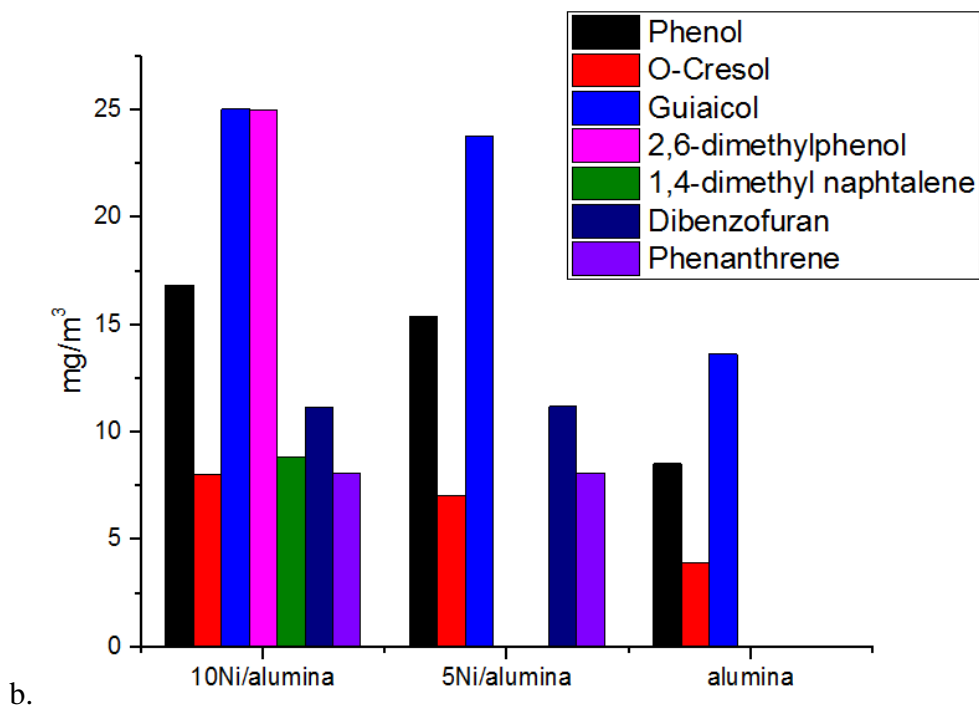


**Figure 6.2-2: Effect of Nickel loading on the tar production (a) and on selected tar compounds (b) of produced liquid in relation to the pyrolysis, plasma-catalysis of biomass with the DBD reactor.**

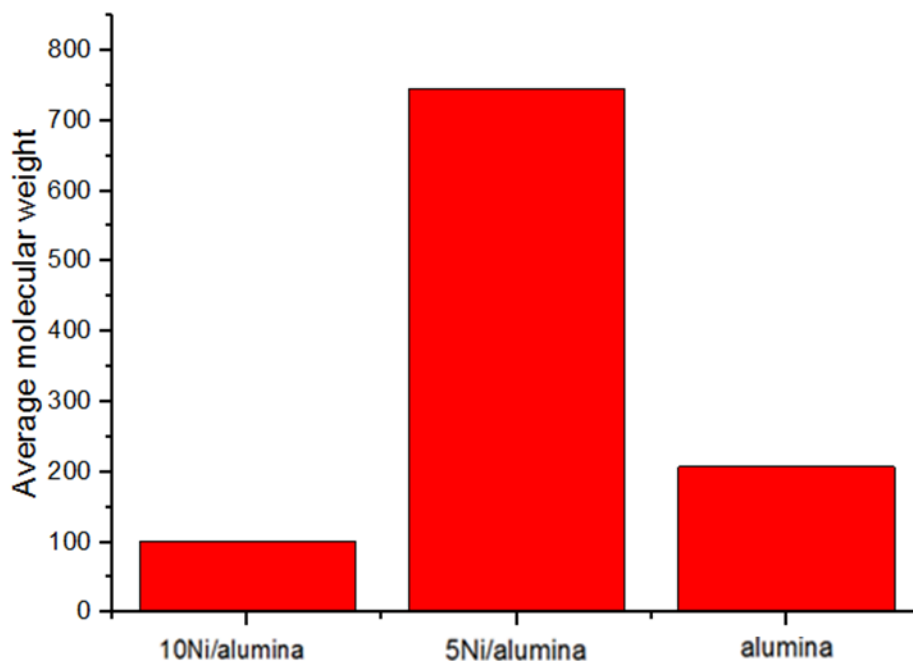


**Figure 6.2-3: Effect of Nickel loading on the weight average (Mw) of produced liquid in relation to the pyrolysis, plasma-catalysis of biomass with the DBD reactor.**

### 6.2.3 Nickel loading effect on reacted catalyst

Temperature programmed oxidation was used to determine the amount of carbonaceous coke deposited on the catalysts after pyrolysis, plasma-catalysis of biomass, as represented in Figure 6.2-4. The 5 wt.% and 10 wt.% nickel supported on alumina catalysts showed a similar coke deposition, around 8 wt.% of the reacted catalyst weight. The highest coke deposition weight was for the use of alumina catalyst, with an amount of coke deposited around 16 wt.%, twice as much as nickel supported on alumina catalyst.

The effect of nickel loading related to coke deposition on nickel supported on alumina catalyst for thermal catalytic steam reforming was studied by Zhang et al (Zhang et al., 2018). They found that, with the increase of nickel loading, the catalytic activity did not vary much but, catalytic stability increased whereas the coke deposition decreased. This confirms the results obtained in this study.

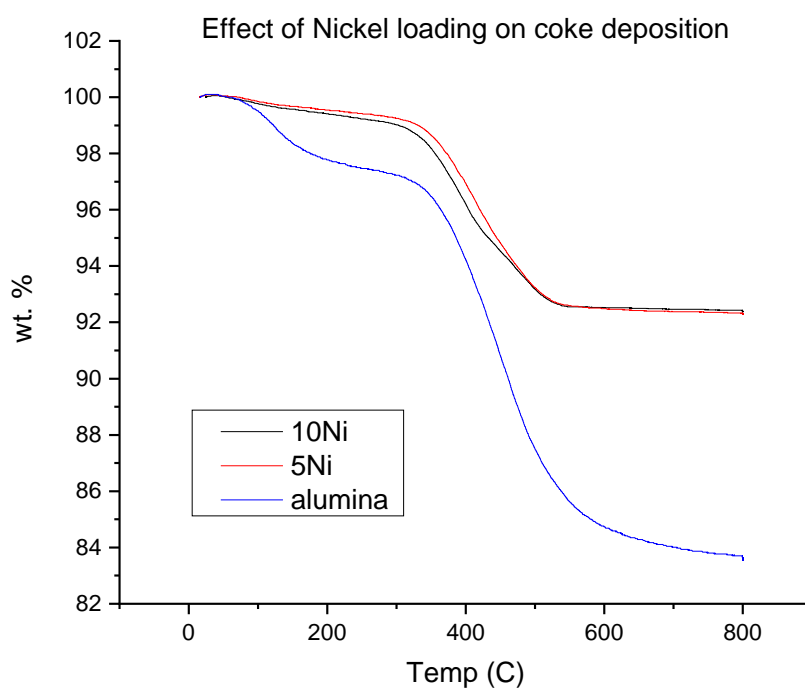


**Figure 6.2-4: Effect of nickel loading on coke deposition on the catalyst in relation to the pyrolysis, plasma-catalysis of biomass for plasma-catalysis system**

## 6.3 Effect of catalyst support

As the amount of nickel loading on the Ni-alumina catalysts did not present a definitive difference between the different loadings, the catalyst support was studied to better understand the importance of the catalyst within the pyrolysis-plasma-catalysis system. To study the effect of catalyst supports on plasma-catalysis, three different support materials were studied: Alumina, a traditional support for thermal processes (Yang et al., 2015); titanium oxide, a catalyst activated by UV stimulation used in many plasma-catalysis studies (Tauster et al., 1978; Bartholomew et al., 1980); and Y-zeolite, possesses properties that has made the catalyst used in industry for oil cracking, refining and gasoline production for its large surface area and pore size makes it a perfect candidate for heavy tar breakdown. (Choi et al., 2006; Möller et al., 2013). These catalyst supports were used in the plasma-catalytic system as catalysts and compared to 5 wt.% nickel supported on Alumina, TiO<sub>2</sub> and Y-zeolite separately.

### 6.3.1 Catalyst support effect on gas production

The results of the influence of the different support materials in terms of product yield and gas composition and yield, in relation to the pyrolysis, plasma-catalysis of biomass are presented in Table 6.3-1. As shown in the previous section, when comparing the experiment with or without nickel, the quantity of gas produced during the experiments was comparable for all promoters. The highest quantity of product gas was obtained for alumina: about 14 wt.% for the 5 wt.% nickel supported on alumina catalyst, and 13 wt.% of gas per experiment for alumina catalyst. Titanium oxide and Y-zeolite experiments resulted in the same gas production: about 13 wt.% for the 5 wt.% nickel supported on catalyst, and 12 wt.% of gas per experiment for support catalyst.

After experiments, the produced gas was analysed by GC-FID and GC-TCD as described in the methods. The production of syngas for these experiments are represented in Figure 6.3-1 (a) and the detailed composition of the product gas is represented in Figure 6.3-1 (b). First, comparing the supports on their own, more syngas was produced using alumina as a catalyst than with another support, leading to a syngas production of 7.07, 5.98 and 5.94 mmol.g<sup>-1</sup><sub>biomass</sub> for alumina, titanium oxide and y-zeolite respectively. The use of titanium oxide and Y-zeolite lead to a

very similar syngas production. Examining the gas composition in detail, the highest hydrogen production was obtained using alumina catalyst, followed by  $\gamma$ -zeolite and titanium oxide catalyst, for a production of 3.9, 3.26 and 3.56  $\text{mmol.g}^{-1}_{\text{biomass}}$  respectively. Carbon monoxide production was the lowest for Y-zeolite, 2.38  $\text{mmol.g}^{-1}_{\text{biomass}}$  compared to 3.17  $\text{mmol.g}^{-1}_{\text{biomass}}$  for alumina catalyst. Thus, Y-zeolite had the highest hydrogen over carbon monoxide ratio for Y-zeolite catalyst.

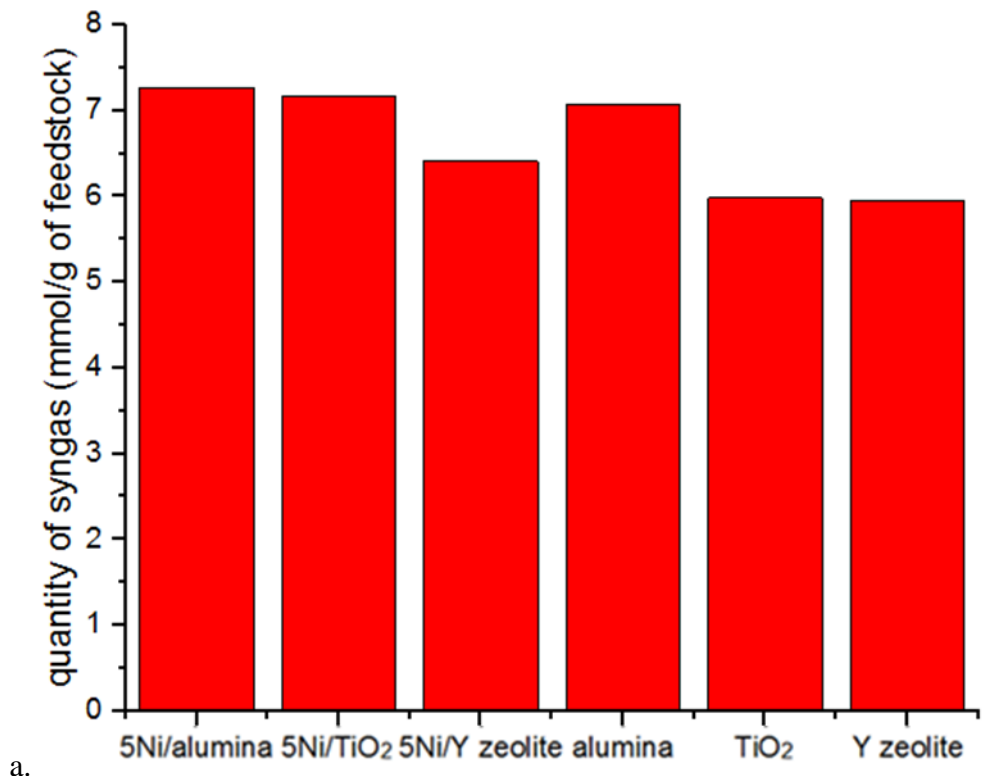
The same trends could be observed when comparing 5 wt.% of nickel supported on the different supports. Nickel supported on alumina catalyst resulted in the highest syngas production with 7.27  $\text{mmol.g}^{-1}_{\text{biomass}}$ , the highest hydrogen production with 4.06  $\text{mmol.g}^{-1}_{\text{biomass}}$ , and the highest carbon dioxide production with 3.92  $\text{mmol.g}^{-1}_{\text{biomass}}$ . Nickel supported on titanium oxide led to the highest carbon monoxide and the highest methane production was obtained for nickel supported on Y-zeolite, with 3.26  $\text{mmol.g}^{-1}_{\text{biomass}}$  and 1.13  $\text{mmol.g}^{-1}_{\text{biomass}}$  respectively.

Then, comparing the nickel supported catalysts and the supports, the impregnation of nickel to the catalyst did not seem to have a real effect to the syngas production for alumina support or Y-zeolite support. The increase of syngas produced between the titanium oxide and the 5 wt.% nickel supported on titanium oxide, from 5.98  $\text{mmol.g}^{-1}_{\text{biomass}}$  to 7.18  $\text{mmol.g}^{-1}_{\text{biomass}}$  when nickel is added onto the catalyst surface, can originate from the change of structure on the surface of titanium oxide, as represented by the XRD plot in Figure 6.3-4 (c), and described in the following section 6.3.3.

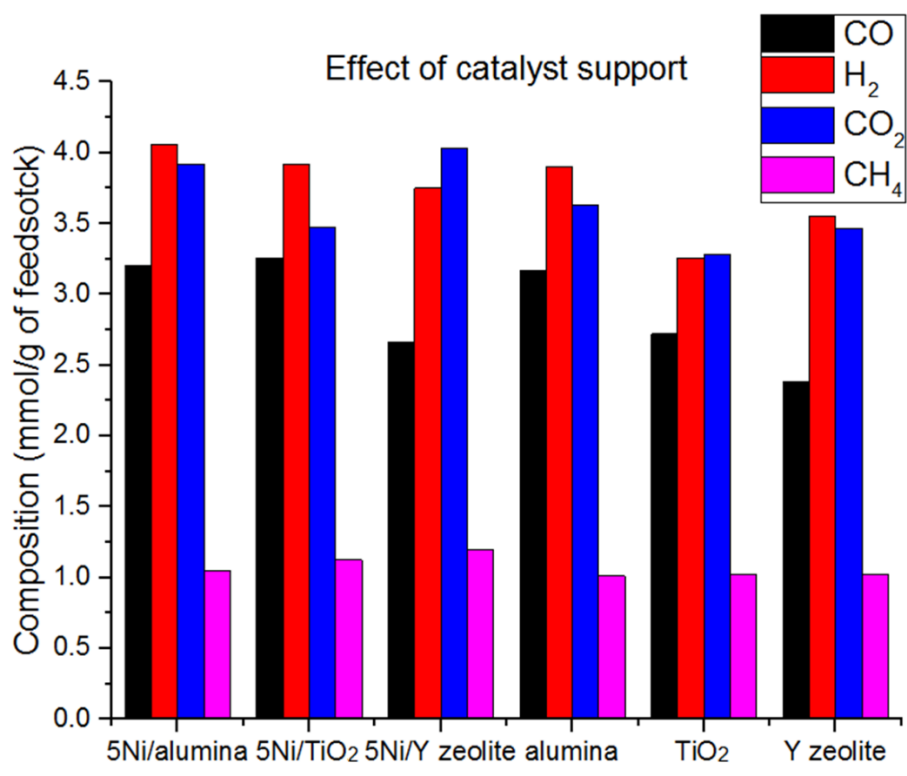
Oh et al. showed that the use of zeolite in a plasma-catalytic reactor to decompose toluene led to a higher toluene decomposition and a lower product selectivity of carbon monoxide, as CO selectivity was linked to the decomposition of adsorbed formaldehyde on the zeolite, a by-product less generated in presence of plasma (Oh et al., 2006), which can explain the hydrogen to carbon monoxide ratio higher for  $\gamma$ -zeolite support catalysts. Moreover, the addition of nickel on a Y-zeolite catalyst led to an improvement of catalytic activity by the enhancement of steam and dry reforming, which was supported by the literature as in Buchireddy et al. work for thermal catalytic processes (Buchireddy et al., 2010).

**Table 6.3-1: Experimental summary for identifying the effect of catalyst support**

Experiment – results in relation to biomass and reacted water	Alumina	5 wt.% Ni/Alumina	Titanium oxide	5 wt.% Ni/Titanium oxide	Y-Zeolite	5 wt.% Ni / Y-Zeolite	% error
Gas (wt.%)	13.19	14.05	12.36	13.30	11.95	13.30	3.3
Liquid (wt.%)	74.03	71.30	72.69	69.83	69.26	69.70	7.4
Char (wt.%)	10.82	10.87	10.57	10.78	10.82	10.39	2.5
Mass Balance (%)	98.04	96.22	95.62	93.90	92.03	93.39	1.3
Composition in mmol/g of feedstock							
CO	3.17	3.21	2.72	3.26	2.38	2.66	4.5
H <sub>2</sub>	3.90	4.06	3.26	3.92	3.56	3.75	7.0
CO <sub>2</sub>	3.63	3.92	3.28	3.47	3.47	1.03	6.7
O <sub>2</sub>	0.87	0.98	0.94	1.03	0.97	0.71	-
CH <sub>4</sub>	1.01	1.05	1.02	1.13	1.02	1.20	6.8



a.



b.

**Figure 6.3-1: Effect of catalyst support on the quantity of syngas produced (a) and its effect on the detailed produced gas composition (b) in relation to the pyrolysis, plasma-catalysis of biomass with the DBD reactor**

### 6.3.2 Catalyst support effect on tar reduction

The produced liquid in relation to the different support materials in relation to the pyrolysis, plasma-catalysis of biomass from the were analysed by GC-MS, represented in Figure 6.3-2. The tar content, represented in Figure 6.3-2 (a), shows that the smallest tar content was obtained for Y-zeolite catalysts, below  $10 \text{ mg.m}^{-3}$  of tar within the recovered product liquid, and the highest for alumina and titanium oxide catalyst, around  $110 \text{ mg.m}^{-3}$  of tar within the recovered product liquid. As in the previous section, selected specific compounds – phenol, o-cresol, guaiacol, 2,6-dimethylphenol, 1,4-dimethylnaphtalene, dibenzofuran, phenanthrene – are represented in Figure 6.3-2 (b), in  $\text{mg.m}^{-3}$ . Within the selected tar compounds, only phenol, o-cresol and guaiacol are expressed, indicating a lower aromatic tar content across all studied catalysts. The tar content of y-zeolite catalysts was especially low, with no detected selected compounds for y-zeolite catalyst and only o-cresol detected for nickel supported on y-zeolite catalyst.

The liquid product was also analysed by SEC to study the effect of catalyst support and nickel impregnation on catalyst. The results are represented in Figure 6.3-3. The smallest average molecular weight was obtained for liquid obtained from experiments using alumina and titanium oxide, with less than 200 average molecular weight. Y-zeolite, with and without nickel impregnation, had a very high average molecular weight (over 3,000), showing the inefficiency of the support to breakdown the tar compounds efficiently. The highest average molecular weight (about 4,000) was obtained for nickel supported by titanium oxide.

The difference between titanium oxide with and without nickel impregnation could come from the difference in the surface of the catalyst. By modifying its surface, titanium oxide might have lost its photocatalyst role leading to a smaller breakdown of tar compounds in the product stream. This will be explored in the following section on reacted catalyst.

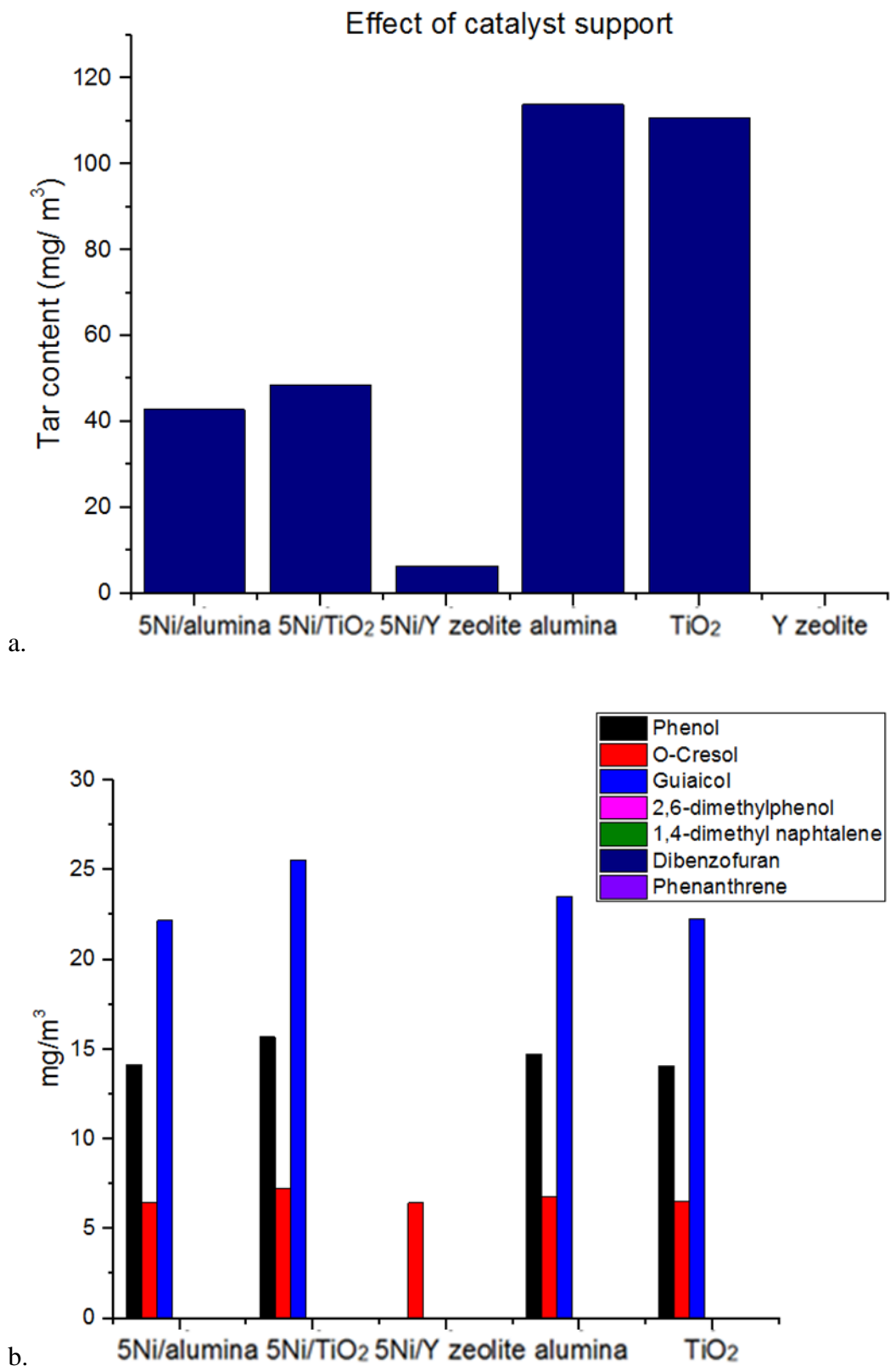


**Figure 6.3-2: Effect of catalyst support on the tar production (a) and on selected tar compounds (b) of produced liquid in relation to the pyrolysis, plasma-catalysis of biomass with the DBD reactor**

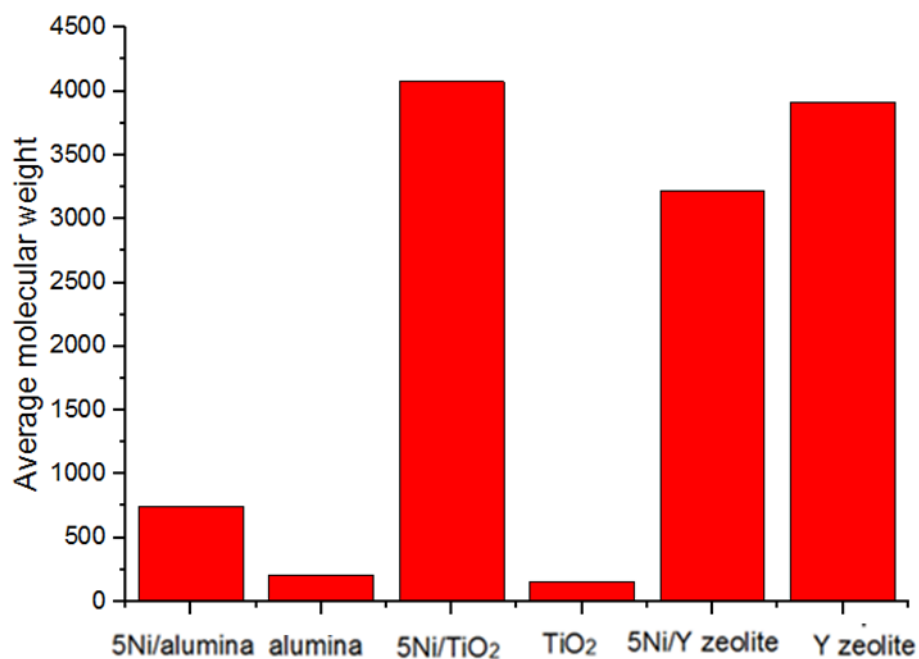


**Figure 6.3-3: Average molecular weight by SEC for Nickel supported catalyst and catalysts for Alumina, Y-zeolite and TiO<sub>2</sub> for the product liquid in relation to the pyrolysis, plasma-catalysis of biomass with the DBD reactor.**

In the case of Y-zeolite support, zeolites are involved in acid-catalysed reactions proceeding through formation of carbocation-like intermediates. Thus, catalytic transformation chemistry is closely linked to carbocation chemistry in a microporous environment. The said-environment is a limitation to mass transfer as the accessibility to micropores for heavy biomass molecules is difficult (Perego and Bosetti, 2011). This promoted the production of organic compounds which are not included in the selected tar compounds, as they are not common, and thus not detected in the studied experimental setup. To highlight the differences between nickel supported on y-zeolite and y-zeolite catalysts, Escola et al found that during catalytic hydroreforming of polyethylene, hydroisomerisation and aromatisation reactions took place over nickel supported hierarchical zeolites (Escola et al., 2011). This promoted the production of organic compounds contained in gasoline which are not fully detected in the studied experimental setup.

### 6.3.3 Catalyst support effect on reacted catalyst

The XRD patterns for nickel supported catalyst and catalysts before reduction, after reduction and after experiment (named “used” catalyst in the legend) for alumina, Y-zeolite and titanium oxide are representing in Figure 6.3-4 (a), Figure 6.3-4 (b) and Figure 6.3-4 (c) respectively. A lower XRD intensity could be observed for used catalyst compared to reduced and fresh catalyst. The diffraction peaks for Nickel particles after reduction of the nickel catalysts can be seen, matching one of the most intense peaks of Ni:  $2\theta = 44.5^\circ$ ,  $51.8^\circ$  and  $76.4^\circ$  (JCPDS 65-2865). More specifically, the reduction of Nickel supported on titanium oxide lead to much smaller peaks at  $25^\circ$ ,  $37^\circ$ ,  $49^\circ$ ,  $64^\circ$  and  $75^\circ$  (mainly peaks from  $\text{TiO}_2$  spectrum), compared to non-reduced Nickel supported on titanium oxide. New peaks appeared on the spectrum around  $28^\circ$ ,  $36^\circ$ ,  $41^\circ$ ,  $45^\circ$ ,  $55^\circ$ ,  $57^\circ$  and  $70^\circ$ , which cannot all be associated to Ni particles, which most intense peaks are cited above. According to Wang et al., the  $28^\circ$ ,  $36^\circ$ ,  $45^\circ$  and  $55^\circ$  peaks can be associated to  $\text{Ti}_2\text{O}_3$  presence on the catalyst surface (N. Wang et al., 2019). Thus, the reduction of Nickel supported on titanium oxide has modified the structure as shown in their differences from XRD plots, leading to different results between  $\text{TiO}_2$  and  $\text{Ni/TiO}_2$  when used for experiments. For the results when using Y-zeolite support, represented in Figure 6.3-4 (b), the materials preserved their surface morphology after impregnation of Ni, calcination and reduction, as it has been previously shown by Escola et al. for various zeolite materials (Escola et al., 2011). Table 6.3-2 summarised the results of crystallite size for different catalyst support showing a reduction of particle size after plasma treatment for virgin support, as shown in section 6.1.3. It also emphasizes the aforementioned difference between the reduced  $\text{TiO}_2$  and non-reduced  $\text{TiO}_2$ .

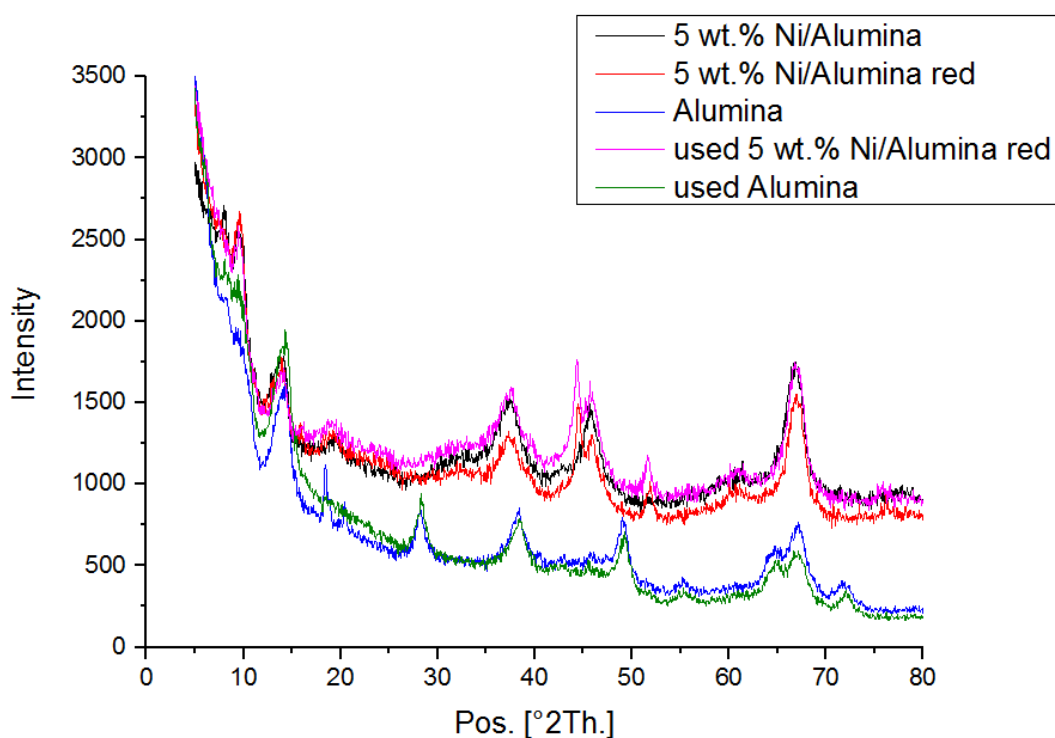
**Table 6.3-2: Crystallite size for different catalyst supports at  $2\theta=44.5^\circ$**

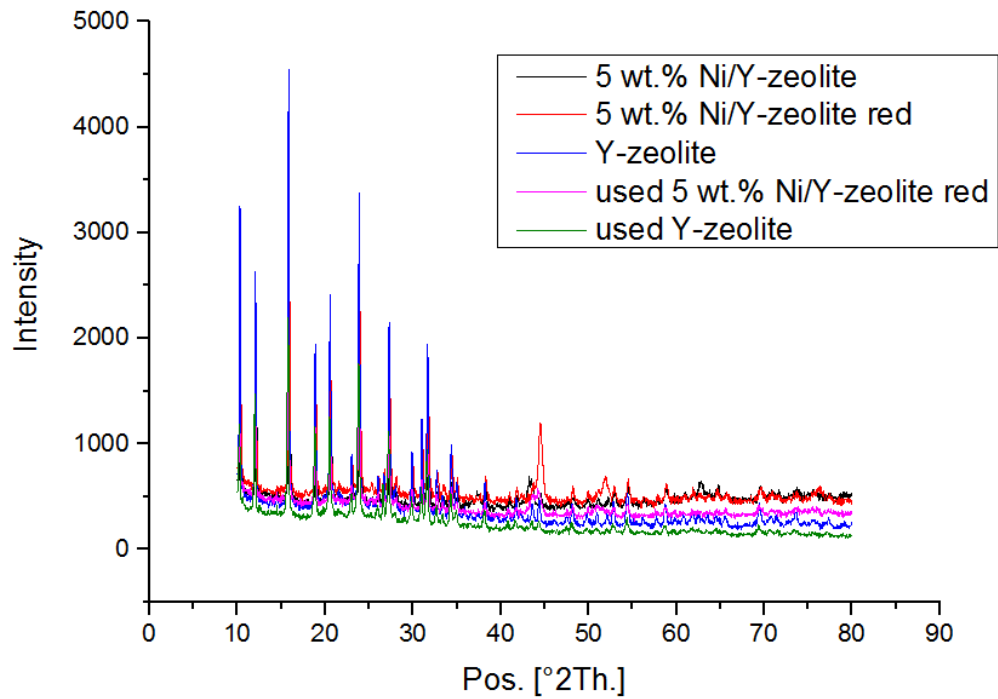
Support	Promoter – 5 wt.% Ni	Particle size before plasma treatment (Å)	Particle size after plasma treatment (Å)
$\text{Al}_2\text{O}_3$	Y	126	199
$\text{TiO}_2$	Y	199	407
Y-zeolite	Y	1290	519
$\text{Al}_2\text{O}_3$	N	169	100
$\text{TiO}_2$	N	1310	290
Y-zeolite	N	919	726

Temperature programmed oxidation was used to determine the amount of carbonaceous coke deposited on the catalysts, as represented in Figure 6.3-5. Comparing the coke deposition on support catalysts, titanium oxide led to a smaller amount of coke deposited on the catalyst, 10 wt.%, compared to the amount of coke deposited on alumina and zeolite, around 16 wt.% for both catalysts. By adding nickel onto the support catalyst surface, less coke was deposited onto the nickel catalyst than on the support catalyst. The reduction of coke deposited was of 100, 50 and 19% for titanium oxide, nickel and Y-zeolite respectively. Coke deposited on nickel supported on titanium oxide could not be detected and thus was assimilated to null. The amount of coke deposited was of 8 wt.% and 13 wt.% for nickel supported on alumina catalyst and nickel supported on y-zeolite catalyst respectively. This result was expected for Y-zeolite catalysts as their main disadvantages are the rapid deactivation resulted from coke deposition (Abu El-Rub et al., 2004). The increase of coke deposition observed on nickel supported on titanium oxide catalyst is due to the oxidation of titanium oxide support after it being reduced before experiments. This is supported by the work of Wu et al., suggested that the mass gain was due to the oxidation of Ni of the reacted catalyst (Wu et al. 2013). Thus, it is very likely that the result differences between nickel supported on titanium oxide catalyst and titanium oxide catalyst are due to the presence of lower oxidation state of titanium within the catalyst, such as  $Ti_2O_3$  mentioned previously.

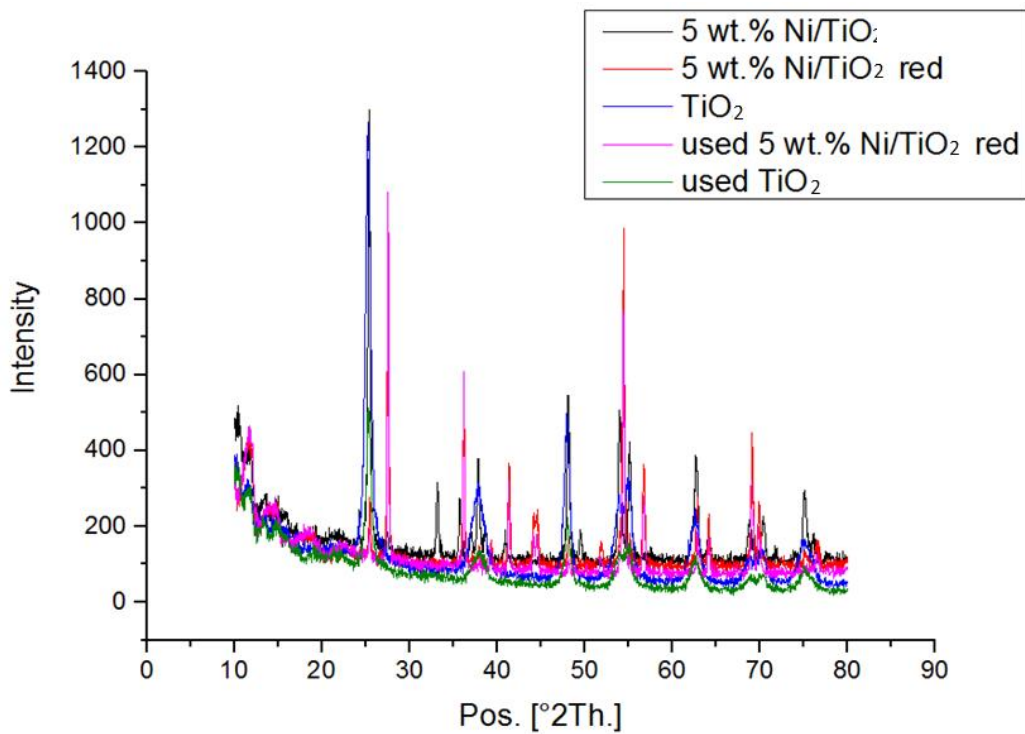
The different catalyst supports were analysed by BET, SEM and their properties are reported in the Method section, Chapter 3, section 3.1.2.3. As previously described, titanium oxide, Y-zeolite and alumina all had a similar isotherm type. The BET surface was around  $150\text{ m}^2.\text{g}^{-1}$  for both alumina and titanium oxide, whereas Y-zeolite had a surface area of  $423\text{ m}^2.\text{g}^{-1}$ . Y-zeolite had the biggest pore size (13.4 nm), followed by titanium oxide (9.7 nm) and alumina had the smallest pore size (3.2 nm). The properties of Y-zeolite has made the catalyst commonly used in industry for oil cracking and refining because of its large surface area and structured pore size makes it a perfect candidate for heavy tar breakdown.(Choi et al., 2006; Möller et al., 2013) Finally,  $TiO_2$  had the highest dielectric constant, about ten times more than alumina's and Y-zeolite dielectric constant is roughly half the dielectric constant of alumina, which is expected as titanium oxide is mainly used as a photocatalyst in industry and plasma chemistry (Tauster et al., 1978; Bartholomew et al., 1980).

To conclude, the use of these different supports, with and without nickel impregnation, favoured the use of alumina over the other supports for a higher syngas and hydrogen production, as well as a better breakdown of tar compounds in the product stream. When considering the different properties of the supports, highlighted in Chapter 3, alumina showed the largest difference compared with the other supports was its smaller pore size (around 3 nm), three times smaller than titanium oxide or Y-zeolite. Thus, in the studied experimental setup, the pyrolysis-plasma-catalysis seemed mainly influenced by the pore size when choosing a catalyst support, instead of the dielectric constant or surface area of the support.



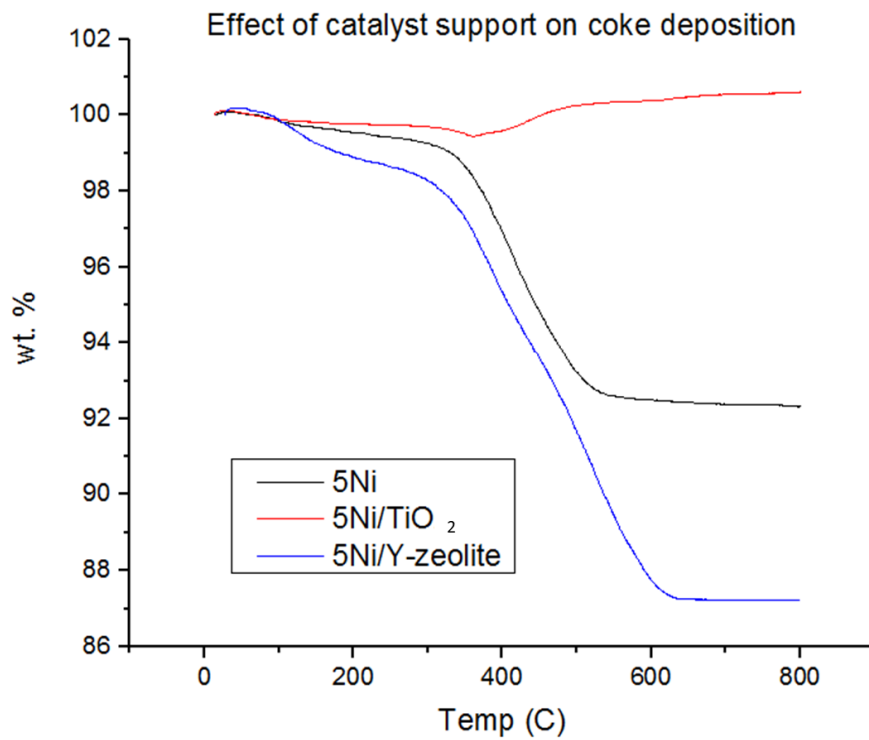


b.

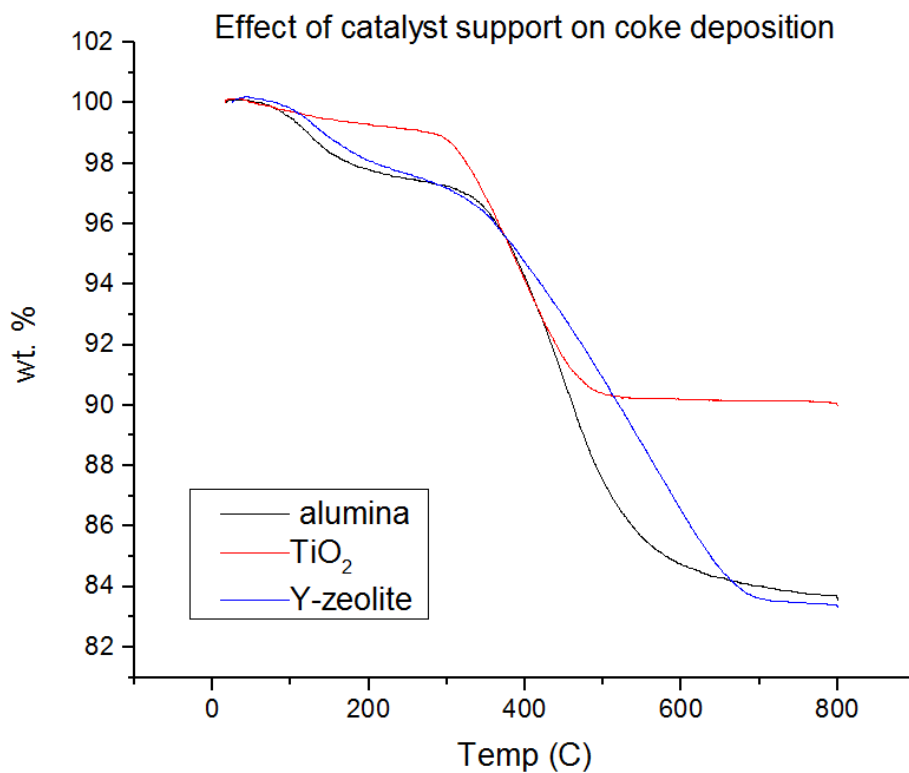


c.

**Figure 6.3-4: XRD plots for Nickel supported catalyst and catalysts before and after reduction and experiment for Alumina (a) Y-zeolite (b) and TiO<sub>2</sub> (c)**



a.



b.

**Figure 6.3-5: Effect of catalyst support on coke deposition on the catalyst for plasma-catalysis systems with Nickel loading (a) or without Nickel (b)**

## 6.4 Summary

The effect of metal promoters was studied on 5 wt.% nickel supported on alumina catalysts. 5 wt.% Mg, Co, Ce, Cu, Fe and Ni were added to the catalyst and, the impact of metal on the gas production, the tar reduction and the reacted catalysts were investigated. Metal promoters did not seem to have a strong influence on the results obtained with a 10 wt.% nickel supported on alumina catalyst. However, subtle changes were observed: the cerium promoter led to the highest syngas and hydrogen production, along with the lowest tar content, whereas the lowest coke deposition was obtained when using the copper promoter.

To further investigate the influence of catalyst metal, the effect of nickel loading on an alumina catalyst was investigated. Loadings of 0, 5 and 10 wt.% of nickel supported on alumina and their influence on gas and liquid products, as well as on reacted catalysts, were reported. The 5 and 10 wt. % of nickel supported on alumina catalysts resulted in the highest syngas production and the lowest tar content respectively. Both loadings led to lowest amount of coke deposited on catalyst. However, these result variations did not seem significant to determine a clear advantage into choosing a specific catalyst.

Finally, the study of different catalyst supports on the pyrolysis-plasma-catalysis of biomass process was presented in the last section. Alumina, titanium oxide and Y-zeolite catalysts were considered for the wide spectra of applications they covered – from steam reforming enhancement and photo-catalysis to oil cracking and refining – and their different properties. These catalyst supports were used in the plasma-catalytic system as catalysts and compared to 5 wt.% nickel supported on Alumina, TiO<sub>2</sub> and Y-zeolite separately. The use of alumina catalyst resulted into the highest production of syngas, with and without nickel added onto the catalyst surface. The use of Y-zeolite catalyst led to the lowest tar content observed, with and without nickel added onto the catalyst surface. The study of the reacted catalyst revealed a change of structure for 5 wt.% nickel supported on titanium oxide catalyst, which led to different results for gas production, tar content and coke deposition between with and without nickel supported on titanium oxide catalyst. For example, nickel deposited on titanium oxide catalyst led to almost no coke deposition on the catalyst.

To better understand the differences between the support catalysts, their properties were investigated. The results showed that the main differences between the support catalysts are the pore size, with the smallest pore size for alumina; the dielectric constant, with the highest dielectric constant for titanium oxide; and the surface area, with the highest surface area for Y-zeolite. Therefore, to obtain a higher syngas quality, the use of alumina can be recommended. To obtain a lower tar content, the use of  $\gamma$ -zeolite should be encouraged, even if the tar content when using nickel supported on alumina catalyst is relatively low. Finally, the use of nickel supported on titanium oxide catalyst would lead to a very low coke deposition on the catalyst. In conclusion, in the studied experimental setup, the use of pyrolysis-plasma-catalysis to obtain high quality syngas and higher tar reduction seemed mainly influenced first by the pore size when choosing a catalyst support, followed by the surface area and of the dielectric constant of the support.

## **Chapter 7: Packed-bed DBD plasma-catalysis to produce higher quality syngas**

This chapter consists of two sections, focusing on the use of a packed bed dielectric barrier discharge (DBD) plasma-catalytic system to produce high-quality syngas. The experiments undertaken for this chapter were using a two stage fixed bed reactor coupled with a packed bed DBD plasma-catalytic system, described in Chapter 3, section 3.2.3. The sections within this chapter are described in the following.

Section 7.1 examines the effect of plasma-catalysis compared to pyrolysis-catalysis (no plasma) systems downstream of the fixed bed reactor. Biomass, alongside its different constitutive compounds – cellulose, hemi-cellulose and lignin – were investigated. The effect of plasma-catalysis on gas production and the packing material are discussed in this section.

Section 7.2 describes the study of the influence of parameters on produced gas composition and reacted packing material. The influence of power input and packing length is reported.

### **7.1 Tar model compounds and biomass components used as feedstock in the packed-bed DBD plasma-catalytic reactor**

In this section, the production of gases from a two-stage biomass pyrolysis with a packed bed DBD plasma-catalysis was investigated alongside the reacted catalysts, via comparison of two stage pyrolysis-catalysis and pyrolysis-plasma-catalysis for the steam reforming of biomass pyrolysis gases. Different feedstocks were used in this section, in order to better understand the differences and breakdown mechanisms: biomass in the form of waste wood and the constituents of biomass – cellulose, hemi-cellulose and lignin. The experiments used the equipment and procedure described in section 3.2.3.4. a power input of 20 W was used to sustain the plasma discharge, barium titanate used as packing material, a packing length of 2.5 cm and an input steam flow rate of 2 g/h to stimulate the steam reforming process.

### 7.1.1 Effect on gas production

The results of the effect of plasma, in terms of product yield and gas composition and yield, via comparison between pyrolysis-catalysis and pyrolysis-plasma-catalysis of biomass and its components – cellulose, hemi-cellulose and lignin - for the packed bed DBD plasma-catalytic system, are represented in Table 7.1-1. On the one hand, the quantity of gas produced increased for biomass and lignin when switching from a pyrolysis-catalysis to a pyrolysis-plasma-catalysis system, from 24.6 to 26.8 wt.% for biomass and from 13.8 to 15.3 wt.% for lignin. On the other hand, the quantity of gas produced decreased when switching from a pyrolysis-catalysis to a pyrolysis-plasma-catalysis system, from 25.8 to 24.8 wt.% for cellulose and from 22.1 to 19.3 wt.% for hemi-cellulose. However, the experimental error obtained from the packed-bed reactor in Chapter 3, section 3.2.3.5, was of 2.43 %. Thus, the aforementioned differences between the mass balances and gas yields for pyrolysis-catalysis and pyrolysis-plasma-catalysis systems, are within the experimental error. Accordingly, similar gas yields were obtained for biomass and its components when switching from a pyrolysis-catalysis system to a pyrolysis-plasma-catalysis system.

The product gas obtained when using pyrolysis-plasma-catalysis and pyrolysis-catalysis systems with the packed bed DBD reactor, was compared in Figure 7.1-1 and Figure 7.1-2, representing syngas production and detailed gas production respectively, for biomass and its components – cellulose, hemi-cellulose and lignin. Figure 7.1-1 (a) and Figure 7.1-2 (a) showed the results for the plasma-catalysis system whereas Figure 7.1-1 (b) and Figure 7.1-2 (b) represented the results for the pyrolysis-catalysis system.

First, in a plasma-catalysis system, the syngas production was the highest for biomass with a 5.22 mmol per gram of feedstock, due to a higher hydrogen and carbon monoxide production of 2.78 and 2.43  $\text{mmol.g}^{-1}_{\text{biomass}}$  respectively. Higher yield of carbon dioxide was obtained when using cellulose, with a production of 3.26  $\text{mmol.g}^{-1}_{\text{biomass}}$ , and higher yield of methane was obtained when using lignin, with a production of 1.49  $\text{mmol.g}^{-1}_{\text{biomass}}$ . Second, when comparing the pyrolysis-catalysis and the plasma-catalysis systems, the trends observed for the plasma-catalysis system were observed in the pyrolysis-catalysis system as well. However, all individual gas

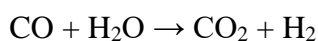
compositions were higher for the plasma-catalysis than for the pyrolysis-catalysis system.

When comparing the different gas yields obtained in presence of and without plasma, it was observed, as in Chapter 5, that the plasma catalytic system produced higher CO and H<sub>2</sub> yields. The yields of methane and carbon dioxide remain stable in pyrolysis-catalysis and pyrolysis-plasma-catalysis processes. This would suggest that steam reforming of pyrolysis hydrocarbons (Equation 7.1) is promoted by the plasma-catalytic process, as observed with the DBD reactor without a packed bed in previous chapters. The absence of metal in the packed bed DBD reactor was shown not promote the water gas shift reaction (Equation 7.2) as the yields of methane and carbon dioxide remained stable in presence of plasma.

**Equation 7.1**



**Equation 7.2**



As discussed in Chapter 5, the pyrolysis of cellulose, hemi-cellulose and lignin led to specific gas products, according to Yang et al. They observed that, due to their chemical structures, hemicellulose was more likely to result into a higher carbon dioxide yield, cellulose a higher carbon monoxide yield, and lignin a methane yield (Yang et al. 2007). However, considering the small difference between the produced quantity of carbon oxides for cellulose and hemi-cellulose, it can be considered that the abundant presence of C-O Chemical groups in cellulose and the numerous C=O chemical groups in hemicellulose both led to similar amount of CO<sub>2</sub> and CO produced in the case of the studied packed bed DBD reactor. Moreover, in plasma reaction zones, it has been reported that carbon dioxide can react to produce excited CO\* and O<sub>2</sub>\* species (Brock et al., 1999; Zheng et al., 2003). This could also favour a small difference between the carbon oxide yields.

The addition of plasma into the packed bed had a significant impact on the production of gas and more specifically on syngas. First, the application of high voltage resulted in the creation of a non-equilibrium plasma within the void space between the packing material beads. By refracting of the electric field on the beads, the electric field

becomes stronger and non-uniform with an intensity dependent on the bead properties, such as porosity or dielectric constant. (Fridman et al., 2011) Roughness and porosity alongside the shape of the packing – i.e. pellets, fibres, granulates – in the discharge volume have shown to be the origin of the enhancement the electric field (Takuma, 1991). The improvement resulting from the use of a packed bed is not only related to the catalytic component of the packing material, but also a physical effect of the packing shape (Neyts et al., 2014). Charge accumulation and polarisation effects on the surface of the dielectric layer resulted into an enhancement of the electric field, which key features are curvature, contact angle and dielectric constant of the packing (Chang, 2000; Woo Seok et al., 2003). Considering the very high dielectric constant of barium titanate, with a dielectric permittivity estimated up to  $10^6 \text{ F.m}^{-1}$  (Valdez-Nava et al., 2009), it can be considered that the packed bed DBD will lead to a very strong and non-uniform electric field which promotes the breakdown of molecules and the production of gas.

This phenomenon has been further described by Mei et al in the conversion of  $\text{CO}_2$  using a  $\text{BaTiO}_3$  packed bed DBD reactor. Higher electrical field and electron energy were observed when  $\text{BaTiO}_3$  was introduced, compared to the introduction of glass beads. These higher electrical field and electron energy will affect plasma chemical reactions, resulting into more effective conversion, even though the residence time is reduced due to smaller discharge volume at same gas flow. Photocatalysis of  $\text{BaTiO}_3$  was also activated by the presence of energetic electrons generated by the discharge. It created electron-hole pairs on the surface of the catalyst which contributed to enhance the  $\text{CO}_2$  conversion (Mei et al., 2015).

In fact, it has been shown that the electric field can be enhanced by packing materials having high dielectric constants, leading to an increase in electron temperature (Takaki et al., 2004; Gómez-Ramírez et al., 2017; Butterworth et al., 2017) Gómez-Ramírez et al. (2017) studied the enhancement of chemical yield during the atmospheric plasma synthesis of ammonia in a ferroelectric packed bed dielectric barrier discharge (DBD). The results showed higher nitrogen conversion for used of packed bed DBD reactor compared to DBD reactors. An inhomogeneous electric field has been reported with ferroelectric pellets as they are characterised with higher values of dielectric constant. With local variations of electric field, local variations of

temperature could lead to substantial changes in the dielectric constant of the ferroelectric pellets and further enhance the plasma intensity and chemical conversion (Gómez-Ramírez et al., 2017) Butterworth et al. (2017) studied the effect of dielectric constant on plasma dynamic for a single pellet DBD reactor for zirconia,  $\text{CaTiO}_3$ ,  $\text{BaTiO}_3$ ,  $\text{SiO}_2$  and  $\text{Al}_2\text{O}_3$  with a highly porous material (alumina) and a very high dielectric constant for barium titanate (about 4000). With increasing dielectric constant, the breakdown voltage for plasma ignition decreased. Moreover, the plasma showed radial expansion and numerous intense localised streamer discharges forming between the poles of the bead and the electrodes. (Butterworth et al., 2017) Takaki et al. (2004) also investigated via modelling the atmospheric pressure of nitrogen plasmas in a ferroelectric packed bed DBD. They showed that with increasing packing dielectric constant and applied voltage, the discharge power and current density increased. Moreover, ions, radical and metastable molecule densities increased with increasing dielectric constant. In particular, The quantity of reactive nitrogen molecule densities increased by more than 10 to 100 times with increasing dielectric constant from 660 to 10,000. (Takaki et al., 2004)

Van Laer et al. (2017) have investigated through fluid modeling the effect of dielectric constant on the plasma behaviour in a packed bed plasma reactor. By keeping the space between electrodes constant, it was demonstrated that plasma discharge behaviour changed depending on the size of packing beds and their dielectric constant. For packing with low dielectric constant, the discharge was spread out over the whole discharge gap, in voids and connecting void channels. When increasing the dielectric constant, the plasma discharge becomes localised in the voids. The larger the beads, the higher the dielectric constant should be to obtain a full gap plasma discharge. (Van Laer et al., 2017)

Moreover, high dielectric constant material used as packing in non-thermal packed bed DBD plasma reactor has been shown to improve the removal efficiency of volatile organic compounds and reduce ozone formation. Ogata et al (1999) investigated benzene decomposition using a nonthermal plasma reactor packed with ferroelectric pellets. Higher relative dielectric constant was found to result into higher conversion at low field strength and higher energy efficiency. Moreover, the conversion of benzene was shown to be affected by the relative dielectric constant of the material

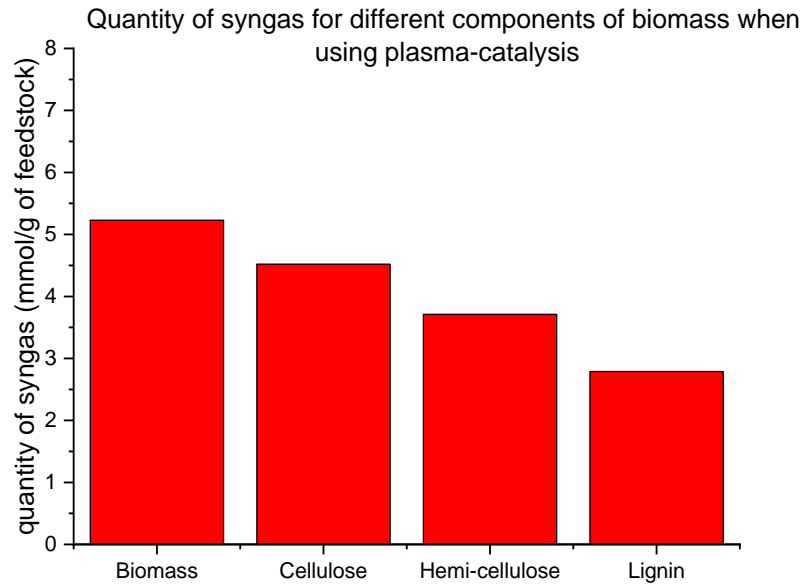
instead and not by the main component contained in the material. (Ogata et al., 1999) Song et al studied the chlorobenzene removal in packed bed non-thermal plasma catalysis reactor over CoMn/TiO<sub>2</sub> and CeMn/TiO<sub>2</sub>. They showed that, with higher dielectric constant, CoMn/TiO<sub>2</sub> resulted into better removal efficiency, carbon dioxide selectivity and ozone decomposition. (Song et al., 2018)

Increasing dielectric constant of the packed materials has shown to enhance the gas ionisation and electron energy (Mei et al., 2015; Wang et al., 2018). Wang et al. (2018) showed that when the dielectric constant shifted from 5 to 1000, the discharge mode changed from surface discharges to local filament discharges between the packing particles, leading to a higher production of reactive species. With higher dielectric constant, resulted higher streamer propagation and discharge development, which led to faster production of reactive species. (Wang et al., 2018)

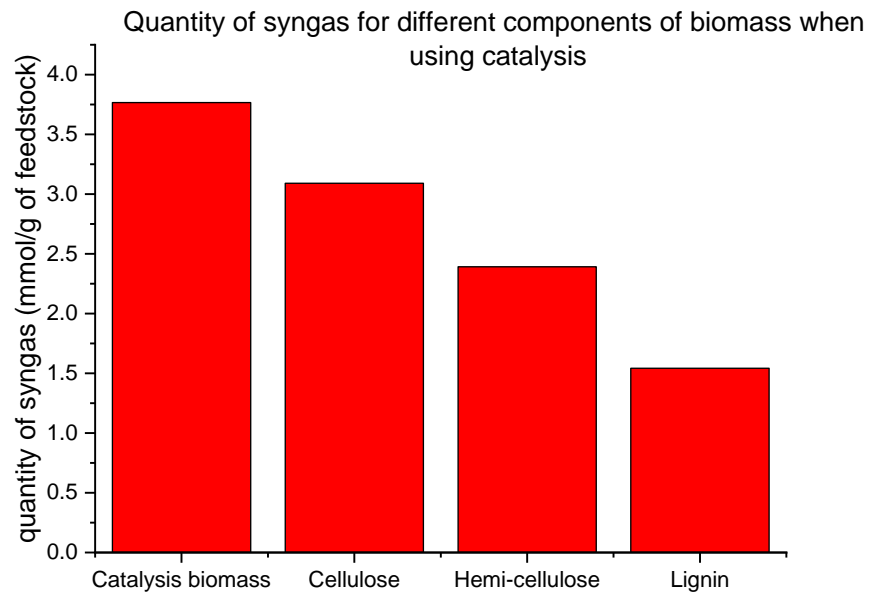
Chung et al (2014) studied the dry reforming of methane with a packed bed DBD reactor using ferroelectric catalysts and showed that filling a DBD reactor might enhance the electric field strength, enhancing the microdischarges (limited by the dielectric constant) which may promote inelastic electrons. However, the trade-off is that the gas retention time is reduced, reducing the void volume as well. For materials with higher dielectric constant such as barium titanate, the packing can store electrons via electrostatic attraction, an effect of polarisation under an electric field, thus promoting the conversion of methane and carbon dioxide for methane dry reforming compared to DBD reactor without packing material. Due to polarisation and the storage of charges on the high dielectric constant material, syngas production could be enhanced through an increase of higher energy electrons leading to effective collision. This could also be explained by the increased density of free electrons when ferroelectrics are placed within the plasma discharge. This phenomenon leads to an increase in radical species – O, H, CH<sub>y</sub> for example – through the increase of electron impact excitation, resulting into a higher syngas production. (Chung et al., 2014)

Finally, Gallon et al. (2012) investigated the effects of packing material for hydrogen production in dry methane reforming in a DBD reactor. The addition of packing into the DBD reactor showed an increase in H<sub>2</sub>/CO molar ratio and a decrease in CO selectivity, highlighting, alongside with low conversion of carbon dioxide, the presence of water gas-shift reaction. The different packing studied by Gallon et al.

were quartz wool, alumina and zeolite 3A, with similar dielectric constant. The difference in conversion results can be linked to the different porosity of the materials, which is linked to the void fraction of the discharge gap wherein filamentary discharge can be generated. As discussed previously, the fully packed bed led to a discharge shift from filamentous to a combination of microdischarges and surface discharges on the packing material surface. Such transition can reduce the discharge volume and thus the effect of plasma-catalysis, resulting into lower conversions and energy efficiency. However, through catalyst activation and improvement of catalytic activity by the plasma discharge, these decreased performances could be compensated. The fact that quartz wool presented the highest methane conversion and hydrogen production most likely due to high void fraction showed that multiple factors will influence the plasma-catalytic discharge, including size, porosity, shape, volume fraction and dielectric properties of the packing material. (Gallon et al., 2012) Thus, it should be highlighted that other parameters alongside the dielectric constant are essential for optimising hydrogen-rich production of syngas in packed-bed DBD plasma-catalytic reactor.



a.

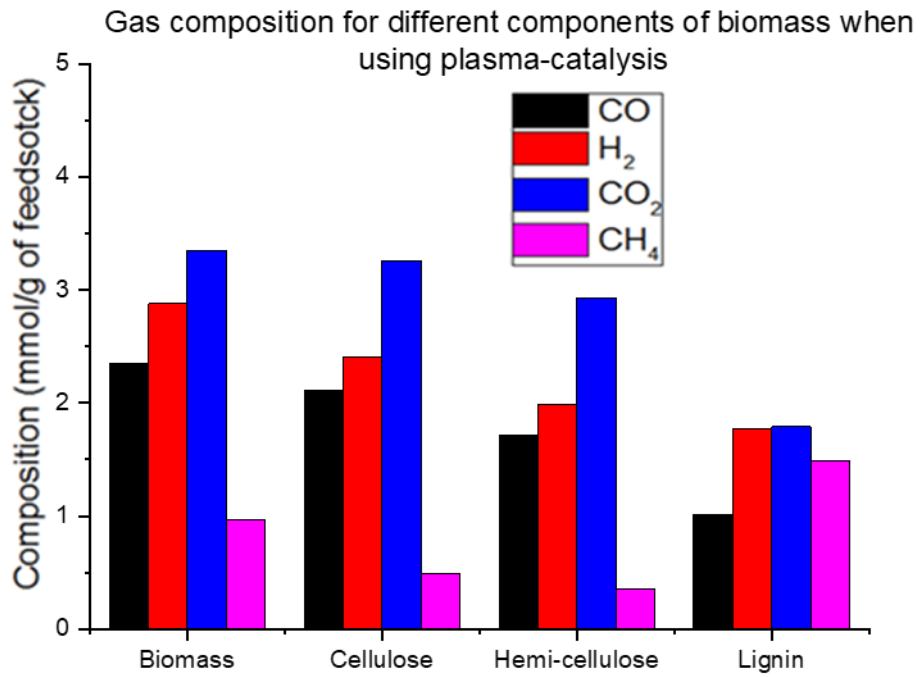


b.

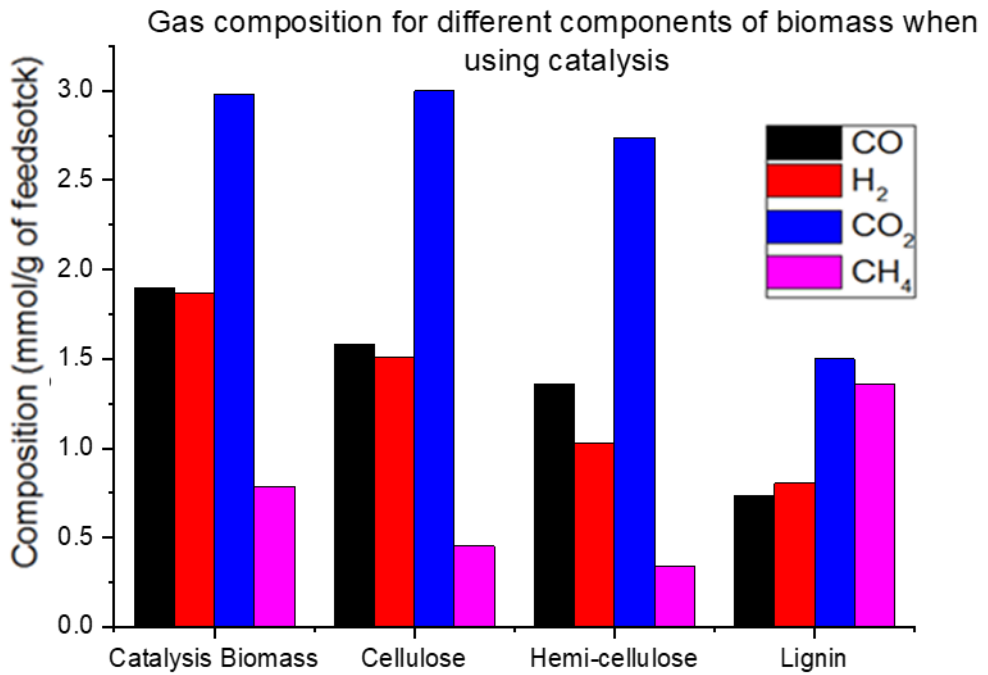
**Figure 7.1-1: Quantity of syngas produced for different biomass components in plasma-catalysis (a) and pyrolysis-catalysis (b) systems**

**Table 7.1-1: Experimental summary for pyrolysis-catalysis and plasma-catalysis experiments using biomass components**

Experiment	Pyrolysis-Catalysis				Plasma-Catalysis 20 W				% error
	Biomass	Cellulose	Hemi-Cellulose	Lignin	Biomass	Cellulose	Hemi-Cellulose	Lignin	
Gas (wt.%)	24.62	25.82	22.13	13.79	26.78	24.83	19.33	15.31	12.6
Liquid (wt.%)	-	-	-	-	-	-	-	-	-
Char (wt.%)	22	18	19	45	22	18	25	48	0
Mass Balance (%)	97.74	93.40	95.75	99.91	87.24	90.91	91.06	95.79	11.0
Composition in mmol/g of feedstock									
CO	1.90	1.58	1.36	0.74	2.43	2.11	1.72	1.02	6.0
H <sub>2</sub>	1.87	1.51	1.03	0.80	2.78	2.42	1.99	1.77	5.8
CO <sub>2</sub>	2.98	3.00	2.74	1.50	3.07	3.26	2.93	1.79	15.8
CH <sub>4</sub>	0.79	0.45	0.34	1.36	0.93	0.50	0.35	1.49	6.7



a.



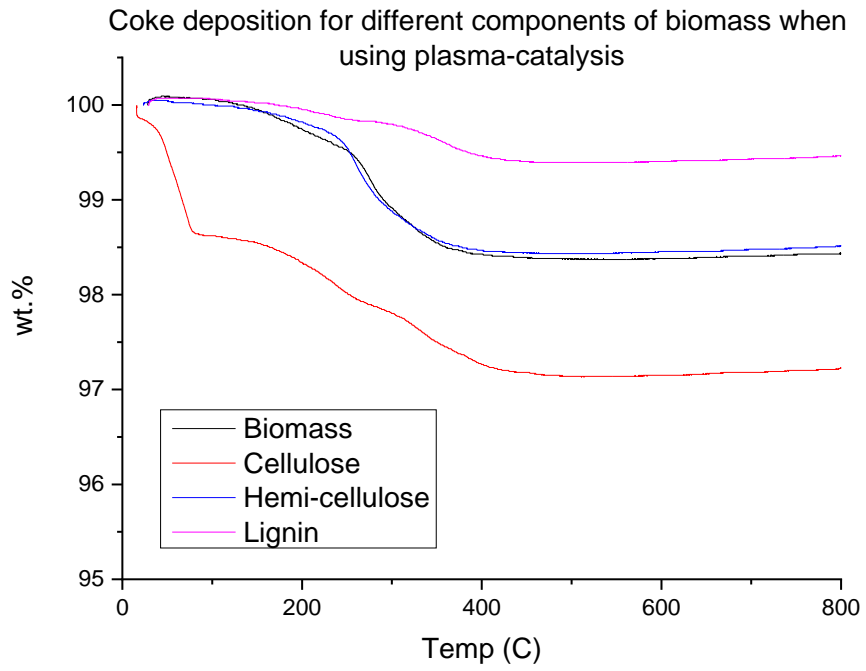
b.

**Figure 7.1-2: Detailed composition of produced gas for different biomass component in plasma-catalysis (a) and pyrolysis-catalysis (b) systems**

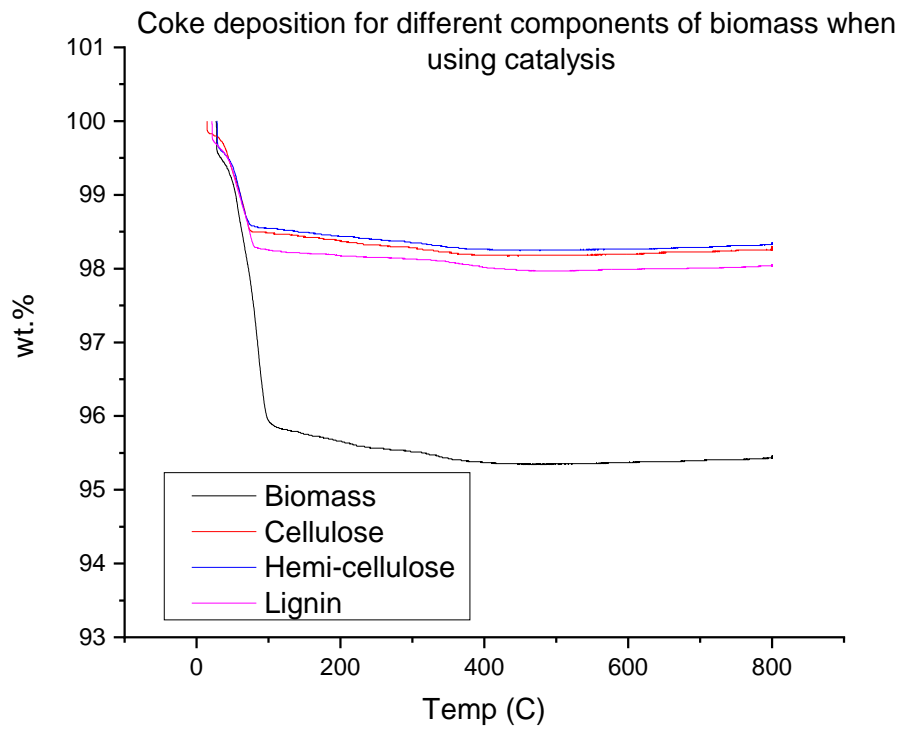
### 7.1.2 Effect on reacted catalyst

Temperature programmed oxidation was used to determine the amount of carbonaceous coke deposited on the packing material after pyrolysis-catalysis and pyrolysis-plasma-catalysis for biomass and its components – cellulose, hemi-cellulose and lignin. The associated results are represented in Figure 7.1-3, (a) for plasma-catalysis process and (b) for pyrolysis-catalysis process. The pyrolysis-catalysis system resulted in higher weight loss compared to the weight loss with the pyrolysis-plasma-catalysis process. In the plasma-catalysis system, the use of cellulose led to the highest catalyst weight loss with 2.8 wt.% and the weight loss was observed by decreasing order: cellulose > hemi-cellulose > lignin > biomass. In the pyrolysis-catalysis system, the use of biomass resulted into the highest weight loss on barium titanate with 4.5 wt.% and the catalyst weight loss was observed in the decreasing order: biomass > lignin > cellulose > hemi-cellulose. The weight loss trend is different to the trend observed in Chapter 5 section 5.2.2.3, as for both pyrolysis-catalysis and pyrolysis-plasma-catalysis the weight loss was obtained in this order: biomass > cellulose > lignin. However, it is worth observing that the quantity of coke deposited on the catalyst surface is already quite negligible, as suggested by previous publications such as the one from Wu et al. (Wu, 2013). Therefore, the differences between the different component of biomass can be considered non-significant.

Cellulose and hemi-cellulose had similar weight loss for the pyrolysis-catalysis and the plasma-catalysis processes whereas, the addition of plasma to the process reduced the catalyst weight loss for biomass and lignin. It can be observed that the weight loss happened mainly around 100 °C, indicating a vaporisation of water which had been adsorbed by the packing material during the steam reforming pyrolysis process. In the pyrolysis-catalysis process, represented in Figure 7.1-3 (b), the weight loss appearing between 100 and 550°C, which indicates the amorphous nature of the carbon deposited on the catalyst (Yao et al., 2014), was smaller than 0.5 wt.%. In the plasma-catalysis process, represented in Figure 7.1-3 (a), the weight loss representing the amorphous carbon deposition, was around 1 wt.% for all feedstocks. Therefore, the coke deposition was considered negligible in both processes, confirming the previous observation made in section 5.3.4: the higher the quantity of catalyst, the less coke will deposit on the catalyst.



a.



b.

**Figure 7.1-3: Coke deposition on reacted catalyst for different biomass component in plasma-catalysis (a) and pyrolysis-catalysis (b) systems**

Finally, the difference within the coke deposition between the plasma-catalysis and the pyrolysis-catalysis processes can be explained by the fact that the plasma-catalysis stimulated the steam reforming process by a higher temperature within the reactor, leading to a lower water adsorption and slightly higher coke deposition, as hydrocarbon cracking can lead to coke deposition on metal oxide catalyst such as barium titanate (Bartholomew, 2001). However, the Boudouard reaction suggested that plasma-catalysis led to higher decoking compared to catalysis only as CO is the most stable carbon oxide at high temperature (Kameshima et al., 2015).

## **7.2 Packing length and input power effect**

In this section, the influence of given parameters, here the packing length and the power input, were investigated by studying the production of gases and reacted catalysts from a two-stage biomass pyrolysis with a packed bed DBD plasma-catalysis for the steam reforming of biomass pyrolysis gases. Different power inputs, from 20 to 40 W, and different packing lengths, from 2.5 cm to 4.5 cm, were included in this study. Higher power inputs were not sustainable on the smaller packed bed length. Therefore, at 20 W, three packing lengths were studied, 2.5, 3.5 and 4.5 cm; whereas for a packing length of 4.5 cm, three power inputs were considered, 20, 30 and 40 W. Intermediary measurement were also considered to enable better study of the influence of packing length and power input on the packed bed DBD plasma-catalytic system. The experiments used the equipment and procedure described in section 3.2.3.4. with barium titanate used as packing material, an input steam flow rate of 2 g/h to stimulate the steam reforming process, and cellulose as feedstock for the biomass pyrolysis.

### **7.2.1 Effect on gas production**

The results of the influence of packing length and power input, in terms of product yield and gas composition and yield for the packed bed DBD plasma-catalytic system, are represented in Table 7.2-1. The quantity of gas produced was the highest for the plasma-catalysis with a power input of 20 W and the packing bed of 2.5-cm length, with a production of 24.8 wt.%. The lowest produced quantity of gas was 18 wt.% for plasma-catalysis with a power input of 20 W and a packing bed length of 3.5 cm. For a given power input, the smallest bed length resulted into the highest quantity of gas

produced, with 24.8 wt. % of gas yield for a power input of 20 W and a bed length of 2.5 cm; 21.7 wt. % of gas yield for a power input of 30 W and a bed length of 3.5 cm; and 21.1 wt. % of gas yield for a power input of 40 W and a bed length of 4.5 cm.

The product gas obtained for the different parameters, was represented in Figure 7.2-1 and Figure 7.2-2, representing syngas production and detailed gas production respectively. Figure 7.2-2 (a) and Figure 7.2-2 (b) showed the results for the influence of packing bed length at a fixed power input of 20 W, and the results for the influence of the power input for a fixed packing bed length of 4.5 cm. First, the highest production of syngas was observed for a power input of 40 W and a packing bed length of 4.5 cm ( $4.65 \text{ mmol.g}^{-1}_{\text{biomass}}$ ), whereas the lowest syngas production was observed for a power input of 20 W and a packing bed length of 4.5 cm ( $3.36 \text{ mmol.g}^{-1}_{\text{biomass}}$ ). In Figure 7.2-1, the quantity of syngas produced is represented for different power input and packing bed length.

For each packing bed length, the highest power input led to the highest production of syngas. This is highlighted in Figure 7.2-2 (b) with the detailed gas composition of the product gas at a constant bed length, here with the example of a bed length of 4.5 cm. The increase of power input at a constant packing bed length resulted into a higher hydrogen production, from 1.46 to 2.51  $\text{mmol.g}^{-1}_{\text{biomass}}$  when the power input doubled. Carbon monoxide slightly increased from 1.9 to 2.14  $\text{mmol.g}^{-1}_{\text{biomass}}$  with the power input increase between 20 and 40 W, whereas the carbon dioxide and methane production are insignificantly changed, within the range of 0.1  $\text{mmol.g}^{-1}_{\text{biomass}}$ .

At a given power input, as shown here in Figure 7.2-2 (a) with the example of a power input of 20 W, the increase of packing bed length resulted into a decreasing hydrogen production, from 2.42 to 1.46  $\text{mmol.g}^{-1}_{\text{biomass}}$  when the packing bed length increased from 2.5 to 4.5 cm. Carbon monoxide slightly decreased from 2.11  $\text{mmol.g}^{-1}_{\text{biomass}}$  for packing length of 2.5 cm, to 1.63 and 1.90  $\text{mmol.g}^{-1}_{\text{biomass}}$  for packing length of 3.5 and 4.5 cm respectively. Carbon dioxide and methane production followed a similar trend, from 3.26 and 0.5  $\text{mmol.g}^{-1}_{\text{biomass}}$  for a packing length of 2.5 cm, to a minimum of 2.33 and 0.43  $\text{mmol.g}^{-1}_{\text{biomass}}$  for packing length of 3.5 cm.

First, as presented in Chapter 5, the increase of power input for a given packing bed length is likely to increase the electric field, electron temperature alongside the temperature of the discharge gas. This will create more active species and energetic

electrons, enhancing an easier breakdown of molecules within the reactor (Paulussen et al., 2010). Thus, the increase of power input for a given packing bed length resulted in an easier breakdown of molecules, leading to a higher production of smaller particles such as hydrogen and carbon monoxide. This has generally been reported throughout multiple studies for the reforming of methane, as mentioned by Gallon et al. (Gallon et al., 2012)

The decomposition of carbon dioxide was studied in a packed DBD plasma reactor for different packing materials at different input voltage was investigated by Ray et al. (2016). It is commonly known that dielectric packing improves the strength of the electric field, mainly at corners and edges, leading to more charges transferred to microdischarges. By comparing different packing materials, Ray et al. showed that the highest discharge power and the highest charge transfer were obtained for TiO<sub>2</sub> packing, the packing with the highest dielectric constant, compared to alumina, glass beads and cerium oxide. Furthermore, carbon dioxide conversion was higher for packed bed DBD than for DBD without packing, which was most likely due to some or all of the following: an improve field strength, homogeneous discharge and surface activation of the packing. Thus, higher power input resulted into a higher conversion for all packing materials. (Ray and Subrahmanyam, 2016)

Looking into the electrical diagnostics of a single-stage plasma-catalytic, Tu et al. (2011) studied the effect of packing using TiO<sub>2</sub> as packing material in nitrogen atmosphere. Tu et al. found that an increase in the applied voltage or discharge power resulted into an enlarge discharge area on the surface of the catalyst. When the DBD reactor is fully packed, the discharge behaviour changes from a filamentary discharge to a combination of surface discharges on the catalyst surface and local microdischarges located in the void space between the packing material and the dielectric barrier. A fully packed reactor required higher applied voltage and input power at the same discharge power, resulting into a smaller current. (Tu, Helen J Gallon, et al., 2011)

The packed bed dielectric barrier discharge plasma reactor was previously modeled by Van Laer et al. (2016) who found that the electric field strength and electron temperature was enhanced at the contact points of the dielectric material due to polarisation of the packed beads by the applied potential. At a low applied potential,

the plasma discharge stays at the contact points and possesses similar properties to a Townsend discharge (described in section 2.3.1 of Chapter 2). When the applied potential is high enough, the plasma discharge will travel through the gaps between the packing beads from wall to wall, resembling a glow discharge. (Van Laer and Bogaerts, 2016) Therefore, the highest gas yield, syngas and hydrogen generation for smaller packed bed length at a given power input might be due to the type of plasma in place: for smaller packed bed length, the applied voltage is high enough to generate a discharge with similar properties to a glow discharge. Instead of involving mainly reactive free electrons like in a Townsend discharge, this type of plasma will involve more excited and reactive molecules, enabling a better chemical breakdown and a higher gas production for smaller packed bed length at a given power input.

Furthermore, the overall temperature in the plasma-catalytic reactor can increase due to the migration flow of charged species (such as electrons or ions) through phenomena including dielectric loss, joule heating and gas heating in the discharge. Jogan et al. (1993) studied ozone generation on a BaTiO<sub>3</sub> packed bed plasma reactor and observed that the use of ferroelectric material may increase the reactor temperature more easily, due to a higher dielectric loss generated for material with higher dielectric constant (Jogan et al., 1993). Thus, the increase of power input at a given packed bed length suggested to result into a higher electric field, as well as a higher dielectric loss, leading to an enhancement of steam reforming of pyrolysis hydrocarbons (Equation 7.1) which resulted into a higher syngas yield. For a given power input, increasing the packed bed length resulted into a smaller gas and syngas production. This could be associated to a decrease of discharge volume with a higher packing volume, leading to a more difficult breakdown of molecules due to lesser collision probability between reactive species. This can be observed in the literature as well, as shown by Linga Reddy et al. (2013) In their work, they studied the effect of packing length on H<sub>2</sub>S conversion through various percent of packed bed (0, 10, 25, 50, 75 and 100%). Their works showed that higher packing led to a decrease in specific energy input, which may be due to a decrease in the effective microdischarge distribution. It was also observed that the increase of packing bed length resulted in lower conversion, which may be linked to a decrease of discharge volume, alongside a sulfur deposit on the surface of the catalyst (Linga Reddy et al., 2013).

Specific energy input has been defined by Kim et al. (2005) as the discharge power divided by the gas flow rate. In their study of the decomposition of dilute aromatic compounds – benzene derivatives and formic acids – by atmospheric plasma-driven catalysis, Kim et al. showed that the decomposition efficiency of these volatile organic compounds was mainly determined by the specific energy input, which was the key scaling factor. An optimum specific input energy must be determined on by-product formation and the decomposition efficiency of volatile organic compounds. (Kim et al., 2005) Thus, the increase of packing length might decrease the gas flow rate through the plasma, reducing the effective microdischarge distribution as pointed out by Linga Reddy et al.

Finally, Magureanu et al (2013) studied the effect on an increase of packing in a DBD reactor for the oxidation of toluene with palladium catalysts. Toluene conversion and carbon dioxide selectivity were observed for a plasma only DBD reactor, 0.56 g of Pd/Al<sub>2</sub>O<sub>3</sub> catalyst and 2.24 g of catalyst which occupied the entire discharge gap. Toluene was first introduced without plasma for few hours to enable saturation of the catalyst bed. When igniting the plasma, a very high toluene concentration was in the bed due to desorption of toluene from Pd/Al<sub>2</sub>O<sub>3</sub> catalyst, higher than the input concentration. As conversion is known to decrease with increase concentration, the DBD reactor showed better toluene removal at given specific energy input. Even if the carbon dioxide selectivity was higher than 80%, the configuration was not optimal for toluene removal. For a smaller amount of catalyst – 0.56 g – the carbon dioxide conversion was very similar to the higher packing quantity, higher than 75% selectivity, and much higher than for the plasma alone experiments which showed a selectivity below 40% regardless of the specific energy input. Toluene removal in this case was very similar to plasma alone due to oxidation of toluene adsorbed on the catalyst. (Magureanu et al., 2013) Therefore, the increase of packing length may also increase the pyrolysis products adsorption on the catalyst, reducing their removal due as they accumulate in the packed bed.

**Table 7.2-1: Experimental summary for different power input and different packing length**

Plasma-Catalysis – power input (W)	20			30		40	% error
	2.5	3.5	4.5	3.5	4.5	4.5	
Bed length (cm)	2.5	3.5	4.5	3.5	4.5	4.5	
Gas (wt.%)	24.83	17.96	23.83	21.73	19.77	21.12	12.6
Liquid (wt.%)	-	-	-	-	-	-	-
Char (wt.%)	18	18	17	17	18	19	0
Mass Balance (%)	90.91	88.92	96.40	91.66	90.81	89.28	11.0
Composition in mmol/g of feedstock							
CO	2.11	1.63	1.90	1.97	1.90	2.14	6.0
H <sub>2</sub>	2.42	1.81	1.46	2.54	2.10	2.51	5.8
CO <sub>2</sub>	3.26	2.33	2.99	3.23	2.90	3.01	15.8
CH <sub>4</sub>	0.50	0.43	0.49	0.59	0.57	0.63	6.7

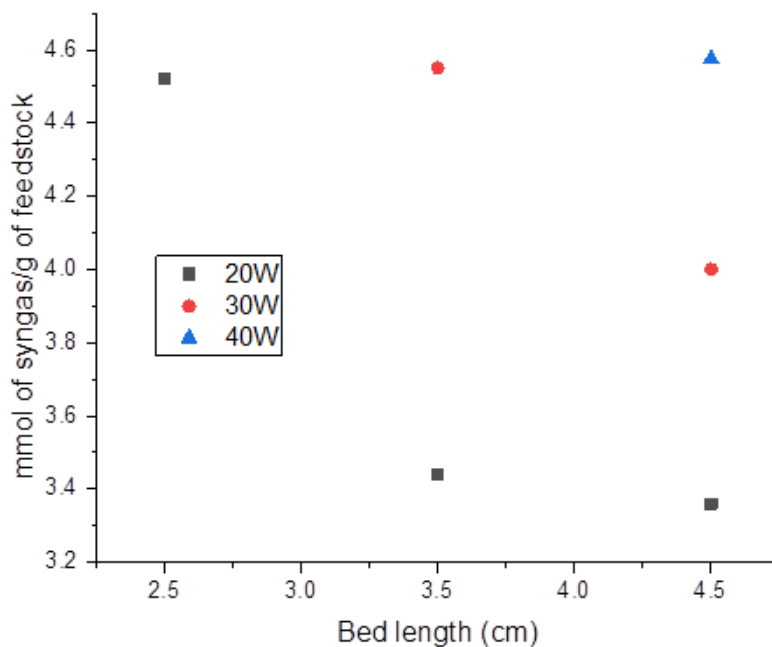
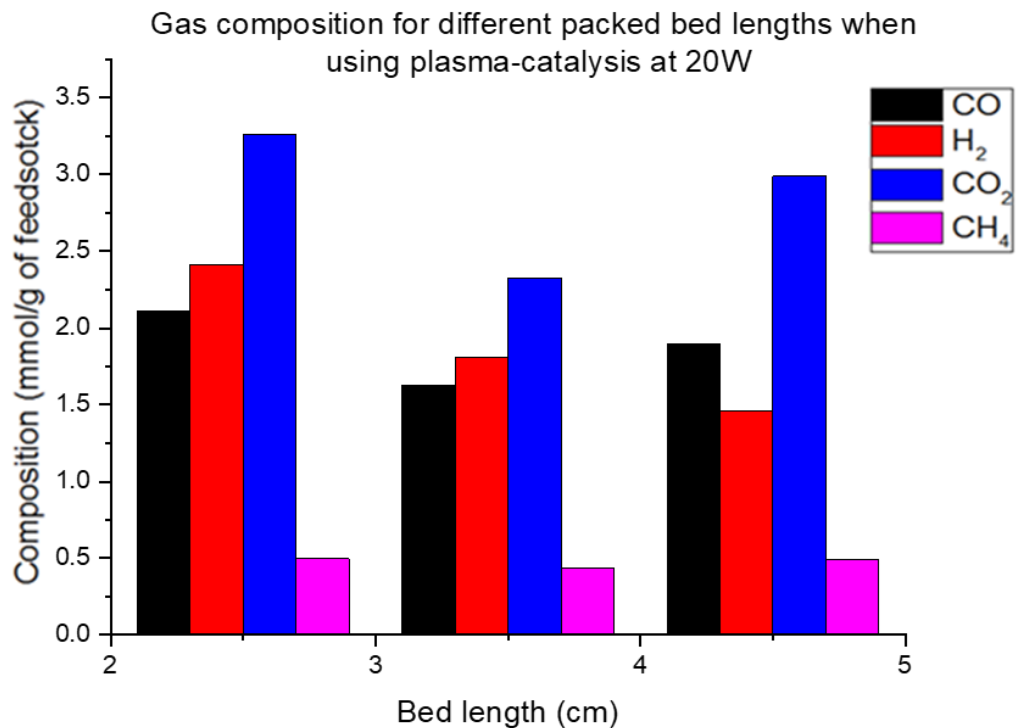
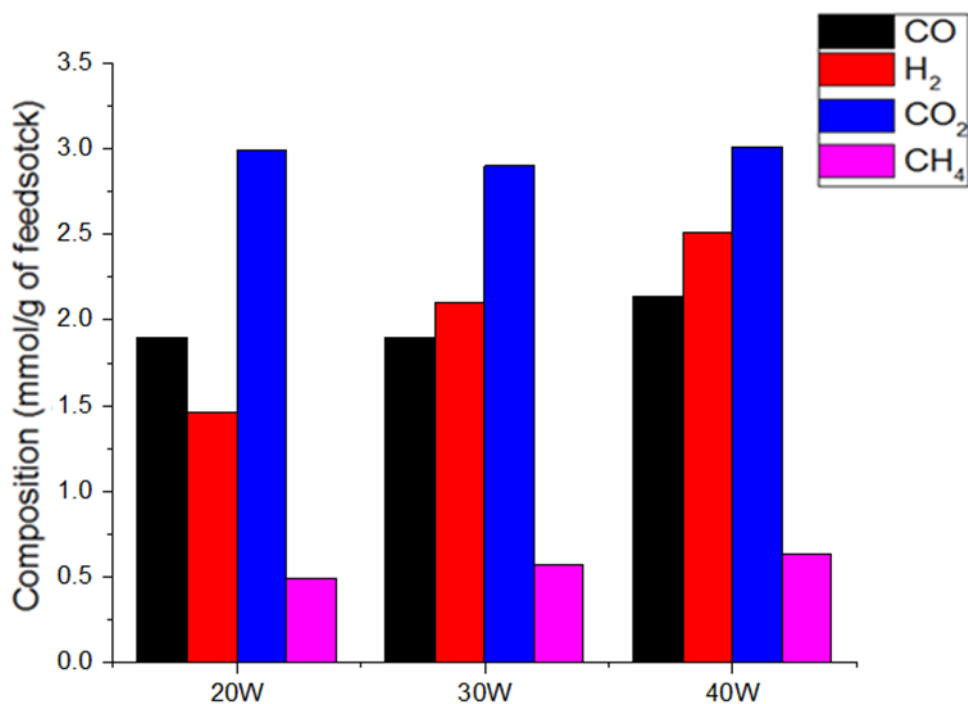


**Figure 7.2-1: Effect of packing length on the quantity of syngas produced at a power input of 20 W (black), 30 W (red) and 40 W (blue)**



a.



b.

**Figure 7.2-2: Detailed composition of produced gas for different packed bed length at 20 W (a) and different power inputs for a packed bed length of 4.5 cm (b)**

### 7.2.2 Effect on reacted catalyst

The fresh packing material, as well as the reacted packing material after reaction at different power input – 20 and 40 W – were characterised by X-ray diffraction (XRD). Figure 7.2-3 shows the XRD spectra for the fresh barium titanate, the barium titanate after reaction with a power input of 20 W and the packing material after reaction with a power input of 40 W. The most intense peaks of the barium titanate have been identified in previous publications – ICSD 29148 (Zali et al., 2014) – and matched with the experimental peaks represented in Figure 7.2-3. These peaks are at  $2\theta = 22^\circ$ ,  $31^\circ$ ,  $39^\circ$ ,  $45^\circ$ ,  $51^\circ$ ,  $56^\circ$ ,  $66^\circ$  and  $75^\circ$ . The similar chromatogram between the three packing showed a stability of the packing topology, which can be one of the reasons why barium titanate is one of the most common packing material used for packed bed DBD (Mei et al., 2015). This has also been shown by Chung et al. (2014) where perovskite structure did not significantly differ before and after plasma treatment (Chung et al., 2014).

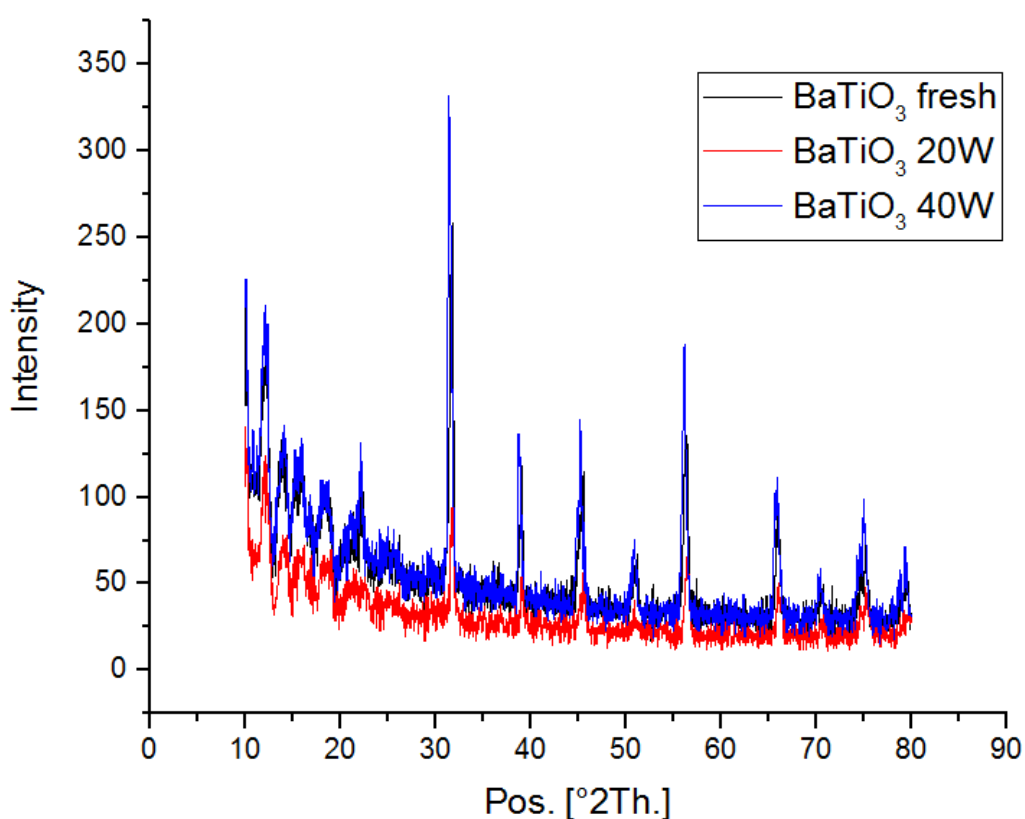


**Figure 7.2-3: XRD on fresh packing material (black), reacted packing material at 20 W (red) and reacted packing material at 40 W (blue)**

First, the diffraction peaks for the barium titanate used at a power input of 40 W were more intense than for barium titanate used at 20 W, whereas they were similar to the fresh barium titanate. This has also been observed by Stere et al. (2017), who investigated the non-thermal plasma activation of gold-based catalysts for low-temperature water-gas shift catalysts. XRD characterisation of the catalysts before and after being exposed to plasma discharge did not show any changes in the XRD patterns: the same peaks were present before and after plasma treatment with a small decrease in intensity in the 30° peaks of CeO<sub>2</sub> after plasma exposure. (Stere et al., 2017) Magureanu et al. also observed the conservation of XRD patterns after plasma treatment on alumina catalysts (Magureanu et al., 2013). However, plasma treatment can affect the XRD patterns as shown by Parastaev et al (2018) when investigating the temperature-programmed plasma surface reaction for Co supported on CeZrO<sub>4</sub> catalysts. The effect of packed bed DBD plasma discharge on the catalyst resulted into the disappearance of the Co<sub>3</sub>O<sub>4</sub> peaks on the catalyst XRD pattern after reaction, as well as an increase in Co peak intensity. (Parastaev et al., 2018) This could be due to the well-known reduction potential of plasma treatment on catalyst.

However, the main difference between the packing material used in this section and the previous catalysts used in this research and aforementioned studies is the nature of the packing used, as described by Mei et al. (2016). BaTiO<sub>3</sub> is a perovskite semiconductor photocatalyst with a band gap of 2.8-3.0 eV for tetragonal phase. Photocatalyst can be activated by the formation of electron-hole pair via the induction of a required minimum photonic energy ( $h\nu$ ) at a specific wavelength, overcoming the band gap of the material, for it to become conductive (Equation 7.3). (Mei et al., 2016) As UV radiation can be generated by plasma discharges, the use of a conductive or semi-conductive packing material can play a role, even minor, on the decomposition of organic volatile compounds.

### Equation 7.3



To determine the amount of carbonaceous coke deposited on the packing material, temperature programmed oxidation was used on the reacted packing material from experiments studying the influence of power input and packing bed length. The

associated results are represented in Figure 7.2-4. As presented in the previous section, the experiment for a power input of 20 W and a bed length of 2.5 cm resulted in the highest weight loss of 2.8 wt.% This weight loss was mainly adsorbed water and amorphous carbon deposited on the packing. For the other reacted packing materials analysed, the amount of carbon deposited was approximately 0.5 wt.% of the analysed reacted packing material. Thus, even more than for nickel supported catalysts studied in Chapter 5 and Chapter 6, the coke deposited on barium titanate was negligible in the studied parameters of this chapter.

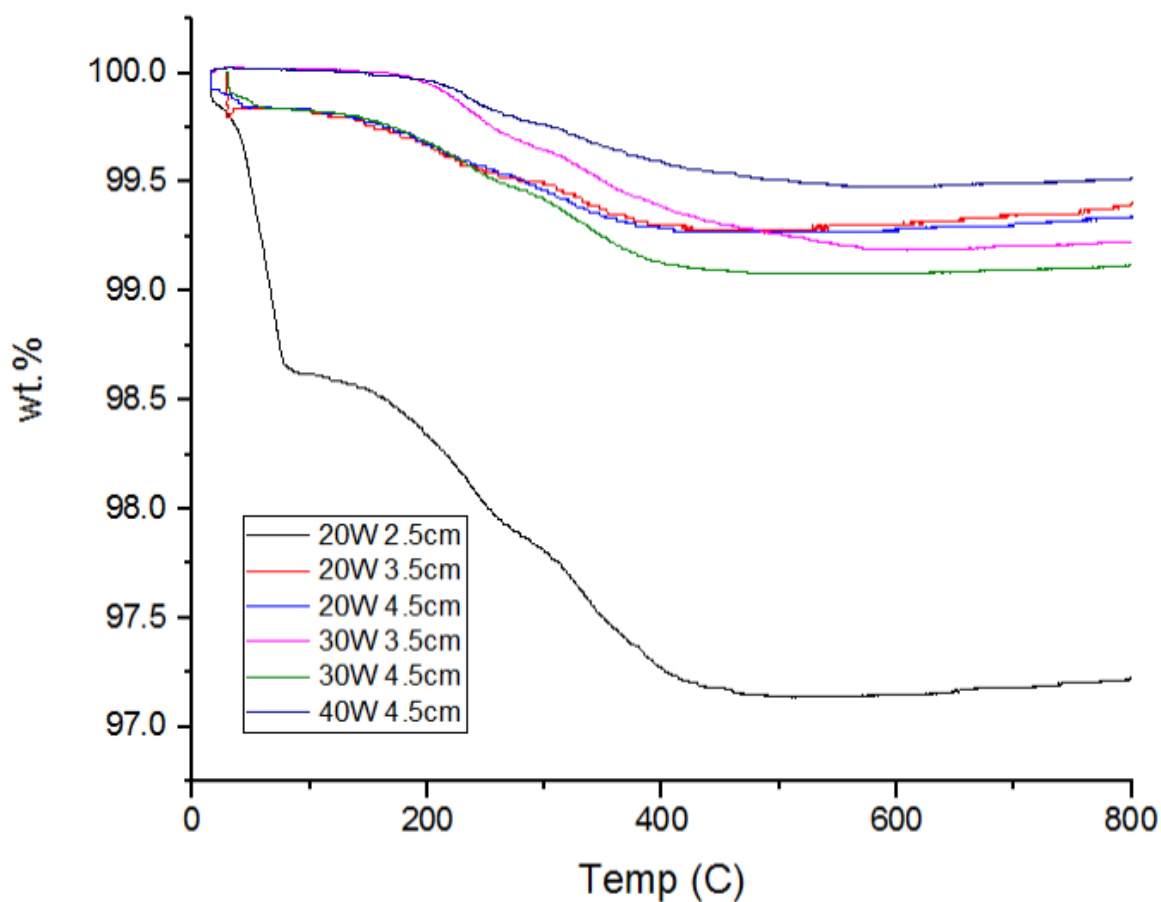


**Figure 7.2-4: Effect of packing length and power inputs on the quantity of coke deposited on the packing material**

### **7.3 Summary**

The plasma-catalysis process has been investigated to produce syngas enriched in hydrogen using biomass and its components – cellulose, hemi-cellulose and lignin – for a packed bed DBD plasma-catalytic system. The influence of plasma was investigated for the different feedstocks. The results showed that plasma-catalysis processes with a packed bed DBD configuration, led to higher production of syngas, higher production of hydrogen and lower weight loss on the reacted packing material for biomass and its components, compared to the pyrolysis-catalysis system. Within the biomass components, the use of cellulose as feedstock resulted into a higher syngas production and higher productions of carbon monoxide, carbon dioxide and hydrogen; whereas the use of lignin as feedstock resulted into a higher production of methane. However, the use of biomass as feedstock showed the highest productions of syngas and hydrogen compared to the use of other feedstocks.

The influence of power input on the packed bed DBD plasma-catalytic system showed that increasing the power input increased the syngas production, as well as the production of hydrogen, at a given packing bed length. At a given power input, the influence of packing bed length showed that increasing the packing bed length decreased the syngas production and hydrogen production. Finally, for this study, the amount of coke deposition was negligible for all parameters studied, with a variable amount of adsorbed water on the reacted packing material.

## Chapter 8: Conclusions and Future Work

This research work was divided into several sections. First, various biomasses were tested during pyrolysis experiments to identify the different products obtained from biomass pyrolysis. Wood pellet was selected from these biomasses and then used to study the effect of plasma in a dielectric barrier discharge (DBD) non-thermal plasma-catalysis system on tar reduction and production of higher quality syngas. To optimise and better understand the breakdown of product compounds, the different components of biomass – cellulose and lignin – and different operating parameters, such as power input, steam flow or catalyst size, were investigated. To further study the plasma-catalysis system, the catalyst was studied to identify a way to improve the plasma-catalysis in the DBD reactor. This study was conducted through the study of metal promoters, metal loading and catalyst support. Finally, to improve the DBD plasma-catalytic system, the experimental setup was modified into a packed bed DBD plasma-catalytic system. This new system was investigated to study the effect of plasma on tar reduction and the production of hydrogen-enriched syngas, alongside the different components of biomass – cellulose, hemi-cellulose and lignin – and different operating parameters, such as power input and packing bed length.

### 8.1 General conclusions

The conclusions presented in the following section were addressed considering the order of the Chapters and results in this research work.

#### 8.1.1 Analysis of gas and vapour products from pyrolysis of selected biomasses: wood pellets, corn stalk, peanut shell and coconut shell

The pyrolysis of various biomass feedstocks – wood pellet, corn stalk, peanut shell and coconut shell – was investigated through the analysis of their gas products and tar content via SPA method. Different feedstocks led to different results. Whereas the pyrolysis of corn stalk resulted into a higher production of gas (31 wt.%), carbon oxides ( $6.97 \text{ mmol.g}^{-1}_{\text{biomass}}$ ) and syngas ( $2.55 \text{ mmol.g}^{-1}_{\text{biomass}}$ ), wood pellet presented the highest proportion of syngas produced from total product gas and the highest hydrogen content (22 mol%) within syngas produced, compared to other biomasses.

The SPA samples from wood pellet pyrolysis showed a less complex tar content, which would be easier to study. Finally, wood pellet had the highest calorific value out of all studied biomasses.

Therefore, to study the plasma-catalytic system, wood pellet was selected, as it was the most interesting feedstock for our study, and chosen as a reference for this research project. The results from wood pellet pyrolysis were compared with the results from pyrolysis-plasma-catalysis to better understand the effect of plasma on tar compounds production and syngas production.

### **8.1.2 Study of the dielectric barrier discharge (DBD) plasma-catalysis system via the effect of plasma, the use of biomass components – cellulose and lignin – and the influence of different operating parameters**

The pyrolysis-plasma-catalysis system using woody biomass was studied for the production of hydrogen-enriched syngas and the reduction of tar compounds. The effect of plasma on the system was first investigated. The use of pyrolysis-plasma compared to the use of pyrolysis-catalysis resulted into an increase of total gas yield (+50%), as well as three times as much hydrogen yield. The introduction of catalyst to the pyrolysis-plasma system led to a small increase in total gas yield (-3%) and a further increase of hydrogen yield from  $3.48 \text{ mmol.g}^{-1}_{\text{biomass}}$  to  $3.94 \text{ mmol.g}^{-1}_{\text{biomass}}$ . The reduction of tar was also studied through the analysis of the condensed hydrocarbon tar phase. Pyrolysis-catalysis system resulted into a reduced tar content, which was further reduced by the introduction of plasma, by 64%. The pyrolysis-plasma system was shown to be more efficient than the pyrolysis-catalysis system to reduce tar, reduced by 21%. The tar reduction of hydrocarbons led to an increase of the hydrogen content within the product gas.

To demonstrate that the new system could reproduce the results obtained in the literature, toluene was used as a feedstock in the pyrolysis-plasma-catalytic system. The use of the plasma-catalytic system led to an improved reduction of toluene, whereas an increase of power input enhanced the removal efficiency of toluene. The effect of plasma was studied for the different components of biomass – cellulose and lignin. As observed for biomass, plasma-catalysis resulted into a higher syngas production (more than twice as much compared to pyrolysis-catalysis), higher

hydrogen production (from less than 1 mmol.g<sup>-1</sup><sub>biomass</sub> for pyrolysis-catalysis to more than 4 mmol.g<sup>-1</sup><sub>biomass</sub> for plasma-catalysis), lower tar content (from more than 200 mg.m<sup>-3</sup> to less than 60 mg.m<sup>-3</sup>) and lower coke deposition (from 6 wt.% to 4 wt.% of reacted catalysts). A high content of lignin in biomass might favour methane production and limit tar reduction, whereas a high content of cellulose might promote a higher carbon monoxide and syngas productions. The highest production of hydrogen was obtained when using the pyrolysis-plasma-catalysis system, with similar yields for both biomass components.

Different operating parameters were studied for the pyrolysis-plasma-catalysis system. An increasing power input up to 80 W resulted into a higher total gas yield and hydrogen content and a lower tar content, with a further reduction of tar content for pyrolysis-plasma-catalysis compared to pyrolysis-plasma. An optimum steam flow rate was demonstrated at 2 g/h for a power input of 40 W, as the saturation of the catalyst surface with water led the plasma-catalytic system to be less efficient, resulting to a decrease in total gas and hydrogen yields, and an increase in tar content. A higher particle size of the catalyst of 1 mm showed a higher syngas and hydrogen production, as well as a lower tar content due to a stronger interaction between plasma and catalyst through the increase of void space and filamentous discharges. As previously observed in catalytic cracking, the higher the catalyst/feedstock ratio, the more catalyst in the system, the highest the production of hydrogen and syngas; and the more efficient is the reduction of tars.

### **8.1.3 Study of influence of the catalyst promoters, metal loading and catalyst support on the DBD plasma-catalysis**

The effect of the catalyst on plasma-catalysis systems was investigated through the study of metal promoters, the metal loading and the catalyst supports. First, the influence of metal promoters – 5 wt.% Mg, Co, Ce, Cu, Fe and Ni – was studied on a 5 wt.% nickel supported on alumina catalyst, to investigate the impact of metal on gas production, tar reduction and reacted catalysts. Ce promoter resulted into the highest syngas (7.36 mmol.g<sup>-1</sup><sub>biomass</sub>) and hydrogen production (4.22 mmol.g<sup>-1</sup><sub>biomass</sub>), as well as the lowest tar content (less than 100 mg.m<sup>-3</sup>), whereas Cu promoter led to the lowest amount of coke deposited on the catalyst (around 5 wt.%). However, these metal

promoters did not result into a significant change compared to the results obtained for 10 wt.% Ni supported on alumina catalyst.

Second, the influence of metal loading on gas production, tar reduction and coke deposition were studied through loading of 0, 5 and 10 wt.% of nickel supported on alumina catalysts. The highest syngas production,  $7.27 \text{ mmol.g}^{-1}_{\text{biomass}}$ , was obtained for 5 wt.% of Ni on alumina, whereas 10 wt.% Ni on alumina resulted into the lowest tar content, around  $100 \text{ mg.m}^{-3}$ . The lowest amount of coke deposited, around 8 wt.%, was obtained for both Ni loadings. Nevertheless, the studied loading did not lead to a significant result change to determine a clear advantage to choosing to impregnate metal onto catalyst support.

Third, the study of the influence of the catalyst support on the pyrolysis-plasma-catalysis was investigated. Alumina, titanium oxide and Y-zeolite were selected in order to cover a wide range of catalyst support, for their properties but also their traditional use – steam reforming enhancement, photocatalysis and oil cracking and refining respectively. These supports were used on their own, as well as impregnated with 5 wt.% Ni. The highest production of syngas was obtained for alumina catalysts,  $7.27 \text{ mmol.g}^{-1}_{\text{biomass}}$  and  $7.07 \text{ mmol.g}^{-1}_{\text{biomass}}$  respectively with or without Ni impregnation. The lowest tar content was observed for Y-zeolite catalysts, about  $5 \text{ mg.m}^{-3}$  and no tar compounds detected respectively with or without addition of Ni on the catalyst surface. Titanium oxide catalysts had different results if Ni was added onto the catalyst surface or not,  $7.18 \text{ mmol.g}^{-1}_{\text{biomass}}$  and  $5.98 \text{ mmol.g}^{-1}_{\text{biomass}}$  respectively. This was due to a change of catalyst structure following the reduction of Ni supported on titanium oxide, resulted into different results for gas production, tar content and coke deposition between the two  $\text{TiO}_2$  catalysts.

The properties of the different catalyst supports were study to better understand what differentiate these supports. Their main differences were the pore size, with the smallest pore size for alumina with 3.2 nm; the dielectric constant, the highest for titanium oxide at 80; and the surface area, the highest surface area for Y-zeolite at  $423 \text{ m}^2.\text{g}^{-1}$ . Thus, alumina or small pore size supports are recommended for a higher quality of syngas production. For a low tar content, higher surface area catalyst, such as Y-zeolite, is recommended. The use of a high dielectric constant, such as titanium oxide, led to a low coke deposition. To conclude, to obtain higher quality syngas and

higher tar reduction in the studied pyrolysis-plasma-catalysis system, the support catalyst is influenced by a small pore size first, followed by a high surface area and a high dielectric constant of the chosen support.

#### **8.1.4 Study of the packed bed DBD plasma-catalytic reactor through the effect of plasma, the effect of biomass components – cellulose, hemi-cellulose and lignin – and the study of the influence of different operating parameters**

A new plasma-catalytic system was investigated to produce hydrogen enriched syngas. The effect of plasma and the influence of the components of biomass – cellulose, hemi-cellulose and lignin – were studied for a packed bed DBD plasma-catalytic reactor. The results showed that, compared to the pyrolysis-catalysis system, pyrolysis-plasma-catalysis with a packed bed DBD configuration resulted into higher syngas production, higher production of hydrogen and lower weight loss on the reacted catalyst for biomass and its components. The use of cellulose resulted into a higher production of syngas ( $4.52 \text{ mmol.g}^{-1}_{\text{biomass}}$ ) and higher production of hydrogen ( $2.42 \text{ mmol.g}^{-1}_{\text{biomass}}$ ) and carbon oxides ( $5.37 \text{ mmol.g}^{-1}_{\text{biomass}}$ ), whereas the use of lignin led to a higher methane production ( $1.49 \text{ mmol.g}^{-1}_{\text{biomass}}$ ). Thus, the use of a biomass with a high content of cellulose will show a higher production of syngas, whereas a biomass with a high lignin content will lead to a high methane production. The use of biomass, a mixture of cellulose, hemi-cellulose and lignin showed the highest production of hydrogen (from +15% compared to cellulose to +57% compared to lignin) and syngas (from +15% compared to cellulose to +87% compared to lignin) compared to the use of biomass components.

The influence of the packed bed length and power input was investigated for this new experimental setup. At a given power input, the increase of the packed bed length resulted into a decrease in the production of syngas and hydrogen. For a fixed packed bed length, an increase of power input led to an increase of hydrogen and syngas productions. The amount of coke deposited on the packing material was negligible for all studied parameters, with a variable amount of water adsorbed on the reacted packing.

### 8.1.5 General remarks

Different experimental setups have been studied and preliminary optimisation have been conducted. To identify the potential commercial and industrial use of these non-thermal plasma-catalytic systems, their energy produced/sent to plasma-catalysis was compared to the one sent into a thermal catalysis experiment, with the same operating conditions. As seen in Table 8.1-1, plasma-catalysis and thermal catalysis are comparable when looking into the production of syngas in  $\text{mmol.g}^{-1}_{\text{biomass}}.\text{MJ}^{-1}$ . Therefore, further optimisation of plasma-catalysis is necessary to be competitive against thermal gasification. Future works to optimise the plasma-catalysis system and better understand it, are described in the following section.

**Table 8.1-1: Comparison of Thermal catalysis and Plasma-catalysis for syngas production**

	<b>Syngas production (mmol/g of feedstock)</b>	<b>Energy needed MJ</b>	<b>Syngas production (mmol/g of feedstock /MJ)</b>
Thermal catalysis (800°C)	~ 28	2.7	10
Plasma catalysis	~ 10	1.3	7.5

### 8.2 Future work

During this research work, some of the original objectives and aims were modified and developed according to the obtained experimental results and the time constraints related to engineering modifications of the experimental setup. Therefore, additional tasks would need to be performed further complete the study of the plasma-catalytic systems and the mechanisms in place to reduce tar compounds and produce higher quality syngas. A brief description of the suggested future work is given below.

### **8.2.1 Analysis and study of the electrical parameters**

Further work could be carried out to study and analyse the effect of electrical parameters such as tension, intensity, frequency and energy sent to plasma reactor. This was not essential in our engineering approach, but it would be of interest to better understand the plasma.

The study of the type of plasma discharge generated in different experiments could be investigated for better information on the plasma behaviour and its properties.

### **8.2.2 Optimisation of packed-bed DBD reactor**

Further study on the packed-bed DBD reactor, with possibility to heat up the second stage plasma-catalytic reactor for more stable plasma, as well as a study of different packing materials could be carried out.

### **8.2.3 Further study of influence of the catalyst on the DBD plasma-catalysis from biomass pyrolysis**

Wider optimisation of the DBD plasma-catalysis system could be studied through the investigation of different particle size, various support and promoter combinations.

Further work could be carried out to study the influence of surface chemistry on the plasma-catalysis by studying the effect of different topology on the reduction of tar and production of hydrogen-rich syngas, or the study of molecule absorption onto the catalyst, such as water.

To demonstrate the longevity of the process, catalyst lifetime could be investigated with the study of longer experiments and/or continuous processes, which could imply the use of a fluidised bed instead of a fixed bed for biomass pyrolysis.

### **8.2.4 Use of different feedstocks within the plasma-catalytic system**

The use of RDF, plastics or other more complex waste biomasses could be studied to identify the best feedstock to use for a non-thermal plasma-catalysis system to reduce tar compounds and produce higher quality syngas.

### **8.2.5 Mechanism or pathways to draw from the decomposition of biomass pyrolysis products in plasma-catalysis system**

Currently, it is very complex to draw mechanisms or pathways for the degradation of biomass vapours within a plasma-catalytic system. As an example, the total number of reactions within a methane plasma is higher than a million. Therefore, considering the state of art, drawing the complete mechanism of biomass vapours within a non-thermal plasma catalytic system seems to be difficult. However, with further study of mixture of tar model compounds, it could be possible to draw more elaborate pathways including surface reactions on the catalyst and plasma reactions.

## References

- Abedi, A. and Dalai, A.K. 2019. Steam gasification of oat hull pellets over Ni-based catalysts: Syngas yield and tar reduction. *Fuel*.
- Abu El-Rub, Z., Bramer, E.A. and Brem, G. 2004. Review of Catalysts for Tar Elimination in Biomass Gasification Processes. *Industrial & Engineering Chemistry Research*. **43**(22), pp.6911–6919.
- Advanced Plasma Power, Cadent Gas and Progressive Energy 2017. *BioSNG Demonstration Plant - Project Close-Down Report* [Online]. Available from: <http://www2.nationalgrid.com/UK/Our-company/Innovation/Gas-distribution-innovation/NIC-Projects/BioSNG/>.
- Akande, A.J., Idem, R.O. and Dalai, A.K. 2005. Synthesis, characterization and performance evaluation of Ni/Al<sub>2</sub>O<sub>3</sub> catalysts for reforming of crude ethanol for hydrogen production. *Applied Catalysis A: General*. **287**(2), pp.159–175.
- Alalwan, H.A., Alminshid, A.H. and Aljaafari, H.A.S. 2019. Promising evolution of biofuel generations. Subject review. *Renewable Energy Focus*. **28**, pp.127–139.
- Alipour, Z., Rezaei, M. and Meshkani, F. 2014. Effect of alkaline earth promoters (MgO, CaO, and BaO) on the activity and coke formation of Ni catalysts supported on nanocrystalline Al<sub>2</sub>O<sub>3</sub> in dry reforming of methane. *Journal of Industrial and Engineering Chemistry*. **20**(5), pp.2858–2863.
- Astrup, T. and Bilitewski, B. 2010. Pyrolysis and Gasification *In*: T. H. Christensen, ed. *Solid Waste Technology & Management*, 1 & 2.
- Aziznia, A., Bozorgzadeh, H.R., Seyed-Matin, N., Baghalha, M. and Mohamadalizadeh, A. 2012. Comparison of dry reforming of methane in low temperature hybrid plasma-catalytic corona with thermal catalytic reactor over Ni/ $\gamma$ -Al<sub>2</sub>O<sub>3</sub>. *Journal of Natural Gas Chemistry*. **21**, pp.466–475.
- AZOMaterials n.d. Material Science|News|Materials. [Accessed 30 September 2019]. Available from: <https://www.azom.com/>.
- Barrett, E.P., Joyner, L.G. and Halenda, P.P. 1951. The Determination of Pore Volume and Area Distributions in Porous Substances. I. Computations from Nitrogen Isotherms. *Journal of the American Chemical Society*. **73**(1), pp.373–380.
- Bartholomew, C.H. 2001. Mechanisms of catalyst deactivation. *Applied Catalysis A: General*. **212**, pp.17–60.
- Bartholomew, C.H., Pannell, R.B. and Butler, J.L. 1980. Support and crystallite size effects in CO hydrogenation on Nickel. *Journal of Catalysis*. **65**(2), pp.335–347.
- Begum, S., Rasul, M.G. and Akbar, D. 2012. An Investigation on Thermo Chemical Conversions of SolidWaste for Energy Recovery. *World Academy of Science, Engineering and Technology*. **62**, pp.624–630.
- Belgiorno, V., De Feo, G., Della Rocca, C. and Napoli, R.M.A. 2003. Energy from gasification of solid wastes. *Waste Management*. **23**, pp.1–15.

- Bilitewski, B., Hardtle, G. and Marek, K. 1997. *Waste Management*. Springer-Verlag Berlin Heidelberg.
- Boot-Handford, M.E., Virmond, E., Florin, N.H., Kandiyoti, R. and Fennell, P.S. 2018. Simple pyrolysis experiments for the preliminary assessment of biomass feedstocks and low-cost tar cracking catalysts for downdraft gasification applications. *Biomass and Bioenergy*.
- Borchert, H., Shevchenko, E. V., Robert, A., Mekis, I., Kornowski, A., Grübel, G. and Weller, H. 2005. Determination of nanocrystal sizes: A comparison of TEM, SAXS, and XRD studies of highly monodisperse CoPt 3 particles. *Langmuir*. **21**(5), pp.1931–1936.
- Brage, C., Yu, Q., Chen, G. and Sjöström Krister 1997. Use of amino phase adsorbent for biomass tar sampling and separation. *Fuel*. **76**(2), pp.137–142.
- Bridgwater, A. V. 1996. Production of high grade fuels and chemicals from catalytic pyrolysis of biomass. *Catalysis Today*.
- Bridgwater, A. V. 2012. Review of fast pyrolysis of biomass and product upgrading. *Biomass and Bioenergy*. **38**, pp.68–94.
- Bridgwater, T. 2006. Review Biomass for energy. *Journal of the Science of Food and Agriculture*. **86**, pp.1755–1768.
- Brock, S.L., Shimojo, T., Marquez, M., Marun, C., Suib, S.L., Matsumoto, H. and Hayashi, Y. 1999. Factors Influencing the Decomposition of CO<sub>2</sub> in AC Fan-Type Plasma Reactors: Frequency, Waveform, and Concentration Effects. *Journal of Catalysis*. **184**(1), pp.123–133.
- Bromberg, L., Cohn, D.R., Rabinovich, A. and Alexeev, N. 2001. Hydrogen manufacturing using low current, non-thermal plasma boosted fuel converters. *ACS Division of Fuel Chemistry, Preprints*. **46**(1), pp.1–4.
- Buchireddy, P.R., Bricka, R.M., Rodriguez, J. and Holmes, W. 2010. Biomass gasification: Catalytic removal of tars over zeolites and nickel supported zeolites. *Energy and Fuels*. **24**(4), pp.2707–2715.
- Butler, E., Devlin, G., Meier, D. and McDonnell, K. 2011. A review of recent laboratory research and commercial developments in fast pyrolysis and upgrading. *Renewable and Sustainable Energy Reviews*. **15**(8), pp.4171–4186.
- Butterworth, T. and Allen, R.W.K. 2017. Plasma-catalyst interaction studied in a single pellet DBD reactor: Dielectric constant effect on plasma dynamics. *Plasma Sources Science and Technology*. **26**(6).
- Chae, J., Moon, S., Sun, H. and Kim, K. 1999. A study of volatile organic compounds decomposition with the use of non-thermal plasma. *KSME International ...* **13**(9), pp.647–655.
- Chang, C.-L., Bai, H. and Lu, S.-J. 2005. Destruction of Styrene in an Air Stream by Packed Dielectric Barrier Discharge Reactors. *Plasma Chemistry and Plasma Processing*. **25**(6), pp.641–657.
- Chang, J.S. 2000. Removal of NF<sub>3</sub> from semiconductor-process flue gases by tandem packed-bed plasma and adsorbent hybrid systems. *IEEE Transactions on Industry Applications*. **36**(5), pp.1251–1259.

- Chang, J.S., Lawless, P.A. and Yamamoto, T. 1991. Corona Discharge Processes. *IEEE Transactions on Plasma Science*. **19**(6), pp.1152–1166.
- Chen, D., Christensen, K.O., Ochoa-Fernández, E., Yu, Z., Tøtdal, B., Latorre, N., Monzón, A. and Holmen, A. 2005. Synthesis of carbon nanofibers: Effects of Ni crystal size during methane decomposition. *Journal of Catalysis*. **229**(1), pp.82–96.
- Chen, H.L., Lee, H.M., Chen, S.H., Chang, M.B., Yu, S.J. and Li, S.N. 2009. Removal of volatile organic compounds by single-stage and two-stage plasma catalysis systems: A review of the performance enhancement mechanisms, current status, and suitable applications. *Environmental Science and Technology*. **43**(7), pp.2216–2227.
- Chiaromonti, D., Bonini, M., Fratini, E., Tondi, G., Gartner, K., Bridgwater, A. V., Grimm, H.P., Soldaini, I., Webster, A. and Baglioni, P. 2003. Development of emulsions from biomass pyrolysis liquid and diesel and their use in engines - Part 2: tests in diesel engines. *Biomass and Bioenergy*.
- Choi, M., Cho, H.S., Srivastava, R., Venkatesan, C., Choi, D.-H. and Ryoo, R. 2006. Amphiphilic organosilane-directed synthesis of crystalline zeolite with tunable mesoporosity. *Nature materials*. **5**(9), pp.718–723.
- Christensen, K.O., Chen, D., Lødeng, R. and Holmen, A. 2006. Effect of supports and Ni crystal size on carbon formation and sintering during steam methane reforming. *Applied Catalysis A: General*. **314**(1), pp.9–22.
- Chun, Y.N., Kim, S.C. and Yoshikawa, K. 2016. Environmental Progress & Sustainable Energy. *Environmental Progress & Sustainable Energy*. **32**(3), pp.837–845.
- Chung, W.C., Pan, K.L., Lee, H.M. and Chang, M.B. 2014. Dry reforming of methane with dielectric barrier discharge and ferroelectric packed-bed reactors. *Energy and Fuels*. **28**(12), pp.7621–7631.
- Cole, H. 1970. Bragg's law and energy sensitive detectors. *Journal of Applied Crystallography*. **3**(5), pp.405–406.
- Coll, R., Salvadó, J., Farriol, X. and Montané, D. 2001. Steam reforming model compounds of biomass gasification tars: Conversion at different operating conditions and tendency towards coke formation. *Fuel Processing Technology*. **74**(1), pp.19–31.
- Conrads, H. and Schmidt, M. 2000. Plasma generation and plasma sources. *Plasma Sources Sci. Technol.* **9**, pp.441–454.
- Crocker, M. 2010. *Thermochemical conversion of biomass to liquid fuels and chemicals*.
- Czernichowski, a. 1994. Gliding arc: Applications to engineering and environment control. *Pure and Applied Chemistry*. **66**(6), pp.1301–1310.
- Czernik, S., French, R., Feik, C. and Chornet, E. 2002. Biomass Thermoconversion Processes. *Industrial & Engineering Chemistry Research*. **41**, pp.4209–4215.
- Dayton, D. 2002. A review of the literature on catalytic biomass tar destruction. *National Renewable Energy Laboratory*. (December), p.28.

- Demidyuk, V. and Whitehead, J.C. 2007. Influence of temperature on gas-phase toluene decomposition in plasma-catalytic system. *Plasma Chemistry and Plasma Processing*. **27**(1), pp.85–94.
- Demirba, A. 2002. Gaseous products from biomass by pyrolysis and gasification: Effects of catalyst on hydrogen yield. *Energy Conversion and Management*. **43**(7), pp.897–909.
- Demirbaş, A. 2000. Mechanisms of liquefaction and pyrolysis reactions of biomass. *Energy Conversion and Management*.
- Deshlahra, P., Schneider, W.F., Bernstein, G.H. and Wolf, E.E. 2011. Direct control of electron transfer to the surface-CO bond on a Pt/TiO<sub>2</sub> catalytic diode. *Journal of the American Chemical Society*. **133**, pp.16459–67.
- Diebold, J.P. and Czernik, S. 1997. Additives to lower and stabilize the viscosity of pyrolysis oils during storage. *Energy and Fuels*. **11**(5), pp.1081–1091.
- Donohue, M.D. and Aranovich, G.L. 1998. Adsorption hysteresis in porous solids. *Journal of Colloid and Interface Science*. **205**(1), pp.121–30.
- Van Durme, J., Dewulf, J., Sysmans, W., Leys, C. and Van Langenhove, H. 2007. Efficient toluene abatement in indoor air by a plasma catalytic hybrid system. *Applied Catalysis B: Environmental*. **74**(1–2), pp.161–169.
- ECN Phyllis Classification 2012. Phyllis2 - ECN Phyllis classification. [Accessed 20 July 2016]. Available from: <https://www.ecn.nl/phyllis2/>.
- Eliasson, B. and Kogelschatz, U. 1991. Nonequilibrium Volume Plasma Chemical Processing. *IEEE Transactions on Plasma Science*. **19**(6), pp.1063–1077.
- Elliott, D.C. 1986. *Analysis and Comparison of Biomass Pyrolysis - Gasification Condensates - Final Report*. PNL-5943. Richland, WA.
- Escola, J.M., Aguado, J., Serrano, D.P., Garcia, A., Peral, A., Briones, L., Calvo, R. and Fernandez, E. 2011. Catalytic hydroreforming of the polyethylene thermal cracking oil over Ni supported hierarchical zeolites and mesostructured aluminosilicates. *Applied Catalysis B: Environmental*. **106**(3–4), pp.405–415.
- European Commission 2017. 2030 Energy Strategy - European Commission. [Accessed 22 June 2017]. Available from: <https://ec.europa.eu/energy/en/topics/energy-strategy-and-energy-union/2030-energy-strategy>.
- European Commission 2010. Directive 2010/75/EU of the European Parliament and of the Council of 24 November 2010 on Industrial Emissions (integrated pollution prevention and control). *Official Journal of the European Union*.
- European Commission 2006. *Integrated Pollution Prevention and Control - Reference document on the Best Available Techniques for Waste Incineration*.
- Evans, R.J. and Milne, T.A. 1987. Molecular Characterization of the Pyrolysis of Biomass. 2. Applications. *Energy and Fuels*. **1**(4), pp.311–319.
- Fabry, F., Rehmet, C., Rohani, V. and Fulcheri, L. 2013. Waste gasification by thermal plasma: A review. *Waste and Biomass Valorization*. **4**(3), pp.421–439.
- Falkenstein, Z. 1997. The influence of ultraviolet illumination on OH formation in

- dielectric barrier discharges of Ar/O/HO: The Joshi effect. *Journal of applied physics*. **81**(February), pp.5–9.
- Fardhyanti, D.S. and Damayanti, A. 2017. Analysis of Bio-Oil Produced by Pyrolysis of Coconut Shell. *International Journal of Chemical and Molecular Engineering*. **11**(9), pp.626–629.
- Fridman, A. 2008. *Plasma chemistry*. Cambridge University Press.
- Fridman, A., Chirokov, A. and Gutsol, A. 2005. Non-thermal atmospheric pressure discharges. *Journal of Physics D: Applied Physics*. **38**(2), p.R1.
- Fridman, A. and Kennedy, L.A. 2011. *Plasma Physics and Engineering*.
- Fridman, A., Nester, S., Kennedy, L. a., Saveliev, A. and Mutaf-yardimci, O. 1999. Gliding arc gas discharge. *Progress in Energy and Combustion Science*. **25**(2), pp.211–231.
- Friedl, A., Padouvas, E., Rotter, H. and Varmuza, K. 2005. Prediction of heating values of biomass fuel from elemental composition. *Analytica Chimica Acta*. **544**(1-2 SPEC. ISS.), pp.191–198.
- Fu, P., Hu, S., Xiang, J., Sun, L., Li, P., Zhang, J. and Zheng, C. 2009. Pyrolysis of maize stalk on the characterization of chars formed under different devolatilization conditions. *Energy and Fuels*. **23**(9), pp.4605–4611.
- Gallon, H.J., Tu, X. and Whitehead, J.C. 2012. Effects of reactor packing materials on H<sub>2</sub> production by CO<sub>2</sub> reforming of CH<sub>4</sub> in a dielectric barrier discharge. *Plasma Processes and Polymers*. **9**(1), pp.90–97.
- Gani, A. and Naruse, I. 2007. Effect of cellulose and lignin content on pyrolysis and combustion characteristics for several types of biomass. *Renewable Energy*.
- Garcia, L., Benedicto, A., Romeo, E., Salvador, M.L., Arauzo, J. and Bilbao, R. 2002. Hydrogen production by steam gasification of biomass using Ni-Al coprecipitated catalysts promoted with magnesium. *Energy and Fuels*. **16**(5), pp.1222–1230.
- Gelb, L.D. and Gubbins, K.E. 2002. Pore Size Distributions in Porous Glasses: A Computer Simulation Study. *Langmuir*. **15**(2), pp.305–308.
- Gil, J., Corella, J., Aznar, M.A.P. and Caballero, M.A. 1999. Biomass gasification in atmospheric and bubbling fluidized bed: Effect of the type of gasifying agent on the product distribution. *Biomass and Bioenergy*. **17**(5), pp.389–403.
- Go, D.B. 2012. *Gaseous Ionization and Ion Transport: An Introduction to Gas Discharges*.
- Gómez-Ramírez, A., Montoro-Damas, A.M., Cotrino, J., Lambert, R.M. and González-Elipe, A.R. 2017. About the enhancement of chemical yield during the atmospheric plasma synthesis of ammonia in a ferroelectric packed bed reactor. *Plasma Processes and Polymers*. **14**(6), pp.1–8.
- Goossens, O., Dekempeneer, E., Vangeneugden, D., Van de Leest, R. and Leys, C. 2001. Application of atmospheric pressure dielectric barrier discharges in deposition, cleaning and activation. *Surface and Coatings Technology*. **142–144**, pp.474–481.

- Greenpeace International, Teske, S. and Sawyer, G.S. 2015. *Energy [R]evolution - a sustainable world energy outlook 2015*.
- Guaitella, O., Thevenet, F., Puzenat, E., Guillard, C. and Rousseau, A. 2008. C<sub>2</sub>H<sub>2</sub> oxidation by plasma/TiO<sub>2</sub> combination: Influence of the porosity, and photocatalytic mechanisms under plasma exposure. *Applied Catalysis B: Environmental*. **80**(3–4), pp.296–305.
- Guo, M. and Bi, J. 2015. Pyrolysis characteristics of corn stalk with solid heat carrier. *BioResources*. **10**(3), pp.3839–3851.
- Guo, Y.F., Ye, D.Q., Chen, K.F., He, J.C. and Chen, W.L. 2006. Toluene decomposition using a wire-plate dielectric barrier discharge reactor with manganese oxide catalyst in situ. *Journal of Molecular Catalysis A: Chemical*. **245**(1–2), pp.93–100.
- Gurevich Messina, L.I., Bonelli, P.R. and Cukierman, A.L. 2017. In-situ catalytic pyrolysis of peanut shells using modified natural zeolite. *Fuel Processing Technology*. **159**, pp.160–167.
- Gusta, E., Dalai, A.K., Uddin, M.A. and Sasaoka, E. 2009. Catalytic decomposition of biomass tars with dolomites. *Energy and Fuels*. **23**(4), pp.2264–2272.
- Han, J. and Kim, H. 2008. The reduction and control technology of tar during biomass gasification/pyrolysis: An overview. *Renewable and Sustainable Energy Reviews*. **12**(2), pp.397–416.
- Hasler, P. and Nussbaumer, T. 1999. Gas cleaning for IC engine applications from fixed bed biomass gasification. *Biomass and Bioenergy*. **16**(6), pp.385–395.
- Hensel, K. 2009. Microdischarges in ceramic foams and honeycombs. *European Physical Journal D*. **54**(2), pp.141–148.
- Hensel, K., Katsura, S. and Mizuno, A. 2005. DC Microdischarges inside porous ceramics.pdf. . **33**(2), pp.574–575.
- Hilaire, S., Wang, X., Luo, T., Gorte, R.J. and Wagner, J. 2004. A comparative study of water-gas-shift reaction over ceria-supported metallic catalysts. *Applied Catalysis A: General*. **258**(2), pp.271–276.
- Holzer, F., Kopinke, F.D. and Roland, U. 2005. Influence of ferroelectric materials and catalysts on the performance of Non-Thermal Plasma (NTP) for the removal of air pollutants. *Plasma Chemistry and Plasma Processing*. **25**(6), pp.595–611.
- Holzwarth, U. and Gibson, N. 2011. The Scherrer equation versus the ‘Debye-Scherrer equation’. *Nature Nanotechnology*. **6**(9), p.534.
- Hong, J., Chu, W., Chernavskii, P.A. and Khodakov, A.Y. 2010. Cobalt species and cobalt-support interaction in glow discharge plasma-assisted Fischer-Tropsch catalysts. *Journal of Catalysis*. **273**(1), pp.9–17.
- Howes, P., Bates, J., Landy, M., O’Brien, S., Herbert, R., Economics, O., Matthews, R. and Hogan, G. 2011. UK and Global Bioenergy Resource - Final Report. . (2).
- Hrbek, J. 2016. Status report on thermal biomass gasification in countries participating in IEA Bioenergy Task 33. . (April), p.163.

- Hu, G., Xu, S., Li, S., Xiao, C. and Liu, S. 2006. Steam gasification of apricot stones with olivine and dolomite as downstream catalysts. *Fuel Processing Technology*. **87**(5), pp.375–382.
- Hu, X., Guo, H., Gholizadeh, M., Sattari, B. and Liu, Q. 2019. Pyrolysis of different wood species: Impacts of C/H ratio in feedstock on distribution of pyrolysis products. *Biomass and Bioenergy*.
- Huber, G.W., Iborra, S. and Corma, A. 2006. Synthesis of transportation fuels from biomass: Chemistry, catalysts, and engineering. *Chemical Reviews*. **106**(9), pp.4044–4098.
- Ijadpanah-Saravy, H., Safari, M., Khodadadi-Darban, A. and Rezaei, A. 2014. Synthesis of Titanium Dioxide Nanoparticles for Photocatalytic Degradation of Cyanide in Wastewater. *Analytical Letters*. **47**(10), pp.1772–1782.
- IPCC 2014. *Summary for Policymakers*.
- Ji, L., Tang, S., Zeng, H.C., Lin, J. and Tan, K.L. 2001. CO<sub>2</sub> reforming of methane to synthesis gas over sol-gel-made Co/ $\gamma$ -Al<sub>2</sub>O<sub>3</sub> catalysts from organometallic precursors. *Applied Catalysis A: General*. **207**, pp.247–255.
- Jogan, K., Chang, J.S., Mizuno, A. and Yamamoto, T. 1993. The effect of residence time on the CO<sub>2</sub> reduction from combustion flue gasses by an AC ferroelectric packed bed reactor. *IEEE Transactions on Industry Applications*. **29**(5), pp.876–881.
- Kameshima, S., Tamura, K., Ishibashi, Y. and Nozaki, T. 2015. Pulsed dry methane reforming in plasma-enhanced catalytic reaction. *Catalysis Today*. **256**(P1), pp.67–75.
- Katyal, S., Thambimuthu, K. and Valix, M. 2003. Carbonisation of bagasse in a fixed bed reactor: Influence of process variables on char yield and characteristics. *Renewable Energy*. **28**, pp.713–725.
- Kaza, S., Yao, L., Bhada-Tata, P. and Van Woerden, F. 2018. *WHAT A WASTE 2.0 A Global Snapshot of Solid Waste Management to 2050* [Online] World Bank. Washington, DC: The World Bank Group. Available from: <https://openknowledge.worldbank.org/handle/10986/30317>.
- Kim, G.M., Lee, D.G. and Jeon, C.H. 2019. Fundamental characteristics and kinetic analysis of lignocellulosic woody and herbaceous biomass fuels. *Energies*. **12**(6).
- Kim, H.-H., Kim, J.-H. and Ogata, A. 2009. Microscopic observation of discharge plasma on the surface of zeolites supported metal nanoparticles. *Journal of Physics D: Applied Physics*. **42**(13), p.135210.
- Kim, H.-H., Oh, S.M., Ogata, A. and Futamura, S. 2004. Decomposition of benzene using Ag/TiO<sub>2</sub> packed plasma-driven catalyst reactor: influence of electrode configuration and Ag-loading amount. *Catalysis Letters*. **96**(3–4), pp.189–194.
- Kim, H.H., Ogata, A. and Futamura, S. 2005. Atmospheric plasma-driven catalysis for the low temperature decomposition of dilute aromatic compounds. *Journal of Physics D: Applied Physics*. **38**(8), pp.1292–1300.
- Kim, H.H., Ogata, A. and Futamura, S. 2006. Effect of different catalysts on the

- decomposition of VOCs using flow-type plasma-driven catalysis. *IEEE Transactions on Plasma Science*. **34**(3 PART 3), pp.984–995.
- Kim, H.H., Ogata, A. and Futamura, S. 2008. Oxygen partial pressure-dependent behavior of various catalysts for the total oxidation of VOCs using cycled system of adsorption and oxygen plasma. *Applied Catalysis B: Environmental*. **79**(4), pp.356–367.
- Kim, H.H., Teramoto, Y., Negishi, N. and Ogata, A. 2014. A multidisciplinary approach to understand the interactions of nonthermal plasma and catalyst: A review. *Catalysis Today*. **256**(P1), pp.13–22.
- Kim, H.H., Teramoto, Y., Ogata, A., Takagi, H. and Nanba, T. 2016. Plasma Catalysis for Environmental Treatment and Energy Applications. *Plasma Chemistry and Plasma Processing*. **36**(1), pp.45–72.
- Kim, H.H., Teramoto, Y., Sano, T., Negishi, N. and Ogata, A. 2015. Effects of Si/Al ratio on the interaction of nonthermal plasma and Ag/HY catalysts. *Applied Catalysis B: Environmental*. **166–167**, pp.9–17.
- Kim, H.H., Tsubota, S., Daté, M., Ogata, A. and Futamura, S. 2007. Catalyst regeneration and activity enhancement of Au/TiO<sub>2</sub> by atmospheric pressure nonthermal plasma. *Applied Catalysis A: General*. **329**, pp.93–98.
- Kinoshita, C.M., Wang, Y. and Zhou, J. 1994. Tar formation under different biomass gasification conditions. *Journal of Analytical and Applied Pyrolysis*. **29**(2), pp.169–181.
- Kirkels, A.F. and Verbong, G.P.J. 2011. Biomass gasification: Still promising? A 30-year global overview. *Renewable and Sustainable Energy Reviews*. **15**(1), pp.471–481.
- Knight, R.A. 2000. Experience with raw gas analysis from pressurized gasification of biomass. *Biomass and Bioenergy*. **18**(1), pp.67–77.
- Kotrel, S., Rosynek, M.P. and Lunsford, J.H. 1999. Intrinsic Catalytic Cracking Activity of Hexane over H - ZSM-5, H - and H - Y Zeolites. , pp.818–824.
- Kumar, A., Sharma, A. and Bhandari, P. 2014. Biomass Gasification and Syngas Utilization. *Sustainable Bioenergy Production*., pp.341–360.
- Kuronen, M., Harjula, R., Jernstro, J., Vestenius, M. and Lehto, J. 2000. Effect of the framework charge density on zeolite ion exchange selectivities. . **2**, pp.2655–2659.
- Van Laer, K. and Bogaerts, A. 2016. Fluid modelling of a packed bed dielectric barrier discharge plasma reactor. *Plasma Sources Science and Technology*. **25**(1).
- Van Laer, K. and Bogaerts, A. 2017. How bead size and dielectric constant affect the plasma behaviour in a packed bed plasma reactor: a modelling study. *Plasma Sources Science and Technology*. **26**(8).
- Langford, J.I. and Wilson, A.J.C. 1978. Scherrer after sixty years: A survey and some new results in the determination of crystallite size. *Journal of Applied Crystallography*. **11**(2), pp.102–113.
- Lee, D.H., Kim, K.T., Song, Y.H., Kang, W.S. and Jo, S. 2013. Mapping plasma

- chemistry in hydrocarbon fuel processing processes. *Plasma Chemistry and Plasma Processing*. **33**(1), pp.249–269.
- Lee, J., Sorescu, D.C. and Deng, X. 2011. Electron-Induced Dissociation of CO<sub>2</sub> on TiO<sub>2</sub> (110). *J. Am. Chem. Soc.* **133**(110), pp.10066–10069.
- Li, C. and Suzuki, K. 2009. Tar property, analysis, reforming mechanism and model for biomass gasification-An overview. *Renewable and Sustainable Energy Reviews*. **13**, pp.594–604.
- Li, Z., Johnson, M.C., Sun, M., Ryan, E.T., Earl, D.J., Maichen, W., Martin, J.I., Li, S., Lew, C.M., Wang, J., Deem, M.W., Davis, M.E. and Yan, Y. 2006. Mechanical and dielectric properties of pure-silica-zeolite low-k materials. *Angewandte Chemie - International Edition*. **45**(38), pp.6329–6332.
- Li, Z., Wu, K., Cao, J. and Wang, Y. 2017. Controlled synthesis of  $\alpha$ -Al<sub>2</sub>O<sub>3</sub> via the hydrothermal-pyrolysis method. *IOP Conference Series: Materials Science and Engineering*. **207**(1).
- Lieberman, M.A. and Lichtenberg, A.J. 2005. *Principles of Plasma Discharges and Materials Processing*.
- Lim, M.S. and Chun, Y.N. 2012. Light tar decomposition of product pyrolysis gas from sewage sludge in a gliding arc plasma reformer. *Environmental Engineering Research*. **17**(2), pp.89–94.
- Linga Reddy, E., Karuppiah, J., Biju, V.M. and Subrahmanyam, C. 2013. Catalytic packed bed non-thermal plasma reactor for the extraction of hydrogen from hydrogen sulfide. *International journal of energy research*. **37**, pp.1280–1286.
- Liu, C.J., Wang, J.X., Yu, K.L., Eliasson, B., Xia, Q., Xue, B. and Zhang, Y.H. 2002. Floating double probe characteristics of non-thermal plasmas in the presence of zeolite. *Journal of Electrostatics*. **54**(2), pp.149–158.
- Liu, L., Wang, Q., Ahmad, S., Yang, X., Ji, M. and Sun, Y. 2017. Steam reforming of toluene as model biomass tar to H<sub>2</sub>-rich syngas in a DBD plasma-catalytic system. *Journal of the Energy Institute*., pp.1–13.
- Liu, L., Wang, Q., Song, J., Ahmad, S., Yang, X. and Sun, Y. 2017. Plasma-assisted catalytic reforming of toluene to hydrogen rich syngas. *Catal. Sci. Technol.* **7**(18), pp.4216–4231.
- Liu, Q., Wang, S., Zheng, Y., Luo, Z. and Cen, K. 2008. Mechanism study of wood lignin pyrolysis by using TG-FTIR analysis. *Journal of Analytical and Applied Pyrolysis*. **82**, pp.170–177.
- Liu, S., Mei, D., Wang, L. and Tu, X. 2017. Steam reforming of toluene as biomass tar model compound in a gliding arc discharge reactor. *Chemical Engineering Journal*. **307**, pp.793–802.
- Liu, S.Y., Mei, D.H., Nahil, M.A., Gadkari, S., Gu, S., Williams, P.T. and Tu, X. 2017. Hybrid plasma-catalytic steam reforming of toluene as a biomass tar model compound over Ni/Al<sub>2</sub>O<sub>3</sub> catalysts. *Fuel Processing Technology*. **166**, pp.269–275.
- Liu, X., Yang, X., Liu, C., Chen, P., Yue, X. and Zhang, S. 2016. Low-temperature catalytic steam reforming of toluene over activated carbon supported nickel

- catalysts. *Journal of the Taiwan Institute of Chemical Engineers*. **65**, pp.233–241.
- Löfberg, A., Essakhi, A., Paul, S., Swesi, Y., Zanota, M.L., Meille, V., Pitault, I., Supiot, P., Mutel, B., Le Courtois, V. and Bordes-Richard, E. 2011. Use of catalytic oxidation and dehydrogenation of hydrocarbons reactions to highlight improvement of heat transfer in catalytic metallic foams. *Chemical Engineering Journal*. **176–177**, pp.49–56.
- Lombardi, L., Carnevale, E. and Corti, A. 2015. A review of technologies and performances of thermal treatment systems for energy recovery from waste. *Waste Management*.
- Lowell, S., Shields, J.E., Thomas, M.A. and Thommes, M. (eds.). 2004. *Characterization of Porous Solids and Powders: Surface Area, Pore Size and Density*. Kluwer Academic Publishers.
- Lucas, C., Szweczyk, D., Blasiak, W. and Mochida, S. 2004. High-temperature air and steam gasification of densified biofuels. *Biomass and Bioenergy*. **27**(6), pp.563–575.
- Magureanu, M., Dobrin, D., Mandache, N.B., Cojocaru, B. and Parvulescu, V.I. 2013. Toluene oxidation by non-thermal plasma combined with palladium catalysts. *Frontiers in Chemistry*.
- Malik, M.A., Minamitani, Y. and Schoenbach, K.H. 2005. Comparison of catalytic activity of aluminum oxide and silica gel for decomposition of volatile organic compounds (VOCs) in a plasmacatalytic reactor. *IEEE Transactions on Plasma Science*. **33**(1 I), pp.50–56.
- Marec, J. and Leprince, P. 1993. *Microwave Discharges, Fundamentals and Applications (NATO ASI Series, Series B: Physics vol 302)* New York: ( ed C. F. and M. Moisan, ed.).
- Massines, F. and Gouda, G. 1998. A comparison of polypropylene-surface treatment by filamentary, homogeneous and glow discharges in helium at atmospheric pressure. *Journal of Physics D: Applied Physics*. **31**, pp.3411–3420.
- McKee, D.W. 1983. Mechanisms of the alkali metal catalysed gasification of carbon \*. *Fuel*. **62**(2), pp.170–175.
- Mei, D. 2016. *Plasma-catalytic conversion of greenhouse gas into value-added fuels and chemicals*. University of Liverpool.
- Mei, D., Liu, S., Wang, Y., Yang, H., Bo, Z. and Tu, X. 2019. Enhanced reforming of mixed biomass tar model compounds using a hybrid gliding arc plasma catalytic process. *Catalysis Today*. **337**(February), pp.225–233.
- Mei, D., Wang, Y., Liu, S., Allati, M., Yang, H. and Tu, X. 2019. Plasma reforming of biomass gasification tars using mixed naphthalene and toluene as model compounds. *Energy Conversion and Management*. **195**(February), pp.409–419.
- Mei, D., Zhu, X., He, Y.L., Yan, J.D. and Tu, X. 2015. Plasma-assisted conversion of CO<sub>2</sub> in a dielectric barrier discharge reactor: Understanding the effect of packing materials. *Plasma Sources Science and Technology*. **24**(1), p.015011.
- Mei, D., Zhu, X., Wu, C., Ashford, B., Williams, P.T. and Tu, X. 2016. Plasma-

- photocatalytic conversion of CO<sub>2</sub> at low temperatures: Understanding the synergistic effect of plasma-catalysis. *Applied Catalysis B: Environmental*.
- Milne, T. a and Evans, R.J. 1998. Biomass Gasifier “ Tars ”: Their Nature , Formation , and Conversion. *Constraints*. (November), v.
- Mizuno, A. 2013. Generation of non-thermal plasma combined with catalysts and their application in environmental technology. *Catalysis Today*. **211**, pp.2–8.
- Moens, L., Black, S.K., Myers, M.D. and Czernik, S. 2009. Study of the neutralization and stabilization of a mixed hardwood bio-oil. *Energy and Fuels*. **23**(5), pp.2695–2699.
- Mohan, D., Pittman, C.U. and Steele, P.H. 2006. Pyrolysis of wood/biomass for bio-oil: A critical review. *Energy and Fuels*. **20**(3), pp.848–889.
- Möller, K. and Bein, T. 2013. Mesoporosity--a new dimension for zeolites. *Chemical Society reviews*. **42**(9), pp.3689–707.
- Mondal, P., Dang, G.S. and Garg, M.O. 2011. Syngas production through gasification and cleanup for downstream applications - Recent developments. *Fuel Processing Technology*. **92**(8), pp.1395–1410.
- Morf, O. 2001. *Secondary reactions of Tar during thermochemical biomass conversion*. Swiss Federal Institute of Technology Zurich.
- Nada, A.M.A. and Hassan, M.L. 2000. Thermal behavior of cellulose and some cellulose derivatives. *Polymer Degradation and Stability*.
- Narvaez, I., Orrio, A., Aznar, M.P. and Corella, J. 1996. Biomass Gasification with Air in an Atmospheric Bubbling Fluidized Bed . Effect of Six Operational Variables on the Quality of. *Ind. Eng. Chem. Res.* **35**(95), pp.2110–2120.
- NASA 2015. IRIS Mission Overview. [Accessed 12 January 2017]. Available from: [https://www.nasa.gov/mission\\_pages/iris/overview/index.html](https://www.nasa.gov/mission_pages/iris/overview/index.html).
- Neef, J., Knoef, H. and Onaji, P. 1999. *Behaviour of tar in biomass gasification systems: tar related problems and their solutions*. Novem.
- Neyts, E.C. and Bogaerts, A. 2014. Understanding plasma catalysis through modelling and simulation—a review. *Journal of Physics D: Applied Physics*. **47**(22), p.224010.
- Nozaki, T., Muto, N., Kado, S. and Okazaki, K. 2004. Dissociation of vibrationally excited methane on Ni catalyst: Part 1. Application to methane steam reforming. *Catalysis Today*. **89**(1–2), pp.57–65.
- Nunnally, T., Tsangaris, A., Rabinovich, A., Nirenberg, G., Chernets, I. and Fridman, A. 2014. Gliding arc plasma oxidative steam reforming of a simulated syngas containing naphthalene and toluene. *International Journal of Hydrogen Energy*. **39**(23), pp.11976–11989.
- Nygaard, K.J. 1965. ‘Electric wind’ gas discharge anemometer. *Review of Scientific Instruments*. **36**(9), pp.1320–1323.
- Ogata, A., Shintani, N., Mizuno, K., Kushiyama, S. and Yamamoto, T. 1999. Decomposition of benzene using a nonthermal plasma reactor packed with ferroelectric pellets. *IEEE Transactions on Industry Applications*. **35**(4),

pp.753–759.

- Oh, S.M., Kim, H.H., Einaga, H., Ogata, A., Futamura, S. and Park, D.W. 2006. Zeolite-combined plasma reactor for decomposition of toluene. *Thin Solid Films*. **506–507**, pp.418–422.
- Olivares-Marin, M. and Maroto-Valer, M. 2012. Development of adsorbents for CO<sub>2</sub> capture from waste materials: a review. *Greenhouse Gases: Science and Technology*. **2**, pp.20–35.
- Özkara-Aydinoğlu, Ş. and Aksoylu, A.E. 2010. Carbon dioxide reforming of methane over Co-X/ZrO<sub>2</sub> catalysts (X = La, Ce, Mn, Mg, K). *Catalysis Communications*. **11**(15), pp.1165–1170.
- Özkara-Aydinoğlu, Ş., Özensoy, E. and Aksoylu, A.E. 2009. The effect of impregnation strategy on methane dry reforming activity of Ce promoted Pt/ZrO<sub>2</sub>. *International Journal of Hydrogen Energy*. **34**(24), pp.9711–9722.
- Parastaev, A., Hoeben, W.F.L.M., van Heesch, B.E.J.M., Kosinov, N. and Hensen, E.J.M. 2018. Temperature-programmed plasma surface reaction: An approach to determine plasma-catalytic performance. *Applied Catalysis B: Environmental*. **239**(2018), pp.168–177.
- Paulussen, S., Verheyde, B., Tu, X., De Bie, C., Martens, T., Petrovic, D., Bogaerts, A. and Sels, B. 2010. Conversion of carbon dioxide to value-added chemicals in atmospheric pressure dielectric barrier discharges. *Plasma Sources Sci. Technol.* **19**(3).
- Perego, G. 1998. Characterization of heterogeneous catalysts by X-ray diffraction techniques. *Catalysis Today*. **41**(1–3), pp.251–259.
- Pérez, J.F., Melgar, A. and Benjumea, P.N. 2012. Effect of operating and design parameters on the gasification/combustion process of waste biomass in fixed bed downdraft reactors: An experimental study. *Fuel*. **96**, pp.487–496.
- Pettersen, R.C. 1984. The chemical composition of wood *In: American Chemical Society, ed. The Chemistry of Solid Wood.*, pp.57–125.
- Poppe, J., Völkening, S., Schaak, A., Schütz, E., Janek, J. and Imbihl, R. 1999. Electrochemical promotion of catalytic CO oxidation on Pt/YSZ catalysts under low pressure conditions. *Physical Chemistry Chemical Physics*. **1**(22), pp.5241–5249.
- Power-technology.com 2014. Power from waste - the world's biggest biomass power plants.
- Pylinina, A.I. and Mikhalenko, I.I. 2013. Activation of Cu-, Ag-, Au / ZrO<sub>2</sub> Catalysts for Dehydrogenation of Alcohols by Low-Temperature Oxygen and Hydrogen plasma. *Theoretical and Experimental Chemistry*. **49**(1), pp.60–63.
- Ray, D. and Subrahmanyam, C. 2016. CO<sub>2</sub> decomposition in a packed DBD plasma reactor: Influence of packing materials. *RSC Advances*. **6**(45), pp.39492–39499.
- Rezaei, H., Yazdanpanah, F., Lim, C.J., Lau, A. and Sokhansanj, S. 2016. Pyrolysis of ground pine chip and ground pellet particles. *Canadian Journal of Chemical Engineering*. **94**(10), pp.1863–1871.

- Rhodes, C., Hutchings, G.J. and Ward, A.M. 1995. Water-gas shift reaction: finding the mechanistic boundary. *Catalysis Today*. **23**, pp.43–58.
- Rogoff, M.J. and Screve, F. 2011. Chapter 3 - WTE technologies *In: Waste to energy*. Oxford: William Andrew, pp.21–43.
- Roth, J.R. 2001. *Industrial Plasma Engineering: Volume 2 - Applications to Nonthermal Plasma Processing*.
- Rouquerol, J., Avnir, D., Fairbridge, C.W., Everett, D.H., Haynes, J.H., Pernicone, N., Ramsay, J.D.F., Sing, K.S.W. and Unger, K.K. 1994. Recommendations for the characterization of porous solids. *Pure and Applied Chemistry*. **66**(8), pp.1739–1758.
- Rousseau, A., Guaitella, O., Röpkcke, J., Gatilova, L. V. and Tolmachev, Y.A. 2004. Combination of a pulsed microwave plasma with a catalyst for acetylene oxidation. *Applied Physics Letters*. **85**(12), pp.2199–2201.
- Rout, T., Pradhan, D., Singh, R.K. and Kumari, N. 2016. Exhaustive study of products obtained from coconut shell pyrolysis. *Journal of Environmental Chemical Engineering*. **4**, pp.3696–3705.
- Ruiz, J.A., Juárez, M.C., Morales, M.P., Muñoz, P. and Mendivil, M.A. 2013. Biomass gasification for electricity generation: Review of current technology barriers. *Renewable and Sustainable Energy Reviews*. **18**, pp.174–183.
- Sánchez-Sánchez, M.C., Navarro, R.M. and Fierro, J.L.G. 2007. Ethanol steam reforming over Ni / Mx Oy-Al<sub>2</sub>O<sub>3</sub> (M = Ce, La, Zr and Mg) catalysts: Influence of support on the hydrogen production. *International Journal of Hydrogen Energy*. **32**, pp.1462–1471.
- Schaschke, C. 2014. *A Dictionary of Chemical Engineering* [Online]. Oxford University Press. Available from: <http://www.oxfordreference.com/view/10.1093/acref/9780199651450.001.0001/acref-9780199651450>.
- Sengupta, S. and Deo, G. 2015. Modifying alumina with CaO or MgO in supported Ni and Ni-Co catalysts and its effect on dry reforming of CH<sub>4</sub>. *Journal of CO<sub>2</sub> Utilization*. **10**, pp.67–77.
- Shafizadeh, F., McGinnis, G.D. and Philpot, C.W. 1972. Thermal degradation of xylan and related model compounds. *Carbohydrate Research*. **25**(1), pp.23–33.
- Shang, S., Liu, G., Chai, X., Tao, X., Li, X., Bai, M., Chu, W., Dai, X., Zhao, Y. and Yin, Y. 2009. Research on Ni/Al<sub>2</sub>O<sub>3</sub> catalyst for CO<sub>2</sub> reforming of CH<sub>4</sub> prepared by atmospheric pressure glow discharge plasma jet. *Catalysis Today*. **148**(3–4), pp.268–274.
- Shen, Y. and Yoshikawa, K. 2013. Recent progresses in catalytic tar elimination during biomass gasification or pyrolysis - A review. *Renewable and Sustainable Energy Reviews*. **21**, pp.371–392.
- Simell, P., Kurkela, E., Stahlberg, P. and Hepola, J. 1996. Catalytic hot gas cleaning of gasification gas. *Catalysis Today*. **27**, pp.55–62.
- Simell, P.A., Leppälahti, J.K. and Bredenberg, J.B. son 1992. Catalytic purification of tarry fuel gas with carbonate rocks and ferrous materials. *Fuel*. **71**(2),

pp.211–218.

- Sing, K.S.W. 1992. Adsorption Methods for Surface Area Determination *In*: N. G. Stanley-Wood and R. W. Lines, eds. *Particle Size Analysis*. The Royal Society of Chemistry, pp.13–32.
- Sing, K.S.W. 1985. Reporting physisorption data for gas/solid systems with special reference to the determination of surface area and porosity (Recommendations 1984). *Pure and Applied Chemistry*. **57**(4), pp.603–619.
- Smith, B. 2010. A Review of the Water Gas Shift Reaction Kinetics. *International Journal of Chemical Reactor Engineering*. **8**(Review R4), pp.1–32.
- Somorjai, G.A. 1992. The experimental evidence of the role of surface restructuring during catalytic reactions. *Catalysis Letters*. **12**(1–3), pp.17–34.
- Song, H., Hu, F., Peng, Y., Li, K., Bai, S. and Li, J. 2018. Non-thermal plasma catalysis for chlorobenzene removal over CoMn/TiO<sub>2</sub> and CeMn/TiO<sub>2</sub>: Synergistic effect of chemical catalysis and dielectric constant. *Chemical Engineering Journal*. **347**(January), pp.447–454.
- de Souza-Santos, M.L. 2010. *Solid Fuels Combustion and Gasification: Modeling, Simulation, and Equipment Operations Second Edition* CRC Press. Taylor & Francis Group.
- Stere, C.E., Anderson, J.A., Chansai, S., Delgado, J.J., Goguet, A., Graham, W.G., Hardacre, C., Taylor, S.F.R., Tu, X., Wang, Z. and Yang, H. 2017. Non-Thermal Plasma Activation of Gold-Based Catalysts for Low-Temperature Water–Gas Shift Catalysis. *Angewandte Chemie - International Edition*. **56**(20), pp.5579–5583.
- Sutton, D., Kelleher, B. and Ross, J.R.H. 2001. Review of literature on catalysts for biomass gasification. *Fuel Processing Technology*. **73**(3), pp.155–173.
- Takaki, K., Chang, J.S. and Kostov, K.G. 2004. Atmospheric pressure of nitrogen plasmas in a ferro-electric packed bed barrier discharge reactor part I: Modeling. *IEEE Transactions on Dielectrics and Electrical Insulation*. **11**(3), pp.481–490.
- Takuma, T. 1991. Field behavior at a triple junction in composite dielectric arrangements. *IEEE transactions on electrical insulation*. **26**(3), pp.500–509.
- Tao, K., Ohta, N., Liu, G., Yoneyama, Y., Wang, T. and Tsubaki, N. 2013. Plasma enhanced catalytic reforming of biomass tar model compound to syngas. *Fuel*. **104**, pp.53–57.
- Tatarova, E., Bundaleska, N., Sarrette, J.P. and Ferreira, C.M. 2014. Plasmas for environmental issues: from hydrogen production to 2D materials assembly. *Plasma Sources Science and Technology*. **23**(6), p.63002.
- Tauster, S.J. and Fung, S.C. 1978. Strong metal-support interactions: Occurrence among the binary oxides of groups IIA–VB. *Journal of Catalysis*. **55**(1), pp.29–35.
- Tchobanoglous, G., Theisen, H. and Vigil, S.. 1993. *Integrated Solid Waste Management: Engineering principles and management issues*. [Online] 2nd Editio. New York: McGraw-Hill. Available from:

<https://lib.ugent.be/catalog/rug01:000312687>.

- Technical Committee CEN/TC 335 2011. BSI Standards Publication Solid biofuels — Determination of total content of carbon, hydrogen and nitrogen — Instrumental methods.
- Tendero, C., Tixier, C., Tristant, P., Desmaison, J. and Leprince, P. 2006. Atmospheric pressure plasmas: A review. *Spectrochimica Acta - Part B Atomic Spectroscopy*. **61**(1), pp.2–30.
- Tran, D.Q. and Rai, C. 1978. A kinetic model for pyrolysis of Douglas fir bark. *Fuel*. **57**(5), pp.293–298.
- Trane, R., Dahl, S., Skjøth-Rasmussen, M.S. and Jensen, A.D. 2012. Catalytic steam reforming of bio-oil. *International Journal of Hydrogen Energy*. **37**, pp.6447–6472.
- Tu, X., Gallon, Helen J., Twigg, M. V., Gorry, P.A. and Whitehead, J.C. 2011. Dry reforming of methane over a Ni/Al<sub>2</sub>O<sub>3</sub> catalyst in a coaxial dielectric barrier discharge reactor. *Journal of Physics D: Applied Physics*. **44**(27), p.274007.
- Tu, X., Gallon, Helen J and Whitehead, J.C. 2011. Electrical and spectroscopic diagnostics of a single-stage plasma-catalysis system: effect of packing with TiO<sub>2</sub>. *Journal of Physics D: Applied Physics*. **44**, p.482003.
- Tu, X. and Whitehead, J.C. 2012. Plasma-catalytic dry reforming of methane in an atmospheric dielectric barrier discharge: Understanding the synergistic effect at low temperature. *Applied Catalysis B, Environmental*. **125**, pp.439–448.
- Uzun, B.B. and Sarioğlu, N. 2009. Rapid and catalytic pyrolysis of corn stalks. *Fuel Processing Technology*. **90**, pp.705–716.
- Valdez-Nava, Z., Guillemet-Fritsch, S., Tenailleau, C., Lebey, T., Durand, B. and Chane-Ching, J.Y. 2009. Colossal dielectric permittivity of BaTiO<sub>3</sub>-based nanocrystalline ceramics sintered by spark plasma sintering. *Journal of Electroceramics*. **22**(1–3), pp.238–244.
- Wang, B., Chi, C., Xu, M., Wang, C. and Meng, D. 2017. Plasma-catalytic removal of toluene over CeO<sub>2</sub>-MnO<sub>x</sub> catalysts in an atmosphere dielectric barrier discharge. *Chemical Engineering Journal*. **322**, pp.679–692.
- Wang, D. 2013. Study of Ni/Char catalyst for biomass gasification in an updraft gasifier: influence of catalyst granular size on catalytic performance. *Bioresources*. **8**(3), pp.3479–3489.
- Wang, L. and Cheng, D. 2014. Biomass Pyrolysis and Bio-Oil Utilisation In: *Sustainable Bioenergy Production*., pp.361–383.
- Wang, L., Weller, C.L., Jones, D.D. and Hanna, M.A. 2008. Contemporary issues in thermal gasification of biomass and its application to electricity and fuel production. *Biomass and Bioenergy*. **32**(7), pp.573–581.
- Wang, N., Sun, F., Zhou, Q., Liao, D.M. and Yan, Y.W. 2019. First-principles study on hydrogen diffusion mechanism of  $\alpha$ -Al<sub>2</sub>O<sub>3</sub>/Ti<sub>2</sub>O<sub>3</sub> interface. *Fusion Engineering and Design*. **142**, pp.40–44.
- Wang, Q. and Sarkar, J. 2018. Pyrolysis behaviors of waste coconut shell and husk biomasses. *International Journal of Energy Production and Management*. **3**(1),

pp.34–43.

- Wang, S. and Lu, G.Q. 1998. Role of CeO<sub>2</sub> in Ni/CeO<sub>2</sub>-Al<sub>2</sub>O<sub>3</sub> catalysts for carbon dioxide reforming of methane. *Applied Catalysis B: Environmental*. **19**, pp.267–277.
- Wang, W., Kim, H.H., Van Laer, K. and Bogaerts, A. 2018. Streamer propagation in a packed bed plasma reactor for plasma catalysis applications. *Chemical Engineering Journal*.
- Wang, X., Wang, K., Plackowski, C.A. and Nguyen, A. V. 2016. Sulfuric acid dissolution of 4A and Na-Y synthetic zeolites and effects on Na-Y surface and particle properties. *Applied Surface Science*.
- Wang, Y., Yang, H. and Tu, X. 2019. Plasma reforming of naphthalene as a tar model compound of biomass gasification. *Energy Conversion and Management*. **187**(February), pp.593–604.
- White, L., Koo, Y., Yun, Y. and Sankar, J. 2013. TiO<sub>2</sub> deposition on AZ31 magnesium alloy using plasma electrolytic oxidation. *Journal of Nanomaterials*. **2013**.
- Whitehead, J.C. 2009. Plasma-catalysis : a solution for environmental problems ? *Ispc\_19.*, pp.13–13.
- Whitehead, J.C. 2010. Plasma catalysis: A solution for environmental problems. *Pure and Applied Chemistry*. **82**(6), pp.1329–1336.
- Williams, P.T. 2005. *Waste Treatment and Disposal* 2nd Editio. John Wiley & Sons, Ltd.
- Willis, K.P., Osada, S. and Willerton, K.L. 2010. Plasma Gasification: Lessons Learned at Eco-Valley WTE Facility. *18th Annual North American Waste-to-Energy Conference.*, pp.133–140.
- Woo Seok, K., Jin Myung, P., Yongho, K. and Sang Hee, H. 2003. Numerical study on influences of barrier arrangements on dielectric barrier discharge characteristics. *Plasma Science, IEEE Transactions on*. **31**(4), pp.504–510.
- Woolcock, P.J. and Brown, R.C. 2013. A review of cleaning technologies for biomass-derived syngas. *Biomass and Bioenergy*. **52**, pp.54–84.
- Wu, C; Williams, PT; Wang, Z; Huang, J. 2013. Pyrolysis/gasification of cellulose, hemicellulose and lignin for hydrogen production in the presence of various nickel-based catalysts. *Fuel*. **106**, pp.697–706.
- Wu, C., Wang, Z., Huang, J. and Williams, P.T. 2013. Pyrolysis/gasification of cellulose, hemicellulose and lignin for hydrogen production in the presence of various nickel-based catalysts. *Fuel*. **106**, pp.697–706.
- Wu, C. and Williams, P.T. 2010. A novel nano-Ni/SiO<sub>2</sub> catalyst for hydrogen production from steam reforming of ethanol. *Environmental Science and Technology*. **44**(15), pp.5993–5998.
- Wu, C. and Williams, P.T. 2013. Advanced Thermal Treatment of Wastes for Fuels, Chemicals and Materials Recovery *In: R. E. Hester and R. M. Harrison, eds. Waste as a Resource*. RSC Publishing, pp.1–43.

- Wu, C.C., Wu, C.I., Sturm, J.C. and Kahn, A. 1997. Surface modification of indium tin oxide by plasma treatment: An effective method to improve the efficiency, brightness, and reliability of organic light emitting devices. *Appl. Phys. Lett.* **70**(11), pp.1348–1350.
- Wu, Z., Zhu, Z., Hao, X., Zhou, W., Han, J., Tang, X., Yao, S. and Zhang, X. 2018. Enhanced oxidation of naphthalene using plasma activation of TiO<sub>2</sub>/diatomite catalyst. *Journal of Hazardous Materials.*
- Wukovits, W., Schnitzhofer, W. and Urbaniec, K. 2012. Process routes of hydrogen production from fossil and renewable resources *In: Hydrogen Production: Prospects and Processes.*, pp.43–94.
- Xu, J., Zhou, W., Li, Z., Wang, J. and Ma, J. 2009. Biogas reforming for hydrogen production over nickel and cobalt bimetallic catalysts. *International Journal of Hydrogen Energy.* **34**(16), pp.6646–6654.
- Yan, X., Liu, Y., Zhao, B., Wang, Z., Wang, Y. and Liu, C.J. 2013. Methanation over Ni/SiO<sub>2</sub>: Effect of the catalyst preparation methodologies. *International Journal of Hydrogen Energy.* **38**(5), pp.2283–2291.
- Yang, H. and Chen, H. 2015. Biomass gasification for synthetic liquid fuel production *In: R. Luque and J. G. Speight, eds. Gasification for Synthetic Fuel Production: Fundamentals, Processes and Applications.* Elsevier, pp.241–275.
- Yang, H., Yan, R., Chen, H., Lee, D.H. and Zheng, C. 2007. Characteristics of hemicellulose, cellulose and lignin pyrolysis. *Fuel.* **86**, pp.1781–1788.
- Yao, D., Wu, C., Yang, H., Hu, Q., Nahil, M.A., Chen, H. and Williams, P.T. 2014. Hydrogen production from catalytic reforming of the aqueous fraction of pyrolysis bio-oil with modified Ni-Al catalysts. *International Journal of Hydrogen Energy.* **39**(27), pp.14642–14652.
- Yao, M.H., Baird, R.J., Kunz, F.W. and Hoost, T.E. 1997. An XRD and TEM investigation of the structure of alumina-supported ceria-zirconia. *Journal of Catalysis.* **166**, pp.67–74.
- Yokoyama, T., Kogoma, M., Moriwaki, T. and Okazaki, S. 1990. The mechanism of the stabilisation of glow plasma at atmospheric pressure. *Journal of Physics D: Applied Physics.* **23**(8), pp.1125–1128.
- Yorgun, S. and Yildiz, D. 2015. Slow pyrolysis of paulownia wood: Effects of pyrolysis parameters on product yields and bio-oil characterization. *Journal of Analytical and Applied Pyrolysis.* **114**, pp.68–78.
- Yoshida, K., Okubo, M. and Yamamoto, T. 2007. Distinction between nonthermal plasma and thermal desorptions for NO<sub>x</sub> and CO<sub>2</sub>. *Applied Physics Letters.* **90**(13), pp.10–13.
- Yu, H., Zhang, Z., Li, Z. and Chen, D. 2014. Characteristics of tar formation during cellulose, hemicellulose and lignin gasification. *Fuel.* **118**, pp.250–256.
- Yu, Y., Yang, Y., Cheng, Z., Blanco, P.H., Liu, R., Bridgwater, A. V. and Cai, J. 2016. Pyrolysis of Rice husk and Corn stalk in Auger Reactor: Part 1. Characterization of Char and Gas at Various Temperatures. *Energy and Fuels.* **30**(c), pp.10568–10574.

- Zali, N.M., Mahmood, C.S., Mohamad, S.M., Foo, C.T. and Murshidi, J.A. 2014. X-ray diffraction study of crystalline barium titanate ceramics. *AIP Conference Proceedings*. **1584**(February 2015), pp.160–163.
- Zeng, Y.X., Wang, L., Wu, C.F., Wang, J.Q., Shen, B.X. and Tu, X. 2018. Low temperature reforming of biogas over K-, Mg- and Ce-promoted Ni/Al<sub>2</sub>O<sub>3</sub> catalysts for the production of hydrogen rich syngas: Understanding the plasma-catalytic synergy. *Applied Catalysis B: Environmental*. **224**(September 2017), pp.469–478.
- Zhang, C., Hu, X., Zhang, Z., Zhang, L., Dong, D., Gao, G., Westerhof, R. and Syed-Hassan, S.S.A. 2018. Steam reforming of acetic acid over Ni/Al<sub>2</sub>O<sub>3</sub> catalyst: Correlation of calcination temperature with the interaction of nickel and alumina. *Fuel*. **227**, pp.307–324.
- Zhang, C., Zhang, R., Li, X., Li, Y., Shi, W., Ren, X. and Xu, X. 2011. Bench-Scale Fluidized-Bed Fast Pyrolysis of Peanut Shell for Bio-Oil Production. *Environmental Progress & Sustainable Energy*. **30**(1), pp.11–18.
- Zhang, H., Zhu, F., Li, X., Xu, R., Li, L., Yan, J. and Tu, X. 2019. Steam reforming of toluene and naphthalene as tar surrogate in a gliding arc discharge reactor. *Journal of Hazardous Materials*.
- Zhang, R., Brown, R.C., Suby, A. and Cummer, K. 2004. Catalytic destruction of tar in biomass derived producer gas. *Energy Conversion and Management*. **45**(7–8), pp.995–1014.
- Zhang, T. and Amiridis, M.D. 1998. Hydrogen Production via the Direct Cracking of Methane over Silica-Supported Nickel Catalysts. *Applied Catalysis A: General*. **167**(2), pp.161–172.
- Zheng, G., Jiang, J., Wu, Y., Zhang, R. and Hou, H. 2003. The Mutual Conversion of CO<sub>2</sub> and CO in Dielectric Barrier Discharge (DBD). *Plasma Chemistry and Plasma Processing*. **23**(1), pp.59–68.
- Zhu, X., Gao, X., Qin, R., Zeng, Y., Qu, R., Zheng, C. and Tu, X. 2015. Plasma-catalytic removal of formaldehyde over Cu-Ce catalysts in a dielectric barrier discharge reactor. *Applied Catalysis B: Environmental*. **170–171**, pp.293–300.
- Zou, X., Chen, T., Liu, H., Zhang, P., Ma, Z., Xie, J. and Chen, D. 2017. An insight into the effect of calcination conditions on catalytic cracking of toluene over 3Fe<sub>8</sub>Ni/palygorskite: Catalysts characterization and performance. *Fuel*.